Morphological, physiological and molecular classification of mouse retinal ganglion cells

A dissertation presented

by

Mu Qiao

to

The Department of Molecular and Cellular Biology

in partial fulfillment of the requirements

for the degree of

Doctor of Philosophy

in the subject of

Biology

Harvard University

Cambridge, Massachusetts

November, 2015

Dissertation Advisor: Professor Joshua R. Sanes Mu Qiao

Morphological, physiological and molecular classification of mouse retinal ganglion cells

Abstract

Visual information is conveyed from the retina to the brain through axons of retinal ganglion cells (RGCs). There are >20 different subtypes of RGCs, each of which detects specific features. Classification of RGC subtypes is thus essential for us to understand how visual information is processed and delivered to the brain.

Here I reported my efforts in classifying different subtypes of RGCs, using morphological, physiological and molecular criteria. A combination of these criteria allowed me to successfully identify subtypes from alpha RGCs, Foxp2-positive RGCs (F-RGCs) and RGCs labeled in a transgenic mouse line W3.

First, I presented studies of classifying subtypes of alpha RGCs. Cell attached recording followed by morphology reconstruction revealed four subtypes of alpha-like RGCs: Off-sustained, Off-transient, On-sustained, On-transient subtypes, each of which has distinct morphological properties. In addition, we found osteopontin (OPN) as a molecular marker for all alpha RGCs. Following this discovery, we studied the role of OPN in alpha RGCs, Analysis showed that alpha RGCs preferentially survive and regenerate compared with other RGCs, leading us to test whether OPN can promote axon regeneration. Indeed, by combining OPN with growth factors, we were able to promote axon regenerations of RGCs.

Second, I presented work in classifying subtypes of F-RGCs, which are recognized by expressing a transcription factor, Foxp2. Combinatory expression of Foxp2 with other transcriptional factors divides F-RGCs into four subtypes, which form two pairs differing in their dendritic field sizes. Cell attached recording showed that one pair, F-mini^{on} and F-mini^{off} RGCs, are direction-selective, while the other pair,

F-midi^{on} and F-midi^{off} RGCs, are not. Thus, we identified four new subtypes of RGCs labeled by transcriptional factor Foxp2.

Third, I described initial efforts in classifying subtypes of RGCs labeled in the transgenic mouse line W3. W3 RGCs can be separated into two group based on their expression levels of fluorescent proteins, with the dimly labeled RGCs (W3D) remained uncharacterized. Initial analysis showed W3D RGCs include at least five subtypes of RGCs, which are different in their structures and physiological properties.

Lastly, I described my work in developing a molecular tool for mapping electrical synaptic connections from genetically defined neurons or neuronal subtypes, making use of a dipeptide transporter, Pept2. Cells expressing Pept2 (in a Cre-dependent way) take up a gap junction permeable fluorescent dipeptide, which then diffuses and labels the coupled cells. We tested this method in cultured cells and validated it in mouse retina using AAV carrying Cre-dependent Pept2. I applied this method to one subtype of RGCs, J-RGCs, to label their coupling partners.

Acknowledgements

I would like to thank my father Weixin Qiao and my mother Huaimin Deng, for their support in my all life. Their understanding and love is always my strength in going forward.

I must thank my wife, Zhanlei Ye, for her love, patience and support throughout our relationship. It is so lucky to have her around and she brought me more joys than I can express.

I must give my sincere thank to my thesis advisor Joshua R. Sanes, for his support and mentorship during these five years. He is a very smart and dedicated scientist and I have learned a lot from him. He spent a lot of time discussing with me about my research, and he is very supportive to my career. All these will continue to encourage me to be a good scientist and mentor in the future.

I should also acknowledge many people in the lab for their help and advice. First, I would like to thank Xin Duan and David Rousso, who were my collaborators. I learned a lot from them during the collaboration and I appreciate it. Second, I would like to thank Arjun, Jin, Jeremy, Julie, Greg, Masa, Brendan, Melanie, Sumeet, Yi-Rong, Dimitar, Emma, Irina, Tomek, Irene, Nick, Laura, Kim, Mariah, Daisy, Mallory, Dawen, Tuan, Ruth, Mili and others. It was a good experience working with them.

I also would like to thank my collaborators Fengfeng Bei, Zhigang He, Brenna Krieger and Markus Meister for their help during working out the project. It was a great experience. Hope we can collaborate again in the future!

Next, I would like to thank my thesis committee members, Venki Murthy, Richard Masland, Xiaowei Zhuang and David Ginty for taking time and serving in my committee. Also, I need to thank Venki, Xiaowei and Richard for their suggestions during each DAC meeting. Their advice was very helpful and I learned much from communications with them.

At last, I should acknowledge the directors of the department of molecular and cellular biology, Catherine Dulac and Alex Schier, for making the department a happy family and organizing different events. It is an unforgettable experience to be a graduate student in this department.

Table of Contents

List of Figures

List of Tables

Chapter 1: Introduction

1.1 Retina

1.1.1 Why retina?

One of the most important questions in neuroscience is how a given neural circuit works? To get an insightful answer to this question, the first step is to generate the part list, namely to classify neuronal subtypes within neural circuits and describe their properties. However, this is still hard to most parts of the brain due to its complexity.

The mouse retina is an attractive model for characterizing subtypes of neurons and further studying their circuits, because of the following reasons: 1. It is part of the central nervous system. But compared with other parts of the brain, it has stereotyped structure and incredible regularity across different species. 2. Neuropil and somas are well separated in the layered structure of the retina, allowing us to study specific neurons of interest easily. 3. The retina is in the back of the eye, outside the skull and thus has pleasing accessibility compared with other part of the brain. 4. The retina receives little if not any feedback inputs from other parts of the central nervous system, thus we can isolate the retina and study it alone. 5. The stimuli to the retina can be well defined by light intensity, stimulus duration and so on. Thus, I chose mouse retina as the model system to study different subtypes of neurons within a group called retinal ganglion cells.

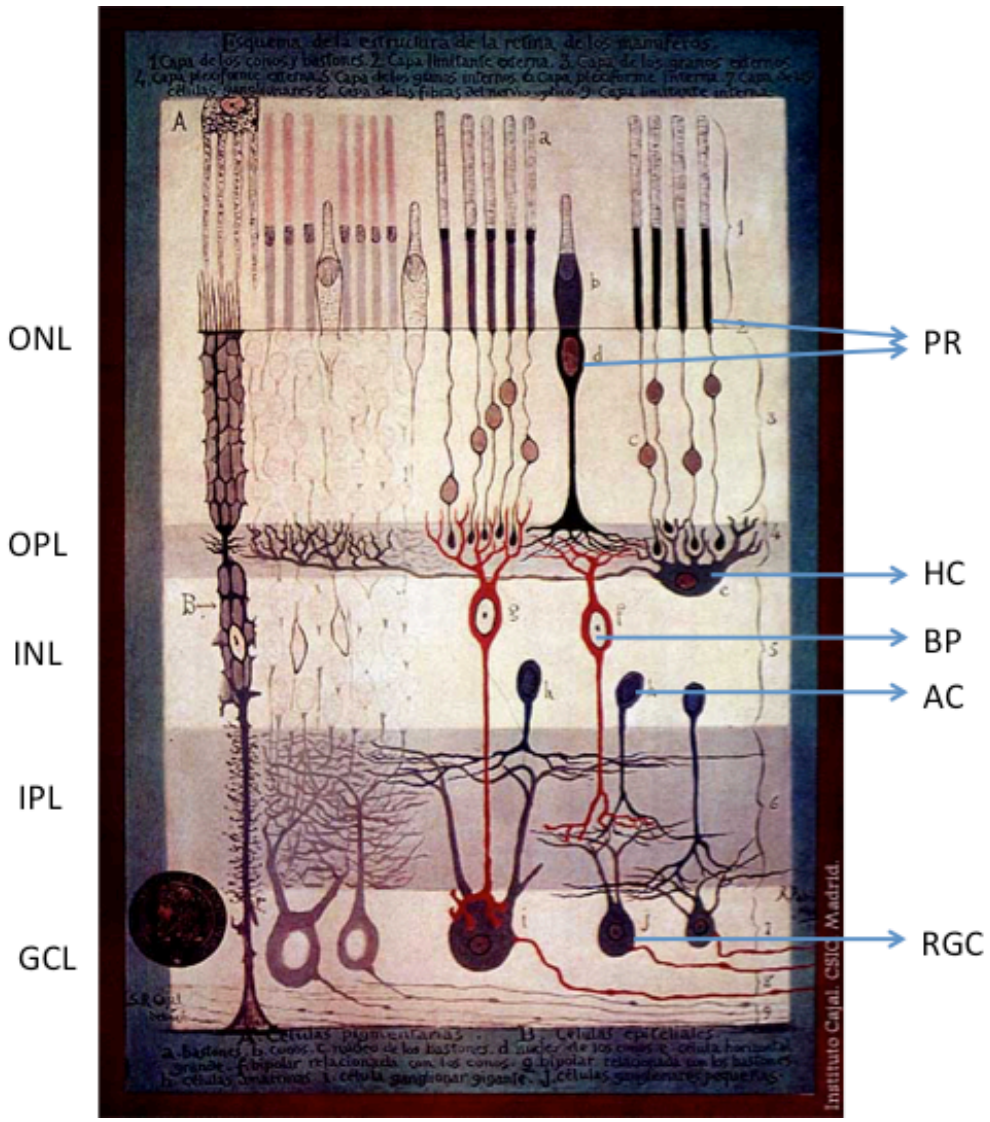

Figure 1.1: Organization of the vertebrate retina

Retina is made of five types of neurons: photoreceptors (PRs), horizontal cells (HCs), bipolar cells (BCs), amacrine cells (ACs), and retinal ganglion cells (RGCs). Their somas form three layers: outer nuclear layer (ONL) contains photoreceptors, inner nuclear layer (INL) contains horizontal cells, bipolar cells, and amacrine cells, and ganglion cell layer (GCL) contains retinal ganglion cells and displaced amacrine cells. Their processes form two layers: outer plexiform layer (OPL) contains synapses between PRs, HCs, and BPs and inner plexiform layer (IPL) contains synapses between BPs, ACs and RGCs. Modified from Santiago Ramon y Cajal,

1.1.2 Organization of the retina

The retina contains five types of neurons (**Figure 1.1**): Photoreceptors (PRs): they are major light detectors in the retina, converting light signals to electrochemical signals; Retinal ganglion cells (RGCs): they are the output neurons in the retina, sending axons to the retinal recipient regions in the brain; Three types of interneurons: horizontal cells (HCs), bipolar cells (BPs) and amacrine cells (ACs). These interneurons process information from the PRs and then transmit it to RGCs.

PRs transduce light signals into electrical signals by hyperpolarization after photon absorption. There are two subtypes of photoreceptors: rods and cones. Rods are more sensitive to light with low intensity, thus are important for night vision. Cones are more sensitive to light with high intensity, thus are important for day vision. These PRs form synapse onto HCs and BPs in the outer plexiform layer (OPL), and hyperpolarization causes decrease of glutamate release from these PRs.

BPs receive inputs from PRs, which can be split into two flavors: ON BPs express metabotropic glutamate receptors, which causes hyperpolarization after glutamate binding. Light onset causes decrease of glutamate inputs from PRs, thus leads to depolarization of these BPs. OFF BPs express ionotropic glutamate receptors, which causes depolarization after glutamate binding. In contrast with ON BPs, OFF BPs hyperpolarize after light onset. ON and OFF BPs have their axons laminate at the inner and outer halves of the inner plexiform layer (IPL) respectively, where they form synapses with ACs and RGCs (Werblin and Dowling, 1969). Thus, ON and OFF channels are physically segregated at the output level of the BPs. (Famiglietti and Kolb, 1976). BPs can be further divided into ~14 subtypes based on their morphological and physiological properties (Baden et al., 2013).

Signals from PRs to BPs can be modulated by HCs. There is only one type of HCs in mouse retina, and they form electrical coupling with each other. HCs form GABAergic synapses with PRs and BPs, and are important in contrast detection of the retina (Bloomfield and Volgyi, 2009; Masland, 2001).

Inputs from BPs are then transmitted directly onto RGCs, or indirectly through ACs. ACs process information from BPs and then transmit it to RGCs by forming synapses, which are predominately inhibitory. RGCs can be divided into three groups based on synaptic inputs they received: ON, OFF and

ON-OFF cells, which respond to light onset, offset and both onset and offset, respectively. RGCs are estimated to be of >20 subtypes, each of which is detecting certain features of the visual inputs (Gollisch and Meister, 2010; Sanes and Masland, 2015).

1.2 Retinal Ganglion Cells

1.2.1 Why so many retinal ganglion cells (RGCs)?

RGCs are strikingly diverse and there are at least 20 different subtypes of RGCs in the mouse retina (Badea and Nathans, 2004; Coombs et al., 2006; Kong et al., 2005; Masland, 2001; Sun et al., 2002; Volgyi et al., 2009). Each subtype of RGCs provides a complete coverage of the visual fields (Sanes and Zipursky, 2010). The conventional understanding of RGCs' functions is that the visual image is pre-filtered through retinal circuits, and RGCs relay this image to the brain. However, if that is the case, then a few RGC subtypes should be enough for the purpose. So why does the retina need so many different subtypes of RGCs?

A partial explanation is that the RGCs are not just relaying the pre-filtered visual image to the brain. Instead, different RGCs integrate visual information from different parallel retinal circuits, and respond to different features of the stimulus (**Figure 1.2**) (Azeredo da Silveira and Roska, 2011).

The idea that RGCs are feature detectors can be traced back to the 1950s. In 1953, Stephen Kuffler found that RGCs in cat retina could be classified into two groups based on their responses to light spots given at the center of their receptive fields: ON type responding to light onset and OFF type responding to light offset (Kuffler, 1953). This indicates that features of visual information can be divided into different subcategories, which are represented by the responses of different RGCs. Since then, researchers have had more understandings of RGCs as feature detectors. For instance, based on the preferred directions, four subtypes of ON-OFF direction-selective RGCs (Barlow and Hill, 1963; Barlow and Levick, 1965; Kim et al., 2008; Levick, 1967; Oyster and Barlow, 1967), three subtypes of ON direction-selective RGCs (Barlow and Hill, 1963; Barlow and Levick, 1965; Kim et al., 2008; Levick, 1967; Oyster and Barlow, 1967), and one type of OFF direction-selective RGCs (Kim et al., 2008), were

reported. These cells respond strongly to moving stimuli in one particular (preferred) direction but rarely respond to stimuli in the opposite (null) direction (Taylor and Vaney, 2003). This is remarkable because these RGCs do not simply respond to the visual images but respond to the feature of directions of moving objectives. There are also other examples including approach detectors and differential-motion detectors (Gollisch and Meister, 2010; Munch et al., 2009; Olveczky et al., 2003).

Evidence of different subtypes of RGCs as feature detectors also comes from morphological studies of the retina. Besides more than 20 different subtypes of RGCs, there are at least 10 different subtypes of bipolar cells and 30 different subtypes of amacrine cells (Masland, 2001). Different subtypes of RGCs connect with these different subtypes of retinal interneurons in a highly specific manner by forming synaptic connections in specific layers of the IPL. Thus, different subtypes of RGCs receive inputs from different subtypes of interneurons, and together they make up parallel circuits that compute different features of the visual stimuli. What's more, if different subtypes of RGCs serve as different feature detectors, one would expect that they have different synaptic targets in the brain. That is exactly what was found in our laboratory(Hong et al., 2011).

The view of different subtypes of RGCs as different feature detectors is strongly supported by these pieces of evidence. Thus, it is important to study different subtypes of RGCs in order to understand how the visual information is computed in the different parallel circuits in the retina. For example, we can know how certain visual information is processed by studying synaptic inputs to a certain subtype of RGCs, and we can know how this information is conveyed to brain by studying the synaptic targets of these RGCs.

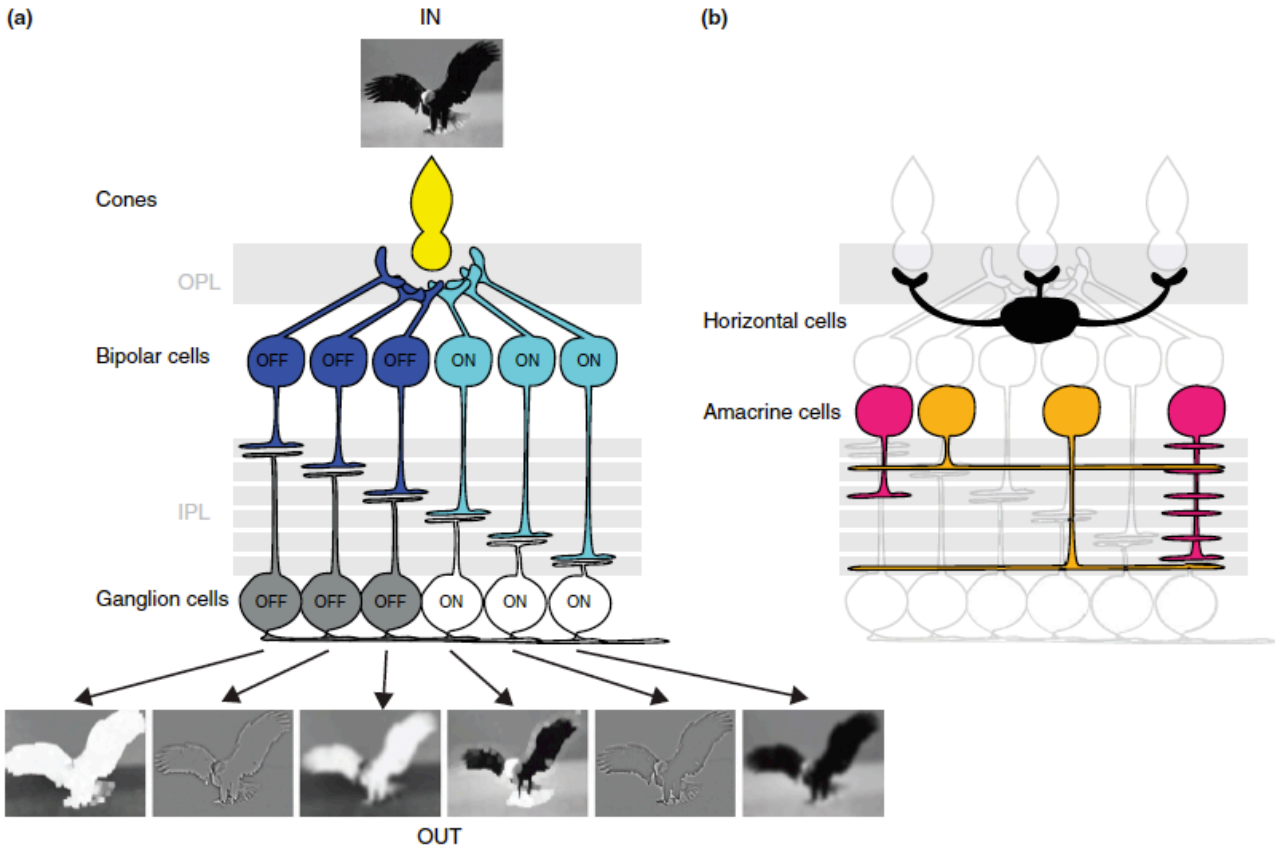

Figure 1.2: Parallel channels of the retinal ganglion cells

Different subtypes of retinal ganglion cells (RGCs) received specific inputs from different subtypes of bipolar cells (a) and different amacrine cells (b), thus form different parallel channels processing different features of the visual inputs. Adapted from Azeredo da Silveira and Roska, 2011.

1.2.2 Challenges in classifying RGCs

The remarkable diversity of RGCs makes it difficult to study them. There are more than 20 subtypes of RGCs, however, there are few if any molecular markers available marking subtypes of RGCs Without a molecular or genetic or molecular marker, it is hard to identify the same subtype of neurons from trial to trial. Further, it is hard to correlate their morphologies to their physiologies and to map their inputs and outputs. Researchers began to overcome this difficulty by generating mouse lines labeling subtypes of RGCs (Badea et al., 2009; Hattar et al., 2002; Huberman et al., 2008; Huberman et al., 2009; Kay et al., 2011a; Kim et al., 2010; Kim et al., 2008; Siegert et al., 2009; Yonehara et al., 2008). This makes it possible to study the morphologies, functions and circuits of the same subtypes of RGCs across animals and experiments.

1.2.3 Alpha RGCs

Alpha RGCs were first described morphologically in the cat retina (Boycott and Wassle, 1974), and later were discovered in many other mammalian species including mice (Peichl, Buhl et al. 1987; Peichl, Ott et al. 1987; Peichl 1991; Pang, Gao et al. 2003; Volgyi, Abrams et al. 2005). Morphologically, they look similar to the Y type retinal ganglion cells defined by their non-linear receptive fields (Enroth-Cugell and Robson, 1966). Initially, alpha RGCs can be divided into two subtypes based on their responses to light: ON alpha RGCs, and OFF alpha RGCs (Wassle et al., 1981).

In general, alpha RGCs are described as RGCs with large cell bodies and large dendritic fields. They can be labeled with antibodies against neurofilaments (Wassle, 2004). In mouse retina, although different researchers have described alpha RGCs, their sub-classifications of alpha RGCs based on the morphologies don't completely correspond to each other (Badea and Nathans, 2004; Coombs et al., 2006; Kong et al., 2005; Sun et al., 2002; Volgyi et al., 2009). For example, in Volgyi, Chheda et al. 2009, the authors define alpha RGCs as subtypes G2 and G3, while Coombs, van der List et al. (2006) define alpha RGCs as subtypes M9 and M10, which correspond to G1, G3 and part of G2, G10 subtypes in Volgyi,

Chheda et al. 2009. This indicates that morphological classifications of mouse alpha RGCs are not consistent.

Functionally, sub-classifications of mouse alpha RGCs have been more consistent. Recording indicates that there are three subtypes based on their responses to light: ON sustained alpha RGCs show sustained responses to light onset; OFF sustained RGCs show sustained responses to light offset and OFF transient show transient firing to light offset (Murphy and Rieke, 2006; Pang et al., 2003; van Wyk et al., 2009).

Two transgentic mouse lines were described to label subsets of alpha RGCs: Calretinin receptor 2 (CB2)-GFP was reported to have OFF transient alpha RGCs labeled(Huberman et al., 2008); W7, a Thy1-YFP transgenic mouse line generated in our laboratory, was reported to label OFF sustained alpha RGCs (Kim et al., 2010).

1.3 Axon regeneration

1.3.1 Challenges in promoting axon regeneration

Axon degeneration, or axon regeneration failure is a devastating disease. In central nervous system, after axotomy, axons degenerate and neurons die (Conta Steencken et al., 2011; Mansour-Robaey et al., 1994). Spinal cord injury, for example, leads to many people living with disabilities. However, current treatment for spinal cord injury is expensive and not effective.

Many previous efforts have been put on studying inhibitory factors around the injury sites that keep axons from regenerate (Yiu and He, 2003). However, studies blocking these extrinsic inhibitory factors showed limited effects in promoting axon regeneration. This suggests that neuronal intrinsic regeneration ability may also be important (Liu et al., 2011; Sun and He, 2010). So far, we know little about the molecular mechanisms behind this intrinsic regeneration ability. It is thought that neurons in young animals have remarkable growth ability, while they lose this ability in adult animals to prevent axon overgrowth. The same mechanism may also play an important role in preventing adult neuronal

regeneration (Zheng et al., 2006). Thus, it is critical to identify these molecular mechanisms in order to promote axon regeneration.

1.3.2 RGCs and optic nerve as a model to study axon regeneration

RGCs and optic nerve serves as a good model to study axon regeneration and identify molecules that can promote axon regeneration, due to the following reasons: 1. The retina and the optic nerve are extremely accessible. One can easily detach the eye ball and the optic nerve from the rest part of the brain, and the retina can be easily dissected out from the eye ball. 2. The method to label optic nerve is available and efficient. One can inject fluorescent tracers in the eye ball and the whole optic nerve can be labeled. 3. It is easy to manipulate RGCs using viral tools. One can inject virus in the eye ball and infect RGCs to overexpress or knock-down certain genes and assay the outcome of the manipulations. 4. Mouse lines with different subtypes of RGCs labeled allow us to study and compare the regeneration ability of different subtypes of RGCs. 5. It is now possible to dissociate the retina and separate different subtypes of RGCs using fluorescence-activated cell sorting (FACS), and study their gene expressions (Kay et al., 2012; Kay et al., 2011a; Kay et al., 2011b). This provides an efficient way to compare and seek molecular mechanisms behind axon regeneration.

1.4 Electrical coupling

1.4.1 Circuit wiring diagrams: chemical synaptic connections and electrical synaptic connections

Neural circuits are assembled by neurons connecting to each other through synapses. There are two kinds of synapse: chemical and electrical (**Figure. 1.3**) (Hormuzdi et al., 2004). The difference between the two kinds of synapses is obvious based on their structures:

Chemical synapses are formed by spaces called synaptic clefts which separate neurons completely. There is no cytoplasmic continuity between the neurons. Action potential at the presynaptic neuron triggers the influx of calcium and the exocytosis of neurotransmitters. Neurotransmitters, which are chemical, diffuse through the synaptic cleft and bind to their receptors at the postsynaptic neurons.

The receptors, binding to the neurotransmitters, can open the ion channels directly or indirectly. Opening of the ion channels of the postsynaptic neurons depolarize the postsynaptic neurons and even trigger the action potentials. Thus, the transmission through chemical synapses is unidirectional and relatively slow.

In contrast, electrical synapses are formed by structures called gap junction channels, which connect the cytoplasm of neurons directly. Gap junction channels are formed by connexins, which allows ions and small messenger molecules to go through. Thus, the transmission of electrical synapses is bidirectional and very fast.

As well as chemical synapses, electrical synapses are prevalent in central nervous system(Bloomfield and Volgyi, 2009; Connors and Long, 2004; Meier and Dermietzel, 2006). They can induce fast electrical communications between neurons and synchronize their activities. In addition, electrical synapses are able to induce metabolic communication by transmitting small molecules (< 1000 molecular weight) like inositol triphosphate (IP_3), cyclic AMP and small peptides (Harris, 2001). Thus, correct wiring of electrical synapses as well as chemical synapses is essential for the normal functions of the nervous system. Defects of chemical synaptic connections are involved in many neurological diseases, and malfunction of electrical synapses is associated with diseases like seizure and neurosensory deafness (Carlen et al., 2000; Laird, 2010; Nemani and Binder, 2005).

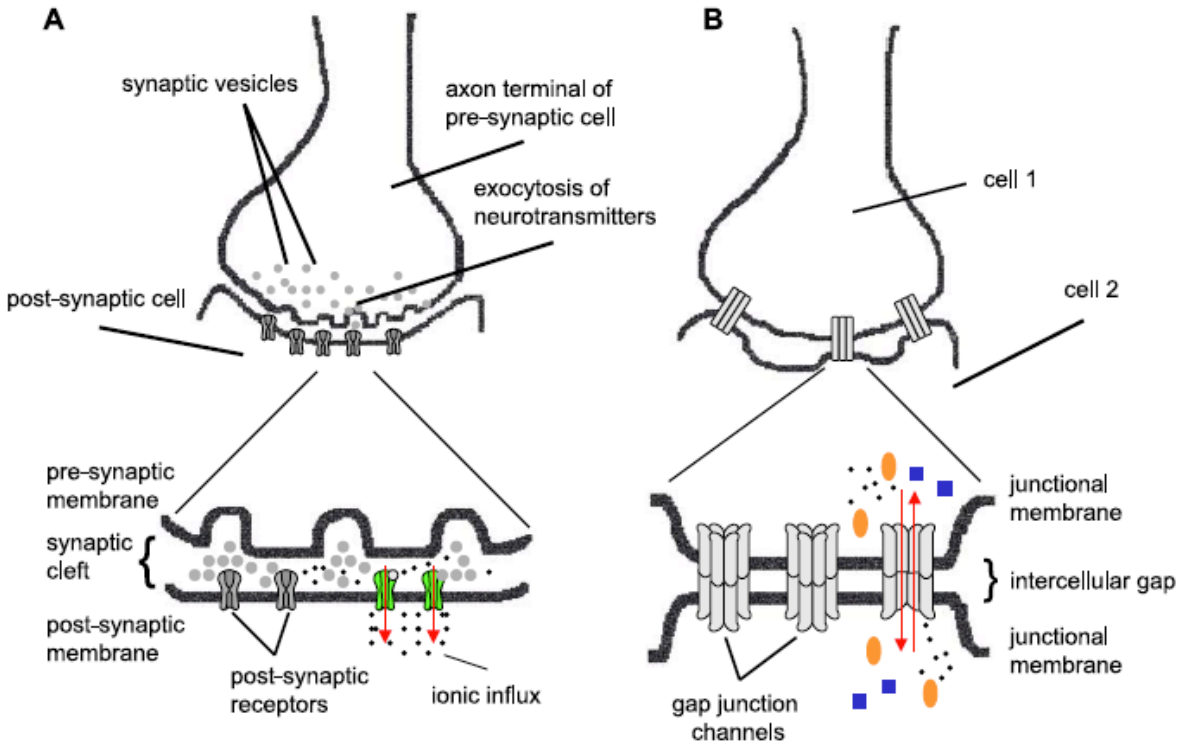

Figure 1.3: Schematic views of chemical synapses and electrical synapses

For chemical synapses, action potential at the presynaptic neuron triggers the influx of calsium and exocytosis of the neurotransmitters. The neurotransmitters diffuse through the synaptic cleft and bind to their receptors at the postsynaptic neurons. The receptors, binding to the neurotransmitters, can open the ion channels directly or indirectly. Opening of the ion channels of the postsynaptic neurons depolarize the postsynaptic neurons (A). Electrical synapses are formed by structures called gap junctions. They are channels formed by connexins. The ions and small messenger molecules can go through gap junctions directly in both directions (B). Adapted from Hormuzdi et al., 2004.

1.4.2 Challenges in studying electrical synaptic connections

However, compared to our good understanding of wiring diagram of chemical synapses, we barely know about that of electrical synapses. For example, several molecules were discovered to involve in chemical synaptic specificity (Sanes and Yamagata, 2009), but none was reported to regulate electrical synaptic specificity. Part of the reason is that compared to the many genetic tools to label chemical synaptic circuits (Boldogkoi et al., 2009; Lo and Anderson, 2011; Pickard et al., 2002; Viney et al., 2007; Wickersham et al., 2007), we have no genetic tools to label electrical synaptic connections. The current method for labeling the neurons connected by electrical synapses is intracellular injection of fluorescent tracers that go across gap junctions (Harris, 2001; Hoshi et al., 2006; Vaney, 1991). It is ineffective in two ways: 1. It can be applied to only a few cells per sample; 2. It is hard to apply to developing tissues or small cells. Therefore, a method that can efficiently and noninvasively label electrical synaptic connections from multiple neurons is desired for studying electrical synaptic connections.

1.5 Description of research

The purpose of my research is to classify subtypes of RGCs and study their properties. Specifically, I used morphological, physiological and molecular criteria to characterize three groups of RGCs called alpha RGCs, F-RGCs and W3 RGCs. Along the way, I found one molecular marker of alpha RGCs, osteopontin, that could be used to promote axon regeneration. In addition, I developed a genetic molecular method that can trace neurons connected by electrical synapses, and applied this method to a subtype of RGCs called J-RGCs.

In Chapters 2, 3, 4, 5, I will describe my efforts in classify alpha RGCs (Chapter 2), F-RGCs (Chapter 4) and W3 RGCs (Chapter 5). I classified these cells based on their morphological and physiological properties and identified molecular markers to label them. Following the work on alpha RGCs, I will describe work in studying the role of osteopontin, a molecular marker of alpha RGCs, which can be used to promote axon regeneration (Chapter 3).

In Chapter 6, I will describe a molecular tool I developed to label electrical synaptic connections from genetically defined neurons. This method allowed us to study electrical synaptic connections from subtypes of RGCs, and I applied it to a subtype of RGCs called J-RGCs.

1.6 References:

Azeredo da Silveira, R., and Roska, B. (2011). Cell types, circuits, computation. Curr Opin Neurobiol *21*, 664-671.

Badea, T.C., Hua, Z.L., Smallwood, P.M., Williams, J., Rotolo, T., Ye, X., and Nathans, J. (2009). New mouse lines for the analysis of neuronal morphology using CreER(T)/loxP-directed sparse labeling. PLoS One *4*, e7859.

Badea, T.C., and Nathans, J. (2004). Quantitative analysis of neuronal morphologies in the mouse retina visualized by using a genetically directed reporter. J Comp Neurol *480*, 331-351.

Baden, T., Berens, P., Bethge, M., and Euler, T. (2013). Spikes in mammalian bipolar cells support temporal layering of the inner retina. Curr Biol *23*, 48-52.

Barlow, H.B., and Hill, R.M. (1963). Selective sensitivity to direction of movement in ganglion cells of the rabbit retina. Science *139*, 412-414.

Barlow, H.B., and Levick, W.R. (1965). The mechanism of directionally selective units in rabbit's retina. J Physiol *178*, 477-504.

Bloomfield, S.A., and Volgyi, B. (2009). The diverse functional roles and regulation of neuronal gap junctions in the retina. Nat Rev Neurosci *10*, 495-506.

Boldogkoi, Z., Balint, K., Awatramani, G.B., Balya, D., Busskamp, V., Viney, T.J., Lagali, P.S., Duebel, J., Pasti, E., Tombacz, D.*, et al.* (2009). Genetically timed, activity-sensor and rainbow transsynaptic viral tools. Nat Methods *6*, 127-130.

Boycott, B.B., and Wassle, H. (1974). The morphological types of ganglion cells of the domestic cat's retina. J Physiol *240*, 397-419.

Carlen, P.L., Skinner, F., Zhang, L., Naus, C., Kushnir, M., and Perez Velazquez, J.L. (2000). The role of gap junctions in seizures. Brain Res Brain Res Rev *32*, 235-241.

Connors, B.W., and Long, M.A. (2004). Electrical synapses in the mammalian brain. Annu Rev Neurosci *27*, 393-418.

Conta Steencken, A.C., Smirnov, I., and Stelzner, D.J. (2011). Cell survival or cell death: differential vulnerability of long descending and thoracic propriospinal neurons to low thoracic axotomy in the adult rat. Neuroscience *194*, 359-371.

Coombs, J., van der List, D., Wang, G.Y., and Chalupa, L.M. (2006). Morphological properties of mouse retinal ganglion cells. Neuroscience *140*, 123-136.

Enroth-Cugell, C., and Robson, J.G. (1966). The contrast sensitivity of retinal ganglion cells of the cat. J Physiol *187*, 517-552.

Famiglietti, E.V., and Kolb, H. (1976). Structural basis for ON-and OFF-center responses in retinal ganglion cells. Science *194*, 193-195.

Gollisch, T., and Meister, M. (2010). Eye smarter than scientists believed: neural computations in circuits of the retina. Neuron *65*, 150-164.

Harris, A.L. (2001). Emerging issues of connexin channels: biophysics fills the gap. Q Rev Biophys *34*, 325-472.

Hattar, S., Liao, H.W., Takao, M., Berson, D.M., and Yau, K.W. (2002). Melanopsin-containing retinal ganglion cells: architecture, projections, and intrinsic photosensitivity. Science *295*, 1065-1070.

Hong, Y.K., Kim, I.J., and Sanes, J.R. (2011). Stereotyped axonal arbors of retinal ganglion cell subsets in the mouse superior colliculus. J Comp Neurol *519*, 1691-1711.

Hormuzdi, S.G., Filippov, M.A., Mitropoulou, G., Monyer, H., and Bruzzone, R. (2004). Electrical synapses: a dynamic signaling system that shapes the activity of neuronal networks. Biochim Biophys Acta *1662*, 113-137.

Hoshi, H., O'Brien, J., and Mills, S.L. (2006). A novel fluorescent tracer for visualizing coupled cells in neural circuits of living tissue. J Histochem Cytochem *54*, 1169-1176.

Huberman, A.D., Manu, M., Koch, S.M., Susman, M.W., Lutz, A.B., Ullian, E.M., Baccus, S.A., and Barres, B.A. (2008). Architecture and activity-mediated refinement of axonal projections from a mosaic of genetically identified retinal ganglion cells. Neuron *59*, 425-438.

Huberman, A.D., Wei, W., Elstrott, J., Stafford, B.K., Feller, M.B., and Barres, B.A. (2009). Genetic identification of an On-Off direction-selective retinal ganglion cell subtype reveals a layer-specific subcortical map of posterior motion. Neuron *62*, 327-334.

Kay, J.N., Chu, M.W., and Sanes, J.R. (2012). MEGF10 and MEGF11 mediate homotypic interactions required for mosaic spacing of retinal neurons. Nature *483*, 465-469.

Kay, J.N., De la Huerta, I., Kim, I.J., Zhang, Y., Yamagata, M., Chu, M.W., Meister, M., and Sanes, J.R. (2011a). Retinal ganglion cells with distinct directional preferences differ in molecular identity, structure, and central projections. J Neurosci *31*, 7753-7762.

Kay, J.N., Voinescu, P.E., Chu, M.W., and Sanes, J.R. (2011b). Neurod6 expression defines new retinal amacrine cell subtypes and regulates their fate. Nat Neurosci *14*, 965-972.

Kim, I.J., Zhang, Y., Meister, M., and Sanes, J.R. (2010). Laminar restriction of retinal ganglion cell dendrites and axons: subtype-specific developmental patterns revealed with transgenic markers. J Neurosci *30*, 1452-1462.

Kim, I.J., Zhang, Y., Yamagata, M., Meister, M., and Sanes, J.R. (2008). Molecular identification of a retinal cell type that responds to upward motion. Nature *452*, 478-482.

Kong, J.H., Fish, D.R., Rockhill, R.L., and Masland, R.H. (2005). Diversity of ganglion cells in the mouse retina: unsupervised morphological classification and its limits. J Comp Neurol *489*, 293-310.

Kuffler, S.W. (1953). Discharge patterns and functional organization of mammalian retina. J Neurophysiol *16*, 37-68.

Laird, D.W. (2010). The gap junction proteome and its relationship to disease. Trends Cell Biol *20*, 92-101.

Levick, W.R. (1967). Receptive fields and trigger features of ganglion cells in the visual streak of the rabbits retina. J Physiol *188*, 285-307.

Liu, K., Tedeschi, A., Park, K.K., and He, Z. (2011). Neuronal intrinsic mechanisms of axon regeneration. Annu Rev Neurosci *34*, 131-152.

Lo, L., and Anderson, D.J. (2011). A Cre-dependent, anterograde transsynaptic viral tracer for mapping output pathways of genetically marked neurons. Neuron *72*, 938-950.

Mansour-Robaey, S., Clarke, D.B., Wang, Y.C., Bray, G.M., and Aguayo, A.J. (1994). Effects of ocular injury and administration of brain-derived neurotrophic factor on survival and regrowth of axotomized retinal ganglion cells. Proceedings of the National Academy of Sciences of the United States of America *91*, 1632-1636.

Masland, R.H. (2001). The fundamental plan of the retina. Nat Neurosci *4*, 877-886.

Meier, C., and Dermietzel, R. (2006). Electrical synapses--gap junctions in the brain. Results Probl Cell Differ *43*, 99-128.

Munch, T.A., da Silveira, R.A., Siegert, S., Viney, T.J., Awatramani, G.B., and Roska, B. (2009). Approach sensitivity in the retina processed by a multifunctional neural circuit. Nat Neurosci *12*, 1308-1316.

Murphy, G.J., and Rieke, F. (2006). Network variability limits stimulus-evoked spike timing precision in retinal ganglion cells. Neuron *52*, 511-524.

Nemani, V.M., and Binder, D.K. (2005). Emerging role of gap junctions in epilepsy. Histol Histopathol *20*, 253-259.

Olveczky, B.P., Baccus, S.A., and Meister, M. (2003). Segregation of object and background motion in the retina. Nature *423*, 401-408.

Oyster, C.W., and Barlow, H.B. (1967). Direction-selective units in rabbit retina: distribution of preferred directions. Science *155*, 841-842.

Pang, J.J., Gao, F., and Wu, S.M. (2003). Light-evoked excitatory and inhibitory synaptic inputs to ON and OFF alpha ganglion cells in the mouse retina. J Neurosci *23*, 6063-6073.

Pickard, G.E., Smeraski, C.A., Tomlinson, C.C., Banfield, B.W., Kaufman, J., Wilcox, C.L., Enquist, L.W., and Sollars, P.J. (2002). Intravitreal injection of the attenuated pseudorabies virus PRV Bartha results in infection of the hamster suprachiasmatic nucleus only by retrograde transsynaptic transport via autonomic circuits. J Neurosci *22*, 2701-2710.

Sanes, J.R., and Masland, R.H. (2015). The types of retinal ganglion cells: current status and implications for neuronal classification. Annu Rev Neurosci *38*, 221-246.

Sanes, J.R., and Yamagata, M. (2009). Many paths to synaptic specificity. Annu Rev Cell Dev Biol *25*, 161-195.

Sanes, J.R., and Zipursky, S.L. (2010). Design principles of insect and vertebrate visual systems. Neuron *66*, 15-36.

Siegert, S., Scherf, B.G., Del Punta, K., Didkovsky, N., Heintz, N., and Roska, B. (2009). Genetic address book for retinal cell types. Nat Neurosci *12*, 1197-1204.

Sun, F., and He, Z. (2010). Neuronal intrinsic barriers for axon regeneration in the adult CNS. Curr Opin Neurobiol *20*, 510-518.

Sun, W., Li, N., and He, S. (2002). Large-scale morphological survey of mouse retinal ganglion cells. J Comp Neurol *451*, 115-126.

Taylor, W.R., and Vaney, D.I. (2003). New directions in retinal research. Trends Neurosci *26*, 379-385.

van Wyk, M., Wassle, H., and Taylor, W.R. (2009). Receptive field properties of ON- and OFF-ganglion cells in the mouse retina. Vis Neurosci *26*, 297-308.

Vaney, D.I. (1991). Many diverse types of retinal neurons show tracer coupling when injected with biocytin or Neurobiotin. Neurosci Lett *125*, 187-190.

Viney, T.J., Balint, K., Hillier, D., Siegert, S., Boldogkoi, Z., Enquist, L.W., Meister, M., Cepko, C.L., and Roska, B. (2007). Local retinal circuits of melanopsin-containing ganglion cells identified by transsynaptic viral tracing. Curr Biol *17*, 981-988.

Volgyi, B., Chheda, S., and Bloomfield, S.A. (2009). Tracer coupling patterns of the ganglion cell subtypes in the mouse retina. J Comp Neurol *512*, 664-687.

Wassle, H. (2004). Parallel processing in the mammalian retina. Nat Rev Neurosci *5*, 747-757.

Wassle, H., Boycott, B.B., and Illing, R.B. (1981). Morphology and mosaic of on- and off-beta cells in the cat retina and some functional considerations. Proc R Soc Lond B Biol Sci *212*, 177-195.

Werblin, F.S., and Dowling, J.E. (1969). Organization of the retina of the mudpuppy, Necturus maculosus. II. Intracellular recording. J Neurophysiol *32*, 339-355.

Wickersham, I.R., Lyon, D.C., Barnard, R.J., Mori, T., Finke, S., Conzelmann, K.K., Young, J.A., and Callaway, E.M. (2007). Monosynaptic restriction of transsynaptic tracing from single, genetically targeted neurons. Neuron *53*, 639-647.

Yiu, G., and He, Z. (2003). Signaling mechanisms of the myelin inhibitors of axon regeneration. Curr Opin Neurobiol *13*, 545-551.

Yonehara, K., Shintani, T., Suzuki, R., Sakuta, H., Takeuchi, Y., Nakamura-Yonehara, K., and Noda, M. (2008). Expression of SPIG1 reveals development of a retinal ganglion cell subtype projecting to the medial terminal nucleus in the mouse. PLoS One *3*, e1533.

Zheng, B., Lee, J.K., and Xie, F. (2006). Genetic mouse models for studying inhibitors of spinal axon regeneration. Trends Neurosci *29*, 640-646.

Chapter 2: Four alpha ganglion cell types in mouse retina: function, structure, and molecular signature

Preface:

The work presented in this chapter was collaboration between Brenna Krieger, a former graduate student in Markus Meister lab and David Rousso, a postdoctoral fellow in Josh Sanes lab. Brenna Krieger and I independently recorded from alpha RGCs labeled in Kcng4-Cre mouse lines and found four subtypes of alpha RGCs. We dye-filled these cells to show their morphologies. I performed initial screening for molecular markers of alpha RGCs and found osteopontin, PV and Brn3 factors. I also analyzed other transgenic animals labeling alpha RGCs, such as W7 and CB2-GFP lines. David Rousso performed screening for other molecular markers of alpha RGCs and analyzed their mosaics. Together, this leads to a paper written by Brenna Krieger, Markus Meister, Josh Sanes and me. This paper is in preparation and close to being submitted.

2.1 Abstract

Visual information is conveyed to the brain through axons of retinal ganglion cells (RGCs). There are >20 different subtypes of RGCs, forming parallel channels detecting different features of the visual world. In order to understand how brain processes visual information, it is important to characterize RGC subtypes. Here we focused on alpha RGCs, a group of RGCs with large somata, stout axons and dendritic fields. We recorded alpha RGCs labeled in a mouse line Kcng4-Cre, and reconstructed their morphologies after recording. We found three known alpha RGC subtypes reported previously: On-sustained, Off-sustained and Off-transient (Pang et al., 2003), and a new subtypes: Off-transient, each of which has distinct morphological and physiological properties. Molecular analysis revealed molecular markers for three alpha RGC subtypes and genetic analysis showed alpha RGCs labeled in Kcng4-Cre line included subtypes of alpha RGCs labeled in CB2-GFP line and W7 line (Huberman et al., 2008; Kim et al., 2010).

2.2 Introduction

The retina communicates visual information to the brain through the action potentials of retinal ganglion cells. This population of neurons consists of more than 25 distinct types, each of which covers the retina to reliably encode its part of the visual message. Among the best recognized types are the so-called alpha ganglion cells. Although their characteristics vary from species to species, they are recognizable as a distinct morphological class by their large cell bodies, stout dendrites and axons, large mono-stratified dendritic arbors, and high levels of neurofilament proteins (Peichl, 1991). Alpha cells also share physiological properties: their visual responses are characterized by a short response latency and fast conducting axons. Thus the alpha cells are among the first to signal a new stimulus to the brain. Retinal ganglion cells with alpha-like morphology have now been confirmed in the retinas of over 20 mammalian species including humans (Peichl, 1989, 1991; Peichl et al., 1987a; Peichl et al., 1987b; Straznicky et al., 1992; Wassle et al., 1981). This suggests that they play an essential role in visual processing.

Despite the considerable attention focused on this class of ganglion cells, some basic uncertainties remain. One question regards the number of cell types in this class. Early work on cat and rabbit retina described two structural types, distinct primarily by the level of dendritic stratification in the inner plexiform layer. These were identified with two functional types, the On- and Off-brisk-transient cells, named thus for their rapid light response. Further morphological analysis in the rabbit retina suggested there may actually be 4 alpha types, with dendrites stratified at 4 levels, neatly symmetric around the On-Off division of the IPL. These additional types were not, however, characterized physiologically. In the mouse retina, the consensus in the literature describes three alpha types. Their visual responses are Off-Transient, Off-Sustained, and On-Sustained. If correct, this would imply an odd asymmetry of functional coverage, with an Off-channel that reports both transient and sustained changes, and an On-channel reporting only sustained signals. The mouse has become an increasingly important model animal in visual neuroscience, including an entire brain institute dedicated to understanding its visual cortex. Because the

alpha cells provide a privileged pathway to the thalamus and visual cortex, there is great value in understanding the visual signals carried by this population.

One obstacle to a fuller understanding of the alpha cells has been the absence of a genetic handle on the entire population. This limits one's ability to target them for physiological recordings or to manipulate them prospectively. Here we used a mouse line that labels a small fraction of RGCs with the expression of Cre recombinase. We found that this line includes all the previously known alpha ganglion cell types. By targeted recording we discovered a fourth type in this class with different visual responses. Furthermore, we identified a new feature of spike generation common to all the alpha types that points to complex intracellular dynamics. Finally, we used morphological and mosaic criteria to provide evidence that each of the four groups constitutes an authentic cell type. A comparison of structural and functional properties across all four types reveals a pleasing symmetry in neural coding by this important class of ganglion cells.

2.3 Results

2.3.1 The KCNG4-Cre mouse line labels four types of alpha RGCs

We made use of a mouse line in which the gene for Cre recombinase was inserted into the locus encoding a potassium channel modifier, kcng4 (Duan et al., 2014).After crosses to a reporter line Thy1-stop-YFP (Buffelli et al., 2003), double-transgenic retinas expressed fluorescent protein in subsets of neurons from all three cellular layers. The Thy1-stop-YFP reporter produced a more restricted pattern limited to some RGCs, bipolar cells, and amacrine cells (Duan et al., 2015). In this line, the labeled neurons in the ganglion cell layer were primarily RGCs with large somata and stout dendrites. These features are suggestive of alpha ganglion cells (Peichl et al., 1991). In addition, these RGCs were labeled with antibodies to neurofilaments (SMI-32) and to osteopontin, which are markers of aRGCs (Duan et al., 2015). The overlap was extensive: 91% of the YFP-positive neurons in KCNG4^{-cre};thy1-stop-YFP1 mice were SMI-positive and 92% were osteopontin-positive; 82% of the SMI-32 positive neurons and 84% of

the osteopontin-positive neurons were YFP positive. Together, these features suggest that the RGCs labeled in KCNG4^{-cre};thy1-stop-YFP1 mice are primarily alpha cells. To test that notion further, we targeted single fluorescent ganglion cells for electrical recording and subsequently filled them with neurobiotin to inspect their structure.

Results from four sample neurons are illustrated in **Figure 2.1**. Each cell was presented with the same visual stimulus: a circular disk centered on the cell body flashing black and white on a gray background. Four kinds of light response were observed: Off-sustained, with maintained firing during the dark phase and little or no firing during the bright phase (**Figure 2.1a**); Off-transient, with a brief burst of spikes at the start of the dark phase followed by rapid decay to little or no firing (**Figure 2.1b**); On-sustained, with maintained firing during the bright phase (**Figure 2.1c**); and On-transient, with a brief burst at the start of the bright phase (**Figure 2.1d**). The whole-mount views of these filled neurons show large cell bodies and large circular dendritic trees. In depth, the dendritic fields of these sample neurons were sharply monostratified, and restricted to the On or Off laminas of the IPL (**Figure 2.1d**).

Inspection of the entire population of recorded neurons revealed only these four functional types (**Figure 2.2**). The dynamics of light responses to the flashing spot clearly separate into On- and Off-polarity (**Figure 2.2a**). Within each polarity, one group of cells fires only briefly after the transition, whereas the other shows a firing rate that decays gently from the initial peak to a maintained level. We analyzed these features further by measuring for each neuron's response the peak firing rate and the exponential decay time of the subsequent decline. Scatter plots of these response parameters showed two well-separated clusters of Off cells (**Figure 2.2b**) and another two clusters of On cells (**Figure 2.2c**). Based on these graphs we therefore identified four functional types: Off-s, Off-t, On-s, or On-t. These names will be used in the remainder of the report.

The first three of these alpha types have been described in prior studies of the mouse retina (Pang et al., 2003), but the On-transient type is new. This raised the concern whether it truly belongs to the conventionally defined alpha class, or represents some quirk of expression in the KCNG4-Cre line. To test for the classic neurofilament label, we identified On-t cells by electrical recording from fluorescent

neurons, then stained the retina using SMI-32 antibody, and identified the recorded neuron in the stained tissue. Three On-t cells tested in this way were all positive for SMI-32 (**Figure 2.3a-d**). As elaborated below the On-t cells share additional features with the three conventional alpha types. Thus we conclude that the On-transient neurons in the KCNG4-Cre line are alpha cells by all the criteria that define that class. Another concern was whether the difference between On-t and the On-s responses (**Figure 2.2c**) might somehow arise as an artifact, owing to variations in the physiological conditions of different retina preparations. Speaking against this interpretation, we frequently observed both sustained and transient On-responses in the same retina and among near-neighboring alpha cells (**Figure 2.3e**).

Figure 2.1 Morphology and light responses of 4 alpha ganglion cell types.

a-d, Sample neurons with whole-mount views (outer images) and responses to a flashing spot (inner plots) for the Off-sustained (a), Off-transient (b), On-sustained (c), and On-transient (d) types. Raster graphs illustrate action potentials on repeated trials of a spot flashing on (white plot) and off (gray plot). e, Stratification of these 4 sample neurons. Each histogram indicates the distribution of the filled dendrites relative to the two ChAT bands in the inner plexiform layer.

Figure 2.1 Morphology and light responses of 4 alpha ganglion cell types. (continued)

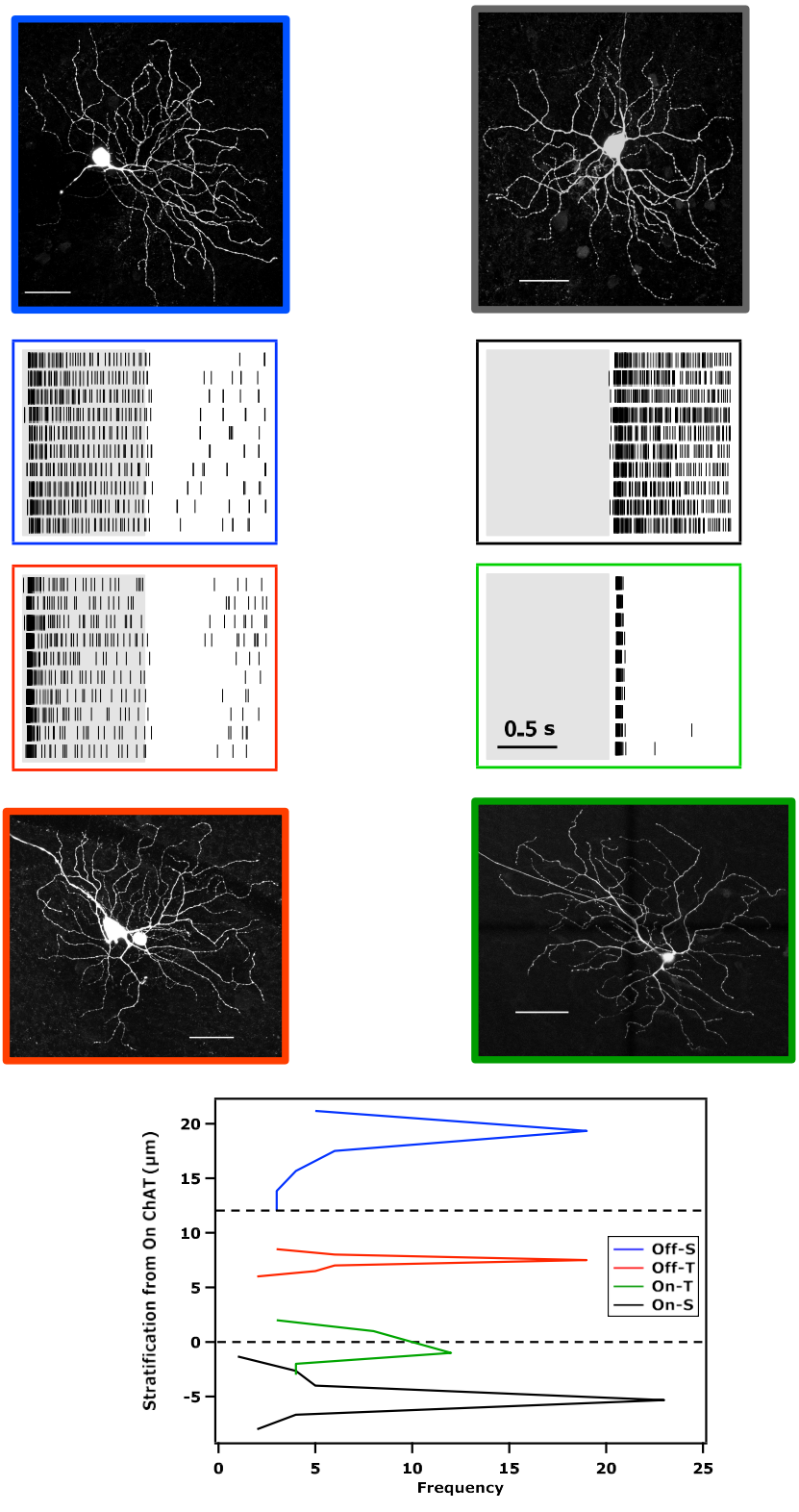

Figure 2.2 Kinetics of the light response for all alpha RGCs.

a: Time course of the firing rate during flashing spot experiments (as in Fig 1), normalized to the peak rate for each cell, and sorted by response type. b, c: Scatter plot of response parameters for all alpha RGCs: For each cell the time course was approximated with an exponential decay. The abscissa shows the time constant of the decay, and the ordinate plots the ratio of initial to final value. Cell types color coded as in panel a.

Figure 2.2 Kinetics of the light response for all alpha RGCs. (continued)

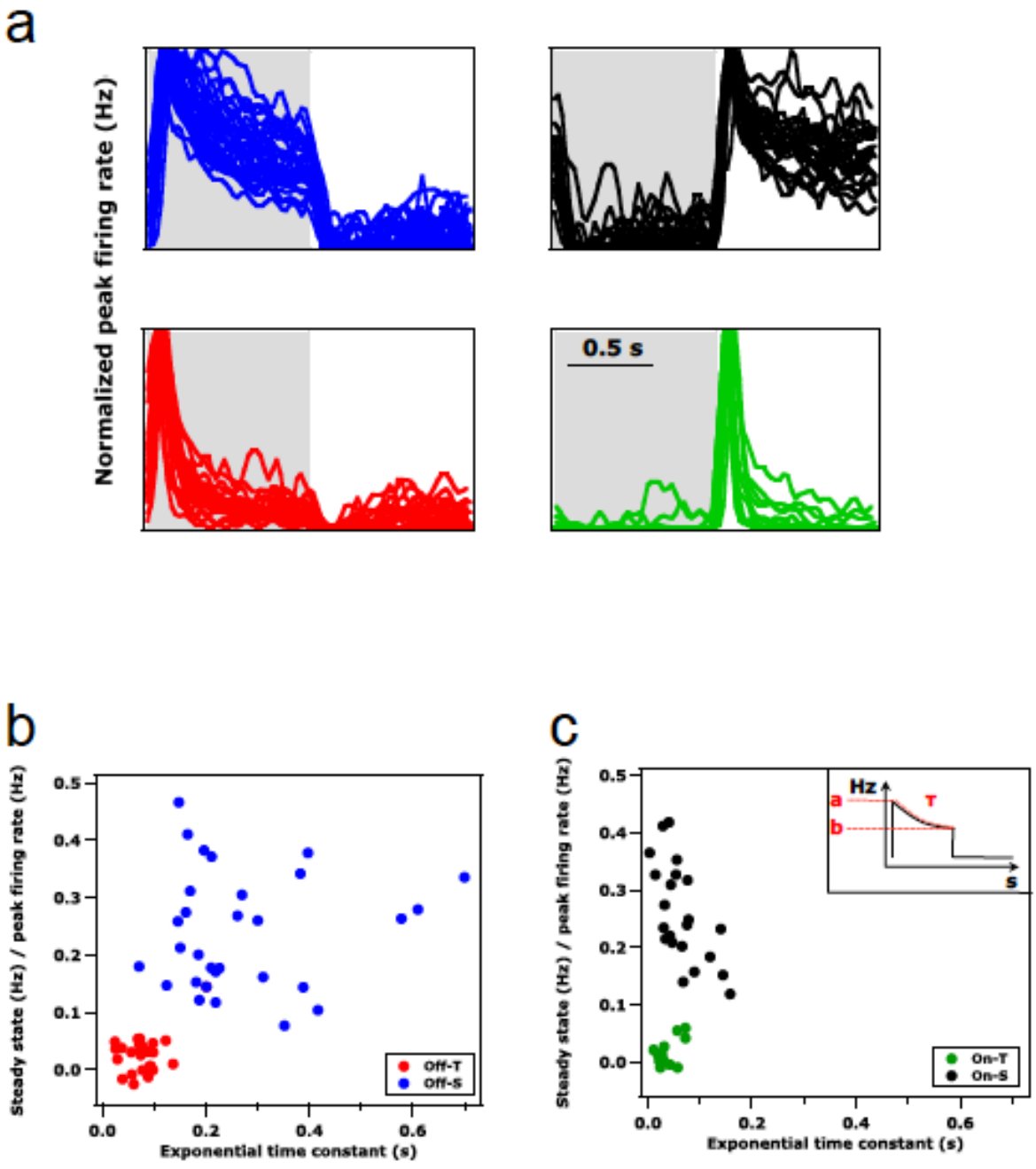

Figure 2.3 Confirmation that On-transient KCNG4-Cre neurons are a separate alpha type.

a-d: On-t cells express neurofilament. A loose patch recording of a fluorescent neuron (a) revealed a transient response to light steps (b). After fixation and antibody staining one can identify the same cell based on YFP label (c) and confirm that it is heavily labeled with the neofilament antibody SMI-32 (d). e: Two fluorescent neurons (black and green arrowheads) in close proximity showed transient (green) and sustained (black) response to a light step.

Figure 2.3 Confirmation that On-transient KCNG4-Cre neurons are a separate alpha type.

(continued)

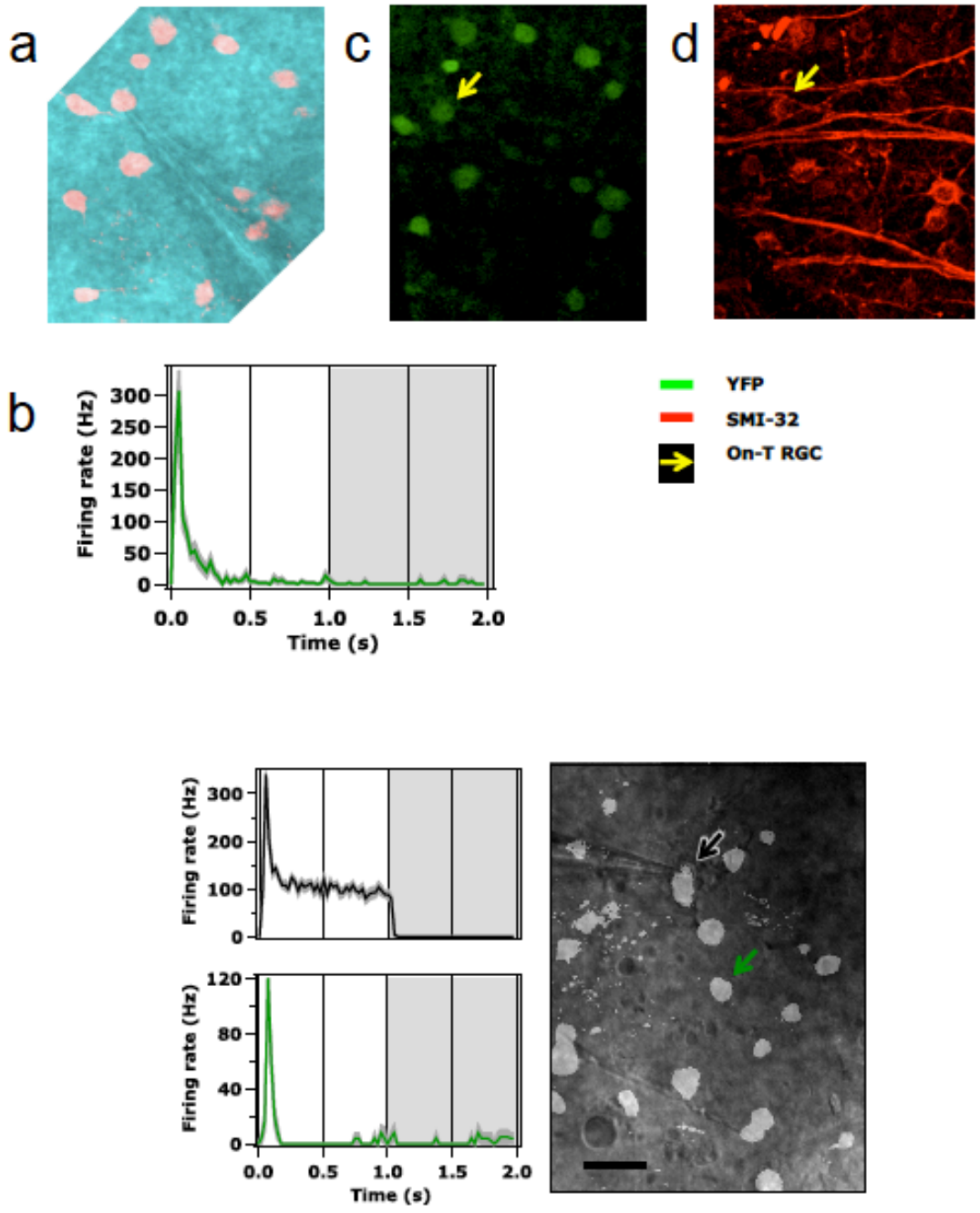

2.3.2 Structural and functional organization of the four alpha RGC types

We analyzed the dendritic arbors of alpha RGCs, both in a planar view and in depth. The inner plexiform layer of the retina is precisely organized, and the synapses of different bipolar and amacrine types are restricted to specific levels within the IPL. Thus the stratification level of a ganglion cell's dendrites determines what signals it can receive (Euler et al., 2014; Masland, 2001; Masland, 2012). All of the alpha cells we inspected were monostratified in narrow bands within the IPL (**Figure 2.4**). As expected, the Off types stratified in the outer portion of the IPL, and the On types in the inner portion. Using the two bands of ChAT expression as a reference, we confirmed the previously reported stratification levels of the Off-s, Off-t, and On-s types (van Wyk et al., 2009). The new On-t type stratified just outside the inner ChAT band, mirroring the Off-t type located just inside the outer ChAT band. In planar view, the four alpha types were less distinct. They all had large dendritic fields of >200 μm diameter (**Figure 2.4a**), rather similar total length of dendrites (**Figure 2.4b**), and large soma diameters >15 μm (**Figure 2.4c**).

We probed the receptive fields of alpha ganglion cells using the conventional spot series method: A small circular spot centered on the ganglion cell body was flashed on and off periodically; then the spot size was gradually increased. The response was measured by the peak firing rate following the On or Off steps (**Figure 2.5a**). With increasing spot size, the response increased at first, then reached a maximum and declined again (**Figure 2.5b**). The spot eliciting the largest response was taken as covering the receptive field center. The size of this center region was similar for all four alpha types: ~200-250 μm in diameter, slightly smaller than the dendritic fields (**Figure 2.6b**). The receptive field surround had a modest effect, producing a response suppression of ~40% from the peak value obtained with center-only stimulation (**Figure 2.6a**). Again, the four types were rather similar in this respect.

We also tested for a nonlinear subunit structure within the receptive field, by covering the receptive field center with a square grating that contrast-reversed periodically (**Figure 2.5c**). While making the grating progressively finer we noted the bar width at which a response was barely detectable. For all but the Off-s type this threshold occurred at bars of ~30 um width (**Figure 2.6c**). This suggests

that the ganglion cell receives rectified input from bipolar cells with a receptive field of ~30 um diameter, 10 times smaller than the receptive field center of the ganglion cell. However, the Off-s type behaved very differently and revealed almost no nonlinear input on a scale smaller than the receptive field center.

The dynamics of the light response were assessed by inspecting the time course of the firing rate under a flashing spot stimulus of optimal size (**Figure 2.5a**). The response latency, from the light step to the peak rate of firing, was very similar across the four types (**Figure 2.6d**). They also all reached the same peak firing rate of ~250 Hz (**Figure 2.6e**). The subsequent relaxation from the peak happened very quickly (~50 ms decay time) in all the alpha types except for Off-s (~250 ms), which stood out clearly in this regard (**Figure 2.6g**). Together with the unusual linearity of its bipolar input (**Figure 2.6f**) this suggests that the Off-s ganglion cell collects input from a qualitatively different type of bipolar cell.

Comparing the steady-state firing rate long after the light step to the peak firing rate, there was a dramatic difference between sustained and transient types (**Figure 2.6i**). This is unsurprising, because that feature served to define the types in the first place (**Figure 2.2b,c**). However, we found a similar difference in their baseline firing rates observed under a steady gray illumination (**Figure 2.6h**), suggesting that these sustained types receive synaptic inputs that are tonically active.

Finally, we tested responses to moving bar stimuli traveling through the receptive field center along the long axis (**Figure 2.5d**). All alpha types responded well to a moving edge, and did so equally for all directions of motion, with no hint of direction selectivity (**Figure 2.6c**).

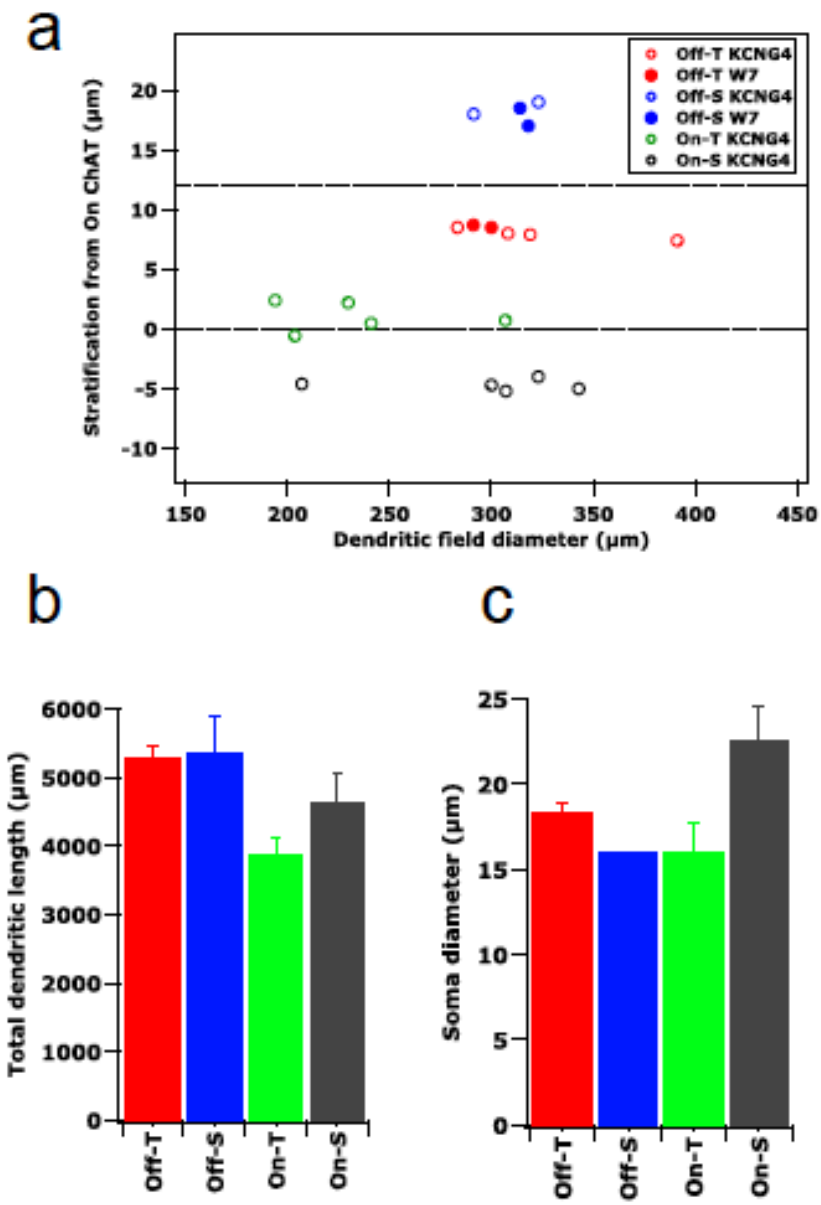

Figure 2.4 Population measures of alpha cell morphology.

a: Depth of dendritic stratification in the IPL. For each neuron this shows the peak of the depth histogram (Figure 2.1e). Fluorescent RGCs were targeted either using the KCNG4-Cre line (all alpha cells) or the W7 transgenic line (Off alpha cells). b-c: Total dendritic length (b) and soma diameter (c) for the 4 alpha types. Mean ± SEM.

Figure 2.5 Receptive field measures, illustrated for single cells (left) and over all cells of each type (right).

a: Spot size series. left: Responses of a sample On-s cell to flashing spots of increasing radius (see inset). Firing rate averaged over 10 repeats. Latency to peak (D) and maximal firing rate (E) are defined based on the spot giving the highest peak firing rate. right: Peak firing rate as a function of spot size from such experiments, averaged over all cells of each type. Mean ± SEM across cells of each type. The baseline firing rate (H), the spot size producing the highest rate (B) and the response to large uniform stimuli (U) are all defined based on this plot. c: Nonlinear receptive field subunits. The stimulus was a bar grating, contrast-reversing every 1 s. A bar boundary was centered on the receptive field. left: A sample RGC fires a burst of spikes on every grating transition until the bar width drops below a threshold (F). right: Peak firing rate as a function of bar width. Mean ± SEM across cells of each type. d: Directional selectivity. left: the stimulus was a bar, moving along the long edge through the receptive field center in 8 directions. This sample neuron produces sustained firing while the bar travels through the center. right: Peak firing rate under this stimulus as a function of direction. Mean ± SEM across cells of each type.

Figure 2.5 Receptive field measures, illustrated for single cells (left) and over all cells of each type (right). (continued)

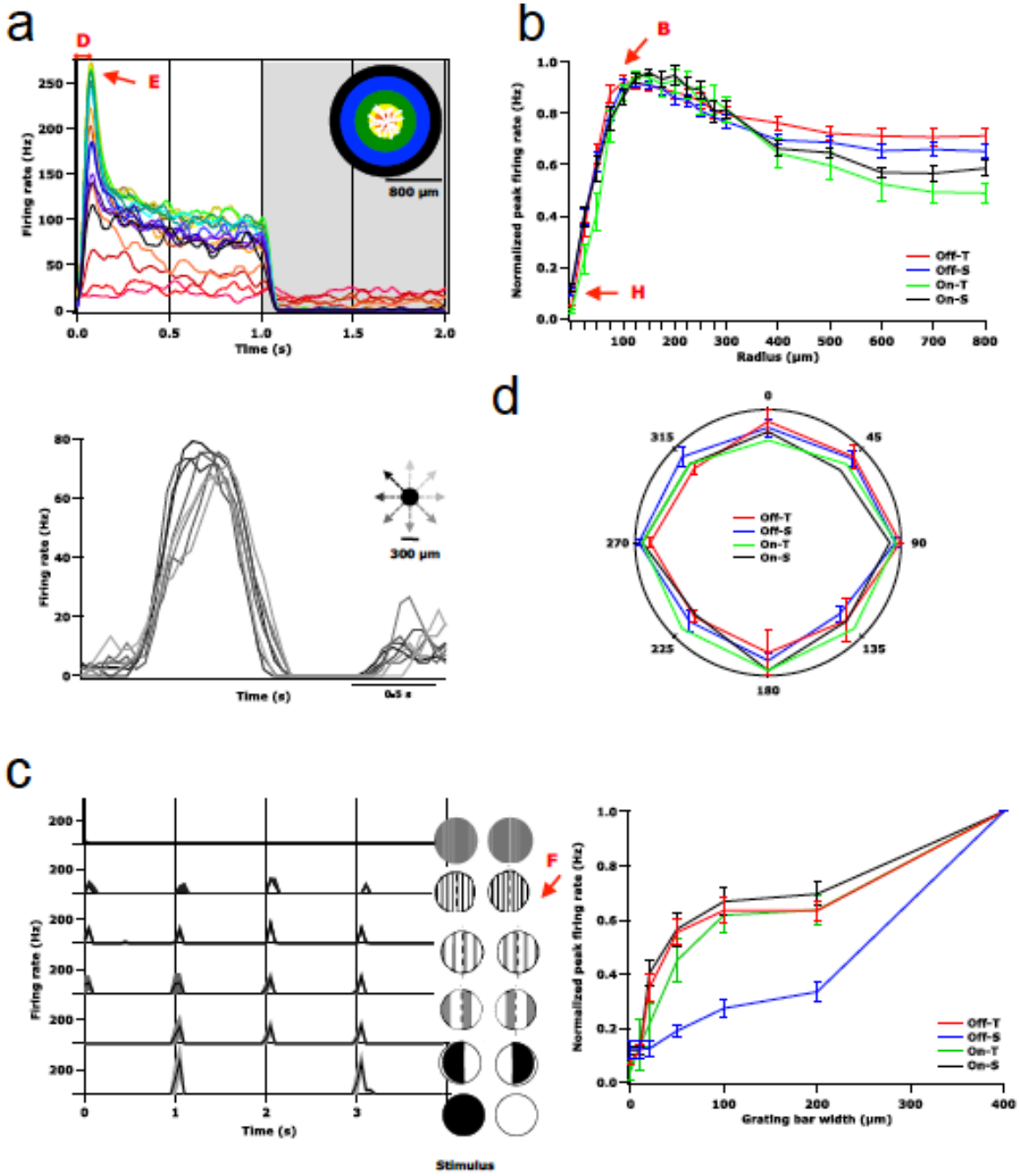

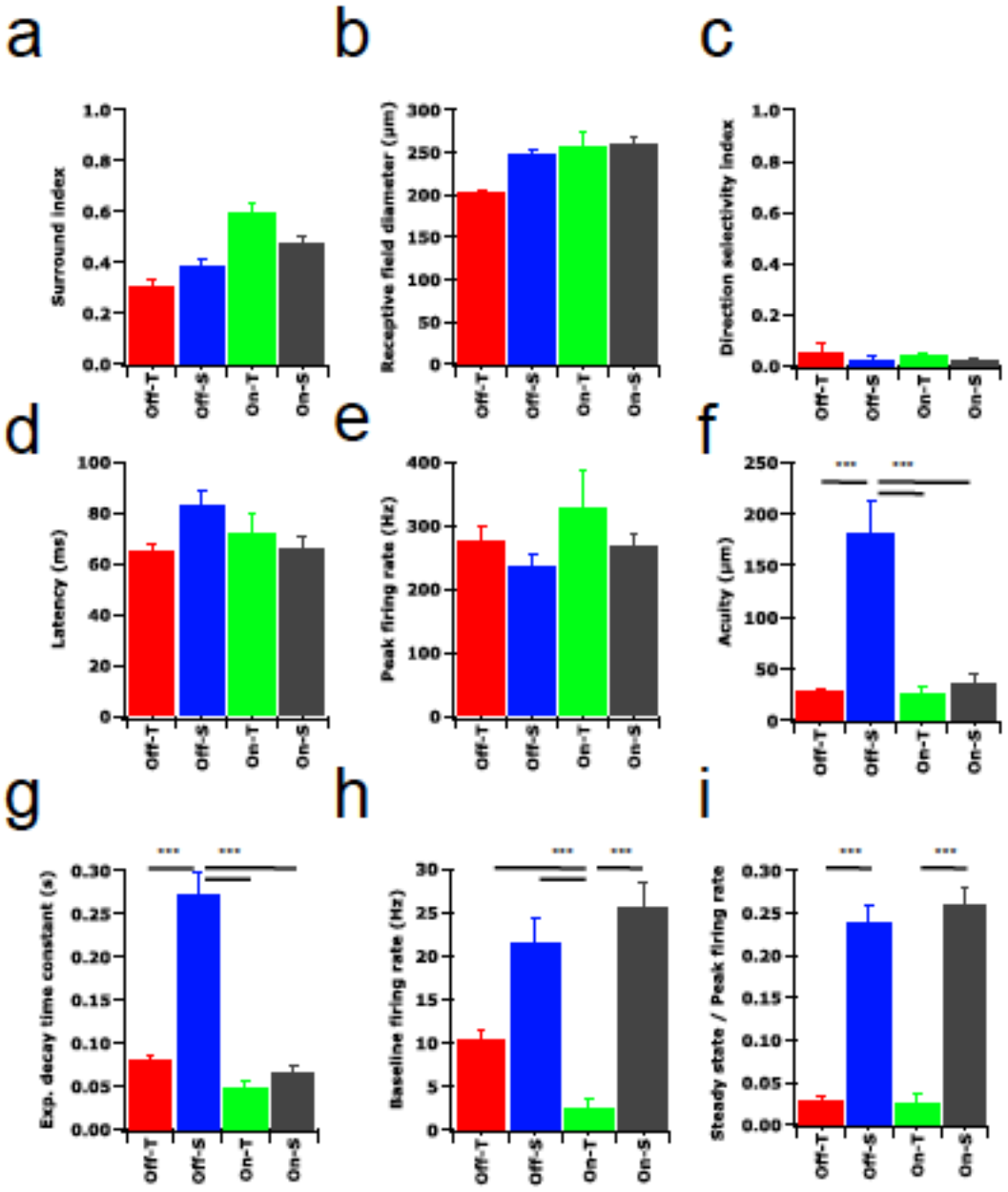

Figure 2.6 Receptive field parameters for all alpha types.

a: Surround suppression. b: Center diameter. c: Direction selectivity index. d: Peak latency. e: Maximal firing rate. f: Nonlinear subunit size. g: Response decay time. g: Steady/peak firing rate. h: Baseline firing rate. i: Steady/peak firing rate.

Mean ± SEM across cells of each type.

2.3.3 The four alpha RGC types have distinct molecular signatures

The four alpha RGC types described above share three molecular features that distinguish them from most or all non-alpha cells: expression of Kcng4 and osteopontin and high levels of neurofilaments (Duan et al. 2015). On the other hand, they each have distinct morphological and physiological features. This suggests that they are likely to be molecularly distinct as well. To seek such distinctions, we adopted a candidate approach. We stained retinal sections or whole mounts with antibodies to osteopontin plus the candidate, then focused on markers present in some but not all osteoptonin-positive cells –i.e., alpha RGCs.

Two groups of proteins proved to be useful in this context. The first were three related transcription factors, Brn3a, b, and c (*Pou4F1-3*), which are known to be differentially and combinatorially expressed by RGC subsets (Badea et al., 2009; Badea and Nathans, 2011). Brn3b appeared to be expressed in most or all alpha RGCs, but Brn3a was expressed in about half and Brn3c was expressed in about one-quarter of alpha RGCs (**Figure 2.7a**). The second was a set of three calcium binding proteins that are differentially and combinatorially expressed by RGC subsets: parvalbumin (PV), calbindin, and calretinin (Farrow et al., 2013; Pasteels et al., 1990). PV was present in most if not all alpha RGCs, consistent with results of Farrow et al. (2013), and no alpha RGCs were calretinin-positive, but calbindin was present in ~25% of alpha RGCs (**Figure 2.7b**).

Based on these results, we analyzed the morphology of the Brn3b-, Brn3c- and calbindin-positive αRGCs. We used a mouse line, Thy1-YFP-H, in which YFP is expressed in a small set of RGCs (Feng et al., 2000). Labeling is sufficiently sparse to permit clear visualization of dendritic morphology (~200 RGCs per retina; (Samuel et al., 2011)) and includes a wide variety of RGC types (Coombs et al., 2006). We triple-stained whole mounts with antibodies to osteopontin, GFP (which recognizes YFP) and the candidate, then imaged individual RGCs. This analysis demonstrated that among alpha RGCs, Brn3a is present in all OFF cells, Brn3c is present only in OFF-t cells, and calbindin is present only in ON-s cells (**Figure 2.7c**).

Figure 2.7 Molecular distinctions among alpha RGCs.

(A, B) Retinal whole mounts were stained with antibodies to Opn (green), plus antibodies to one of 3 POU-domain transcription factors (Brn3a, Brn3b or Brn3c; red in A) or one of 3 calcium binding proteins (parvalbumin [PV], calbindin or calretinin; red in B). Brn3b and PV mark most alpha RGCs whereas Brn3a, Brn3c and calbindin mark subsets; alpha RGCs are calretinin-negative. (C) Whole mounts of YFP-H retina were stained for YFP, Opn, vAChT and the indicated marker. Cells that were OPN, YFP, and marker triple-positive cells were identified (green, cyan and red, respectively in top panels) and imaged (YFP only, middle panels). Stratification of YFP-positive dendrites was then determined with reference to that of startburst amacrines (vAChT-positive, red in bottom panels). Arrows point to the same cell displayed in each panel. Results are representative of 7-10 cells per type from 5 mice.

Figure 2.7 Molecular distinctions among alpha RGCs. (continued)

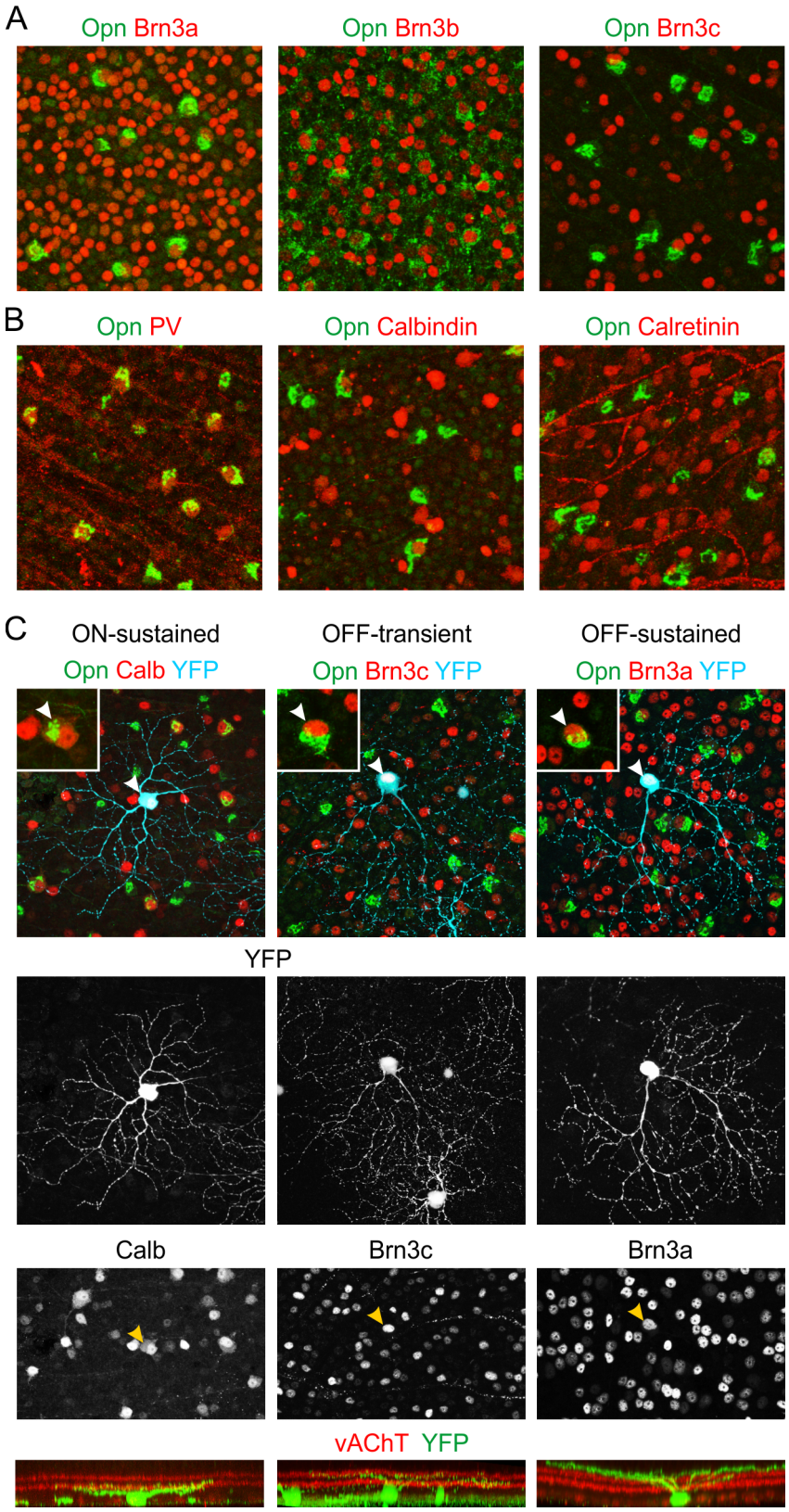

2.3.4 Transgenic lines label subsets of alpha RGCs

We have shown here that the Kcng4cre line labels all four alpha RGC types. Previous studies have reported that two transgenic mouse lines, TYW7 (Kim et al., 2010) and CB2-GFP (Huberman et al., 2008), label subsets of alpha RGC. These two lines express YFP (TYW7) or GFP (CB2) under control of Thy1 and calbindin2 regulatory elements, respectively, with patterns of expression governed by position effects that may differ from those of the endogenous gene. We asked whether these alpha RGCs were included within the types labeled by Kcng4, or whether they represented additional populations.

Morphological and physiological analyses revealed that YFP-positive cells in the TYW7 line were of two types, corresponding to OFF-t and OFF-s alpha RGC (**Figure 2.8a**). To determine whether these are the same OFF-t and OFF-s cells labeled in the KCNG4-cre line, we made use of the fact that TYW7 is a "cre-off" line in which expression of cre leads to loss of YFP (Kim et al., 2010; **Figure 2.8b**). We crossed TYW7 mice to Kcng4-Cre and asked whether expression of YFP was extinguished. YFP expression was attenuated in Kcng4-Cre;TYW7 retinas by postnatal day 15 (P15), shortly after cre is activated in Kcng4-cre mice (~P12); the loss was dramatic by P25 and complete by P35 (**Figure 2.8c**). No loss of YFP was seen when Kcng4-Cre was crossed to a similarly constructed line, TYW3, labels a distinct subset of RGCs (Kim et al., 2010; Krishnaswamy et al., 2015; Zhang et al., 2012), indicating the specificity of the effect (**Figure 2.8d**).

Huberman et al. (2008) demonstrated that the CB2-GFP line labels OFF-t alpha RGCs. To ask whether these cells were included among Kcng4-Cre alpha RGCs, we analyzed triple transgenic mice CB2-GFP; Kcng4-Cre; Rosa-CAG-STOP-RFP (**Figure 2.8e**). All GFP-positive neurons were also RFP positive (**Figure 2.8f**). Together these results indicated that the αRGC labeled in Kcng4-cre mice include those labeled in TYW7 and CB2-GFP mice, consistent with out hypothesis that all alpha RGCs are Kcng4- and osteopontin-positive.

Figure 2.8 Transgenic lines label subsets of alpha RGCs.

(A) Morphology and physiological responses of YFP-positive cells in the TYW7 line. Structure and function were assessed as in Figure. 1. All cells recorded corresponded to the OFF-s alpha RGC (top panels, x of y cells) and OFF-t alpha RGC types (bottom panels, x of y cells). (B) Use of the cre-off feature of the TYW3 and TYW7 lines. YFP if flanked by lox sites in these lines, so it is excised if cells also express cre in the Kcng4-cre line. (C) Loss of YFP from retinas in TYW7; Kcng4-cre double transgenics at indicate postnatal (P) ages. (D) YFP persists in TYW3; Kcng4-cre double transgenics; TYW3 labels a set of non- alpha RGCs. (E) Triple transgenic strategy to label both Kcng4-positive alpha RGCs (red) and CB2-GFP alpha RGCs (green). (F) In these triple transgenics, CB2-GFP-positive alpha RGCs are also Kcng4-positive.

Figure 2.8 Transgenic lines label subsets of alpha RGCs. (continued)

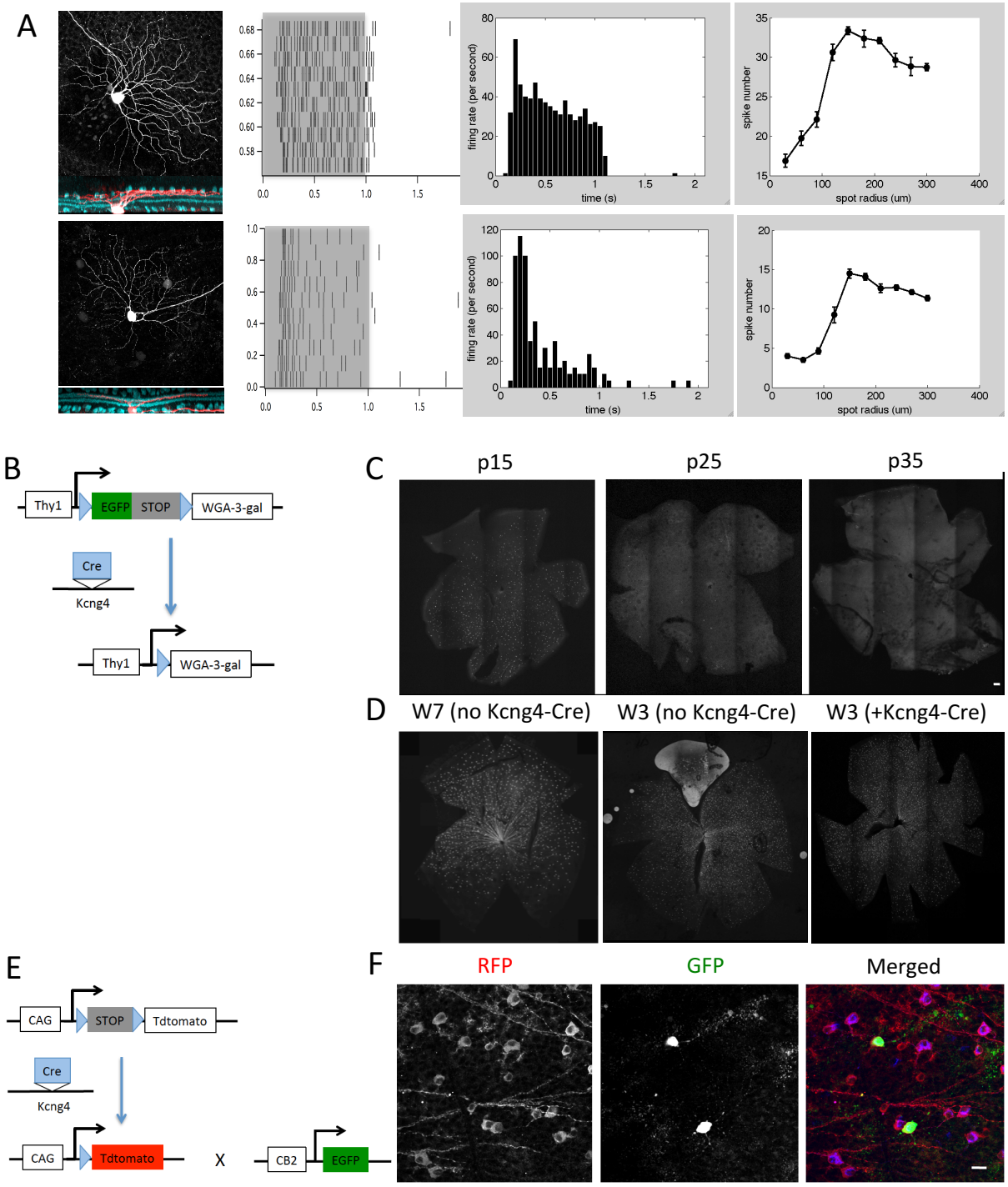

2.3.5 Mosaic analysis of alpha RGC types

Can the four groups of alpha RGCs we have described be subdivided further or are they true "types." In the retina, neurons of a specific type are arranged non-randomly in a pattern called a mosaic, with two cells of a single type less likely to be near neighbors than would be expected by chance (Rodieck, 1991). In contrast, cells of different types are arranged randomly with respect to each other. Thus, mosaic spacing, as assessed by density recovery profile (DRP) analysis provides a means of testing whether a population comprises a types, multiple types, or only part of a type (Rodieck, 1991; Zhang et al., 2012). We therefore performed DRP analysis on three alpha RGC types (On sustained, Off sustained and Off transient), using the markers described above and the TYW7 line. Each of the alpha RGC types forms a unique mosaic (**Figure 2.9**).

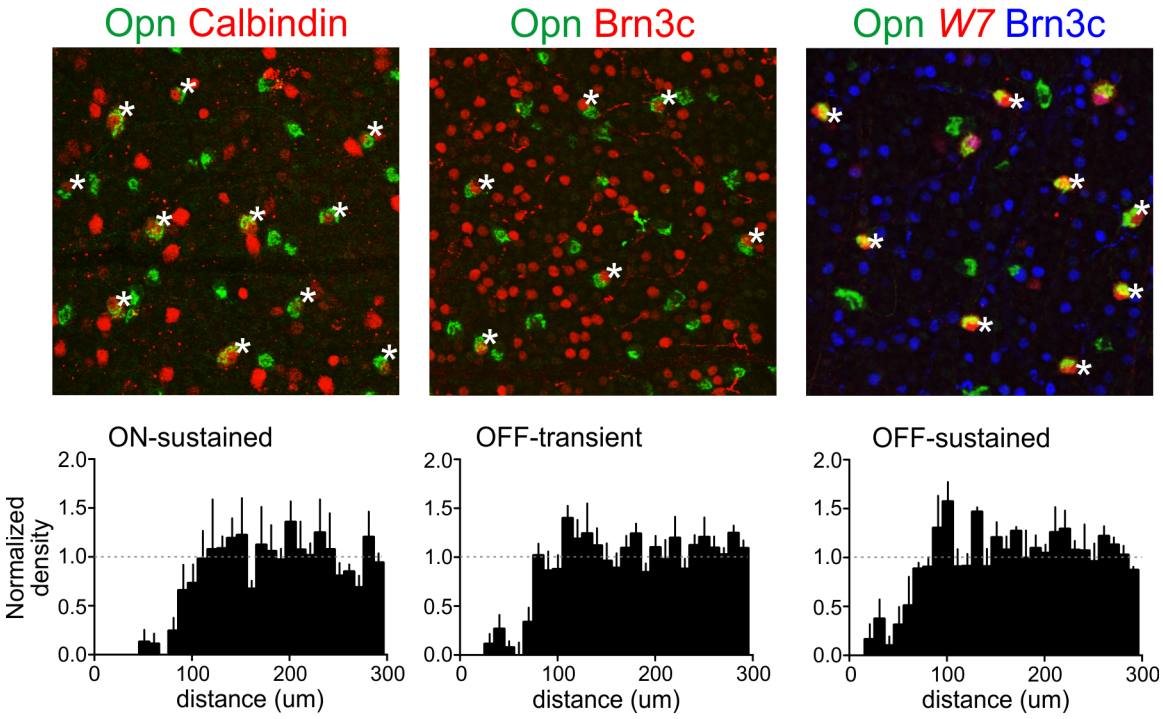

Figure 2.9 Mosaic organization of alpha RGCs types.

Four types of alpha RGCs were distinguished in retinal whole mounts by the molecular markers indicated above the top panels (see text and Figure 8 for details; asterisks show cells of the indicated type). The TYW7 line was used instead of Brn3a to label all OFF alpha RGCs, because of species incompatibilities of antibodies. Density recovery profile (DRP) analysis was then performed on each alpha RGC type (bottom panels; n=3-5 retinas per type from 3 mice). Dashed line, normalized average density.

2.4 Discussion

Here we described work of classifying subtypes of alpha RGCs labeled in Kcng4-Cre mouse retina. We found four subtypes of alpha RGCs: On-sustained, On-transient, Off-sustained and Off-transient alpha RGCs, each of which has distinct morphological and physiological properties. One subtype, Off-transient alpha RGCs, to our knowledge, was not reported previously.

2.4.1 Alpha RGC family includes four subtypes

We started this work by analyzing alpha RGCs labeled in Kcng4-Cre; thy1-stop-YFP1 mouse retina. These cells were noticed by their large somas, stout axons and dendrites, and expression of neurofilament (recognized by antibody SMI32), a molecular marker known to be expressed in alpha RGCs. Kcng4-Cre mice were generated by inserting Cre in the endogenous locus of the Kcng4 gene, which encodes a potassium channel modulator. Thus, the observation that alpha RGCs were labeled in Kcng4-Cre mice indicates that alpha RGCs express Kcng4.

Besides neurofilament and Kcng4, we also discovered that osteopontin is expressed in nearly all the alpha RGCs but not other RGCs. Together, these three molecular markers set alpha RGCs from other RGCs, indicating that these cells belong to a family.

Within the alpha RGC family, we classified four subtypes based on their morphological and physiological properties. This indicates that RGCs can be classified in a hierarchical manner, first into classes and then into subtypes. Another example is On-Off direction selective RGCs. There are four subtypes of On-Off direction selective RGCs, which are similar in morphological and physiological properties but differ in their preferred directions (Borst and Helmstaedter, 2015; Vaney et al., 2012). These On-Off direction selective RGCs form a family and share a molecular marker, CART (cocaine- and amphetamine-regulated transcript), which distinguish them from other RGCs. Together, these brought forward the intriguing idea of hierarchical distinctions of RGCs, which remained to be determined in other RGC subtypes.

2.4.2 A new subtype of alpha RGCs: On-transient alpha RGCs

Pang et al. (2003) reported three subtypes of alpha RGCs based on their physiological properties in mouse retina: On-sustained, Off-sustained and Off-transient. Later studies confirmed this observation (Bleckert et al., 2014; Murphy and Rieke, 2006; van Wyk et al., 2009). We also found these three subtypes of alpha RGCs, whose morphological and physiological properties are consistent with previous studies. However, we found a new subtype of alpha RGCs labeled in Kcng4-Cre mouse lines. This subtype has transient responses to light onset, thus is called On-transient alpha RGCs. On-transient alpha RGCs also have large soma and dendritic fields, but differ from other subtypes in their dendritic laminations. We confirmed that this subtype belonged to alpha RGC family by identifying On-transient RGCs from recording, staining the retina with the antibody against neurofilament and determining that these cells are neurofilament-positive. Thus, we believe this is a new subtype of alpha RGCs that was not reported before.

One possible reason for early studies to miss this subtype is that they only count for a small proportion of the alpha RGC population. ~20% of the On alpha RGCs are On-transient and the rest are On-sustained. Thus, it is possible that during experiments of random patching alpha RGCs, most of the On alpha RGC encountered were On-sustained, and the small proportion of On-transient alpha RGCs recorded were discarded as anomalous or misclassified into On-sustained group. Given that On-transient alpha RGCs are similar to On-sustained alpha RGCs in many aspects including dendritic fields, receptive fields and so on, it is hard to identify them without detailed analysis. Indeed, we found that On-transient alpha RGCs differ from On-sustained alpha RGCs mainly in two aspects: dendritic laminations and the ratio of peak firing rate to baseline firing rate.

With the new On-transient subtype, the four alpha RGC subtypes can now be viewed as forming two pairs in the two senses: 1. On and Off pairs; 2. transient and sustained pairs. This pleasing symmetry of On and Off pairs corresponds to an organizational principle observed in other mammalian retina, called paramorphism, which means a set of channels has been duplicated to generate On and Off representations

of each feature detector (Famiglietti, 2004, 2005; Famiglietti and Kolb, 1976). In mouse retina, this has not been described in detail for RGCs. Here we showed alpha RGCs as an example of paramorphism. It is intriguing but remains to be determined whether paramorphism also exists in other groups of RGCs in mouse retina.

2.5 Methods

2.5.1 Mice

Generation and characterization of KCNG4^{Cre}, CB2-GFP, TYW3 and TYW7 transgenic mouse lines has been reported previously (Duan et al.,2014, 2015; Huberman 2008; Kim et al., 2010). Cre-positive cells in KCNG4^{Cre} were visualized by crossing with *Thy1-STOP-YFP line 1* (Buffelli et al. 2003). Mice were maintained on a C57B6 background. All experiments were conducted in accordance with protocols approved by the Institutional Animal Care and Use Committees at Harvard University and the California Institute of Technology.

2.5.2 Electrophysiology

Mice were dark adapted for at least 1 hour prior to euthanization by cervical dislocation. The retina was isolated under infrared illumination into Ames oxygenated with 95% O2, 5% CO2 at room temperature. A ~2-3 mm aperture was cut into nitrocelluose filter paper and the retina was mounted ganglion cells (RGCs) facing up. The experiment was conducted with the retina in a superfusion chamber heated to 34-36 degrees C. A two-photon microscope was used to identify fluorescent RGCs for loose cell-attached recording. Data acquisition and the two-photon microscope were controlled using custom LabView software. Patch electrodes (2-5 MOhm) filled with Ames medium were used to record action potentials that were subsequently amplified with a Multiclamp 700B amplifier (Molecular Devices). Custom programs in IGOR (Wavemetrics Inc.) were used for spike thresholding and analysis.

2.5.3 Stimulation

Light stimuli were created using the Psychophysics Toolbox extensions in Matlab[5–7]. A modified Texas Instruments Lightcrafter with a custom lens system focused the stimuli onto the retinal photoreceptors (frame rate 60 Hz, magnification 9.1 um/pixel, intensity 10 mW/m^2). Cones mediate vision at high light levels and, in the mouse retina, they typically coexpress two opsins: short (S) – and middle (M) wavelength sensitive with peak sensitivities of 360 and 508 nm, respectively[8]. The average stimulus

intensity expressed in photoisomerizations per second for each of the three mouse photoreceptors corresponds to 5.7×10^3 R*/s for rod, 2.1×10^3 R*/s for M cone, and 4.8×10^3 R*/s for S cone.

2.5.4 Histology

After electrophysiological experiments, some retinas were fixed in fresh 4% paraformaldehyde in PBS at 4 degrees C for 1 hour. After fixation, the retinas were washed and incubated at 4 degrees C with primary antibodies for 4-5 days. Secondary antibody incubation at room temperature for 2 hours preceded mounting on a glass slide with spacers, ganglion cell side up, with Prolong Gold. Whole mount images were obtained on a LSM 710 inverted NLO microscope at 20X or 40X (Zeiss). The primary antibodies used were: anti-green fluorescent protein (~rabbit, IgG, Life Technologies) and anti-nonphosphoneurofilament H (~mouse [1:1000], SMI-32, Sternberger Monoclonals Incorporated).

2.6 References:

Badea, T.C., Hua, Z.L., Smallwood, P.M., Williams, J., Rotolo, T., Ye, X., and Nathans, J. (2009). New mouse lines for the analysis of neuronal morphology using CreER(T)/loxP-directed sparse labeling. PLoS One *4*, e7859.

Badea, T.C., and Nathans, J. (2011). Morphologies of mouse retinal ganglion cells expressing transcription factors Brn3a, Brn3b, and Brn3c: analysis of wild type and mutant cells using genetically-directed sparse labeling. Vision Res *51*, 269-279.

Bleckert, A., Schwartz, G.W., Turner, M.H., Rieke, F., and Wong, R.O. (2014). Visual space is represented by nonmatching topographies of distinct mouse retinal ganglion cell types. Curr Biol *24*, 310-315.

Borst, A., and Helmstaedter, M. (2015). Common circuit design in fly and mammalian motion vision. Nat Neurosci *18*, 1067-1076.

Buffelli, M., Burgess, R.W., Feng, G., Lobe, C.G., Lichtman, J.W., and Sanes, J.R. (2003). Genetic evidence that relative synaptic efficacy biases the outcome of synaptic competition. Nature *424*, 430-434.

Coombs, J., van der List, D., Wang, G.Y., and Chalupa, L.M. (2006). Morphological properties of mouse retinal ganglion cells. Neuroscience *140*, 123-136.

Duan, X., Krishnaswamy, A., De la Huerta, I., and Sanes, J.R. (2014). Type II cadherins guide assembly of a direction-selective retinal circuit. Cell *158*, 793-807.

Duan, X., Qiao, M., Bei, F., Kim, I.J., He, Z., and Sanes, J.R. (2015). Subtype-specific regeneration of retinal ganglion cells following axotomy: effects of osteopontin and mTOR signaling. Neuron *85*, 1244-1256.

Euler, T., Haverkamp, S., Schubert, T., and Baden, T. (2014). Retinal bipolar cells: elementary building blocks of vision. Nat Rev Neurosci *15*, 507-519.

Famiglietti, E.V. (2004). Class I and class II ganglion cells of rabbit retina: a structural basis for X and Y (brisk) cells. J Comp Neurol *478*, 323-346.

Famiglietti, E.V. (2005). "Small-tufted" ganglion cells and two visual systems for the detection of object motion in rabbit retina. Vis Neurosci *22*, 509-534.

Famiglietti, E.V., Jr., and Kolb, H. (1976). Structural basis for ON-and OFF-center responses in retinal ganglion cells. Science *194*, 193-195.

Farrow, K., Teixeira, M., Szikra, T., Viney, T.J., Balint, K., Yonehara, K., and Roska, B. (2013). Ambient illumination toggles a neuronal circuit switch in the retina and visual perception at cone threshold. Neuron *78*, 325-338.

Huberman, A.D., Manu, M., Koch, S.M., Susman, M.W., Lutz, A.B., Ullian, E.M., Baccus, S.A., and Barres, B.A. (2008). Architecture and activity-mediated refinement of axonal projections from a mosaic of genetically identified retinal ganglion cells. Neuron *59*, 425-438.

Kim, I.J., Zhang, Y., Meister, M., and Sanes, J.R. (2010). Laminar restriction of retinal ganglion cell dendrites and axons: subtype-specific developmental patterns revealed with transgenic markers. J Neurosci *30*, 1452-1462.

Krishnaswamy, A., Yamagata, M., Duan, X., Hong, Y.K., and Sanes, J.R. (2015). Sidekick 2 directs formation of a retinal circuit that detects differential motion. Nature.

Masland, R.H. (2001). The fundamental plan of the retina. Nat Neurosci *4*, 877-886.

Masland, R.H. (2012). The tasks of amacrine cells. Visual Neuroscience *29*, 3-9.

Murphy, G.J., and Rieke, F. (2006). Network variability limits stimulus-evoked spike timing precision in retinal ganglion cells. Neuron *52*, 511-524.

Pang, J.J., Gao, F., and Wu, S.M. (2003). Light-evoked excitatory and inhibitory synaptic inputs to ON and OFF alpha ganglion cells in the mouse retina. J Neurosci *23*, 6063-6073.

Pasteels, B., Rogers, J., Blachier, F., and Pochet, R. (1990). Calbindin and calretinin localization in retina from different species. Vis Neurosci *5*, 1-16.

Peichl, L. (1989). Alpha and delta ganglion cells in the rat retina. J Comp Neurol *286*, 120-139.

Peichl, L. (1991). Alpha ganglion cells in mammalian retinae: common properties, species differences, and some comments on other ganglion cells. Vis Neurosci *7*, 155-169.

Peichl, L., Buhl, E.H., and Boycott, B.B. (1987a). Alpha ganglion cells in the rabbit retina. J Comp Neurol *263*, 25-41.

Peichl, L., Ott, H., and Boycott, B.B. (1987b). Alpha ganglion cells in mammalian retinae. Proc R Soc Lond B Biol Sci *231*, 169-197.

Rodieck, R.W. (1991). The density recovery profile: a method for the analysis of points in the plane applicable to retinal studies. Vis Neurosci *6*, 95-111.

Samuel, M.A., Zhang, Y., Meister, M., and Sanes, J.R. (2011). Age-related alterations in neurons of the mouse retina. J Neurosci *31*, 16033-16044.

Straznicky, C., Vickers, J.C., Gabriel, R., and Costa, M. (1992). A neurofilament protein antibody selectively labels a large ganglion cell type in the human retina. Brain Res *582*, 123-128.

van Wyk, M., Wassle, H., and Taylor, W.R. (2009). Receptive field properties of ON- and OFF-ganglion cells in the mouse retina. Vis Neurosci *26*, 297-308.

Vaney, D.I., Sivyer, B., and Taylor, W.R. (2012). Direction selectivity in the retina: symmetry and asymmetry in structure and function. Nat Rev Neurosci *13*, 194-208.

Wassle, H., Peichl, L., and Boycott, B.B. (1981). Morphology and topography of on- and off-alpha cells in the cat retina. Proc R Soc Lond B Biol Sci *212*, 157-175.

Zhang, Y., Kim, I.J., Sanes, J.R., and Meister, M. (2012). The most numerous ganglion cell type of the mouse retina is a selective feature detector. Proceedings of the National Academy of Sciences of the United States of America *109*, E2391-2398.

Chapter 3: Subtype-specific regeneration of retinal ganglion cells following axotomy: effects of osteopontin and mTOR signaling

Preface:

The work presented in this chapter was collaboration between Xin Duan, a postdoctoral fellow in Josh Sanes lab and Fengfeng Bei, a postdoctoral fellow in Zhigang He lab. Xin Duan generated the transgenic mouse line Kcng4-Cre, and made the initial discovery that overexpression of osteopontin increases soma size. I analyzed the expression of osteopontin in alpha RGCs and the phenotype of osteopontin overexpression and knockout. Fengfeng Bei performed the cell survival and axon regeneration assays and we analyzed the results together. The work presented here resulted in the paper, which was written by Xin Duan, Josh Sanes and me:

X. DUAN*, **M. QIAO***, F. BEI*, I-J. KIM, Z. HE, J. R. SANES (2015) Subtype-specific regeneration of retinal ganglion cells following axotomy: effects of osteopontin and mtor signaling. Neuron. (* Co-first authors with equal contributions)

This chapter looks pretty much like the paper except for a few minor changes.

3.1 Abstract

In mammals, few retinal ganglion cells (RGCs) survive following axotomy and even fewer regenerate axons. This could reflect differential extrinsic influences on a homogeneous population, or the existence of subpopulations that vary in their responses to injury. We tested these alternatives by comparing responses of molecularly distinct subsets of mouse RGCs to axotomy. Survival rates varied dramatically among subtypes, with alpha-RGCs (αRGCs) surviving preferentially. Moreover, among survivors, αRGCs accounted for nearly all regeneration following down-regulation of PTEN, which activates the growth-promoting mTOR signaling pathway. αRGCs have uniquely high mTOR signaling levels among RGCs and also selectively express osteopontin (OPN) and receptors for the growth factor, insulin-like growth factor 1 (IGF-1). When administered in combination with IGF-1, exogenous OPN promotes regeneration as effectively as down-regulation of PTEN; however, regeneration is still confined to αRGCs. Our results reveal dramatic subtype-specific differences in the ability of RGCs to survive and regenerate following injury, and they identify promising agents for promoting axonal regeneration.

3.2 Introduction

Regeneration following injury to the mammalian brain or spinal cord is notoriously poor: few survivors extend axons beyond the injury site (Ramon y Cajal, 1928) and in some cases, many of the axotomized neurons die (Mansour-Robaey et al., 1994; Park et al., 2008) (Conta Steencken et al., 2011). Limited regeneration can be explained in at least two different ways. First, non-genetic differences among neurons could account for differences in outcome – for example, stochastic variation, history of activity or proximity to environmental cues that modulate growth. Alternatively or in addition, distinct subpopulations within a seemingly homogeneous population could regenerate preferentially, owing to preexisting qualities that improve their lot. Distinguishing among these and other alternatives is important both in guiding searches for protective factors and in assessing interventions designed to enhance regeneration.

Here, we analyzed retinal ganglion cells (RGCs) to address this issue. All visual information is conveyed from the eye to the brain by RGC axons, which run though the optic nerve to retinorecipient areas such as the superior colliculus and lateral geniculate nucleus. Although all RGCs share numerous attributes, they can be divided into ~30 distinct subpopulations, based on morphological, physiological and molecular criteria (Masland, 2012; Sanes and Masland, 2015; Yamagata and Sanes, 2010). Following damage to the mouse optic nerve, >80% of RGCs die, and <1% of the survivors extend axons past the site of damage (Mansour-Robaey et al., 1994; Park et al., 2008). Regeneration of a substantial number of RGC axons can be elicited, however, by manipulations of the neurons themselves or the environment through which they grow (Aguayo et al., 1991; Benowitz and Popovich, 2011; Liu et al., 2011; Maier and Schwab, 2006; Park et al., 2008; Smith et al., 2009; Sun et al., 2011). Thus, one can ask whether specific subsets of RGCs differ in their abilities to survive following nerve crush and/or regenerate axons following treatment.

In the first part of this study, we assessed survival of eleven RGC subtypes following transection of the optic nerve in mice. Subtypes differed dramatically in susceptibility to damage, with the largest

RGC types, alpha-RGCs (αRGCs), surviving preferentially but not exclusively. We then promoted regeneration by suppressing expression of PTEN, which acts, at least in part, by enhancing mTOR activity (Jaworski et al., 2005; Kim et al., 2009; Park et al., 2008; Zukor et al., 2013). We found that αRGCs accounted for nearly all of the regenerating axons in this paradigm.

Based on these results, we sought features of αRGCs that might account for their regenerative ability and found three: they have high endogenous levels of mTOR activity, they selectively express a secreted phosphoprotein, osteopontin (OPN) (Bellahcene et al., 2008; Wang and Denhardt, 2008), which is capable of stimulating mTOR activity (Ahmed and Kundu, 2010), and they selectively express receptors for insulin-like growth factor 1 (IGF-1), which promotes regeneration of some neuronal types (Dupraz et al., 2013). Ectopic expression of OPN in combination with IGF-1 promotes regeneration of αRGCs as effectively as PTEN suppression. Together, our work identifies a neuronal-intrinsic factor that can promote regeneration and provides a strategy to identify additional regeneration-promoting factors.

3.3 Results

3.3.1 Differential survival of RGC subtypes

We used immunohistochemical or transgenic approaches to mark molecularly distinct subsets of RGCs in mice:

- There are four groups of ON-OFF direction-selective RGCs (ooDSGCs), each tuned to motion in a single direction: ventral, dorsal, nasal and temporal. Antibodies to the neuropeptide cocaine- and amphetamine-regulated transcript (CART) label all four groups (Kay et al., 2011) while a transgenic line, HB9-GFP, labels the subset tuned to ventral motion (Trenholm et al., 2011).
- W3 RGCs are labeled with YFP in the TYW3 mouse line (Kim et al., 2010). W3 RGCs are among the smallest RGCs in terms of soma size and dendritic diameter and are among the most numerous RGCs. They comprise at least two populations: W3B, which are motion-sensitive but not direction-selective, and W3D, which remain physiologically uncharacterized (Zhang et al., 2012).
- Antibodies to melanopsin label M1- and M2-RGCs, two subsets of intrinsically photosensitive RGCs that can be distinguished by the sublaminae of the inner plexiform layer (IPL) within which their dendrites arborize (Berson et al., 2010; Ecker et al., 2010).
- The RGCs with the largest somata are αRGCs. In mice, they comprise at least three subtypes, which differ in physiological properties as well as dendritic stratification (Estevez et al., 2012; Pang et al., 2003; Schubert et al., 2005; van Wyk et al., 2009; Volgyi et al., 2005). We recently generated and characterized a mouse line in which Cre recombinase is inserted into the locus encoding a potassium channel modulator, *kcng4*. When crossed to a reporter line (Buffelli et al., 2003), subsets of bipolar cells and RGCs were YFP-positive in double-transgenic offspring (Kcng4-cre;Thy1-stop-YFP line 1; called Kcng4-YFP here) (Duan et al., 2014). Further analysis

revealed that the labeled RGCs had large somata and dendrites and were rich in a neurofilament-associated epitope, SMI32 (**Figure 3.1**). These features identified them as αRGCs (Berson, 2008; Peichl, 1991). Morphological and physiological analysis revealed that labeled RGCs included all three types of αRGCs, and no other RGCs (Fig. 1B and M.Q., X.D., J.R.S., B. Krieger and M. Meister, in preparation). Thus, the Kcng4-cre line provides selective genetic access to aRGCs. Together, these markers allowed us to assay the survival of 11 RGC subtypes (4 ooDSGCs, 2 W3-RGCs, 3 αRGCs, and 2 melanopsin-positive RGCs).

We crushed the optic nerves of wild-type or transgenic mice and then assessed RGC survival 14 days post crush (dpc). Consistent with previous reports (Park et al., 2008), ~20% of RGCs survived, as assessed by staining for class III beta-tubulin (Tuj1), a pan-RGC marker (**Figure 3.2 A, C**). The survival rate varied greatly among RGC subtypes. Over 80% of the αRGCs (Kcng4-YFP RGCs) and over 70% of the M1 RGCs survived, whereas few if any M2 RGCs or ooDSGCs (HB9-GFP and $CART^+$ RGCs) survived (**Figure 3.2 A-C**). Survival of W3 RGCs was intermediate (~10%). Examination of Kcng4-YFP retinal cross-sections, in which the three αRGC subtypes can be distinguished by dendritic lamination, indicated that all three subtypes survived (**Figure 3.2 B**). As a consequence, αRGCs and M1-RGCs, which comprise ~6% and ~3% of all RGCs in the normal retina, respectively, accounted for 23% and 11% of surviving RGCs by 14 dpc (**Figure 3.2 E**).

To ask whether the apparently preferential survival of αRGCs represented a delayed cell loss, we examined animals after two additional weeks (28 dpc). Although ~10% of the RGCs were lost between 14 dpc and 28 dpc, αRGCs and M1 RGCs were still preferentially spared, and comprised ~25% and ~15% of all surviving RGCs, respectively (**Figure 3.2 D, E**). Thus, αRGCs and M1 RGCs survive preferentially but not exclusively following nerve crush.

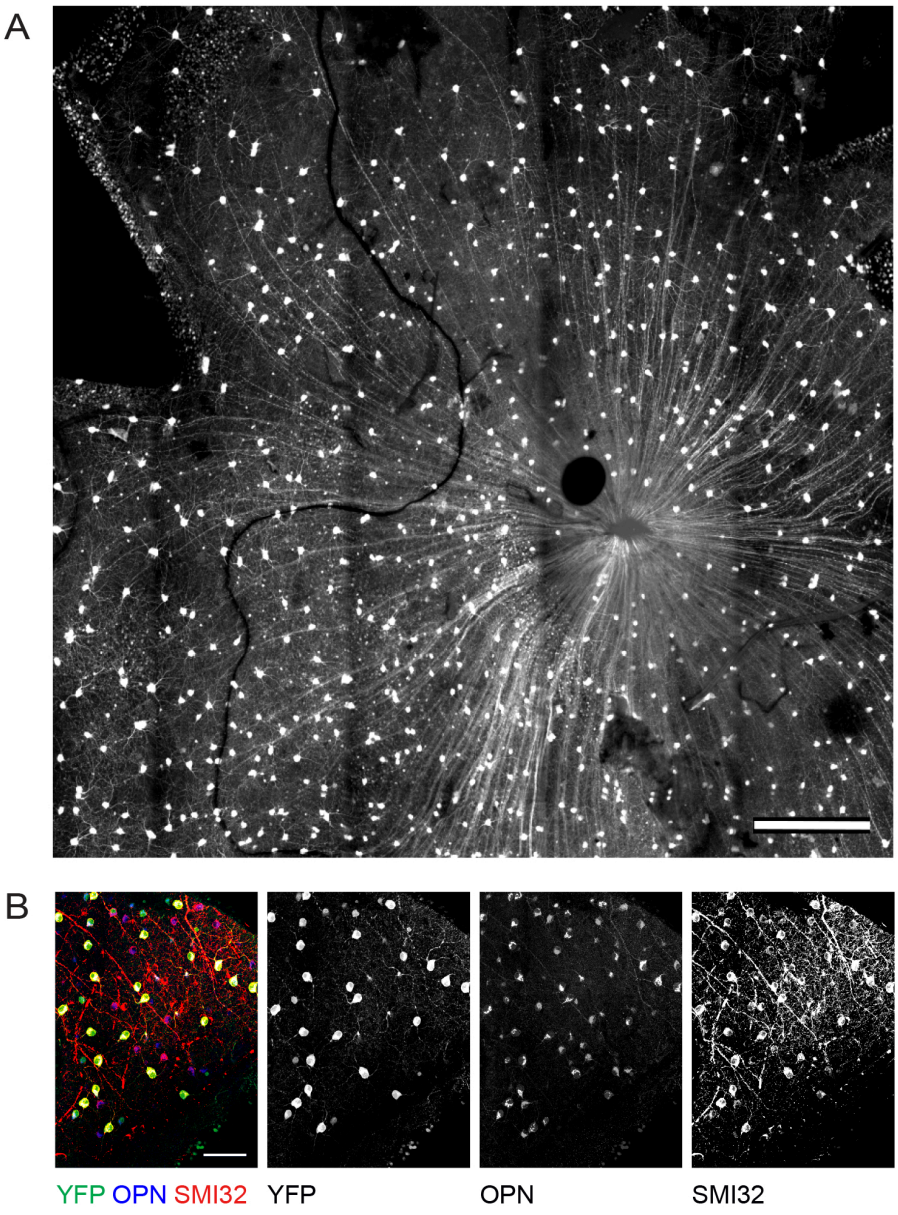

Figure 3.1 αRGCs are labeled in Kcng4-YFP mice.

A. Whole-mount of Kcng4-YFP retina. Scale bar, 300μm.

B. Field from Kcng4-YFP triply-stained with anti-YFP, anti-neurofilament (SMI32) and anti-osteoptonin. >90% of the YFP$^+$ RGCs are SMI32$^+$ and OPN$^+$. Scale bar, 100μm.

Figure 3.2 Differential survival of RGC subtypes following axotomy.

A. Whole-mount views of retinas. Top panels show retina labeled with antibody Tuj1, which marks all RGCs. Lower panels show retinas from Kcng4-YFP, TYW3 and HB9-GFP mice, in which αRGCs, W3-RGCs, and ooDSGCs, respectively, are labeled. dpc, days post-crush. Scale bar, 50μm.

B. Retinal sections labeled with anti-melanopsin in wild-type mice to label M1 and M2 cells, and YFP in Kcng4-YFP mice to label αRGCs. 1 and 2 indicate M1 and M2 RGCs, which can be distinguished by dendritic lamination; only M1 RGCs survive. 3-5 indicate examples of ON-, OFF-transient and OFF-sustained αRGCs, which can be distinguished by dendritic lamination; all 3 survive axotomy. Scale bar, 20μm.

C, D. Fraction of RGCs of each subtype that survive axotomy at 14dpc (C) or 28dpc (D); data from preparations such as those shown in A and B. n=2-3 retinas per type.

E. Fraction of all RGCs comprised by each subtype in intact retina, 14dpc, and 28dpc.

Figure 3.2 Differential survival of RGC subtypes following axotomy. (continued)

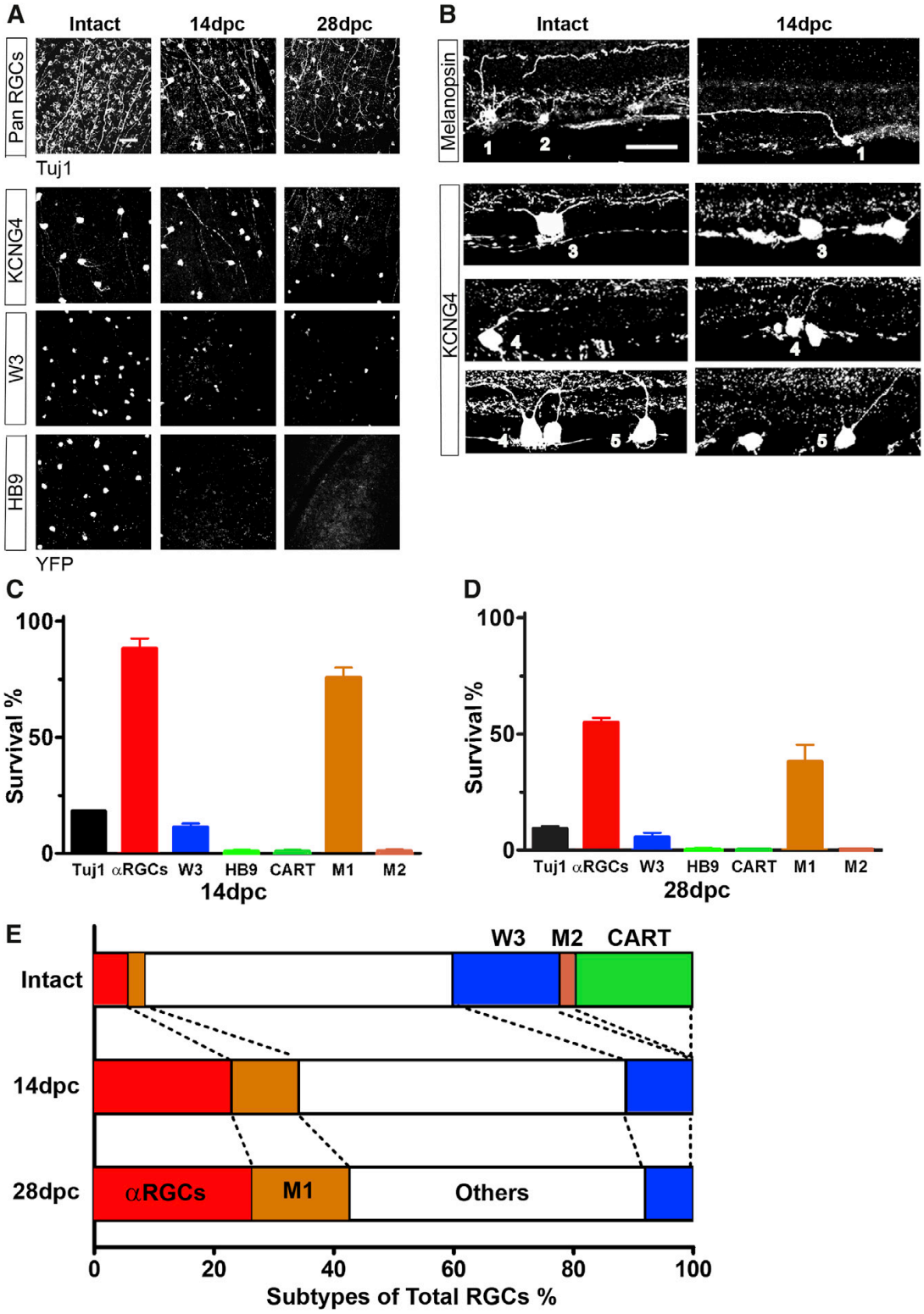

3.3.2 Selective regeneration of αRGCs

Next, we compared the ability of RGC subtypes to extend axons following injury. To promote regeneration, we injected an adeno-associated virus (AAV) encoding a previously-validated short hairpin RNA directed against PTEN (shPTEN) (Zukor et al., 2013), a negative regulator of mTOR signaling. We used immunostaining for a phosphorylated form (Ser235/236) of ribosome protein S6 (pS6) to assay the efficacy of shPTEN, based on previous studies showing that pS6 provides a reliable estimate of mTOR activity (Laplante and Sabatini, 2012; Park et al., 2008). Levels of pS6 were increased in ~60% of RGCs in optimally infected areas by 2 weeks following infection with AAV-shPTEN (Fig. 2A). Thus, AAV infects, and PTEN restricts mTOR signaling in, most if not all RGC subtypes. A control AAV (AAV-GFP) infected a similar fraction of RGCs but had no effects on pS6. AAV-shPTEN had no detectable effect on retinal structure or integrity (data not shown).

To assess regeneration, we crushed the optic nerve Kcng4-YFP, HB9-GFP and TYW3 mice two weeks after AAV-shPTEN administration, then analyzed retina and optic nerve 14 dpc. Selective survival of αRGCs following depletion of PTEN was similar to that observed in control retinas after crush (**Figure 3.3)**. Regeneration was detected by counting YFP or GFP-positive axons in longitudinal sections through the optic nerves. We observed substantial regeneration of αRGC axons but no detectable regeneration of ooDSGC or W3-RGC axons (**Figure 3.4 B**).

To visualize all regenerating axons, we injected the anterograde tracer cholera toxin subunit B (CTB) into the retina 2-3 days before sacrifice. In all lines, approximately 150 axons per retina regenerated at least 0.5mm past the crush site, accounting for ~3.5% of surviving RGCs (**Figure 3.4 C, D**). Importantly, >90% of the CTB-positive axons in the Kcng4-YFP retina were also YFP-positive (**Figure 3.4 D**). No markers were available to label M1-RGC axons, but the near-complete overlap of CTB- and YFP-positive axons in the Kcng4-YFP line suggests that few if any M1-RGCs or other RGC subtypes regenerate. Thus, αRGC account for the vast majority of the regenerating axons following

down-regulation of PTEN.

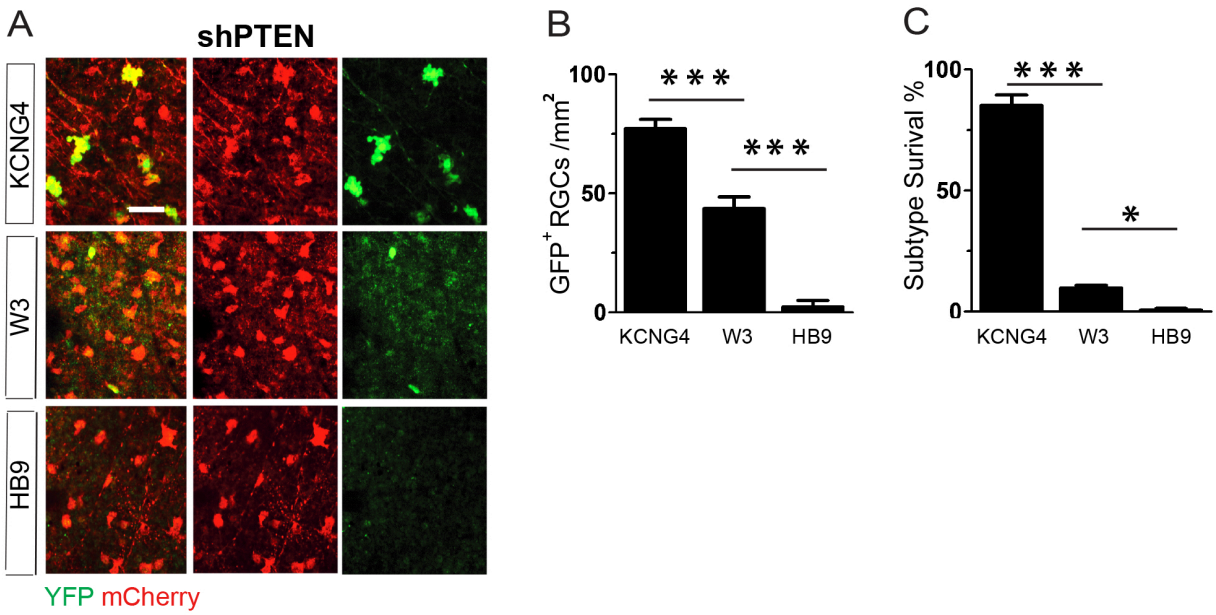

Figure 3.3 Selective survival of αRGCs in retinas injected with AAV-shPTEN-mCherry.

A. Whole-mount views of retinas from indicated mouse lines at 14 dpc and 28 day after injection of AAV-shPTEN-mCherry. Scale bar, 50μm.

B, C. Quantification of surviving RGCs in the RGC layer expressed as absolute values and as percent of values from control retinas. *, p<0.05, ***, p < 0.001.

Figure 3.4 Selective regeneration of αRGCs following axotomy.

A. Sections from control retina, and a retina infected 2 weeks previously with AAV-shPTEN. Sections were stained with anti-pS6 and Tuj1. PTEN knockdown leads to increased mTOR signaling, revealed by increased levels of pS6. Scale bar, 20μm.

B. Sections from optic nerves of Kcng4-YFP, TYW3 and HB9-GFP mice at 14dpc and 28 day after injection of AAV-shPTEN. * marks lesion site. Scale bar, 200μm.

C. Section from Kcng4-YFP mouse, as in B but injected with cholera toxin B (CTB) to label all regenerated axons. All CTB-positive axons are YFP^+ αRGCs. Scale bar, 200μm.

D. Number of labeled regenerating axons 0.5mm distal to the lesion site at 14dpc, based on counts from sections such as those shown in (C), mean+/- S.D., n=3-5 optic nerves per type. *, $p<0.05$ (Two-ANOVA with Bonferroni Posttests).

Figure 3.4 Selective regeneration of αRGCs following axotomy. (continued)

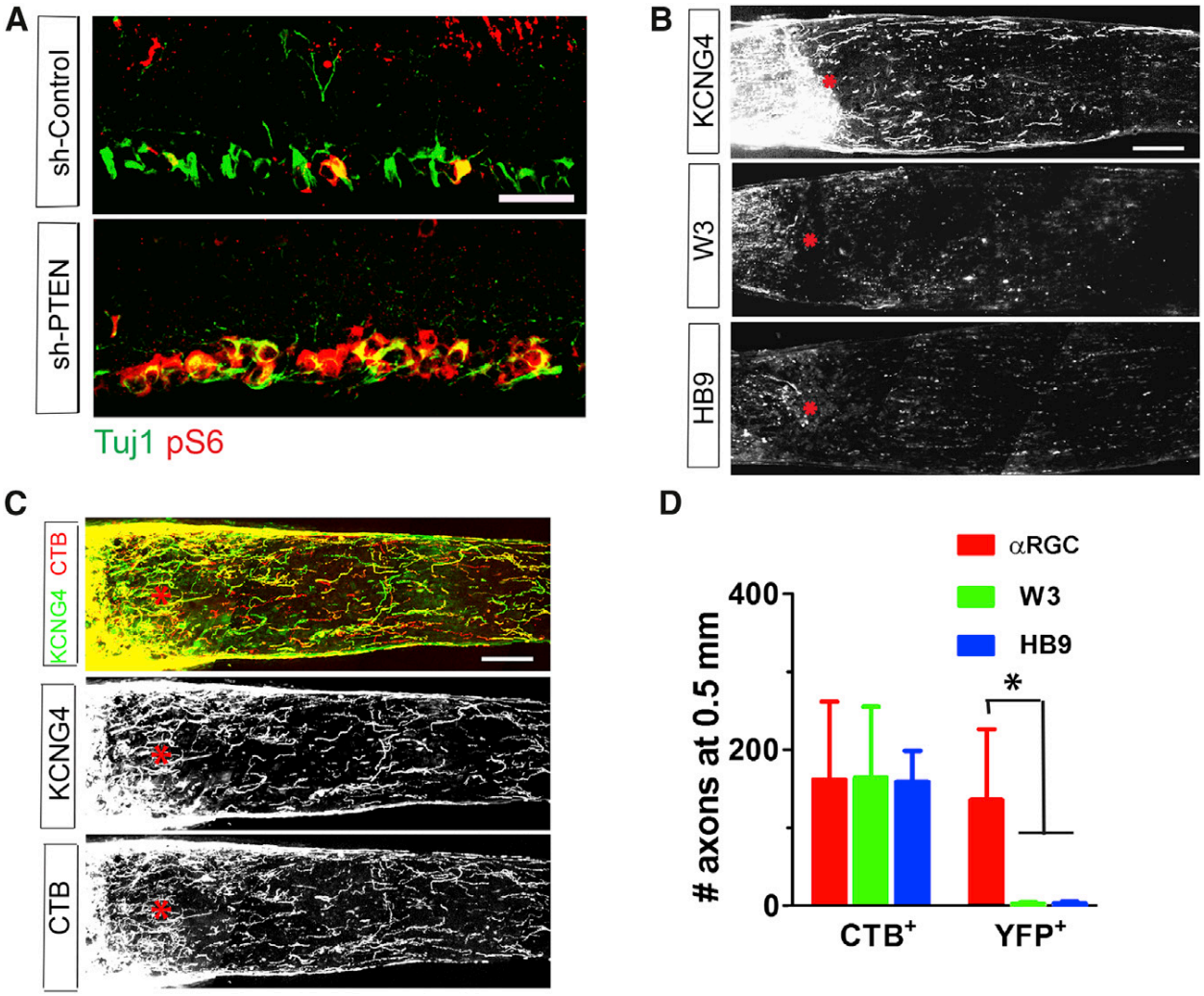

3.3.3 αRGCs have high mTOR activity and are rich in osteopontin

In adult retina, ~10% of RGCs are stained intensely with anti-pS6, and therefore have high mTOR activity (Park et al., 2008). We asked whether the pS6-rich cells are αRGCs. In initial studies, we found variable pS6 levels in RGCs of adult mice (data not shown). We reasoned that neuronal activity, which is known to stimulate phosphorylation of pS6 (Knight et al., 2012), contributed to this variability. We therefore dark-adapted mice overnight to decrease activity of RGCs, then stained retinas of Kcng4-YFP mice for pS6. In dark-adapted retina, ~6% of RGCs were clearly pS6-rich, and the others were not detectably pS6-positive (**Figure 3.5 A**). The pS6-rich RGCs were αRGCs: >90% of Kcng4-YFP$^+$ RGCs neurons were rich in pS6 and >85% of pS6-rich neurons were YFP$^+$ (**Figure 3.5 B**). In contrast, few if any M1 RGCs were pS6-rich (data not shown).

mTOR acts through two signaling complexes called mTORC1 and mTORC2 (Laplante and Sabatini, 2012). Phosphorylation of S6 is downstream of mTORC1, indicating that mTORC1 activity is enhanced in aRGCs. To test this idea, we stained retinas with antibodies specific to phosphorylated-Raptor (pRaptor) and phosphorylated-Rictor (pRictor), which are mTORC1- and mTORC2-specific signaling components, respectively. pRaptor was concentrated in αRGCs, whereas pRictor was present at low levels in non-αRGCs and barely detectable in αRGCs (**Figure 3.5 C,D**). Thus, mTORC1 is active in αRGCs.

We then asked whether αRGCs express other genes that could play roles in their selective survival and regeneration. In initial studies, we detected expression of osteopontin (OPN; gene symbol *Spp1* for secreted phosphoprotein-1) in large RGCs in adult retina (M. Yamagata and J.R.S, unpublished). We selected this candidate for further analysis because OPN is expressed by a subset of RGCs in rats (Ju et al., 2000), can enhance mTOR activity (Ahmed and Kundu, 2010) and has been implicated in injury responses of other neuronal types (see Discussion). Immunostaining in the Kcng4-YFP line revealed that

>90% of αRGCs were OPN^+, and 84% of OPN^+ RGCs were αRGCs (Fig. 3E, F). Likewise, OPN and neurofilament SMI32 staining overlapped by >90% (**Figure 3.1**).

To ask whether OPN regulates mTOR activity in the retina, we used AAV-mediated gene transfer to express OPN in multiple RGC subtypes. Over 60% of RGCs were strongly OPN^+ in optimally infected areas two weeks after infection, and levels of pS6 were high in ~60% of OPN-rich RGCs (**Figure 3.5 G,H**). Since aRGCs comprise only 6% of RCGs, OPN is clearly able to stimulate mTOR signaling in non-aRGCs We also used OPN null mutant mice ($OPN^{-/-}$) to ask whether the high mTOR levels of αRGCs require expression of OPN. Levels of pS6 in αRGCs did not differ detectably between controls and $OPN^{-/-}$ mice (**Figure 3.5 I,J**). Thus, OPN stimulates mTOR activity, but is presumably not the only factor that maintains high levels of mTOR activity in αRGCs.

Figure 3.5 Selective mTOR activity and OPN expression in αRGCs.

A, B. Section of Kcng4-YFP retina labeled with antibodies to pS6 plus YFP (A) and quantification of their overlap (B).

C,D. Sections of Kcng4-YFP retina labeled with antibodies to pRaptor (C) or pRictor (D) plus YFP.

E, F. Section of Kcng4-YFP retina labeled with antibodies to OPN and YFP (E) and quantification of their overlap (F).

G, H. Section of control retina (top) and retina infected with AAV-OPN (bottom) 2 weeks previously, labeled with antibodies to OPN and pS6 (G). (H) shows fraction of OPN^+ and $pS6^+$ cells in both conditions.

I, J. Section of Kcng4-YFP;$OPN^{-/-}$ retina labeled with antibodies to pS6 and YFP (I) and fraction of YFP^+ cells that were $pS6^+$ (J).

n.s., not significant. n=3 retinas per condition. Scale bars are 50μm.

Figure 3.5 Selective mTOR activity and OPN expression in αRGCs. (continued)

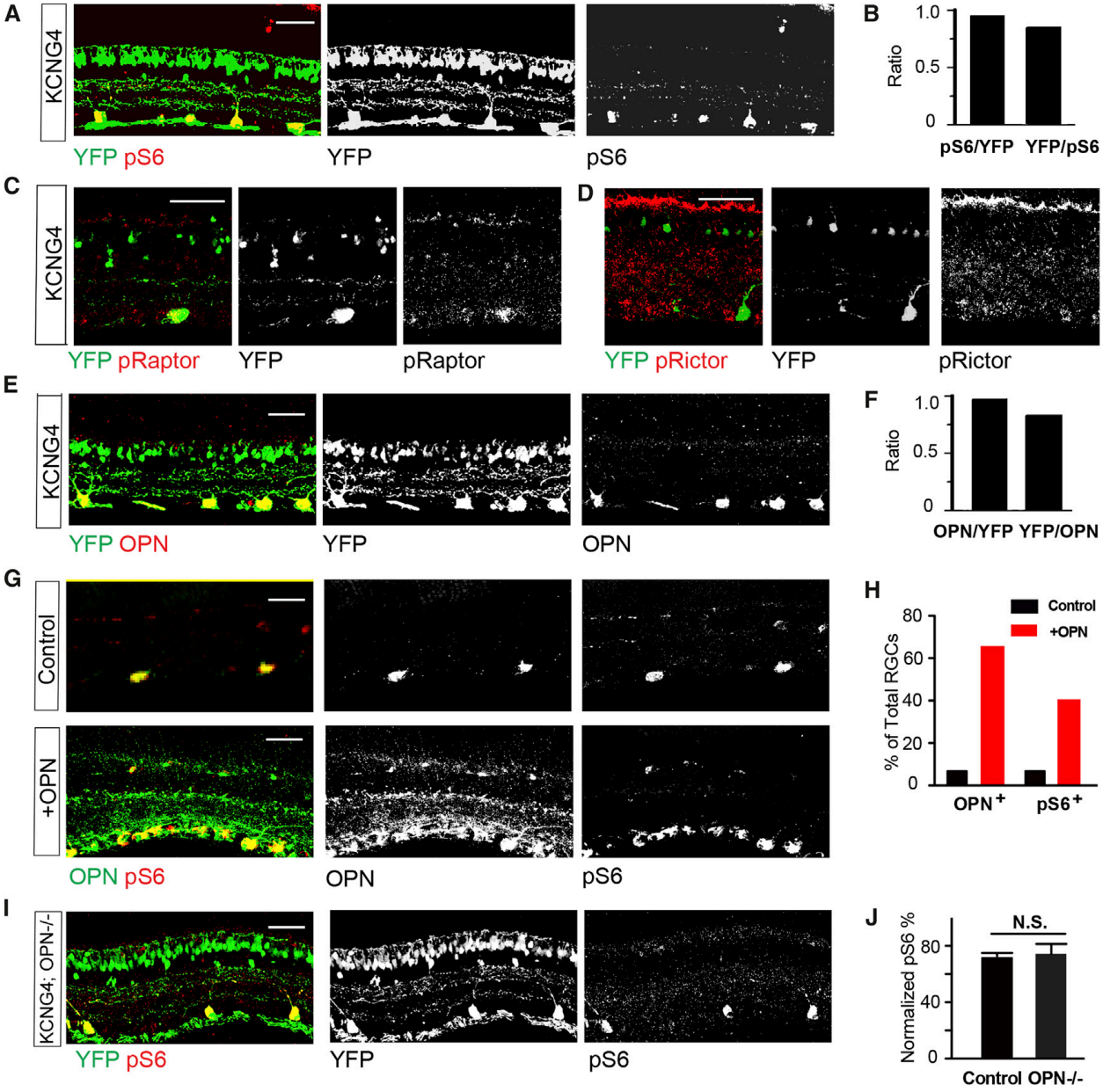

3.3.4 Osteopontin promotes RGC growth of non-αRGCs

Before assessing the ability of OPN to affect regeneration, we investigated its role in the normal development of αRGCs. We found that the difference in size between αRGC and non-αRGC somata arose during the first postnatal week, whereas OPN was not detectable in RGCs until the second postnatal week (**Figure 3.6 A, B**). These results suggested that OPN is dispensable for the initial growth of RGCs. Consistent with this idea, we found no significant difference in size between control and $OPN^{-/-}$ αRGCs during the period of peak growth or in adulthood (**Figure 3.7 A** and data not shown). Moreover, the majority of RGCs were rich in pS6 during the first postnatal week and pS6 immunoreactivity did not become restricted to aRGCs until the third postnatal week (Park et al., 2008). Thus, neither selective mTOR signaling or selective expression of OPN is required for αRGCs to reach their normal size.

We also asked whether OPN can promote growth of RGCs in adults using AAV-mediated gene transfer of OPN, as described above. RGC soma size (measured by area in sections) increased by ~30% over controls 4 weeks after introduction of OPN to a broad range of RGC types using Thy1-cre mice (**Figure 3.6 C, D**). Analysis with subtype-specific markers indicated that small W3 RGCs were affected disproportionately (80% increase in area), whereas the size of αRGCs did not increase in the presence of supernormal levels of OPN (**Figure 3.6 E and Figure 3.7 B**); this is consistent with the presence of additional growth-promoting factors in these neurons. Together, these results indicate that OPN does not play an essential role in the development of αRGCs but can elicit RGC growth and mTOR signaling in adult retina.

Figure 3.6 Role of OPN in developing retina.

A. Sections from retinas from TYW7 mice of indicated ages stained with antibodies to YFP and OPN. TYW7 labels OFF αRGCs (Kim et al. 2010 and B. Krieger, M.Q, X.D., J.R.S. and M. Meister, in preparation). OPN^+ YFP^- cells are presumably ON αRGCs. Staining is absent in retinas from $OPN^{-/-}$ mice. Scale bar, 50μm.

B. Soma sizes of developing αRGCs and non-αRGCs, and OPN levels in αRGCs in developing retina. OPN levels were measured from sections such as those in (A), as described in Methods.

C. Retinas from Thy1-cre mice infected 4 weeks previously with Cre-dependent AAV-YFP, with or without Cre-dependent AAV-OPN. Sections were labeled with antibodies to YFP and OPN. Bar, 20μm

D. RGC soma area, calculated from images such as those in C.

E. Soma size increase of W3-RGCs and αRGCs, measured from sections such as those in Fig. S3B. ** $p<0.01$.

Figure 3.6 Role of OPN in developing retina. (continued)

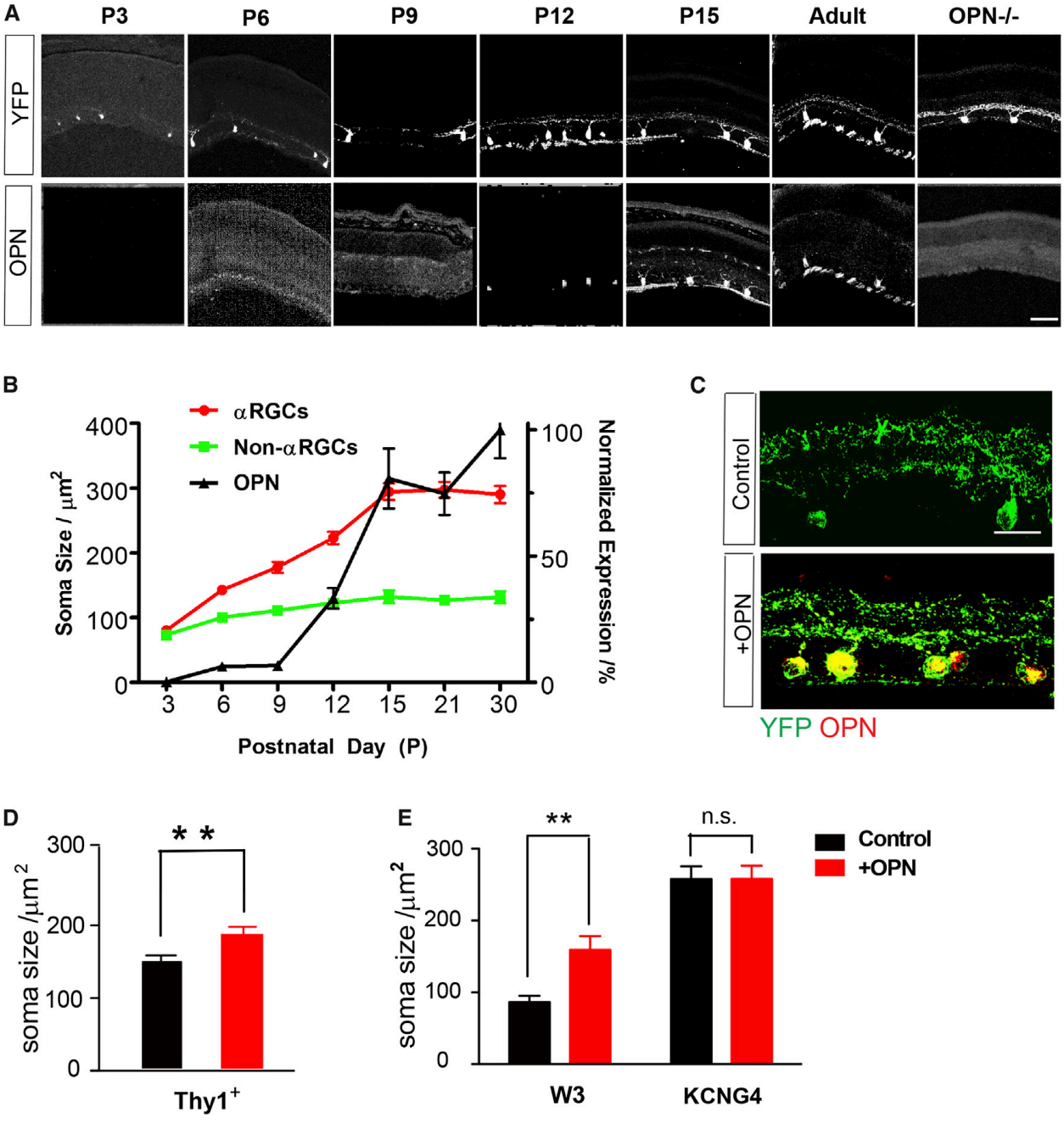

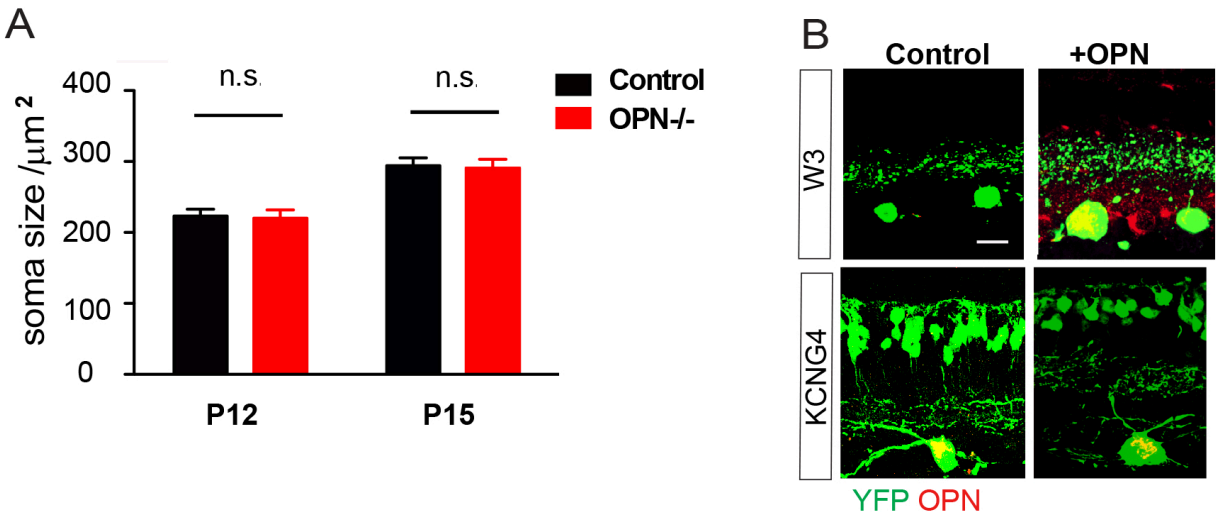

Figure 3.7 Effect of manipulating OPN expression on RGC size.

A. Soma sizes of αRGCs in control and OPN$^{-/-}$ mice at P12 and P15. n.s., not significant.

B. Sections of retina from TYW3 and Kcng4-YFP retinas, uninfected (control) or infected two weeks previously with AAV-OPN. Scale bar, 10μm.

3.3.5 Osteopontin plus IGF-1 promotes axonal regeneration

To ask whether OPN could promote axonal regeneration following nerve injury, we used the optic nerve crush protocol described above but infected retinal cells with AAV expressing OPN instead of shPTEN. Immunostaining showed expression of OPN in ~80% of RGCs in injured retina (data not shown) but regeneration was not significantly more effective in its presence than in control retinas (**Figure 3.8 A, B**). We therefore combined AAV-OPN administration with intravitreal injection of a growth factor. We chose IGF-1 because it has neuroprotective and regeneration-promoting abilities in other contexts (Dupraz et al., 2013; Hollis et al., 2009) and because its receptor, IGF1R, is expressed by RGCs (Bu et al., 2013; Tagami et al., 2009) and see below). IGF-1 alone had no detectable effect on regeneration, but the combination promoted regeneration as effectively as shPTEN (**Figure 3.8 A, B**). In some cases, axons regenerated and extended more than 2 mm (**Figure 3.9**). OPN and IGF-1 promoted RGC survival to a modest extent (**Figure 3.10 A, B**), but the effect on survival was insufficient to account for the effect on axonal regeneration.

We then tested the relationship of OPN, IGF-1 and mTOR activation as promoters of regeneration. IGF-1 on its own had no detectable effect of mTOR signaling in RGCs following axotomy, but expression of OPN, with or without IGF-1 enhanced mTOR signaling, following axotomy as it did in normal retina; (**Figure 3.11 A, B**). Moreover, rapamycin, a potent and specific inhibitor of mTOR (Laplante and Sabatini, 2012), blocked axonal regeneration promoted by OPN plus IGF-1 (**Figure 3.8 C, D**) as well as the OPN-induced increase in pS6 levels (**Figure 3.11 C**) with minimal effects on neuronal survival (**Figure 3.10 C**). Conversely, regeneration promoted by shPTEN is affected little if at all in $OPN^{-/-}$ mice (data not shown). These data place mTOR signaling downstream of OPN in a molecular pathway that promotes regeneration.

We also tested the combination of OPN and brain-derived neurotrophic factor (BDNF), because BDNF promotes RGC branching and its receptor, TrkB, is expressed by RGCs (Cui et al., 2002;

Sawai et al., 1996). Like IGF-1, BDNF was ineffective on its own at promoting regeneration and had a modest effect on survival. However, OPN plus BDNF stimulated regeneration to a similar extent as OPN plus IGF-1 (**Figure 3.8 E, F and Figure 10 B**). Thus the stimulatory role of IGF-1 was not unique and OPN can promote substantial axon regeneration when paired with growth factors.

Figure 3.8 OPN promotes regeneration of axotomized RGCs.

A. Sections of optic nerves at 14dpc. Retinas were untreated, infected with AAV-OPN, injected with IGF-1 or BDNF, or both infected and injected.

B. Numbers of regenerating fibers at indicated distances from lesion site, measured from sections such as those in (A).

C. Sections of optic nerves from Kcng4-YFP mice injected with (AAV-OPN+IGF-1) with or without rapamycin.

D. Numbers of regenerating fibers, measured from sections such as those in (C) and Fig. S5C.

n = 3-5 optic nerves per condition.

E. Sections of optic nerves from Kcng4-YFP mice injected with BDNF with or without AAV-OPN.

F. Numbers of regenerating fibers measured from sections such as those in (E).

Scale Bar for A, C, E, 200μm. *, p<0.05.

Figure 3.8 OPN promotes regeneration of axotomized RGCs. (continued)

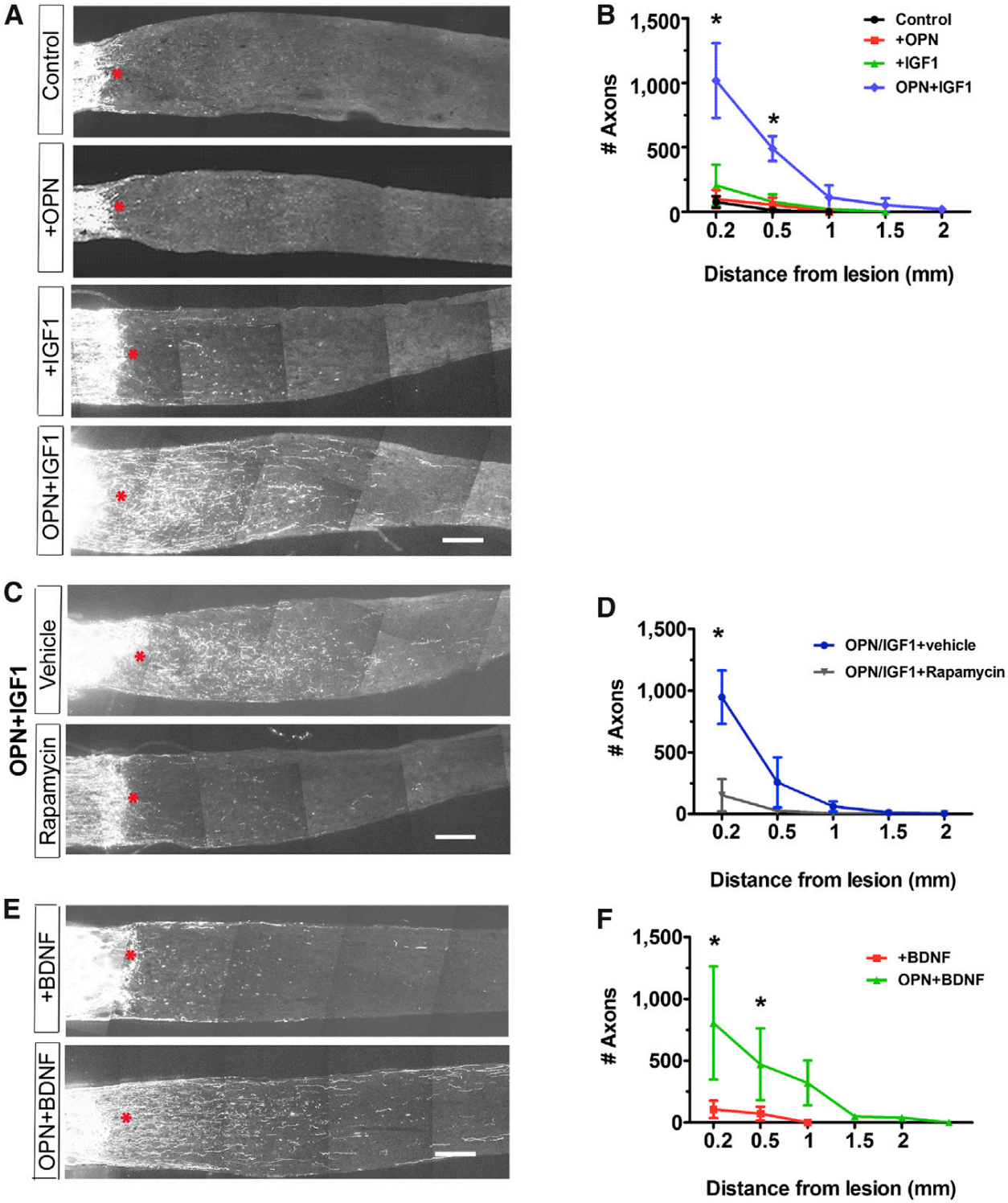

Figure 3.9 Effect of OPN on regeneration of RGCs following axotomy.

Section of optic nerves from wild-type mouse treated with AAV-OPN and IGF1, showing long distance regeneration. Boxed area shown at higher magnification in inset. Bar, 200μm.

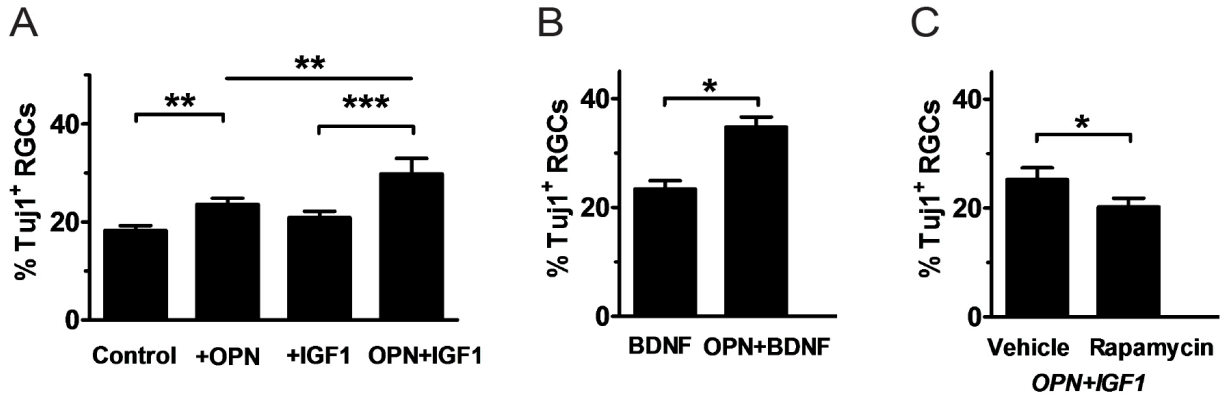

Figure 3.10 Effect of OPN and rapamycin on survival of RGCs following nerve crush.

A. Survival of RGCs at 14 dpc and 28 days after injection of IGF-1 and/or AAV-OPN.

B. Survival of RGCs at 14 dpc and 28 days after injection of BDNF, with or without AAV-OPN.

C. Survival of RGCs at 14 dpc and 28 days after injection of IGF-1 and AAV-OPN, with or without rapamycin. See Experimental Procedures for detailed protocols and doses.

***, p<0.05, **p<0.01; ***, p < 0.001.**

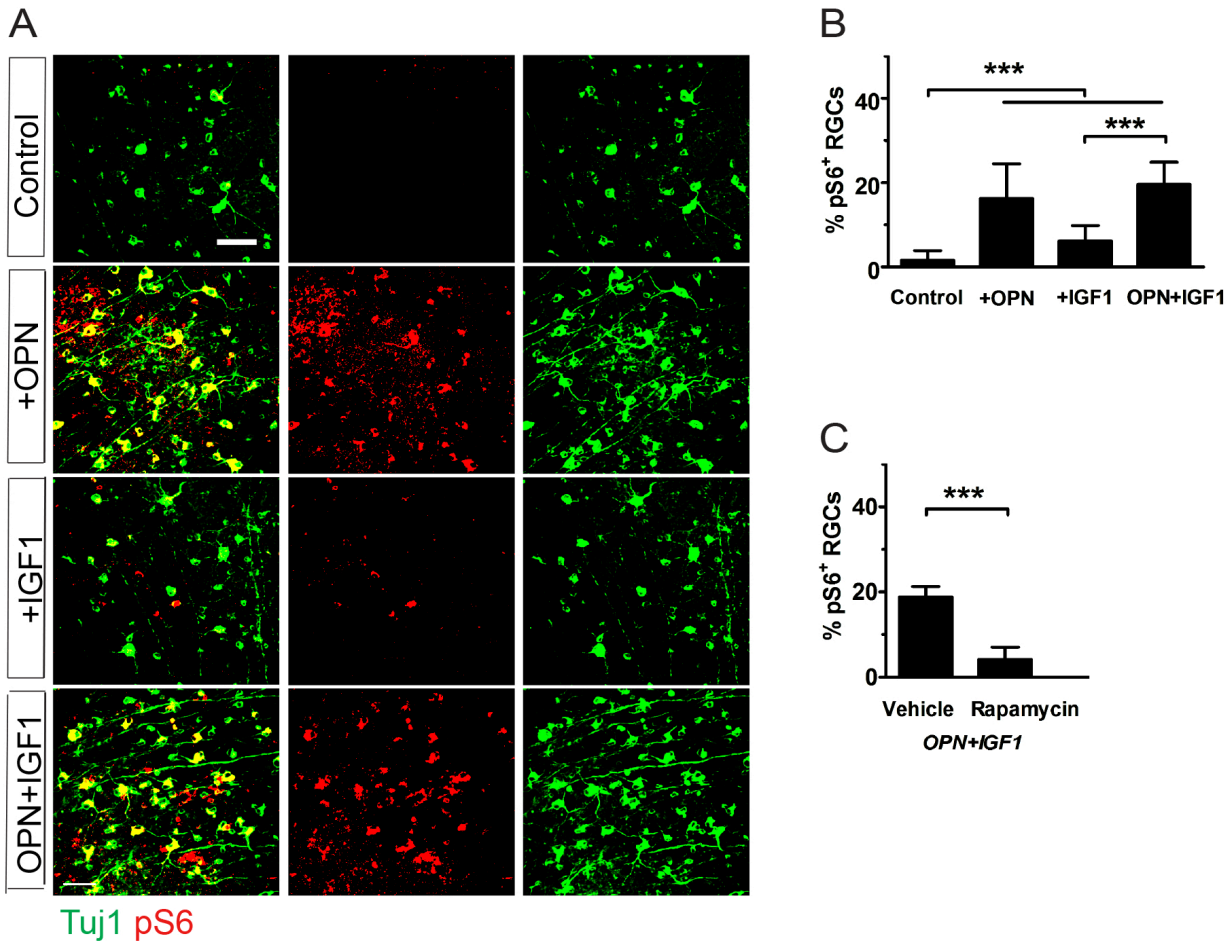

Figure 3.11 Effect of OPN on pS6 levels following axotomy.

A,B. Whole-mount images (A) show that pS6 level is elevated with AAV-OPN treatment (B) and that the elevation is blocked by rapamycin (C). Scale bar = 50μm. ***, $p < 0.001$.

3.3.6 Osteopontin plus IGF-1 promotes selective regeneration of αRGCs

We expected that administration of OPN plus IGF-1 to most or all RGCs would promote regeneration in multiple RGC types. To test this idea, we introduced AAV-OPN and IGF-1 intravitreally in Kcng4-YFP, HB9-GFP, and TYW3 mice to label αRGCs, ooDSGCs and W3-RGCs, respectively. Surprisingly, using protocols and criteria described above, we found that nearly all regenerating axons arose from αRGCs (**Figure 3.12 A, B**).

The ability to selectively target aRGCs provides an opportunity to ask whether the delivery of OPN directly to aRGCs promote regeneration. To this end, we used an AAV in which expression of OPN was Cre-dependent, and limited over-expression to αRGCs by infecting retinas of Kcng4-YFP mice. αRGC-specific expression of OPN promoted αRGC regeneration following nerve crush (**Figure 3.12 C, D**).

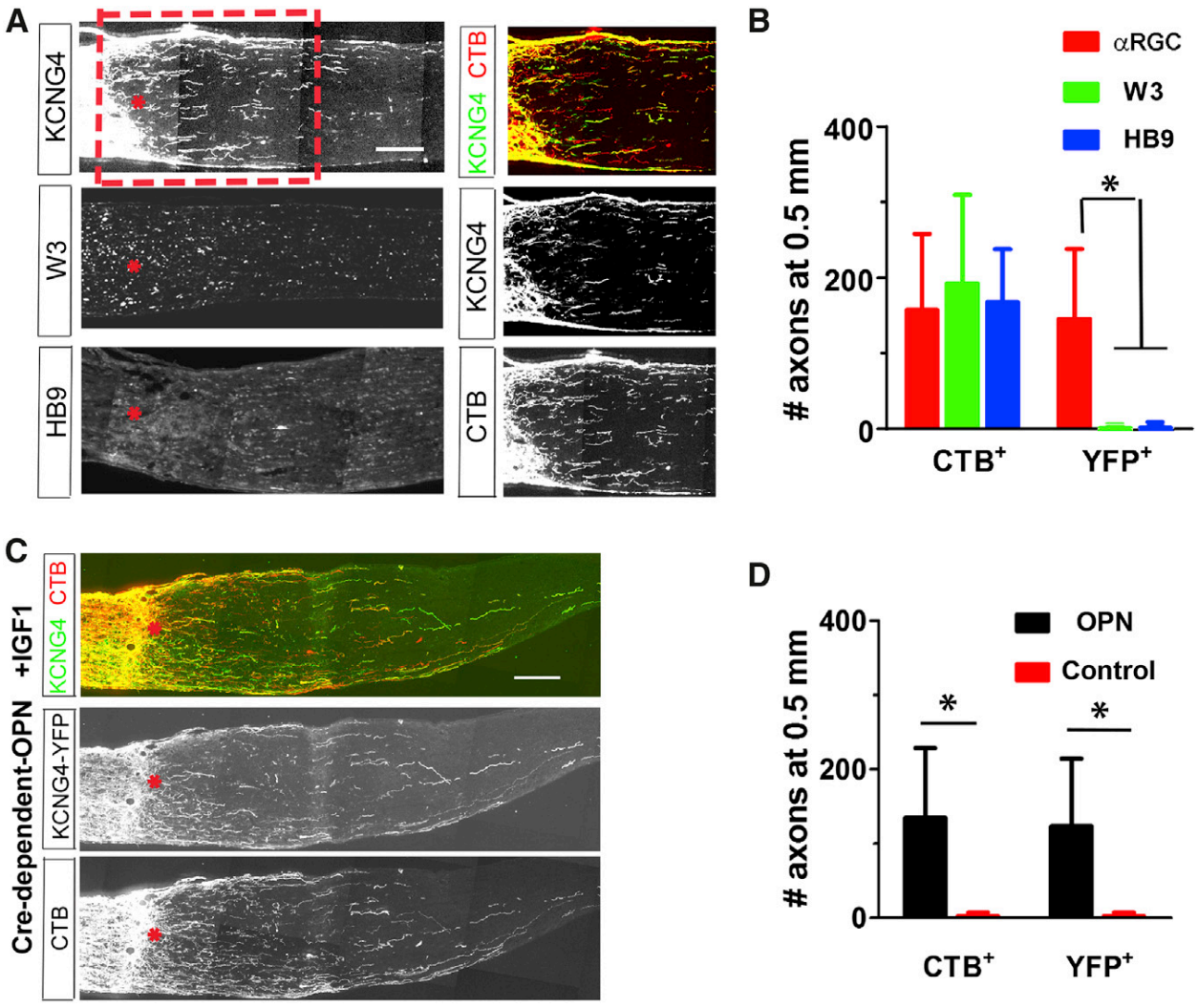

Figure 3.12 Osteopontin promotes selective regeneration of αRGCs.

A. Sections of optic nerves of Kcng4-YFP, TYW3, and HB9-GFP mice at 14dpc treated with AAV-OPN and IGF-1 and injected with CTB at 12dpc. Right panels show region boxed in top, left panel.

B. Numbers of regenerating fibers 0.5 mm from lesion site from sections such as those in F. n = 3-4 optic nerves per type. *, p<0.05.

C. Section of optic nerves from Kcng4-YFP mice injected with Cre-dependent AAV-OPN plus IGF-1.

D. Numbers of regenerating fibers 0.5 mm from lesion sites, measured from sections such as those in (C). P<0.05 (Two-ANOVA with Bonferroni Posttests).

3.3.7 Selective IGF1R expression and mTOR signaling in axotomized αRGCs

The result that AAV-OPN and IGF-1 are insufficient to promote regeneration of other RGC subtypes to which they are delivered implies that αRGCs differ from non-a-RGCs in some quality that enhances their regenerative responses following injury. The restriction of shPTEN-induced regeneration to αRGCs leads to the same conclusion. The difference could be in the ability of RGC subtypes to respond to IGF-1, to up-regulate mTOR signaling, or to respond appropriately to IGF-1- and mTOR-initiated signals. As a first step in distinguishing these alternatives, we compared levels of the IGF-1 receptor, IGF1R in αRGCs and non-αRGCs. IGF1R was selectively expressed in αRGCs in both control adult retina, and in retinas 3 dpc and 7 dpc , although some expression in non-aRGCs and Müller glial cells was observed following axotomy (**Figure 3.13 A**). TrkB showed a similar expression pattern, although the expression was less selective and the neuropil was also intensely stained (**Figure 3.14**). Thus, one factor contributing to selective responsiveness of αRGCs to OPN plus growth factors is selective expression of the growth factor receptors.

We also compared levels of mTOR signaling in axotomized αRGCs and non-αRGCs, using pS6 as a marker. Levels of pS6 fell dramatically in RGCs following axotomy, as shown previously (Park et al., 2008), and introduction of shPTEN or OPN plus IGF-1 restored its levels. These treatments were 9-fold and 3-fold more effective, respectively in increasing pS6 levels in axotomized αRGCs than in neighboring non-αRGCs (**Figure 3.13 B, E**). Moreover, even though αRGCs comprise only 20% of surviving RGCs at 14 dpc, they accounted for ~90% of pS6-rich RGCs following shPTEN treatment and ~60% of pS6-RGCs following OPN plus IGF-1 treatment. As in control retina (Fig. 3A), levels of pRaptor paralleled those of pS6, αRGCs accounted for >90% of pRaptor-rich RGCs following either shPTEN treatment or OPN plus IGF-1 administration (**Figure 3.13 C** and data not shown). However, the levels of pRictor were low, with <5% of total αRGCs being pRictor-positive. The expression level did not differ detectably between αRGCs and non-αRGCs, and did not change detectably following shPTEN treatment or OPN plus IGF-1 administration(**Figure 3.13 D**). (The ability of the pRictor antibody to

detect mTORC2 signaling is demonstrated by staining of non-neuronal cells in injured but not intact retina) Thus, a second property of αRGCs that can help account for their ability to regenerate is their ability to maintain or restore mTORC1 levels following axotomy.

Figure 3.13 Selective expression of IGF1R and activation of mTOR signaling in axotomized αRGCs.

A. IGF1R expression in aRGCs (labeled with OPN) in control retina, 3dpc and 7dpc.

B-D. Sections from mice injected with control vector, AAV-shPTEN or AAV-OPN plus IGF-1. Optic nerves were crushed 14 days later and retinas analyzed 14dpc with anti-pS6 (B), anti-pRaptor (C) or anti-pRictor (D). Scale bars are _50μm.

E. Fraction of αRGC and other RGCs (YFP^+ and YFP^-, respectively in Kcng4-YFP) that are $pS6^+$, from sections such as those in (B). n=4-6 retinas per treatment.

F. Model showing pathways by which PTEN knock-down or exogenous OPN expression could promote regeneration. a,b,c indicate steps at which differences between αRGC and non-αRGCs could affect their regenerative abilities. Results in A-E implicate steps "a" and "b" as critical differences.

Figure 3.13 Selective expression of IGF1R and activation of mTOR signaling in axotomized αRGCs.

(continued)

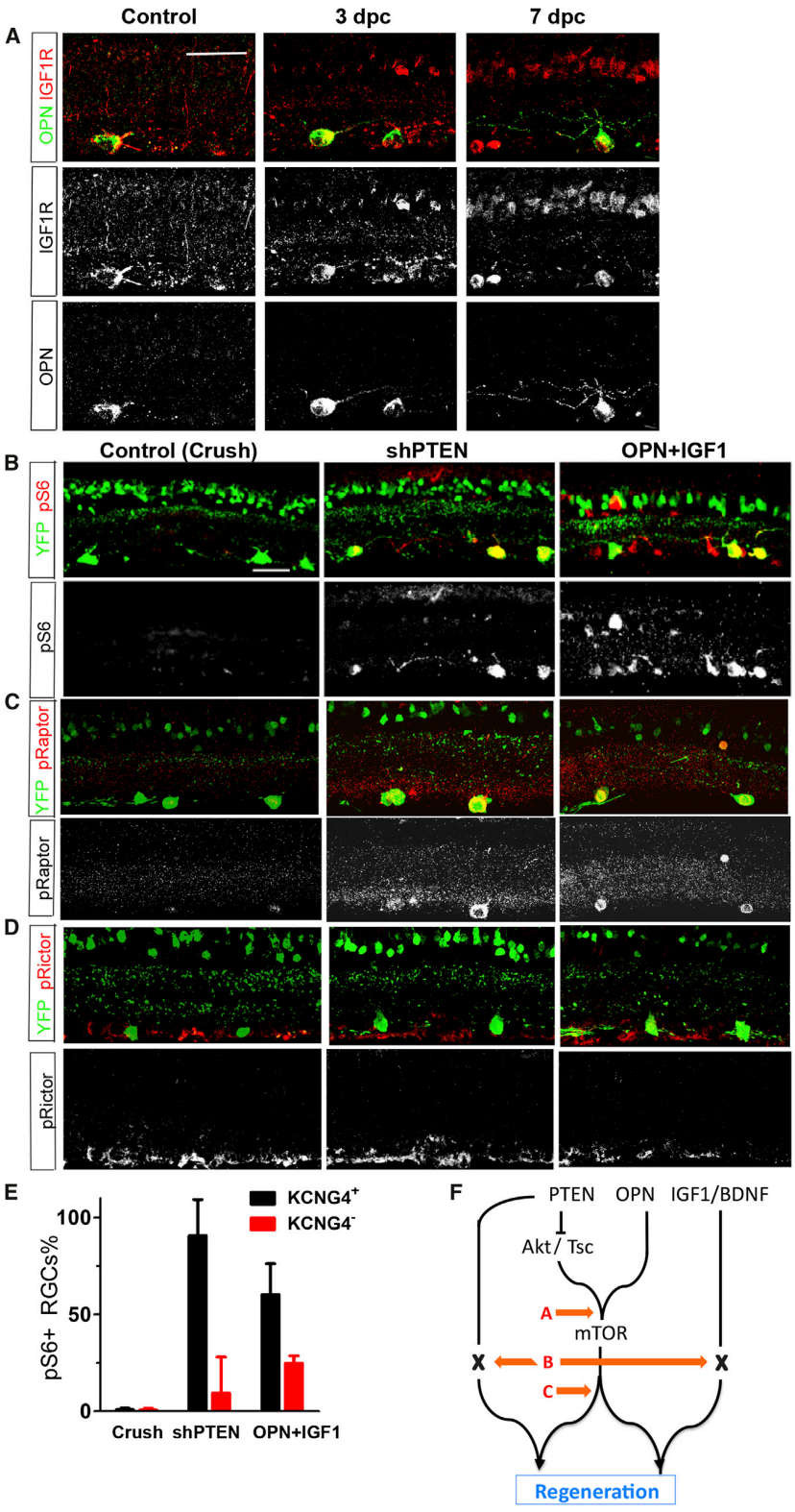

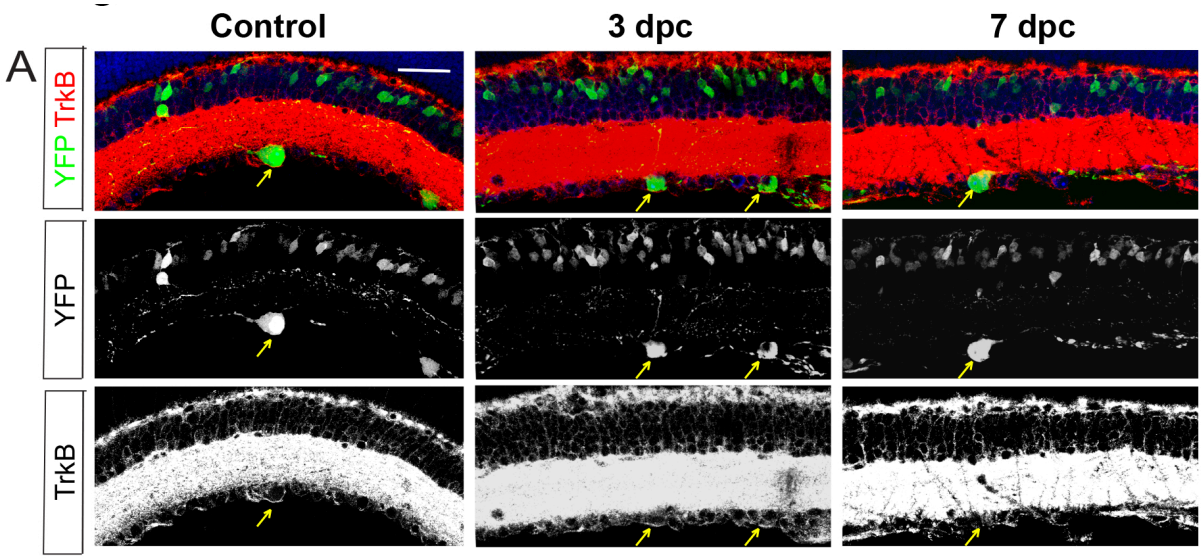

Figure 3.14 Expression of TrkB in uninjured adult retina, 3 and 7 days following axotomy.

TrkB was localized by immunostaining. αRGCs were marked by YFP expression in Kcng4-YFP mice. Scale bar = 50μm.

3.4 Discussion

Following damage to the optic nerve, few RGCs survive and even fewer can be coaxed to extend new axons (Aguayo et al., 1991; Liu et al., 2011). Using markers of eleven RGC subtypes, we found that limited survival and regeneration does not reflect uniformly low vigor of many subtypes; instead it results from selective survival and regeneration of specific subtypes. We then analyzed factors that promote regeneration of those RGCs that survive, and identified OPN as a promoter of RGC growth and regeneration. Together, our results provide new insights into both the cellular and molecular bases of axon regeneration in the mammalian CNS.

3.4.1 Selective survival and regeneration of αRGCs

We found dramatic differences among RGC subtypes in their ability to survive axotomy. Some populations, such as ooDSGCs, are almost completely eliminated within two weeks, whereas most αRGCs and M1-RGCs survive. These results are consistent with previous reports that M1 RGCs preferentially survive axotomy in rats, and that alpha-like RGCs selectively regenerate in cats (Perez de Sevilla Muller et al., 2014; Robinson and Madison, 2004; Watanabe et al., 1993); (Watanabe and Fukuda, 2002; Watanabe et al., 1995). Differential susceptibility to injury has also been reported in a mouse model of glaucoma, although the subtypes affected were not molecularly identified (Della Santina et al., 2013). As a consequence of selective survival, the repertoire of visual features that the retina could potentially report to the brain is fundamentally altered (**Figure 3.2 D**), a change that will need to be taken into account if efforts to promote regeneration of RGC survivors succeed.

Among surviving RGCs, the ability to regenerate is specific to αRGCs, an evolutionarily conserved RGC type characterized by large somata, smooth dendrites, high levels of neurofilaments and large receptive fields (Berson, 2008; Peichl, 1991). αRGCs comprise ~6% of all RGCs in intact retina and ~25% of the RGCs that survive axotomy, but give rise to >90% of the axons that extend >0.5mm beyond

the site of nerve crush following down-regulation of PTEN. In that αRGCs and non-αRGCs are intermingled in the retina, and their axons are intermingled in the optic nerve, it is almost certain that the differences in their regenerative abilities reflect intrinsic differences rather than differences in their environments.

One caveat to the conclusion that αRGCs regenerate selectively is that we tested only two regeneration-promoting treatments, PTEN knock-down and OPN plus a growth factor. It will be important to ask whether other interventions, such as deletion of suppressor of cytokine signaling 3 (SOCS3) or provoking an inflammatory response (Benowitz and Popovich, 2011; Morgan-Warren et al., 2013; Park et al., 2008; Smith et al., 2009; Sun et al., 2011; Watkins et al., 2013) can promote regeneration of additional RGC subtypes.

3.4.2 Osteopontin as a promoter of axon regeneration

OPN promotes RGC regeneration when introduced in combination with either IGF-1 or BDNF, neither of which promotes significant regeneration on its own. OPN is a secreted, glycosylated phosphoprotein; it was discovered as a component of bone matrix but has since been shown to be synthesized by many cell types and to affect multiple cellular processes, including adhesion, proliferation and survival (Kahles et al., 2014; Kazanecki et al., 2007; Wang and Denhardt, 2008). It is expressed by subsets of neurons as well as several classes of glial cells including Schwann cells, Muller glia and microglia. Levels are affected by neural injury in several systems, and OPN is reported to exert both pro- and anti-inflammatory roles that can promote neuronal survival and regeneration (Carecchio and Comi, 2011; Chidlow et al., 2008; Del Rio et al., 2011; Hashimoto et al., 2007; Misawa et al., 2012; Wright et al., 2014). In most cases, these effects have been ascribed to depots in glial cells; for OPN-stimulated regeneration of injured motor axons, elegant transplantation experiments have demonstrated that this is the case (Wright et al., 2014). In the retina, in contrast, directed delivery reveals that neuron-derived OPN promotes regeneration.

OPN may be useful for promoting regeneration for several reasons. First, PTEN is a tumor suppressor. Whereas OPN, like PTEN knockdown, acts in part by elevating mTOR, PTEN inhibition also activates many additional pathways that likely contribute to its tumor suppressor activity. OPN may circumvent this potentially dangerous activity. Second, soluble protein therapeutics are clearly promising for treatment of a variety of neural injuries and neurological diseases (Thoenen and Sendtner, 2002). In other systems, OPN acts as an extracellular cytokine (Kahles et al., 2014). Therefore, a soluble form of OPN, together with a growth factor, might represent a therapeutic method of transiently activating regenerative ability in mature neurons.

3.4.3 Growth promoting capabilities of αRGCs

Regeneration promoted by OPN plus IGF-1 or shPTEN is restricted to αRGCs. This surprising result raises two questions. First, why are endogenous OPN and mTOR, both of which are enriched in adult αRGCs, insufficient to promote their regeneration? Second, why is regeneration restricted to αRGCs even when OPN plus IGF-1 or shPTEN is supplied to most RGCs?

One answer to the first question is that mTOR signaling decreases dramatically following axon damage (Park et al., 2008). We hypothesized that OPN might also decrease following axotomy, but detected no striking changes in OPN levels by immunohistochemistry or in OPN mRNA levels by RT-PCR (data not shown). However, our immunohistochemical methods are non-quantitative, and decreases in OPN mRNA abundance in RGCs would have been masked by known increases in microglia (Chidlow et al., 2008). Moreover, OPN is heterogeneous in several respects: there are several alternatively spliced isoforms (at least in humans), many forms of post-translational modification, and an alternative translation product that remains intracellular and mediates activities distinct from those of the secreted isoform (Gimba and Tilli, 2013; Inoue and Shinohara, 2011; Kazanecki et al., 2007). It remains to be

determined which forms promote regeneration and whether the active forms, which may be a small fraction of the total, are affected by axotomy.

In considering the second question, we note that at least two signaling pathways are activated by the interventions we have assayed here (**Figure 3.13 F**). The first is mTOR signaling, as indicated by the sensitivity of PTEN shRNA and OPN-induced regeneration to the mTOR-specific blocker, rapamycin (Park et al., 2008) ("a" in **Figure 3.13 F**). For reasons we do not yet understand, OPN upregulates mTOR signaling selectively in αRGCs following axotomy, even though it can upregulate mTOR signaling in most RGCs in uninjured retina.

mTOR signaling alone is insufficient for robust regeneration, however. PTEN regulates several pathways other than mTOR (Hill and Wu, 2009; Manning and Cantley, 2007; Morgan-Warren et al., 2013) and interventions that more selectively up-regulate mTOR signaling, such as deletion of TSC1, are significantly less effective in eliciting regeneration than down-regulation of PTEN (Park et al., 2008). Likewise, OPN can up-regulate mTOR signaling in the presence or absence of a growth factor, but does not induce regeneration unless accompanied by a growth factor. Thus, mTOR-dependent and –independent pathways must be co-activated for optimal regeneration. We suggest that IGF-1, which does not detectably enhance mTOR signaling, activates the mTOR-independent pathway ("b" in **Figure 3.13 F**). Selective activation of this pathway in αRGCs is likely based on the selective expression of IGF1R by αRGCs. Other salient differences between αRGCs and non-αRGCs may well exist, for example at later steps in the signaling pathway ("c" in **Figure 3.13 F**). Molecular comparison of subtypes refractory and susceptible to the effects of injury will be a promising approach for identifying these and other factors that promote survival and regeneration.

3.5 Methods

3.5.1 Animals

OPN mutant mice were produced by inserting CreER into the translation start codon of the *spp1* gene using lambda phage-mediated recombineering (Chan et al., 2007), followed by homologous recombination in embryonic stem cells. Chimeras were produced by the Harvard University Genome Modification Facility. High percentage chimeras transmitting the knock-in alleles were bred to animals expressing FLP recombinase from the beta-actin promoter (Rodriguez et al., 2000) to remove the PGK-NEO cassette. Primers used for genotyping OPN^{CreER} are: OPN Common Forward Primer (TTGGTGGTGATCTAGTGGTGCCAA), CreER Reverse Primer (CATCGACCGGTAATGCAGGCAAAT), OPN wild-type Reverse Primer (CAAGGAAATGCGTGTGAGTGTGCT). The primers amplify fragments of 500bp for the knock-in allele and 225bp for the wild-type allele. Insertion of CreER led to generation of a null allele (Fig. 4A and data not shown). However, we detected very low levels of CreER expression and activity in this line, so it was not useful for marking OPN-expressing cells.

HB9-GFP transgenic mice (Trenholm et al., 2011) were obtained from K. Eggan (Stem Cell and Regenerative Biology Department, Harvard) and Thy1-cre transgenic mice (Dewachter et al., 2002) were obtained from Jackson Laboratories. Other lines were generated and characterized in our laboratory as described previously: Kcng4-Cre (Duan et al.,2014); TWY3-YFP (Kim et al., 2010; Zhang et al., 2012); TWY7-YFP (Kim et al., 2010); and Thy1-STOP-YFP (Buffelli et al., 2003). Mice were maintained on a C57/BL6 background and experiments were done according to protocols approved by both the Harvard University Standing Committee on the Use of Animals in Research and Teaching and IACUC at Boston Children's Hospital.

3.5.2 Gene transfer and surgical methods

A cDNA encoding OPN was cloned from a mouse retina cDNA library (Kay et al, 2012) and inserted into AAV plasmids for ubiquitous or Cre-dependent expression (Cardin et al., 2009). The coding sequence corresponds to that in accession number BC020355 (NCBI-Nucleotide). AAV-U6-shPTEN-CMV-mCherry was modified from a previously characterized vector AAV-U6-shPTEN-CMV-GFP (Zukor et al. 2013) by changing the fluoresecent protein. The targeting sequence was AGGTGAAGATATATTCCTCCAA. AAV serotype 2/2 was produced at Boston Children's Hospital Viral Core. AAV2 was titered to $>1x10^{12}$ genome copies per ml.

Detailed surgical methods were described by Park et al. (2008). For injection, adult animals were anesthetized with ketamine/xylazine (100/10 mg/kg). AAV (~3 μl) was injected intravitreally with a fine glass pipette. Optic nerves were crushed with a pair of Dumont #5 forceps (Roboz) 2 weeks after injection. IGF-1 or BDNF (1 μl, 1 μg/μL, Peprotech) was injected into the vitreal space of the eye at 0 dpc and 7 dpc. 1 μl of Alexa-conjugated CTB568 or 647 (Invitrogen) was injected intravitreally 2-3 days before euthanasia to label all regenerating axons. Rapamycin (6 mg/kg, LC Laboratories) was delivered intraperitoneally every two days from the time of AAV injection.

3.5.3 Histology

Anesthetized mice were transcardially perfused with 4% paraformaldehyde (PFA). Eyes and optic nerves were dissected out and post-fixed in 4% PFA at 4°C overnight. For frozen sections, tissues were immersed in 30% sucrose for two days before sectioning in a cryostat (20 μm for retina, 10 μm for optic nerve). For some experiment, eyes were fixed in 4% PFA at 4°C by immersion for ~30-60 mins, immediately after the mice were sacrificed by a lethal overdose of anesthesia.

For immunohistochemistry, sections were incubated in PBS with 3% donkey serum and 0.3% Triton X-100 for blocking, followed by primary antibodies overnight at 4° C and secondary antibodies for ~2 hrs at room temperature. Wholemounts were incubated in PBS with 5% donkey serum and 0.5%

Triton X-100 for blocking, followed by primary antibodies for ≥48 hrs at 4°C and secondary antibodies for ≥16 hrs at 4°C. Finally, sections were washed with PBS and mounted in Vectashield (Vectorlabs).

Primary antibodies used were: rabbit anti-GFP (1:1000, Millipore), chicken anti-GFP (1:500, Abcam); rabbit anti-RFP (1:500, Abcam); rabbit anti-CART (1:2500, Phoenix Peptide); rabbit anti-melanopsin (1:1000, gift from I. Provencio, University of Virginia); rabbit anti-phosphorylated S6 Ser235/236 (1:200, Cell Signaling Technology); mouse anti-neurofilament (SMI32, 1:1000, Convance); rabbit anti-IGF1R (1:1000, Sigma); goat anti-mouse TrkB (1:500, R&D systems); rabbit anti-phosphorylated-Raptor (Ser792) (1:200, Cell Signaling Technology), rabbit anti-phosphorylated-Rictor (Thr1135) (1:200, Cell Signaling Technology) and goat anti-osteopontin (1:1000, R&D Systems); Nuclei were labelled with NeuroTrace Nissl 435/455 (1:1000, Invitrogen). Secondary antibodies were conjugated to DyLight 649 (Jackson ImmunoResearch), Alexa Fluor 568 or Alexa Fluor 488 (Invitrogen) and used at 1:500.

3.5.4 Imaging and quantification

For whole mounts of retinas, at least eight areas (~0.5 x 0.5 mm) across the whole retinas were imaged with a standard epi-fluorescence microscope (Nikon) focusing on the retinal ganglion layer. Cells were counted and the counts obtained from all areas were averaged to generate a single value for each retina.

For retina sections, images were taken with a confocal microscope (Olympus FV1000 or Zeiss LSM-710) using 440/488–515/568 and 647 lasers with a step size of 0.5μm and a 40X (NA 1.3) lens. Images were analyzed using ImageJ (NIH) software. One field from at least eight sections per sample were imaged and analyzed. The numbers from all sections were averaged to generate a single value for each retina.

For soma size measurement, Z stacks were projected onto a single plane and the largest area was measured with ImageJ. To measure level of immunoreactivity, slides were stained, mounted and imaged

in parallel, and the signals were imaged within a linear range. Fluorescent intensity was measured in ImageJ to indicate the relative expression level.

For nerve sections, regenerating axons were identified and counted as described by (Park et al., 2008). In analyzing YFP^+ axons, signals from fluorescent or autofluorescent tissue debris was excluded.

Only contrast and brightness were adjusted for all images. Caution was taken not to over-saturate the images and only brightly-stained cells were counted when positive staining was to be identified.

3.6 Acknowledgement

We thank Masa Yamagata and Terrance Kummer for providing the first evidence that osteopontin is expressed by aRGCs, members of the Sanes and He laboratories for advice and discussions, and M. Evarts for technical assistance. AAV was generated by C. Wang in the Boston Children's Hospital Viral Core, supported by NIH P30EY012196. Mice were generated at the Harvard Genome Modification Core supported by NIH P30NS062685. This work was supported by grants from NIH to J.R.S (NS029169, EY022073), and Z.H. (EY021342, EY021526), and a HHMI-LSRF Fellowship to X.D.

3.7 References

Aguayo, A.J., Rasminsky, M., Bray, G.M., Carbonetto, S., McKerracher, L., Villegas-Perez, M.P., Vidal-Sanz, M., and Carter, D.A. (1991). Degenerative and regenerative responses of injured neurons in the central nervous system of adult mammals. Philosophical transactions of the Royal Society of London Series B, Biological sciences 331, 337-343.

Ahmed, M., and Kundu, G.C. (2010). Osteopontin selectively regulates p70S6K/mTOR phosphorylation leading to NF-kappaB dependent AP-1-mediated ICAM-1 expression in breast cancer cells. Molecular cancer 9, 101.

Bellahcene, A., Castronovo, V., Ogbureke, K.U., Fisher, L.W., and Fedarko, N.S. (2008). Small integrin-binding ligand N-linked glycoproteins (SIBLINGs): multifunctional proteins in cancer. Nature reviews Cancer 8, 212-226.

Benowitz, L.I., and Popovich, P.G. (2011). Inflammation and axon regeneration. Current opinion in neurology 24, 577-583.

Berson, D.M. (2008). Retinal ganglion-cell types and their central projections. In The Senses: A Comprehensive Reference, A.K. Allan I. Basbaum, Gordon M. Shepard and Gerald Westheimer, ed. (San Diego: Academic Press), pp. 491-520.

Berson, D.M., Castrucci, A.M., and Provencio, I. (2010). Morphology and mosaics of melanopsin-expressing retinal ganglion cell types in mice. The Journal of comparative neurology 518, 2405-2422.

Bu, S.Y., Yu, G.H., and Xu, G.X. (2013). Expression of insulin-like growth factor 1 receptor in rat retina following optic nerve injury. Acta ophthalmologica 91, e427-431.

Buffelli, M., Burgess, R.W., Feng, G., Lobe, C.G., Lichtman, J.W., and Sanes, J.R. (2003). Genetic evidence that relative synaptic efficacy biases the outcome of synaptic competition. Nature 424, 430-434.

Cardin, J.A., Carlen, M., Meletis, K., Knoblich, U., Zhang, F., Deisseroth, K., Tsai, L.H., and Moore, C.I. (2009). Driving fast-spiking cells induces gamma rhythm and controls sensory responses. Nature 459, 663-667.

Carecchio, M., and Comi, C. (2011). The role of osteopontin in neurodegenerative diseases. Journal of Alzheimer's disease : JAD 25, 179-185.

Chan, W., Costantino, N., Li, R., Lee, S.C., Su, Q., Melvin, D., Court, D.L., and Liu, P. (2007). A recombineering based approach for high-throughput conditional knockout targeting vector construction. Nucleic Acids Res 35, e64.

Chidlow, G., Wood, J.P., Manavis, J., Osborne, N.N., and Casson, R.J. (2008). Expression of osteopontin in the rat retina: effects of excitotoxic and ischemic injuries. Investigative ophthalmology & visual science 49, 762-771.

Conta Steencken, A.C., Smirnov, I., and Stelzner, D.J. (2011). Cell survival or cell death: differential vulnerability of long descending and thoracic propriospinal neurons to low thoracic axotomy in the adult rat. Neuroscience 194, 359-371.

Cui, Q., Tang, L.S., Hu, B., So, K.F., and Yip, H.K. (2002). Expression of trkA, trkB, and trkC in injured and regenerating retinal ganglion cells of adult rats. Investigative ophthalmology & visual science 43, 1954-1964.

Del Rio, P., Irmler, M., Arango-Gonzalez, B., Favor, J., Bobe, C., Bartsch, U., Vecino, E., Beckers, J., Hauck, S.M., and Ueffing, M. (2011). GDNF-induced osteopontin from Muller glial cells promotes photoreceptor survival in the Pde6brd1 mouse model of retinal degeneration. Glia 59, 821-832.

Della Santina, L., Inman, D.M., Lupien, C.B., Horner, P.J., and Wong, R.O. (2013). Differential progression of structural and functional alterations in distinct retinal ganglion cell types in a mouse model of glaucoma. Journal of Neuroscience 33, 17444-17457.

Dewachter, I., Reverse, D., Caluwaerts, N., Ris, L., Kuiperi, C., Van den Haute, C., Spittaels, K., Umans, L., Serneels, L., Thiry, E., et al. (2002). Neuronal deficiency of presenilin 1 inhibits amyloid plaque formation and corrects hippocampal long-term potentiation but not a cognitive defect of amyloid precursor protein [V717I] transgenic mice. Journal of Neuroscience 22, 3445-3453.

Duan, X., Krishnaswamy, A., De la Huerta, I., and Sanes, J.R. (2014). Type II cadherins guide assembly of a direction-selective retinal circuit. Cell 158, 793-807.

Dupraz, S., Grassi, D., Karnas, D., Nieto Guil, A.F., Hicks, D., and Quiroga, S. (2013). The insulin-like growth factor 1 receptor is essential for axonal regeneration in adult central nervous system neurons. PloS one 8, e54462.

Ecker, J.L., Dumitrescu, O.N., Wong, K.Y., Alam, N.M., Chen, S.K., LeGates, T., Renna, J.M., Prusky, G.T., Berson, D.M., and Hattar, S. (2010). Melanopsin-expressing retinal ganglion-cell photoreceptors: cellular diversity and role in pattern vision. Neuron 67, 49-60.

Estevez, M.E., Fogerson, P.M., Ilardi, M.C., Borghuis, B.G., Chan, E., Weng, S., Auferkorte, O.N., Demb, J.B., and Berson, D.M. (2012). Form and function of the M4 cell, an intrinsically photosensitive retinal ganglion cell type contributing to geniculocortical vision. Journal of Neuroscience 32, 13608-13620.

Gimba, E.R., and Tilli, T.M. (2013). Human osteopontin splicing isoforms: known roles, potential clinical applications and activated signaling pathways. Cancer letters 331, 11-17.

Hashimoto, M., Sun, D., Rittling, S.R., Denhardt, D.T., and Young, W. (2007). Osteopontin-deficient mice exhibit less inflammation, greater tissue damage, and impaired locomotor recovery from spinal cord injury compared with wild-type controls. Journal of Neuroscience 27, 3603-3611.

Hill, R., and Wu, H. (2009). PTEN, stem cells, and cancer stem cells. The Journal of biological chemistry 284, 11755-11759.

Hollis, E.R., 2nd, Lu, P., Blesch, A., and Tuszynski, M.H. (2009). IGF-I gene delivery promotes corticospinal neuronal survival but not regeneration after adult CNS injury. Experimental neurology 215, 53-59.

Inoue, M., and Shinohara, M.L. (2011). Intracellular osteopontin (iOPN) and immunity. Immunologic research 49, 160-172.

Jaworski, J., Spangler, S., Seeburg, D.P., Hoogenraad, C.C., and Sheng, M. (2005). Control of dendritic arborization by the phosphoinositide-3'-kinase-Akt-mammalian target of rapamycin pathway. Journal of Neuroscience 25, 11300-11312.

Ju, W.K., Kim, K.Y., Cha, J.H., Kim, I.B., Lee, M.Y., Oh, S.J., Chung, J.W., and Chun, M.H. (2000). Ganglion cells of the rat retina show osteopontin-like immunoreactivity. Brain research 852, 217-220.

Kahles, F., Findeisen, H.M., and Bruemmer, D. (2014). Osteopontin: A novel regulator at the cross roads of inflammation, obesity and diabetes. Molecular metabolism 3, 384-393.

Kay, J.N., De la Huerta, I., Kim, I.J., Zhang, Y., Yamagata, M., Chu, M.W., Meister, M., and Sanes, J.R. (2011). Retinal ganglion cells with distinct directional preferences differ in molecular identity, structure, and central projections. Journal of Neuroscience 31, 7753-7762.

Kazanecki, C.C., Uzwiak, D.J., and Denhardt, D.T. (2007). Control of osteopontin signaling and function by post-translational phosphorylation and protein folding. Journal of cellular biochemistry 102, 912-924.

Kim, I.J., Zhang, Y., Meister, M., and Sanes, J.R. (2010). Laminar restriction of retinal ganglion cell dendrites and axons: subtype-specific developmental patterns revealed with transgenic markers. Journal of Neuroscience 30, 1452-1462.

Kim, J.Y., Duan, X., Liu, C.Y., Jang, M.H., Guo, J.U., Pow-anpongkul, N., Kang, E., Song, H., and Ming, G.L. (2009). DISC1 regulates new neuron development in the adult brain via modulation of AKT-mTOR signaling through KIAA1212. Neuron 63, 761-773.

Knight, Z.A., Tan, K., Birsoy, K., Schmidt, S., Garrison, J.L., Wysocki, R.W., Emiliano, A., Ekstrand, M.I., and Friedman, J.M. (2012). Molecular profiling of activated neurons by phosphorylated ribosome capture. Cell 151, 1126-1137.

Laplante, M., and Sabatini, D.M. (2012). mTOR signaling in growth control and disease. Cell 149, 274-293.

Liu, K., Tedeschi, A., Park, K.K., and He, Z. (2011). Neuronal intrinsic mechanisms of axon regeneration. Annual review of neuroscience 34, 131-152.

Maier, I.C., and Schwab, M.E. (2006). Sprouting, regeneration and circuit formation in the injured spinal cord: factors and activity. Philosophical transactions of the Royal Society of London Series B, Biological sciences 361, 1611-1634.

Manning, B.D., and Cantley, L.C. (2007). AKT/PKB signaling: navigating downstream. Cell 129, 1261-1274.

Mansour-Robaey, S., Clarke, D.B., Wang, Y.C., Bray, G.M., and Aguayo, A.J. (1994). Effects of ocular injury and administration of brain-derived neurotrophic factor on survival and regrowth of axotomized retinal ganglion cells. Proceedings of the National Academy of Sciences USA 91, 1632-1636.

Masland, R.H. (2012). The neuronal organization of the retina. Neuron 76, 266-280.

Misawa, H., Hara, M., Tanabe, S., Niikura, M., Moriwaki, Y., and Okuda, T. (2012). Osteopontin is an alpha motor neuron marker in the mouse spinal cord. Journal of neuroscience research 90, 732-742.

Morgan-Warren, P.J., Berry, M., Ahmed, Z., Scott, R.A., and Logan, A. (2013). Exploiting mTOR signaling: a novel translatable treatment strategy for traumatic optic neuropathy? Investigative ophthalmology & visual science 54, 6903-6916.

Pang, J.J., Gao, F., and Wu, S.M. (2003). Light-evoked excitatory and inhibitory synaptic inputs to ON and OFF alpha ganglion cells in the mouse retina. Journal of Neuroscience 23, 6063-6073.

Park, K.K., Liu, K., Hu, Y., Smith, P.D., Wang, C., Cai, B., Xu, B., Connolly, L., Kramvis, I., Sahin, M., et al. (2008). Promoting axon regeneration in the adult CNS by modulation of the PTEN/mTOR pathway. Science 322, 963-966.

Peichl, L. (1991). Alpha ganglion cells in mammalian retinae: common properties, species differences, and some comments on other ganglion cells. Visual neuroscience 7, 155-169.

Perez de Sevilla Muller, L., Sargoy, A., Rodriguez, A.R., and Brecha, N.C. (2014). Melanopsin ganglion cells are the most resistant retinal ganglion cell type to axonal injury in the rat retina. PloS one 9, e93274.

Ramon y Cajal, S. (1928). Degeneration and Regeneration of the Nervous System, Reprinted 1991 (New York: Oxford Univ. Press).

Robinson, G.A., and Madison, R.D. (2004). Axotomized mouse retinal ganglion cells containing melanopsin show enhanced survival, but not enhanced axon regrowth into a peripheral nerve graft. Vision research 44, 2667-2674.

Rodriguez, C.I., Buchholz, F., Galloway, J., Sequerra, R., Kasper, J., Ayala, R., Stewart, A.F., and Dymecki, S.M. (2000). High-efficiency deleter mice show that FLPe is an alternative to Cre-loxP. Nat Genet 25, 139-140.

Sanes, J., and Masland, R. (2015). The types of retinal ganglion cells: current status and implications for neuronal classifcation. Annual Review Neuroscience (In Press).

Sawai, H., Clarke, D.B., Kittlerova, P., Bray, G.M., and Aguayo, A.J. (1996). Brain-derived neurotrophic factor and neurotrophin-4/5 stimulate growth of axonal branches from regenerating retinal ganglion cells. Journal of Neuroscience 16, 3887-3894.

Schubert, T., Degen, J., Willecke, K., Hormuzdi, S.G., Monyer, H., and Weiler, R. (2005). Connexin36 mediates gap junctional coupling of alpha-ganglion cells in mouse retina. The Journal of comparative neurology 485, 191-201.

Smith, P.D., Sun, F., Park, K.K., Cai, B., Wang, C., Kuwako, K., Martinez-Carrasco, I., Connolly, L., and He, Z. (2009). SOCS3 deletion promotes optic nerve regeneration in vivo. Neuron 64, 617-623.

Sun, F., Park, K.K., Belin, S., Wang, D., Lu, T., Chen, G., Zhang, K., Yeung, C., Feng, G., Yankner, B.A., et al. (2011). Sustained axon regeneration induced by co-deletion of PTEN and SOCS3. Nature 480, 372-375.

Tagami, Y., Kurimoto, T., Miyoshi, T., Morimoto, T., Sawai, H., and Mimura, O. (2009). Axonal regeneration induced by repetitive electrical stimulation of crushed optic nerve in adult rats. Japanese journal of ophthalmology 53, 257-266.

Thoenen, H., and Sendtner, M. (2002). Neurotrophins: from enthusiastic expectations through sobering experiences to rational therapeutic approaches. Nature neuroscience 5 Suppl, 1046-1050.

Trenholm, S., Johnson, K., Li, X., Smith, R.G., and Awatramani, G.B. (2011). Parallel mechanisms encode direction in the retina. Neuron 71, 683-694.

van Wyk, M., Wassle, H., and Taylor, W.R. (2009). Receptive field properties of ON- and OFF-ganglion cells in the mouse retina. Visual neuroscience 26, 297-308.

Volgyi, B., Abrams, J., Paul, D.L., and Bloomfield, S.A. (2005). Morphology and tracer coupling pattern of alpha ganglion cells in the mouse retina. Journal of comparative neurology 492, 66-77.

Wang, K.X., and Denhardt, D.T. (2008). Osteopontin: role in immune regulation and stress responses. Cytokine & growth factor reviews 19, 333-345.

Watanabe, M., and Fukuda, Y. (2002). Survival and axonal regeneration of retinal ganglion cells in adult cats. Progress in retinal and eye research 21, 529-553.

Watanabe, M., Sawai, H., and Fukuda, Y. (1993). Number, distribution, and morphology of retinal ganglion cells with axons regenerated into peripheral nerve graft in adult cats. Journal of Neuroscience 13, 2105-2117.

Watanabe, M., Sawai, H., and Fukuda, Y. (1995). Number and dendritic morphology of retinal ganglion cells that survived after axotomy in adult cats. Journal of neurobiology 27, 189-203.

Watkins, T.A., Wang, B., Huntwork-Rodriguez, S., Yang, J., Jiang, Z., Eastham-Anderson, J., Modrusan, Z., Kaminker, J.S., Tessier-Lavigne, M., and Lewcock, J.W. (2013). DLK initiates a transcriptional program that couples apoptotic and regenerative responses to axonal injury. Proceedings of the National Academy of Sciences USA 110, 4039-4044.

Wright, M.C., Mi, R., Connor, E., Reed, N., Vyas, A., Alspalter, M., Coppola, G., Geschwind, D.H., Brushart, T.M., and Hoke, A. (2014). Novel roles for osteopontin and clusterin in peripheral motor and sensory axon regeneration. Journal of Neuroscience 34, 1689-1700.

Yamagata, M., and Sanes, J.R. (2010). Synaptic localization and function of Sidekick recognition molecules require MAGI scaffolding proteins. Journal of Neuroscience 30, 3579-3588.

Zhang, Y., Kim, I.J., Sanes, J.R., and Meister, M. (2012). The most numerous ganglion cell type of the mouse retina is a selective feature detector. Proceedings of the National Academy of Sciences USA 109, E2391-2398.

Zukor, K., Belin, S., Wang, C., Keelan, N., Wang, X., and He, Z. (2013). Short hairpin RNA against PTEN enhances regenerative growth of corticospinal tract axons after spinal cord injury. Journal of Neuroscience 33, 15350-15361.

Chapter 4: Foxp2 defines paramorphic pairs of retinal ganglion cells that differ in size, shape, and selectivity to directional motion

Preface:

The work presented in this chapter was collaboration between David Rousso, a postdoctoral fellow in Josh Sanes lab. David Rousso identified F-RGCs that were labeled by transcriptional factor Foxp2, and described morphological properties and distribution of F-RGCs. I recorded from these cells and described their physiological properties. The work presented here resulted in a paper, and I involved in writing parts of the paper. This paper is close to being submitted.

4.1 Abstract

Visual information is conveyed to the brain by axons of retinal ganglion cells (RGCs). Each of ≥30 RGC types reports on specific visual features, such as directional motion. Identification of these types is prerequisite to understanding visual perception and development, but fewer than half of RGCs in mouse belong to known types. Here we identify a novel family of RGCs that we call F-RGCs based on their shared expression of the transcription factor Foxp2. Combinatorial expression of additional transcription factors divides F-RGCs into four types. The four types comprise two paramorphic pairs: they are closely related, differing in their depth of dendritic stratification, which correlates with their physiological responses. One pair, F-mini^{ON} and F-mini^{OFF}, shows robust direction-selectivity. They are the smallest and most abundant RGCs identified to date. The other pair, F-midi^{ON} and F-midi^{OFF}, are larger and direction non-selective. Together, F-RGCs comprise >20% of RGCs in the mouse retina, halving the number of RGCs that remain to be classified and characterized.

4.2 Introduction

The vertebrate retina contains 5 neuronal classes that transduce light into electrical signals (photoreceptors), process the information (bipolar, horizontal and amacrine cells) and pass it to retinal ganglion cells (RGCs), which send it to the rest of the brain through the optic nerve (Masland, 2012; Sanes and Zipursky, 2010) (Figure 1A). Each class is divided into multiple types, enabling the complex computations that result in different RGCs being tuned to distinct visual features such as contrast, color, or motion in a specific direction (Sanes and Masland, 2015). A full accounting of the types of RGCs and their functional properties is therefore prerequisite to understanding how the visual system works. Initial classification schemes for RGCs were based on their morphological and physiological properties (Badea and Nathans, 2004; Coombs et al., 2007; Kong et al., 2005; Sun et al., 2002; Völgyi et al., 2009), leading to identification of ~20 RGC types. Recently these methods have been supplemented by molecular and genetic approaches in mice (Badea and Nathans, 2011; Dhande and Huberman, 2014; Huberman et al., 2008; Kim et al., 2008; Tien et al., 2015), increasing the estimated number of RGC types to >30. Nonetheless, the total number is unclear and nearly half of all RGCs in mice remain unknown or unclassified (Sanes and Masland, 2015).

To identify novel RGC types we analyzed combinatorial expression of transcription factors (TFs), a strategy that has been useful for defining cell types in other parts of the CNS (Catela et al., 2015; Lodato and Arlotta, 2015). We screened retinas for expression of >40 TFs and found that the forkhead/winged-helix domain protein Foxp2 was expressed by 20-25% of RGCs, few if any of which corresponded to previously known types. Combinatorial co-expression of additional TFs (Foxp1 and the Pou4f factors, Brn3a-c) divided F-RGCs into four discrete types that differ in size, dendritic lamination, and physiological responsiveness. They comprise a pair of small, direction-selective (DS) RGCs, F-mini^{ON} and F-mini^{OFF}, and a pair of larger, direction non-selective RGCs, F-midi^{ON} and F-midi^{OFF}. Together, F-RGCs comprise >20% of RGCs in the mouse retina, halving the number of RGCs that remain to be classified and characterized.

Our molecular, morphological and physiological analyses revealed several noteworthy features of

F-RGCs. First, F-mini and F-midi RGCs each comprise a paramorphic pair, defined as "neuronal cell types differing from one another mainly at the level of dendritic stratification but otherwise more similar to one another than to other types" (Berson, 2008). Paramorphism is a common feature of RGCs in many species, but has been little studied in mice; the F-RGCs provide new insights into its basis. Second, the F-mini RGCs are direction-selective. The computation of directional motion by retinal neurons is a topic of intense current interest, with most studies focusing on just one population: ON-OFF direction selective RGCs (ooDSGCs), which "inherit" direction selectivity from starburst amacrine cells (Borst and Helmstaedter, 2015; Vaney et al., 2012). The F-mini RGCs do not co-stratify with starburst amacrine processes; they are therefore unlikely to receive substantial input from them, and must compute direction by another mechanism. Finally, F-mini RGCs are the smallest and most numerous RGC types yet identified in mouse. In these and many other (but not all) respects, they resemble midget RGCs, a paramorphic pair comprising the smallest and most abundant RGCs in primates (Dacey and Packer, 2003; Szmajda et al., 2005). To date, no midget equivalent has been identified in rodent retina. Motivated by this parallel, we analyzed macaque retina, and identified RGC subsets that express combinations of Foxp and Brn3 transcription factors. One population shares the unusual distribution reported for midget RGCs (Watanabe and Rodieck, 1989).

Figure 4.1 Foxp2 expression distinguishes F-RGCs from currently known types

(A) Model showing the major neuronal classes in the retina.

(B, C) Antibody costaining analysis for Foxp2 combined with molecular markers for RGCs, Brn3a and RBPMS (B), and amacrine cells, Pax6 and Ap2 (C), in the adult mouse retina. Arrows point to the same cells in each panel.

(D) Immunostaining for Foxp2 combined with a cocktail of 3 antibodies specific to individual Brn3-transcription factors (a, b, c; "pan-Brn3") shows the total RGC population and the proportion expressing Foxp2.

(E) Contribution of Foxp2 RGCs and other molecularly defined RGC types to the total RGC population. Estimates for other RGC types based on Sanes and Masland (2015).

(F) Analysis of Foxp2 RGCs combined with markers for the following RGC types: Osteopontin, alpha-RGCs (left); Melanopsin, ip-RGCs (middle); and Cart, ooDSGC (right).

(G) Foxp2 and Brn3a coexpression at different stages of retinal neurogenesis. All images are taken from the central/ventral region of the retina. Scale bar = 100 um.

Figure 4.1 Foxp2 expression distinguishes F-RGCs from currently known types (continued)

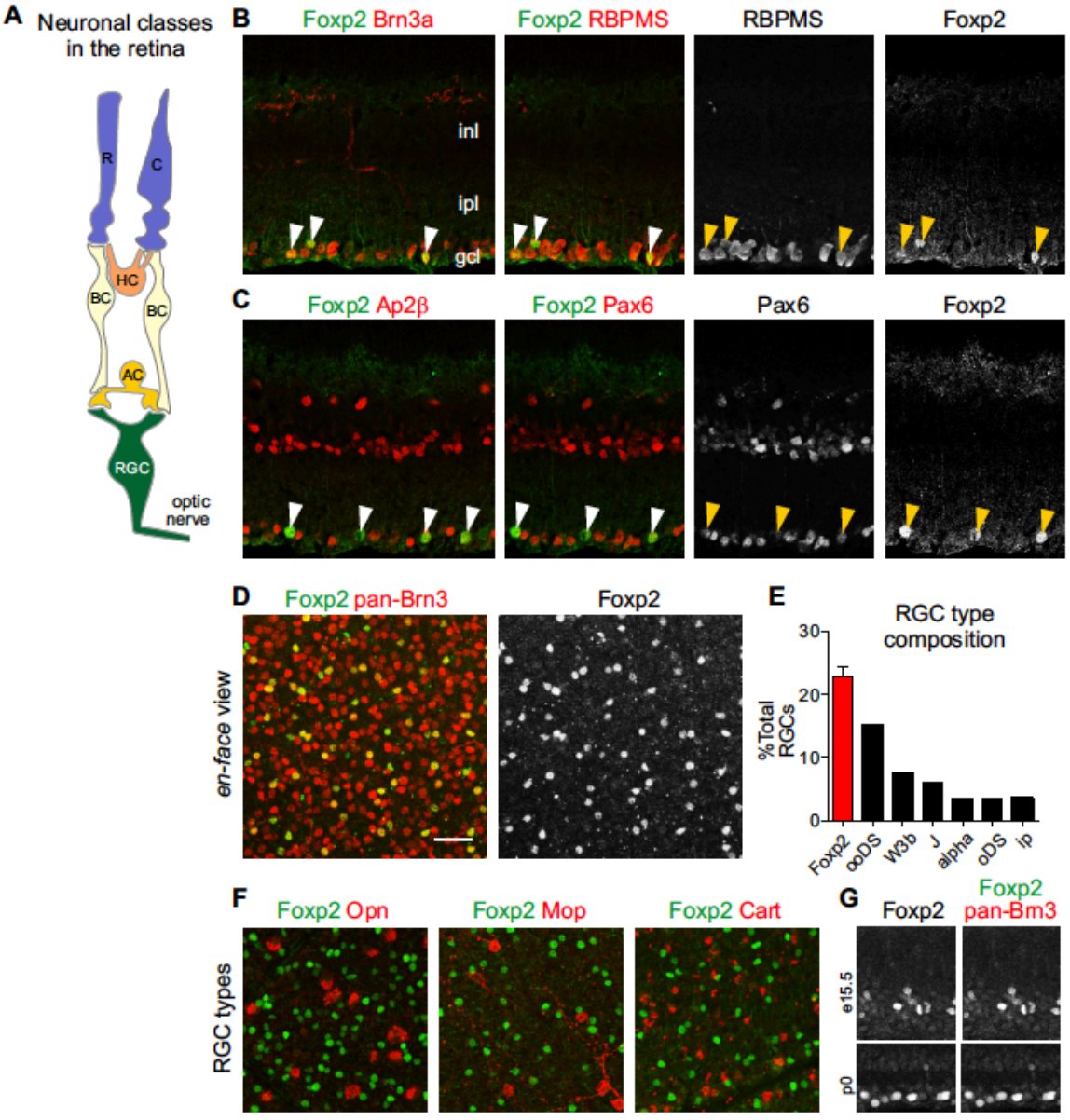

4.3 Results

4.3.1 Foxp2 is expressed by a group of RGCs distinct from currently known types

To identify RGC types we assembled a panel of antibodies to ~40 TFs that have been used to classify neurons throughout the CNS (**Table 4.1**) and analyzed their expression in adult mouse retina. Antibodies that showed significant and selective labeling (between ~10 and ~40%) of RGCs were studied further. Here, we focus first on Foxp2, which, as documented below, labels ~20% of RGCs. Foxp proteins have been shown to define different classes of neurons in the spinal cord (Dasen et al., 2008; Rousso et al., 2008, 2012) but their expression in retina has not been examined.

Over 90% of Foxp2$^+$ cells were localized to the ganglion cell layer (GCL). This layer contains both RGCs and amacrine cells. Foxp2$^+$ cells expressed RBPMS, which marks most if not all RGCs, but expressed little if any Pax6 or Ap2, which mark most amacrine cells (**Figure 4.1 B, C**; Bisgrove and Godbout, 1999; de Melo et al., 2003; Rodriguez et al., 2014). Thus >90% of Foxp2$^+$ retinal cells are RGCs; hereafter, we refer to them as F-RGCs.

We estimated the fraction of RGCs that are F-RGCs by double-labeling with pan-RGC markers. The distribution of F-RGCs varied across the retina (see below), with a peak density of 840 ± 50 cells/mm^2 in the central/ventral region, accounting for 23 ± 2% of all RGCs in this region, or 26 ± 2% based on previous estimates of RGC density (mean ± SE) (**Figure 4.1 D, E**; Jeon et al., 1998).

We used double-staining with markers for known RGC types to characterize F-RGCs. Remarkably, despite their abundance, F-RGCs were distinct from previously characterized types for which we had markers, including alpha-RGCs, ip-RGCs, ooDSGCs, J-RGCs, and W3B-RGCs (Figure 1F and data not shown; (Duan et al., 2015; Hattar et al., 2002; Kay et al., 2011; Kim et al., 2008, 2010; Sanes and Masland, 2015). These results raised the possibility that Foxp2 is expressed by previously undescribed RGC types.

Our initial screen was performed on adult retinas. We surveyed the expression of Foxp2 at different stages of retinal neurogenesis and observed its expression selectively within a subset of RGCs

by embryonic [e] day 15.5, the earliest time examined (**Figure 4.1 G**). Thus FoxP2 may be useful for analyzing the development of F-RGCs.

TF	Host	Source	RGCs	Others
bHLHb5	Guinea pig	Ben Novitch		X
Brn3a	Mouse	Millipore	X	
Brn3b	Goat	Santa Cruz	X	
Brn3c	Mouse	Santa Cruz	X	
Ctip2	Rat	Abcam	X	X
Ebf3	Rabbit	Millipore	X	X
Er81	Rabbit	Covance	X	
Evx1	Guinea pig	Tom Jessell		
Foxp1	Guinea pig	Ben Novitch	X	X
Foxp2	Goat	Abcam	X	
Foxp4	Rat	Ben Novitch		
Fog2	Rabbit	Paola Arlotta		X
Gata3	Goat	Santa Cruz		
Hb9	Guinea pig	Sam Pfaff		
Islet1	Goat	R&D systems	X	X
Islet2	Guinea pig	Abcam	X	
Lbx1	Guinea pig	Tom Jessell		
Lhx3	Guinea pig	Sam Pfaff		X
Lhx4	Rabbit	Sam Pfaff		X
NeuN	Mouse	Millipore	X	X
NF1A	Rabbit	Active Motif	X	X
Nkx2.2	Rabbit	Tom Jessell		
Nkx6.1	Rabbit	Tom Jessell		
Onecut1	Rabbit	Frederic Clotman		X
Onecut2	Guinea pig	Frederic Clotman		X
Onecut3	Rat	Frederic Clotman		X
Olig2	Guinea pig	Ben Novitch		
Pax2	Rabbit	Tom Jessell		X
Pax6	Mouse	DSHB		X
Pitx3	Rabbit	Life Technologies		
PLZF	Rabbit		X	X
Pou3f1	Rabbit	Ilia et al, 2002		X
Runx1	Rabbit	Aviva	X	X
Sall1	Mouse	R&D Sys.		
Satb1	Rabbit	Epitomics (Abcam)	X	X
Satb2	Mouse	Abcam	X	X
Sox2	Goat	Santa Cruz		X
Sox9	Rabbit	Chemicon		X
Tbr2	Rabbit	Abcam	X	X

Table 4.1 Transcriptional factors screened for retinal labeling

4.3.2 Combinatorial expression of transcription factors defines four F-RGC types

We next asked whether F-RGCs include one, a few, or a multitude of RGC types. To this end, we exploited the "mosaic" arrangement that is a characteristic of most retinal neuron types analyzed to date: neurons of a single type are less likely to be near neighbors than would be expected by chance alone whereas neurons of any individual type are randomly distributed with respect to neurons of other types (**Figure 4.2 A, B**; Kay et al., 2012; Reese, 2012; Rockhill et al., 2000). Thus, analysis of spatial distribution using the density recovery profile (DRP) provides a means of assessing whether a set of labeled neurons comprises a natural cell type (Rodieck, 1991). Moreover, the distribution of a mixture of types is distinguishable from that of a single type, allowing for the estimation of the fraction (f) of an array that constitutes a seemingly homogeneous population ($f < 1$, partial array; $f > 1$, mixed arrays) (Figure 2B; Zhang et al., 2012). Non-integral numbers may indicate the existence of multiple types that differ in abundance. Following this logic, we analyzed the spatial distribution of F-RGCs and found that they deviated significantly from that of a random distribution, with $f = 2.2$ (**Figure 4.2 C, D**), suggesting they comprise at least 2 regularly arranged types.

We reexamined TFs from the initial screen to seek combinatorial expression patterns that would subdivide F-RGC into discrete types. A related protein, Foxp1, divided F-RGCs into 2 groups whose spatial distributions more closely resembled single arrays, yet appeared to contain more than one type each ($f > 1$) (**Figure 4.2 E, F**). Pou4f/Brn3 proteins further subdivided each of these 2 groups into one abundant and one sparse type (abundant, Foxp1$^+$Foxp2$^+$Brn3b$^-$; sparse, Foxp1$^+$Foxp2$^+$Brn3b$^+$; abundant, Foxp1$^-$ Foxp2$^+$Brn3c$^-$; and sparse, Foxp1$^-$ Foxp2$^+$Brn3c$^+$) (**Figure 4.2 G-J**). The density relationship between the abundant and sparse types for each group was ~1/4. DRP and nearest-neighbor spatial analysis confirmed that each type exhibited a region of exclusion surrounding cell bodies of the same type (A → A), but not to members of another type (A → B) (**Figure 4.2 H, J**, **Figure 4.3**). Moreover, the exclusion distance of each group was matched by predicted hexagonal arrays of similar side length ($f \approx 1$, each). Thus, Foxp1 and Brn3 proteins divide F-RGCs into 4 molecularly distinct RGC types.

We simultaneously labeled the 4 types and tabulated their contribution to the total Foxp2 population (**Figure 4.2 K, L**). Cumulatively they accounted for >90% of all Foxp2$^+$ cells. Most of the remaining Foxp2$^+$ cells had smaller somata, did not label with Brn3 proteins, and expressed lower levels of Foxp2; we presume they are amacrine cells. Thus, F-RGCs are likely to comprise 4 and only 4 types (**Figure 4.2 M, N**).

Figure 4.2 Combinatorial expression of transcription factors divide F-RGCs into 4 types

(A) Retinal mosaics can be modeled as close-packed hexagonal arrays with positional jitter. Asterisks represent single arrays (red or green) of the same side-length, as defined by (Zhang et al., 2012; A).

(B) DRP on a single array (A→A) produces a characteristic slope that scales with side-length (black dotted line). DRP on a mixture of 2 arrays (A+B→A+B) produces a slope mid-way between a random distribution and a single array (grey dotted line), allowing for the estimation of the fraction f of an array labeled (f<1, partial array; f>1, mixture of arrays). A random distribution is represented by the gray dashed line.

(C, D) Immunolabeling of Foxp2 in adult mouse retina (C). DRP of total Foxp2 RGCs is reminiscent to that of a mixed array comprising at least 2 types (f=2.2; D).

(E, F) Foxp1 divides Foxp2 RGCs into 2 groups, OFF and ON (E). DRP on the following RGC populations: Foxp1+ (OFF) F-RGCs (orange line); Foxp1+ (ON) F-RGCs (red line); mixture of 2 arrays (gray dashed line); and a single array of similar side length (dashed black line).

(G, H) Brn3b divides OFF-F-RGCs into 2 types, one abundant (Mini, asterisks) and one sparse (Midi, circles). The two OFF-F-RGC types are identified by the following TF combinations: $Foxp1^{+}/Foxp2^{+}/Brn3b^{-}$, $F\text{-}mini^{OFF}$; $Foxp1^{+}/Foxp2^{+}/Brn3b^{+}$, $F\text{-}midi^{OFF}$. DRP of $F\text{-}mini^{OFF}$ (orange line) and $F\text{-}midi^{OFF}$ (peach line) RGCs resemble matched single arrays of similar side-lengths (dashed lines), indicating they each form a single array (f≈1 each; H).

(I, J) Brn3c divides ON-F-RGCs into two types, one abundant (Mini, asterisks) and one sparse (Midi, circles). The 2 ON-F-RGC types are identified by the following TF combinations: $Foxp1^{-}/Foxp2^{+}/Brn3c^{-}$, $F\text{-}mini^{ON}$; $Foxp1^{-}/Foxp2^{+}/Brn3c^{+}$, $F\text{-}midi^{OFF}$. DRP of $F\text{-}mini^{ON}$ (red line) and $F\text{-}midi^{ON}$ (pink line) F-RGCs resemble matched single arrays of similar side-lengths (dashed lines), indicating they each form a single array (f≈1 each; J).

Figure 4.2 Combinatorial expression of transcription factors divide F-RGCs into 4 types (continued)

(K, L) Quadruple immunolabeling with Foxp1, Foxp2, Brn3b, and Brn3c marks the 4 F-RGC types simultaneously. Asterisks represent the relative position and identity of molecularly defined F-RGC types (L).

(M) Contribution of each F-RGC type to the total Foxp2 population.

(N) Dendogram showing the 4 molecularly defined F-RGC types and their combinatorial TFs.

n = 3 retinas from 3 animals per type. Scale bar = 50 um.

Figure 4.2 Combinatorial expression of transcription factors divide F-RGCs into 4 types (continued)

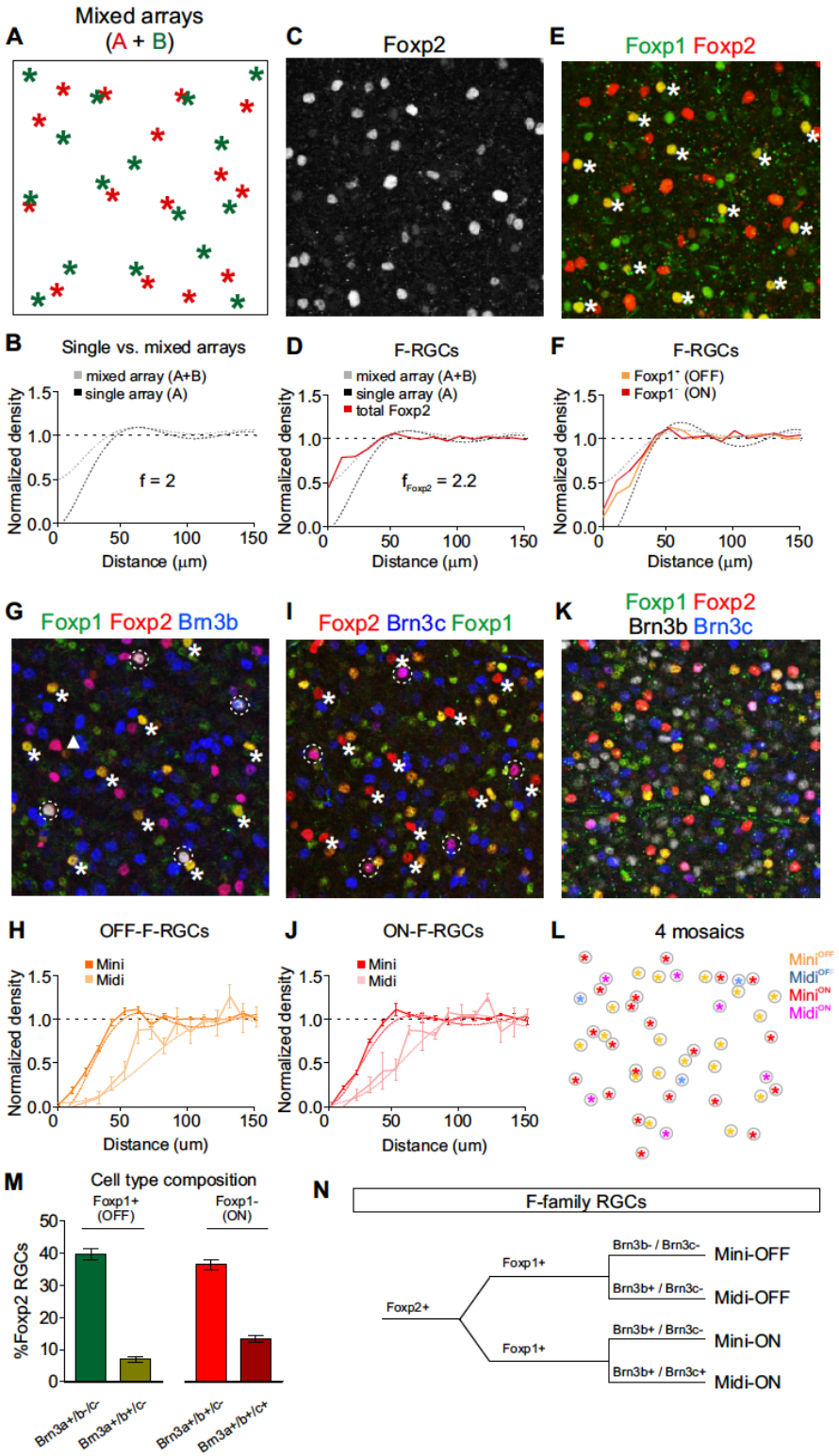

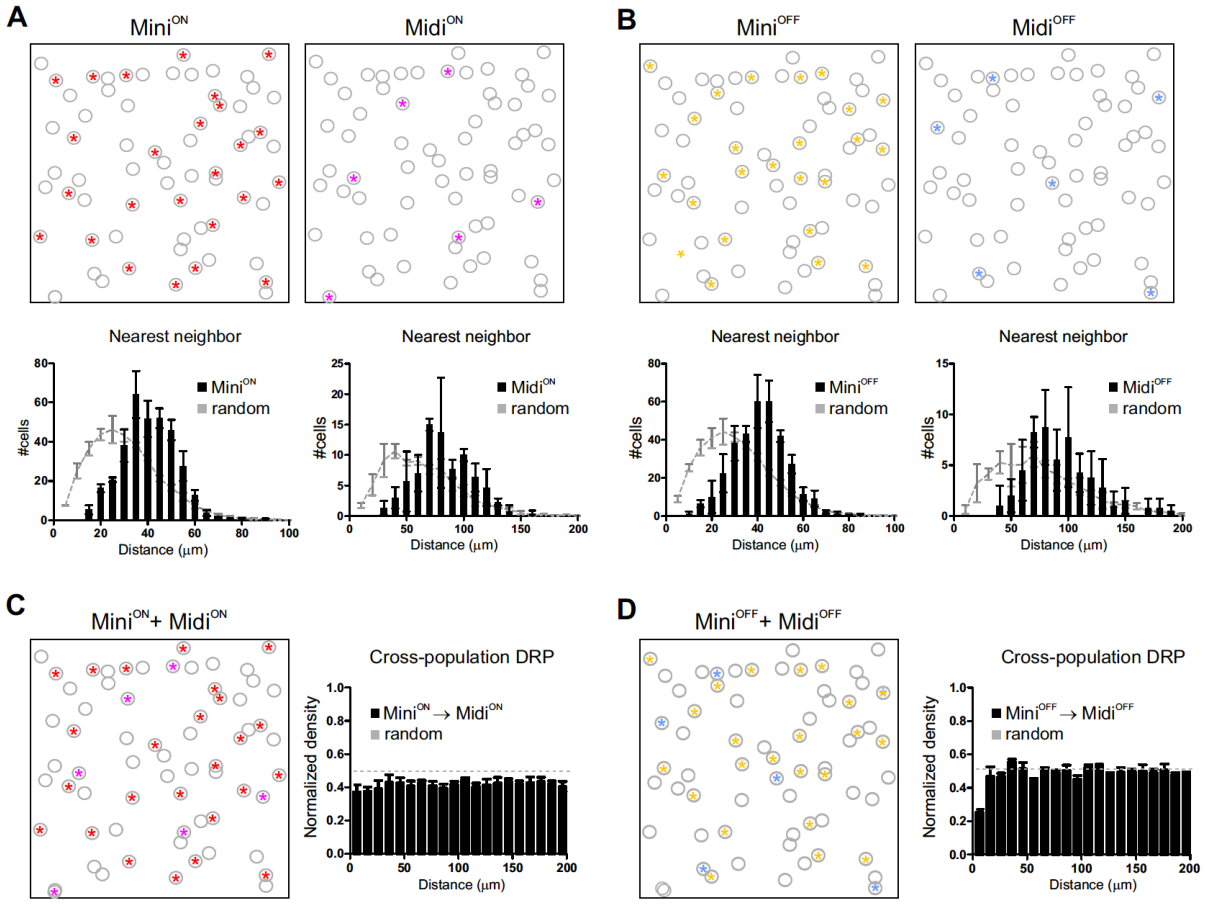

Figure 4.3 Analysis of spatial organization within and between F-RGC types.

(A, B) Color-coded asterisks indicate the relative position and identity of F-RGC types as defined by the following combinatorial markers: Foxp2^{+}/Foxp1^{-}/Brn3b^{+}/Brn3c^{-}, F-mini^{ON} (red); and Foxp2^{+}/Foxp1^{-}/Brn3b^{+}/Brn3c^{+}, F-midi^{ON} (magenta) (A); Foxp2+/Foxp1+/Brn3b^{-} /Brn3c^{-} , F- mini^{OFF} (yellow) and Foxp2^{+}/Foxp1^{+}/Brn3b^{+}/Brn3c^{-}, F-midi^{OFF}(cyan) (B). Nearest neighbor analysis shows that cells within each type are spaced at regular intervals from one another, forming mosaics.

(C, D) Analysis of spatial relationship between F-RGC types using cross-population DRP. Cells of one type are spaced randomly with respect to cells of another type, indicating that each type forms an independent mosaic.

4.3.3 Correspondence of morphological and molecular distinctions among F-RGCs

To gain genetic access to F-RGCs, we generated animals in which Cre recombinase was inserted at the Foxp2 locus (*Foxp2-Cre*; **Figure 4.4 A**). When these mice were crossed to reporter lines in which strong expression of a fluorescent protein was Cre-dependent, labeling was widespread, perhaps reflecting broad expression of *Foxp2* at low levels during early development. In contrast, when we used an adeno-associated virus (AAV) to deliver a Cre-dependent GFP cassette (*AAV2/9$^{flex\text{-}GFP}$*) to mature retina, Foxp2 cells were selectively labeled, as judged by co-expression of GFP and Foxp2 (**Figure 4.4 B**). We used AAV marking to characterize F-RGCs morphologically.

Each of the 4 molecularly identified F-RGC types exhibited a stereotyped morphology (**Figure 4.4 C-F**). Dendrites of two types stratified in the outer portion of the IPL (S1 of 5 strata) indicating they were likely to be OFF cells, a presumption confirmed below. Dendrites of the other two types stratified in the middle portion of the IPL (S3), suggesting that they were ON or ON-OFF cells. In each pair, dendritic arbors of one were considerably larger than the other. These characteristics led us to name the cell types F-mini^{OFF} (FoxP1^{+}/Brn3b^{-}), F-midi^{OFF} (FoxP1^{+}/Brn3b^{+}), F-mini^{ON} (FoxP1^{-}/Brn3c^{-}) and F-midi^{ON} (FoxP1^{-}/Brn3c^{+}). As predicted from their molecular profile, the F-mini types were ~4-fold more abundant than the F-midi types. The F-midi RGCs stratified slightly below or above their F-mini counterparts, respectively (**Figure 4.4 G**).

The F-mini RGCs were exceptionally small, having dendritic radii of ~40-60 μm and field areas of ~5-8,000 um^2, making them nearly half the size of W3B-RGCs, the smallest RGCs previously described (Figure 3H) (Kim et al., 2010; Krishnaswamy et al., 2015; Zhang et al., 2012). F-midi RGCs covered larger dendritic territories than F-mini cells, but are smaller than several other RGC types, including ooDSGCs, J-RGCs and alpha-RGCs (**Figure 4.4 H**).

Remarkably, all 4 F-RGC types exhibited dendritic asymmetry oriented on the vertical axis (**Figure 4.4 I**).This asymmetry resembled that of previously described J-RGCs and HB9-RGCs (Kim et al., 2008; Trenholm et al., 2011). Indeed, the OFF-F-RGCs share dendritic asymmetry and lamination patterns nearly identical with J-RGCs, differing mainly in their relative sizes (**Figure 4.5**).

A hallmark of most RGC types characterized to date is that their dendrites cover the retinal surface at least once, allowing them to report on a visual feature over the entire visual field. Thus, the coverage factor for RGC types, defined as the product of dendritic field area and 1/density (spatial frequency) is ≥ 1. For F-mini RGCs, the coverage factor is ~1X. F-midi RGCs have a four-fold lower density but also a four-fold larger dendritic area, so their coverage factor is also ~1X (**Figure 4.4 K**). These results support the idea that all four F-RGC groups comprise authentic RGC types.

Figure 4.4 Morphological characterization of Foxp2 RGCs

(A) Schematic of the *Foxp2-ires-Cre:GFP (Foxp2^{Cre})* allele.

(B) Immunostaining for Foxp2, Foxp1 and GFP in adult *Foxp2^{Cre}* retinas following intravitreal injection of high-titer *AAV2/9^{flexGFP}*. F-RGCs from both groups (OFF and ON) are labeled with similar frequency.

(C-F) Injection of low-titer *AAV2/9^{flexGFP}* into *Foxp2-Cre* mice reveals 4 morphologically distinct types that correspond with their molecular identities: Mini^{OFF}-F (C); Midi^{OFF}-F (D); Mini^{ON}-F (E); Midi^{ON}-F (F). Scale bar = 50 um.

(G) Dendritic stratification depth of individually segmented OFF (G) and ON (H) F-RGC types (n = 5 cells per type).

(H) Box plot of dendritic field areas for indicated RGC types (n=7-10 cells per type).

(I) Analysis of AI calculated for indicated RGC types (0 = perfect symmetry; 1 = perfect asymmetry; n=7-10 cells per type).

(J) Quantification of dendritic coverage factor. Comparison to other RGC types were derived from Kim et al., 2008, 2010.

Figure 4.4 Morphological characterization of Foxp2 RGCs (continued)

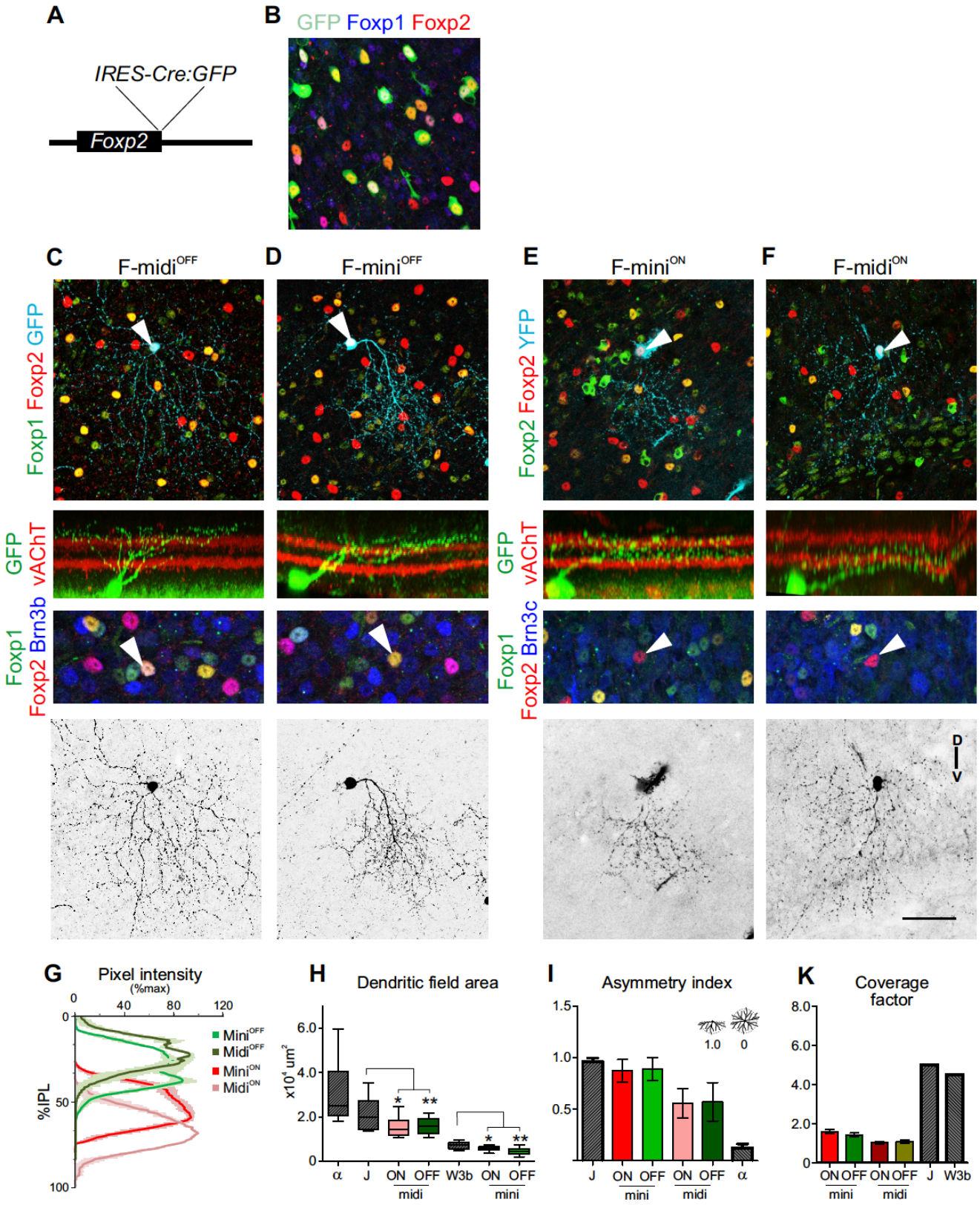

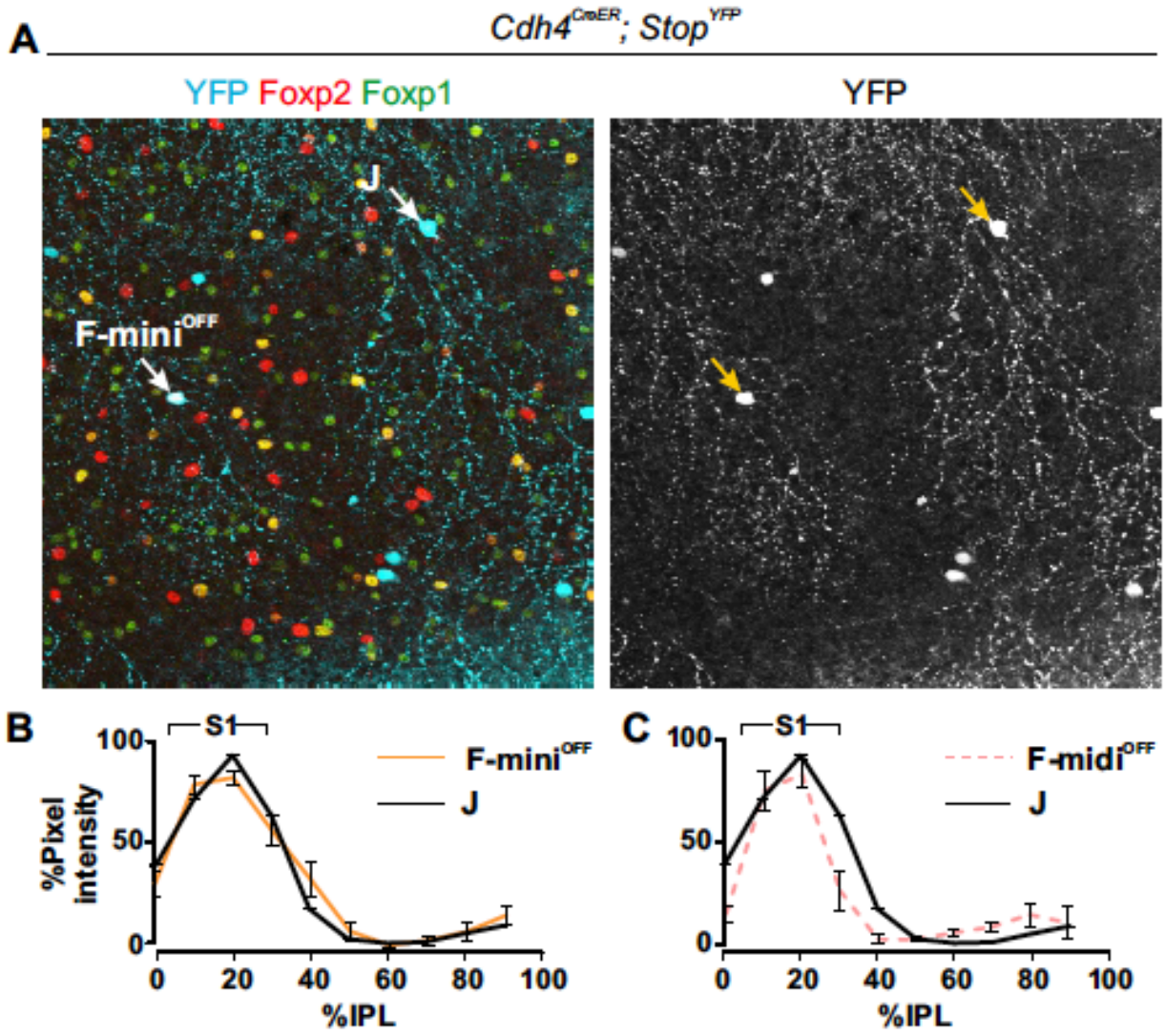

Figure 4.5 Morphological comparison of F-RGCs and J-RGCs labeled in *Cdh4*^{CreER} mice.

(A) J- and F-RGCs are labeled in *Cdh4*^{CreER} mice, allowing for their direct morphological comparison. J- and OFF-F-RGCs exhibit asymmetric dendrites oriented toward the ventral pole, differing mainly in their dendritic field sizes.

(B, C) Quantification of dendritic lamination patterns of J- and OFF-F-RGCs. Each type stratifies at roughly the same depth within the inner plexiform layer, ~S1.

4.3.4 Molecular profiling of F-RGCs

To further characterize F-RGCs molecularly, we performed triple-immunostaining on retinal whole mounts and sections. Molecules identified included ion channels and channel-associated proteins (Kv4.2 and calsenilin), calcium binding proteins (calbindin, calretinin, parvalbumin [PV]), G protein phosphatase Ppp1r17, and additional TFs from our initial screen (**Table 4.2** and **Figure 4.6 A-D**). All F-RGCs express NeuN and Isl2. Within F-RGCs, Isl1 and PV were selectively expressed only by the OFF types. Ppp1r17 was expressed only by the F-mini^{ON} type, and Satb1/2, Ctip2, and Ebf3 were expressed only by the F-midi^{ON} type. These results extend the distinctions among F-RGCs.

In parallel we stained several previously characterized transgenic lines with markers for F-RGCs. For Cre-expressing lines, we used a Cre-dependent reporter, *Thy1-stop-YFP* (Buffelli et al., 2003). Few if any F-RGCs were labeled in lines *Cdh3^{GFP}* (marks a set of ip-RGCs; Osterhout et al., 2011); *Hb9^{GFP}* or *Cdh6^{CreER}* (mark sets of ooDSGCs; Kay et al., 2011; Trenholm et al., 2011), *JamB^{CreER}* (marks J-RGCs; Kim et al., 2008), or *Thywy7* (marks a set of alpha-RGCs; Kim et al., 2010), consistent with the finding that F-RGCs do not correspond to previously characterized types. OFF-F RGCs were labeled in the *PV^{Cre}* line, consistent with results from immunostaining. Interestingly, all F-RGCs were labeled in a *Cdh4^{CreER}* line and the F-mini types were labeled in a *Cdh13^{CreER}* line (**Figure 4.6 E-G**) providing insight into recognition molecules that might influence synaptic choices of these cells.

		Mini-ON	Midi-ON	Mini-OFF	Midi-OFF	Others
Transcription	Brn3a	+	+	+	+	+
factors	Brn3b				+	+
	Brn3c		+			+
	Ctip2		+d			+
	Ebf3		+			+
	Foxp1			+	+	
	Foxp2	+	+	+	+	
	Isl1			+d	+d	+
	Isl2	+	+	+	+	+
	NeuN	+	+	+	+	+
	Satb1		+d			+
	Satb2		+d			+
	Tbr2					+
Cytosolic /	Calbindin					+
membrane proteins	Calretinin	+	+	+	+	+
	Parvalbumin			+d	+d	+
	Calsenilin	+		+		+
	Cart					+
	Kv4.2	+		+		+
	Melanopsin					+
	Ppp1r17	+d				+
	Osteopontin					+
Genetic lines	Cdh3-GFP					+
	Cdh4-CreER	+	+	+	+	+
	Cdh6-CreER					+
	Cdh13-CreER	+		+		+
	Hb9GFP					+
	JamB-CreER					+
	PV-Cre			+	+	+
	Thwga3	+d				+
	Thwga7					+

+d, indicates dim but detectable protein levels

Table 4.2 Molecular characterization of F-RGCs

Figure 4.6 Molecular profile of F-RGCs.

(A-D) Immunostaining for Foxp1, Foxp2, and different markers in adult mouse retina. Among candidates screened, four proteins were found to be differentially expressed within the four F-RGC types: Kv4.2 is expressed by F-mini^{ON} and F-mini^{OFF} RGCs (A), parvalbumin is expressed by F-mini^{OFF} and F-midi^{OFF} RGCs (B), Ppp1r17 is uniquely expressed by F-mini^{ON} RGCs (C) and Ebf3 uniquely marks F-midi^{ON} RGCs (D).

Figure 4.6 Molecular profile of F-RGCs. (continued)

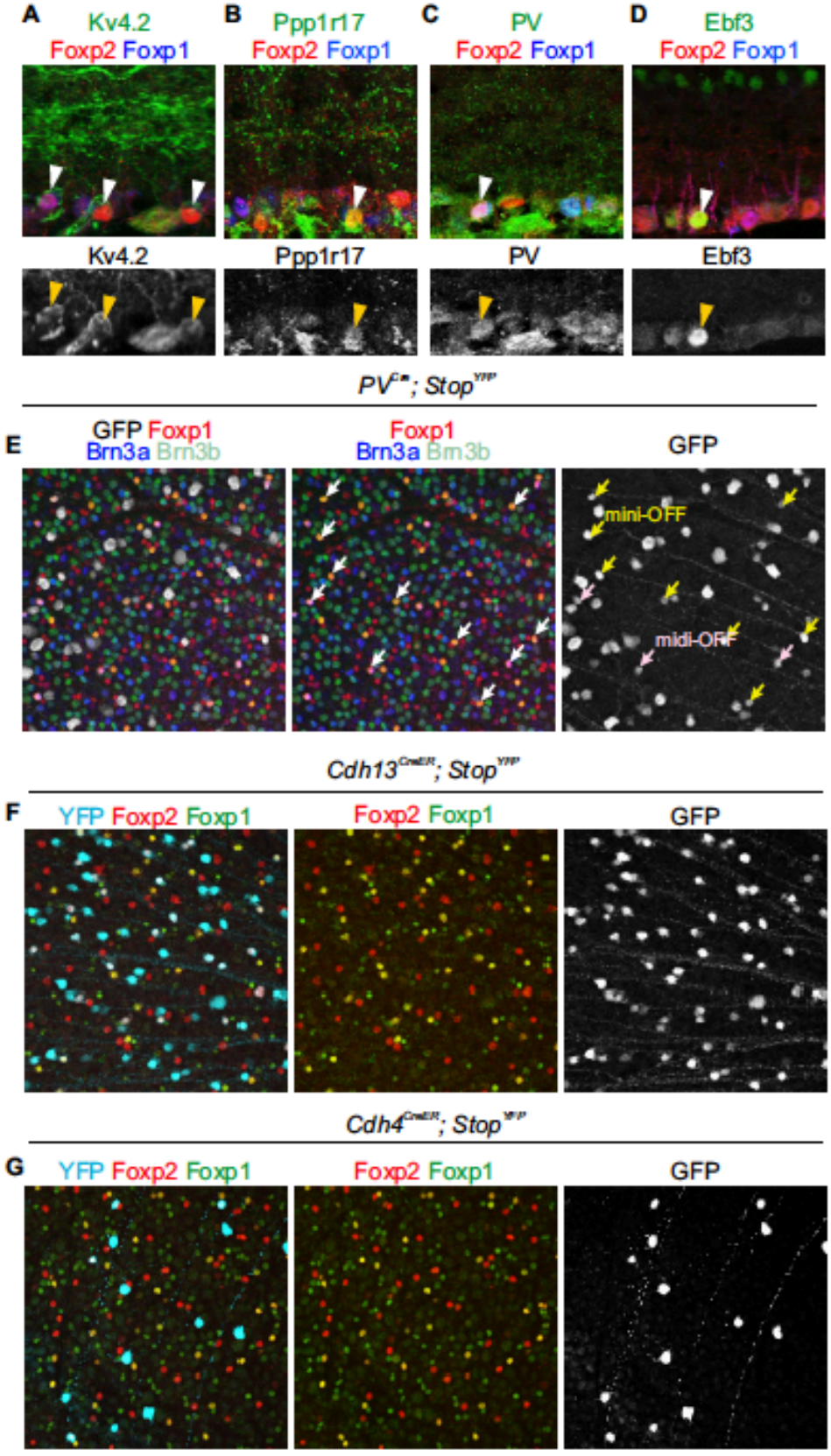

4.3.5 F-RGCs vary in density, size, and orientation along the dorsal-ventral axis

Until recently, the topographic distribution and size of RGC types in mouse was thought to be fairly uniform across the retina. However, recent studies have revealed anisotropies in some types (Bleckert et al., 2014; Zhang et al., 2012). The density of F-RGCs is graded along the vertical axis: highest in the central/ventral (C/V) region and lowest in the dorsal (D) region (**Figure 4.7 A**). We asked whether this feature is shared by all F-RGC types. Both of the F-mini RGCs were distributed in a ventral-high / dorsal-low gradient, resembling that of F-RGCs in total (**Figure 4.7 B, C**). F-midi^{OFF} RGCs were distributed in a steeper gradient; very few cells of this type are found in the dorsal third of the retina (**Figure 4.7 D**). In contrast, F-midi^{ON} RGCs were >2-fold more numerous in dorsal retina than in ventral retina (**Figure 4.7 E**).

We asked whether non-uniformity in distribution influenced dendritic field coverage and mosaic organization of F-RGCs. F-mini^{OFF}, F-mini^{ON} and F-midi^{OFF} RGCs, which are denser in ventral than dorsal retina were also smaller in ventral than dorsal retina. Conversely, F-midi^{ON} RGCs, which are denser in dorsal than ventral retina were smaller in dorsal than ventral (**Figure 4.7 F-I**). Thus, dendritic field areas are scaled with local density, resulting in uniform coverage. Moreover, while fluctuations in density along the DV-axis altered the spacing between cells, it did not disrupt their overall mosaic architecture (**Figure 4.7 F-I**; Mean regularity index = 3.44 ± 1.08; Regularity/random ratio = 1.78 ± 0.18). Thus, F-RGC size, density, and soma distance co-vary proportionately along the DV-axis, maintaining in ~1X coverage globally across the retina despite large local variances.

Finally, we assessed the asymmetry of F-RGC dendrites as a function of retinal position. Dendrites of F-mini^{OFF}, F-midi^{ON} , and F-midi^{ON} RGCs pointed ventrally at all positions in the retina. In striking contrast, the orientation of F-mini^{ON} RGC dendrites was position-dependent, pointing ventrally in dorsal retina and dorsally in ventral retina (**Figure 4.7 J,K**, and **Figure 4.8**). Further analysis revealed that the dendritic orientation of F-mini^{ON} RGCs switched sharply along a horizontal swath ~ 1 mm above the optic disc, around the same location that the density of total F-RGCs markedly drops (**Figure 4.8**).

This landmark corresponds to a region called the opsin transition zone, in which expression of opsins in cones switch from predominantly short (S) wavelength to middle (M) wavelength opsin. This correspondence may provide clues to the spatial patterning of F-RGCs (see Discussion).

Figure 4.7 Foxp2 RGCs are organized anisotropically along the DV-axis of the retina.

(A) Foxp2 immunostaining of whole retina viewed en-face. Heat map (inset) highlights the sharp decline of total Foxp2 RGCs in the dorsal [D] compared to the central/ventral [C/V] regions of the retina.

(B-E) Contoured density heat maps for each F-RGC type.

(F-I) Analysis of morphological and spatial patterning. Scatter plots of dendritic field area versus local density, and or area versus CF. Density and area co-vary while CF stays relatively constant. DRP at different axial positions shows that mosaic spacing is globally maintained for each F-RGC type despite local changes in density.

(J) GFP-labeled mini^{ON}-F RGCs located at different axial positions. Cells exhibit bimodal morphologies depending on their position.

(G) Retinal map showing position and dendritic orientation of mini^{ON} (red) and mini^{OFF} (purple) F-RGCs. The dendritic orientation of mini^{ON} RGCs located in the ventral retina are inverted with respect to mini^{ON} RGCs located in the dorsal retina. In contrast, Mini^{OFF} RGCs maintain ventral orientation independent of retinal position.

Figure 4.7 Foxp2 RGCs are organized anisotropically along the DV-axis of the retina. (continued)

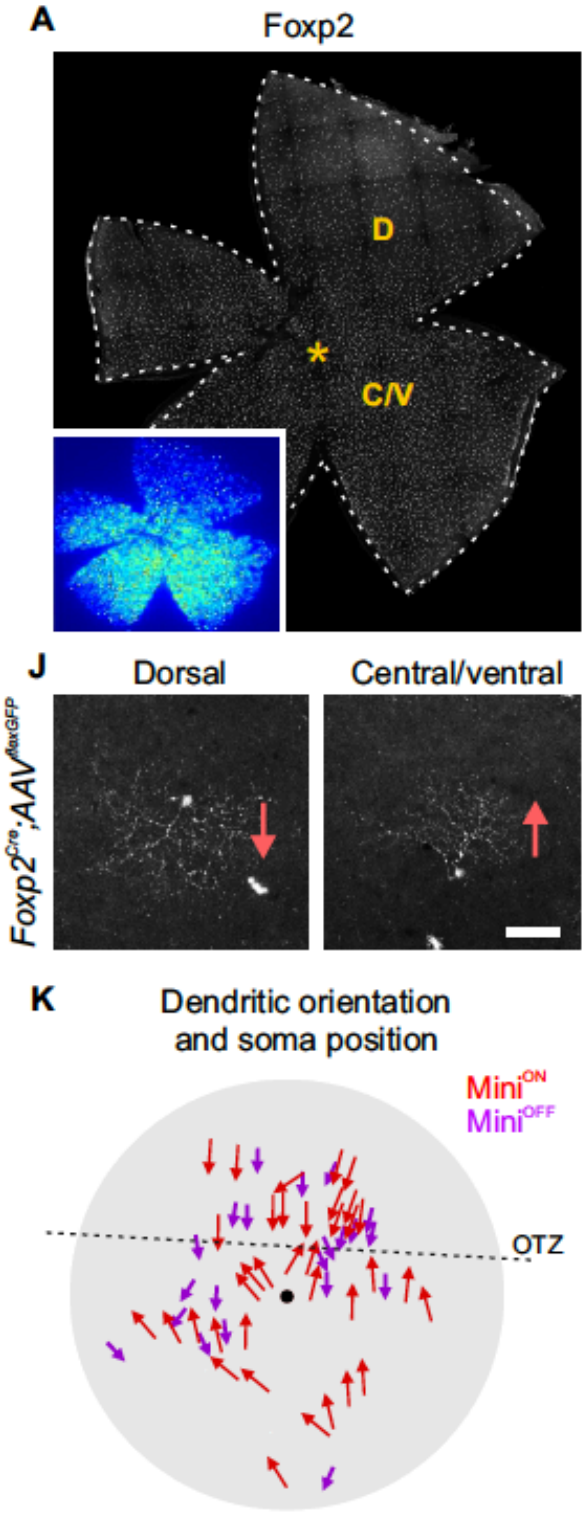

Figure 4.7 Foxp2 RGCs are organized anisotropically along the DV-axis of the retina. (continued)

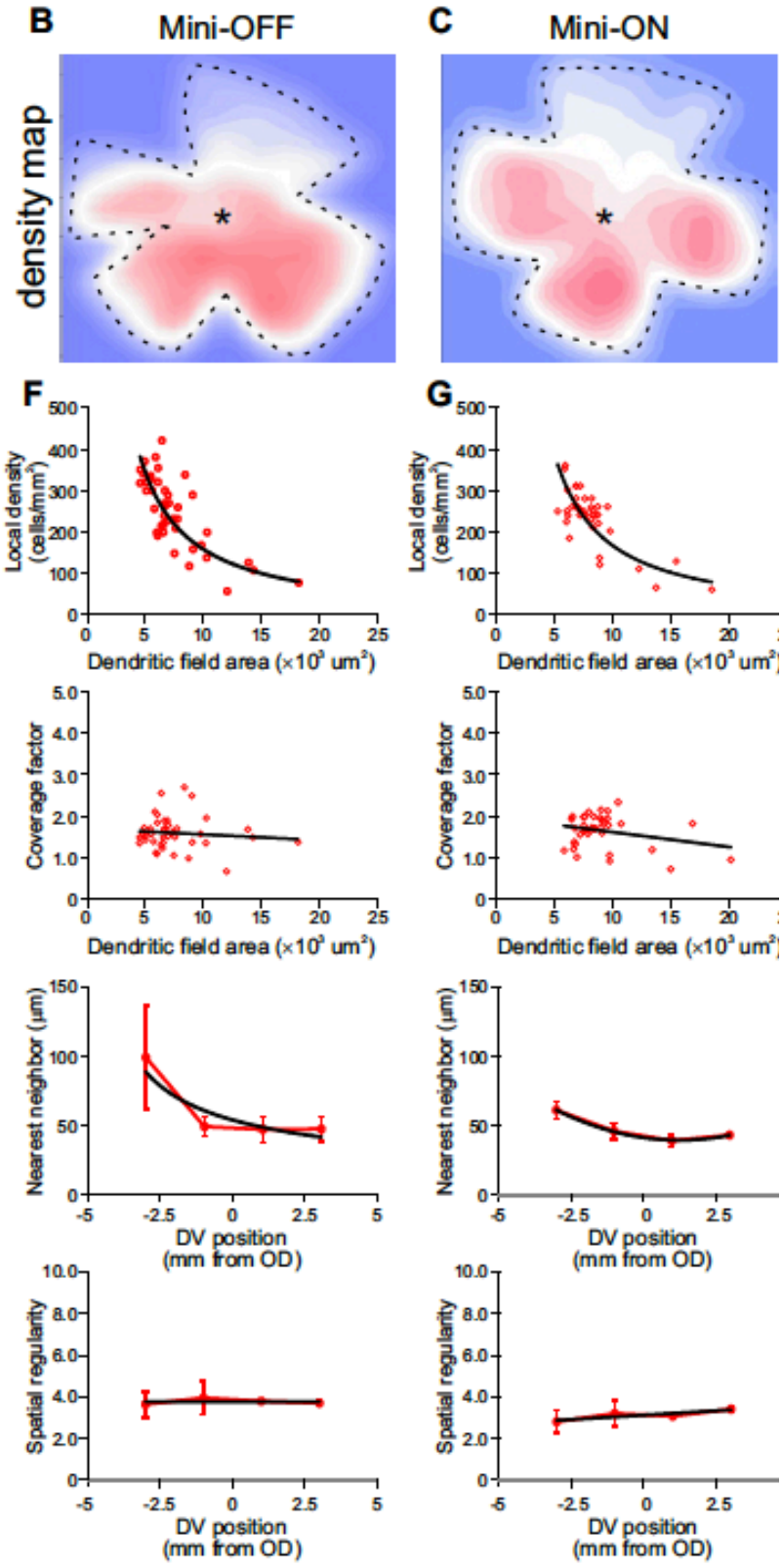

Figure 4.7 Foxp2 RGCs are organized anisotropically along the DV-axis of the retina. (continued)

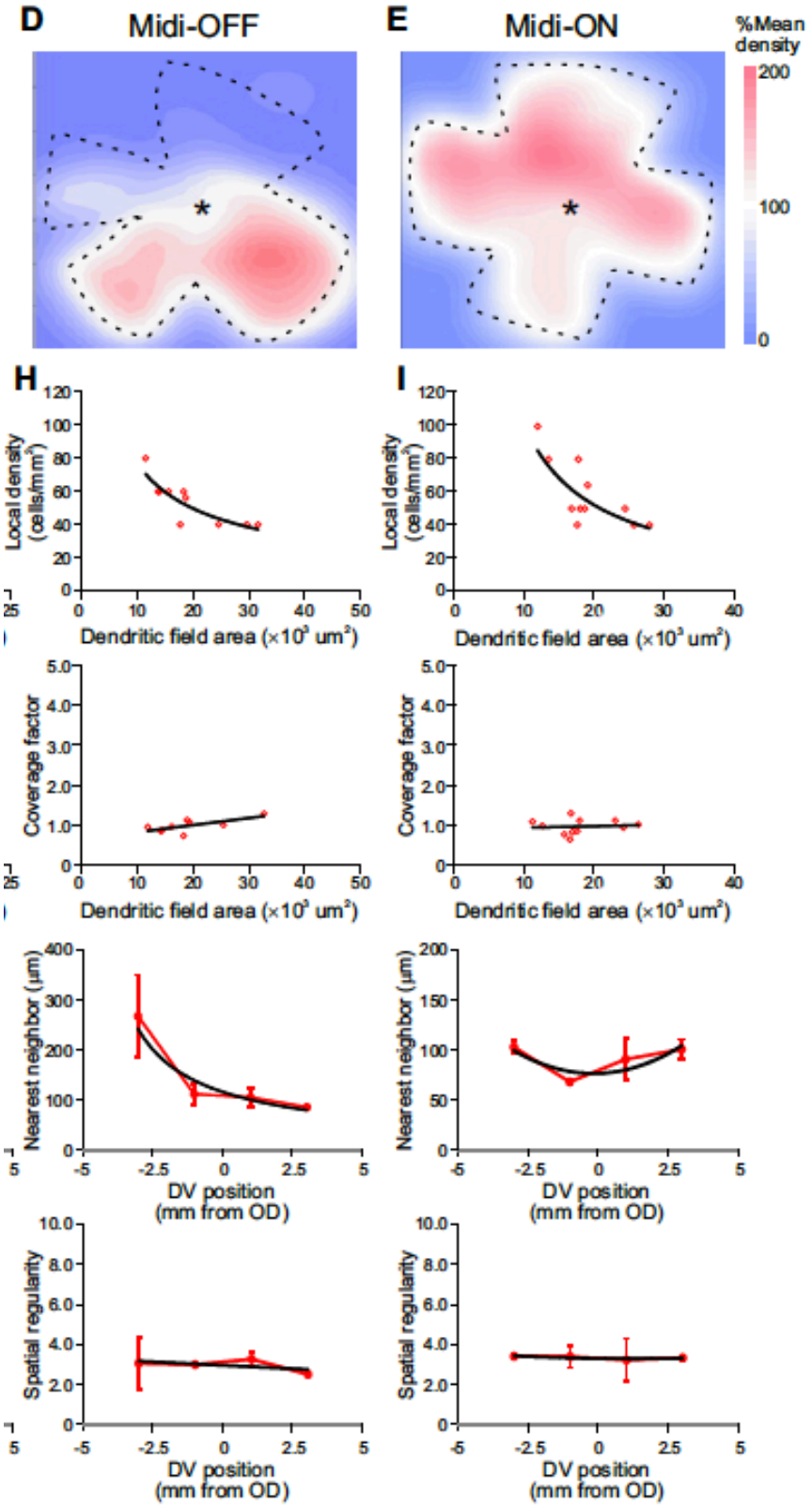

Figure 4.8 Dendritic orientation of F-RGCs at different retinal positions.

(A, B) AAV-labeled F-mini RGCs showing dendritic orientations in opposite directions: F-mini^{OFF}, ventrally; F-mini^{ON}, dorsally. Higher power view of the boxed region shows neighboring F-mini^{OFF} and F-mini^{ON} RGCs as identified based on Foxp1 and Foxp2 coexpression and dendritic stratification depth.

(C) AAV-labeled F-mini RGCs showing dendritic orientations in the same direction, toward the ventral pole.

(D) F-mini^{ON} RGCs exhibit bimodal morphologies depending on their location relative to the opsin transition zone (OTZ), as demarcated either by opsin staining (left panel) or by the decline in total Foxp2 density in this region (right panel). Asterisk and caret indicate the approximate location of cells shown in B and C.

(E) Polar plots of dendritic field orientations for F-mini^{ON} (top) and F-mini^{OFF} (bottom) RGCs located at different DV-positions (Dorsal, dashed lines; central/ventral, solid lines).

(F) F-RGC morphologies from different positions of the retina.

Figure 4.8 Dendritic orientation of F-RGCs at different retinal positions. (continued)

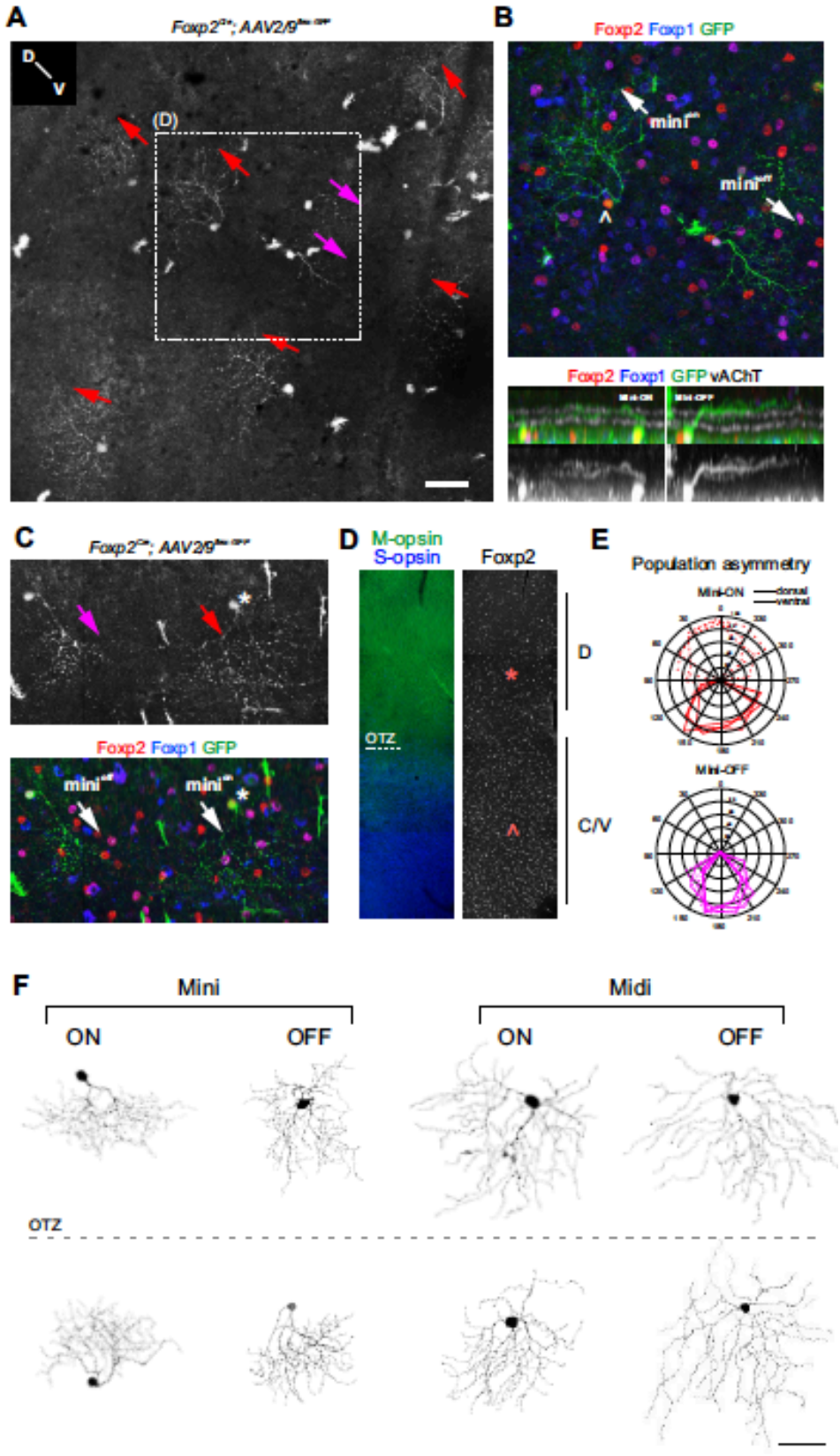

4.3.6 F-RGCs project to image-forming brain targets

RGCs project to 20-40 retinorecipient areas in the brain, with distinct RGC types differing in projection patterns (Dhande et al., 2015). To identify central targets of F-RGCs we analyzed brains following intravitreal injection of *AAV2/9*$^{flex\text{-}GFP}$ into *Foxp2*^{Cre} mice. Fluorophore-conjugated cholera toxin B (CTB) was co-injected to label all RGC axons, allowing us to compare, for each target, the density of innervation by F-RGC axons with the overall density of RGC innervation from contralateral and ipsilateral retinas (**Figure 4.9 A**). F-RGC axons terminated in the dorsal lateral geniculate nucleus and superior colliculus, which are sites in which information about spatial features are processed. Within the dLGN, F-RGC axons terminated selectively within the lateral shell (**Figure 4.9 B, C**). Within the colliculus, F-RGC axons stratified broadly within layers 2 and 3 (upper and lower stratum griseum superficiale [SGS]; (**Figure 4.9 D, E**). In both the thalamus and SC, termination fields of F-RGCs are similar to those reported for J-RGCs and ooDSGCs (Huberman et al., 2009; Kay et al., 2011; Kim et al., 2008). In contrast F-RGC axons bypassed suprachiasmatic nucleus, to which non-image-forming ip-RGCs project, as well as accessory optic nuclei such as the medial terminal nucleus and olivary pretectal nucleus (**Figure 4.9 F-I**), to which non-image-forming ON-DSGCs project. These innervation patterns are consistent with the idea that F-RGCs are not critical for light reflexive behaviors or circadian functions but instead participate in the generation of visual perception (**Figure 4.9 J**).

Figure 4.9 F-RGC axons selectively innervate image-forming visual targets in the brain.

(A-I) Analysis of F-RGC central projections following intravitreal injection of *AAV2/9*^{flexGFP} and fluorophore-conjugated cholera toxin b (CTB) in adult *Foxp2*^{Cre} mice. Sections are from the following brain regions: dorsal and ventral lateral geniculate nuclei of the thalamus, vLGN, dLGN (B,C); stratum griseum superficiale of the superior colliculus, SGS (D, E); suprachiasmatic nucleus, SCN (F,G); medial terminal nucleus, MTN, and preoptic area, POA (H, I). Brackets demark regions enriched with terminating GFP^{+} fibers.

(J) Schematic summary of F-RGC central projections.

Figure 4.9 F-RGC axons selectively innervate image-forming visual targets in the brain. (continued)

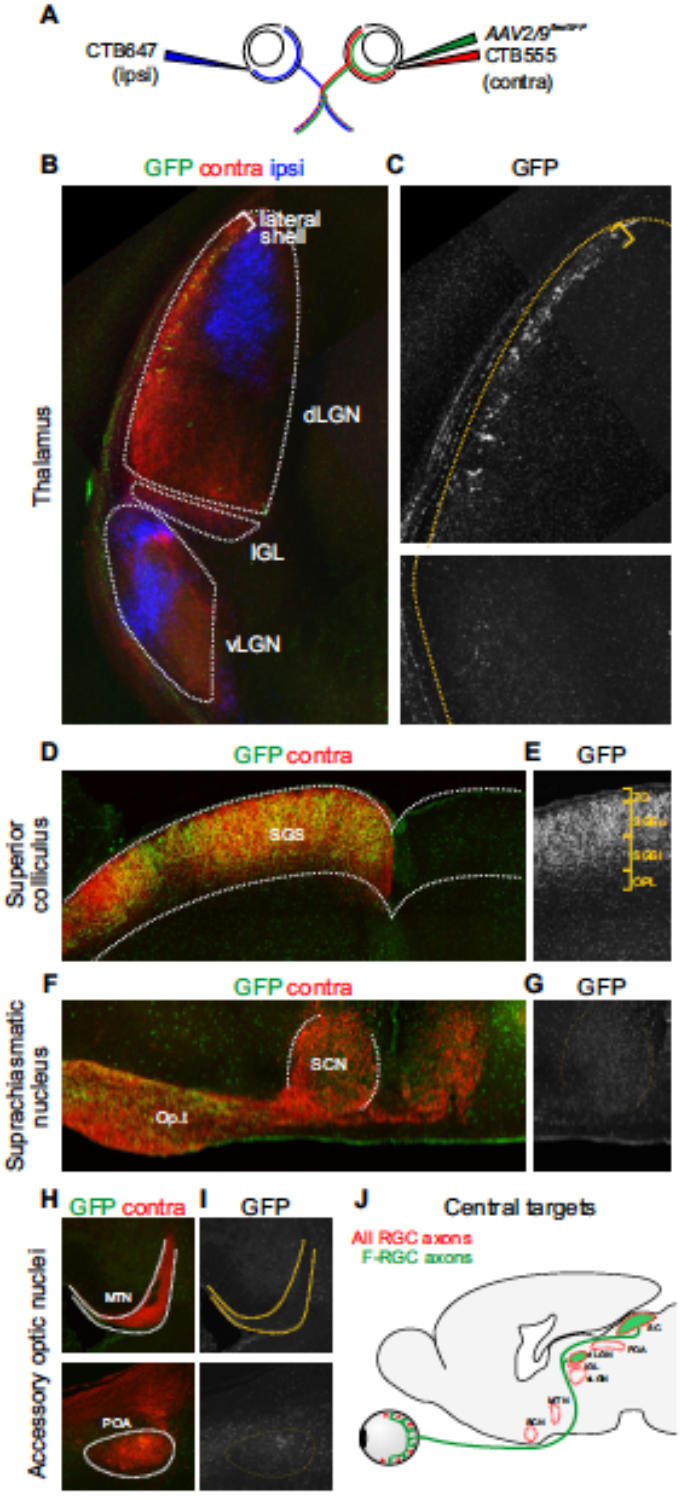

4.3.7 Visual responses of F-RGCs

We labeled F-RGCs in *FoxP2*^{Cre} mice and targeted them for recording with patch pipettes. We then stimulated them with light and dark spots of varying size, and moving bars of various speeds and direction. Following recording, targeted cells were marked by dye injection through the pipette and the retina was fixed. Cell type was then assessed by morphologic or immunohistochemical criteria. Consistent with their relative densities, F-midi cells were encountered ~1/3 as frequently as F-mini cells.

We predicted that there would be two differences among F-RGC types based on their morphological properties. First, RGCs with dendrites that stratify in S1 generally fire when the level of illumination diminishes (OFF response), while RGCs with dendrites in S3 fire either when the level of illumination increases or at both light onset and offset (ON or ON-OFF responses). As expected, F-mini^{OFF} and F-midi^{OFF} RGCs were pure OFF cells. In contrast, F-mini^{ON} and F-midi^{ON} RGCs were pure ON cells. Responses were transient for three of the four F-RGC types, and sustained only for F-midi^{OFF} RGCs (**Figure 4.10 A-D**).

Second, because the radius of an RGC's receptive field center is generally determined by the radius of its dendritic arbor, we expected that F-mini RGCs would have smaller fields than F-midi RGCs. This prediction was also fulfilled: as measured by peak response to light or dark spots of varying sizes. The radius of the receptive field centers were ~60 μm and ~80 μm for F-mini and F-midi RGCs, respectively (**Figure 4.10 E-H, M**).

We also examined direction-selectivity using bars moving in each of 8 directions. Examples are shown in **Figure 4.10 I-L** and summarized in **Figure 4.10 N**. Both F-mini cell types were direction-selective, with their preferred direction corresponding to the direction in which their dendrites pointed. Thus, all F-mini^{OFF} RGCs preferred ventral motion, whereas for F-mini^{ON} RGCs, the preferred direction depended on retinal position: cells in dorsal retina preferred ventral and cells in ventral retina preferred dorsal motion. We tested DS responses over a range of slow to high speeds, and found that F-mini cells were strongly tuned to bars moving at ~0.5-0.6 mm/s (**Figure 4.10 O**). This range of speed selectivity is faster than slow-tuned ON-DSGCs (~0.25 mm/s) (Yonehara et al., 2009), but slower than broadly-tuned

ooDSGCs. We wondered whether the light responses of F-mini RGCs influenced their selectivity to directional motion. Indeed, we found that F-mini^{ON} RGCs fired rapidly at the leading edge of the moving stimulus, whereas F-mini^{OFF} RGCs responded only at the trailing edge of motion (**Figure 4.11**). Thus, F-mini^{ON} and F-mini^{OFF} RGCs report ON and OFF components of directional motion, respectively.

Figure 4.10 Visual response properties of F-RGCs

(A-D) Representative responses to a spot flashing on (white) and off (grey) over the receptive field center for each cell. Raster plot of spikes from x cells over x repeats. Histograms (right panels) show frequency of spikes over time.

(E-H) Responses to flashing spots of different radii. The number of spikes are plotted during the optimal response period (ON or OFF) for each type, normalized to the maximum response.

(I-L) Responses to moving bars across the receptive field center in different directions. Polar plots represent the number of spikes fired for bars moving in each of the eight directions. Direction selectivity index (DSI) is indicated in boxes above each plot. Only F-mini show directional tuning (DSI>0.25); F-midi cells are direction non-selective (DSI ≈ 0).

(M) Quantification of receptive field size by the optimal spot radius. Comparison to other RGC types are drawn from Kim et al., 2010.

(N) Speed tuning curves for F-mini RGCs. Comparison with ON-DSGCs is drawn from Yonehara et al., 2009.

Figure 4.10 Visual response properties of F-RGCs (continued)

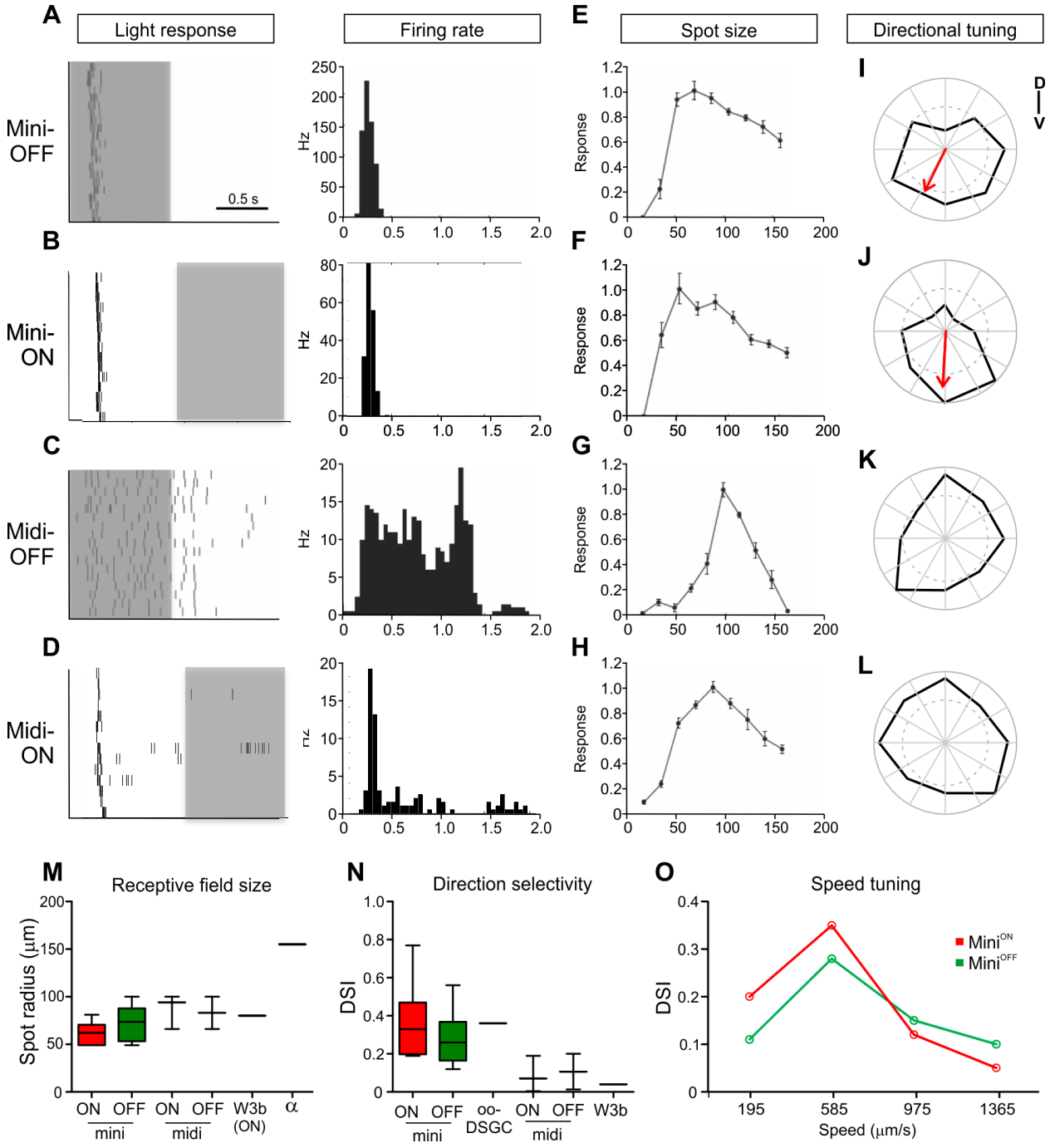

Figure 4.11 Responses of F-mini^{ON} and F-mini^{OFF} cells to moving bars

(A, B) Responses of F-mini^{on} and F-mini^{off} cells to bright moving bars from 8 directions in 2 repeats. Yellow shadow indicates when the bars sweep over the receptive fields of the two cells, and the leading edge and trailing edge of the bars are labeled by arrows. F-mini^{ON} cells respond to the leading edge (A) and F-mini^{OFF} cells respond to the trailing edge (B).

Figure 4.11 Responses of F-mini^{ON} and F-mini^{OFF} cells to moving bars (continued)

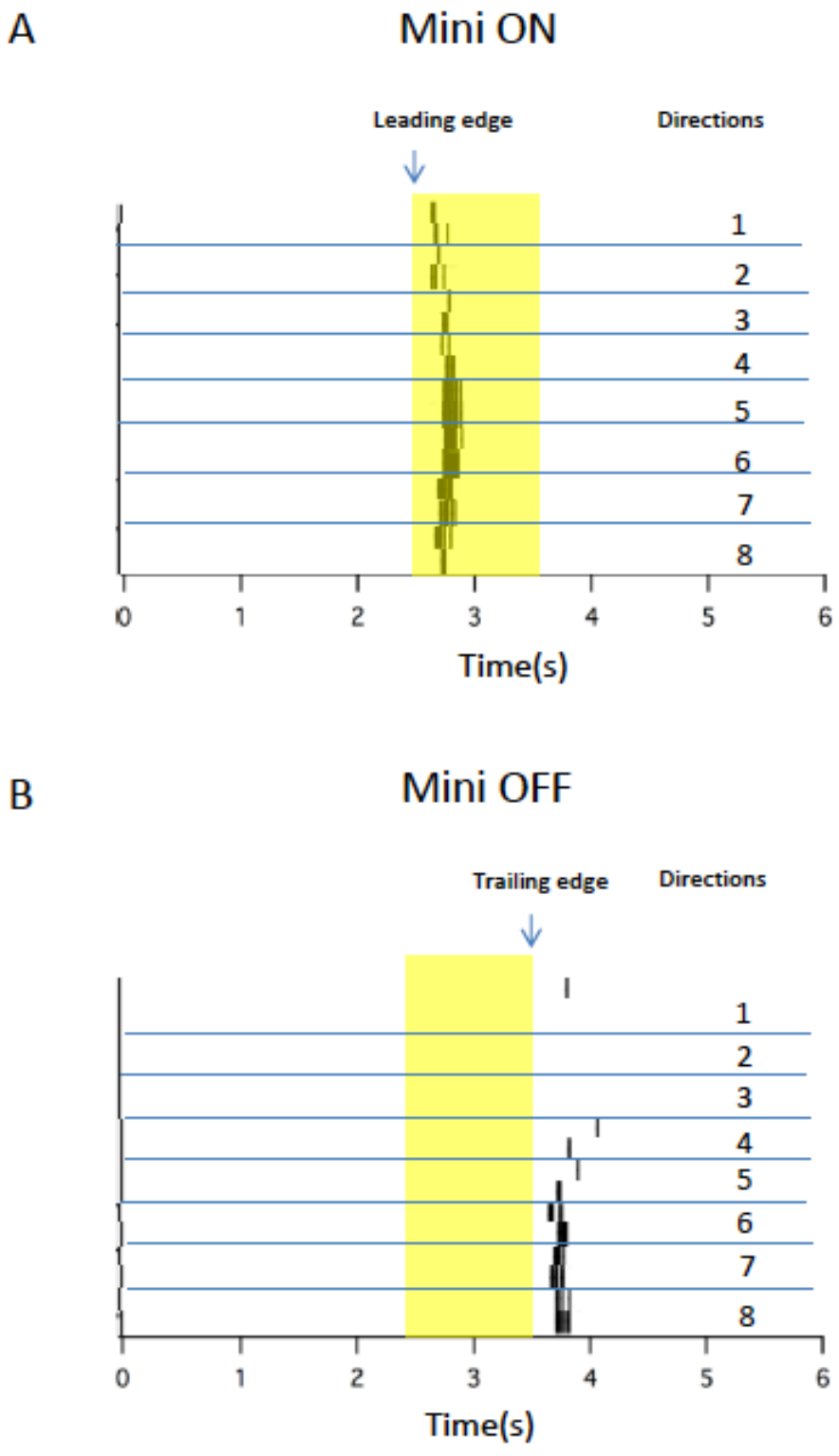

4.3.8 Foxp2 RGCs in primate retina

Finally, we asked whether combinatorial expression of Foxp and Brn3 transcription factors marks subsets of RGCs in primates as it does in mice. We first stained sections of adult macaque retina with antibodies to Foxp1, Foxp2, Brn3a, Brn3b, and Brn3c. All five proteins were expressed by subsets of cells located in the ganglion cell layer (**Figure 4.12 A, B**). All of these cells were RGCs as assessed by co-expression of RBPMS and the glutamate transporter vGlut2, which distinguish RGCs from inhibitory interneurons also located in the GCL (**Figure 4.13 A**).

Because the Foxp-positive subsets were sparse, we used retinal whole mounts to assay co-expression with each other and with Brn3 proteins. In a region approximately 1-2 mm from the fovea, ~2% of RGCs were $Foxp1^-/Foxp2^+$, ~0.5% were $Foxp1^+/Foxp2^-$ and ~0.25% were $Foxp1^+/Foxp2^+$ (**C** and **Figure 4.13 B**). These three groups differed in which Brn3 genes they expressed (**Figure 4.12 D**) Thus, combinatorial co-expression of Foxp and Brn3 proteins defines multiple RGC types in primates.

The total Foxp2-positive subset does not form mosaic spatial patterning ($f > 1$), indicating that is likely to comprise multiple RGC types. However, the $Foxp1^+/Foxp2^+/Brn3^+$ triple-positive RGCs do exhibit a regular mosaic distribution (**Figure 4.12 E** and **Figure 4.13 C**), indicating they are a single RGC type in primate retina, as in mice.

We imaged larger regions of retina to assess the distribution of the $FoxP2^+$ RGCs. The total density of RGCs (Brn3a-positive cells) changed little over the first 4mm from the fovea, consistent with previous report (Watanabe and Rodieck, 1989). However, the fraction of all RGCs that were Foxp2-positive declined ~3-fold over that distance (**Figure 4.12** and **Figure 4.13 D**). This pattern is similar to that reported for midget RGCs (see Discussion).

Figure 4.12 Foxp and Brn3 proteins distinguish RGC types in primate retina

(A, B) Antibody co-staining analysis of Brn3a, Brn3b, Brn3c, Foxp1, and Foxp2 proteins in adult macaque retina. Each antibody marks a population of RGCs localized to the ganglion cell layer (A). Double-staining for Foxp and Brn3 shows their co-localization within subsets (B).

(C) Whole mount retinas stained for Foxp1, Foxp2, and Brn3b. Foxp1 and Foxp2 combinatorially distinguish 3 RGC subsets (Foxp1+/Foxp2-, Foxp1+/Foxp2+, and Foxp2+/Foxp1-). Brn3b is coexpressed by the Foxp1+/Foxp2+ group (asterisks indicate triple-positive cells).

(D) Table summarizing RGC subsets marked by Foxp and Brn3 proteins.

(E) DRP analysis of total Foxp2 RGCs suggests that they are a mixture of RGC types (f>1). DRP of the Foxp1+Foxp2+Brn3b+ subset reveals their non-random mosaic organization, indicating they are a single RGC type.

(F) Density map of Foxp2 RGCs, showing their enrichment around the fovea.

(G) Quantification of total Brna+ RGCs and the fraction that are Foxp2+ at different distances from the fovea. Foxp2 RGC density drops by more than half while overall RGC density remains stable.

Figure 4.12 Foxp and Brn3 proteins distinguish RGC types in primate retina (continued)

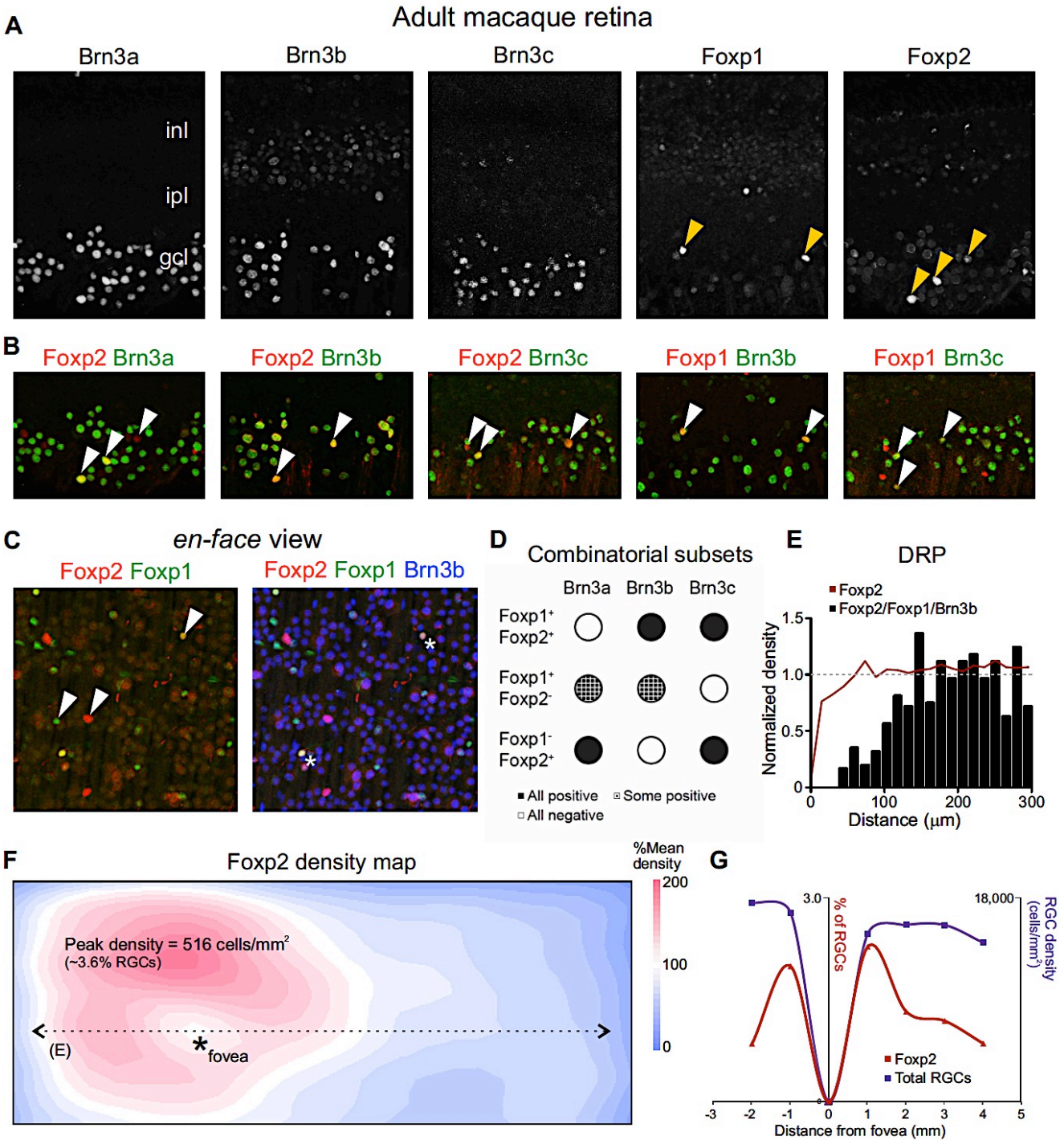

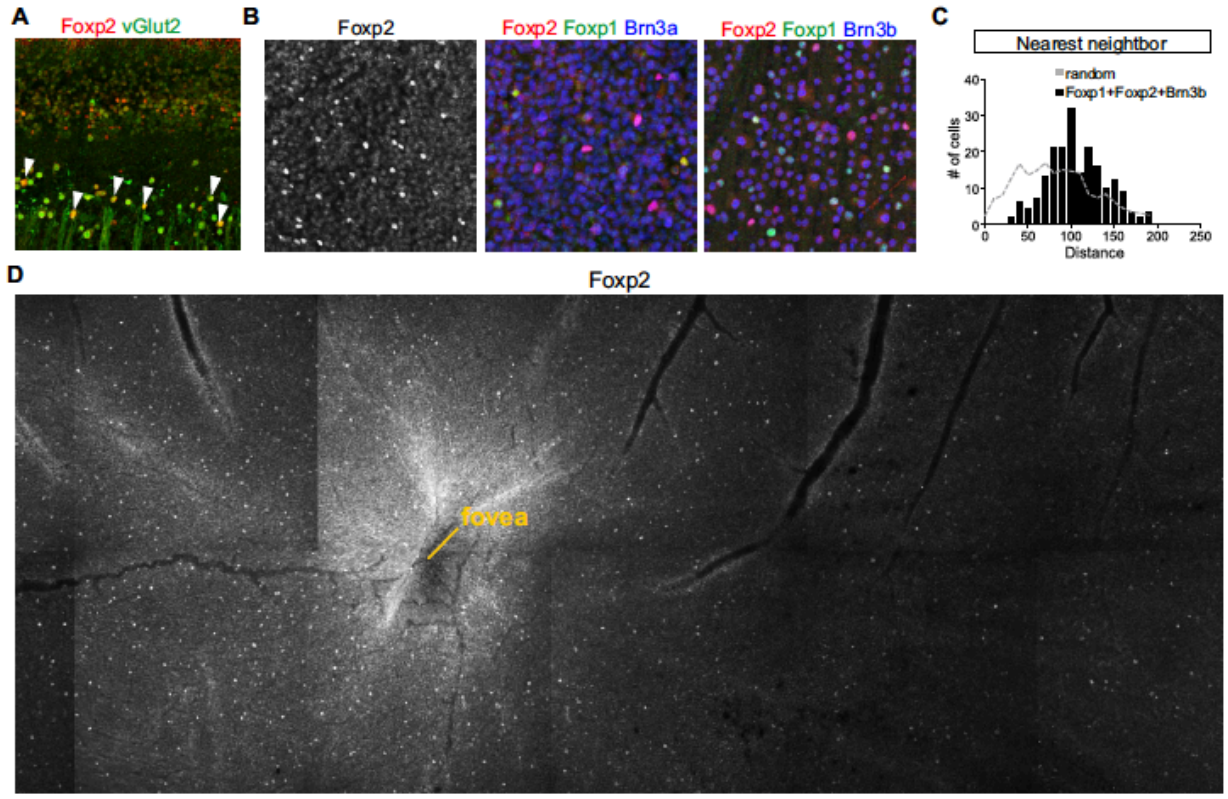

Figure 4.13 Characterization of Foxp2 RGCs in primate retina.

(A) Antibody costaining of Foxp2 and vGlut2 in adult macaque retina. Extensive colocalization indicates that Foxp2-positive cells are RGCs.

(B) Whole mount retina viewed en-face stained with Foxp and Brn3 antibodies. Different Foxp2 subsets are distinguishable based on combinatorial expression patterns (arrows).

(C) Nearest- neighbor analysis of the Foxp1+Foxp2+Brn3b subset reveals their spatial regularity typical of single retinal neuron types.

(D) View of fovea and parafovea regions reveal a density gradient of Foxp2 around the fovea (highest near the fovea).

4.4 Discussion

We have described F-RGCs, a set of 4 RGC types in mouse that have not, to our knowledge, been defined or described previously. Their main features are summarized in **Figure 4.14**. At least five properties of these cells are noteworthy, and enrich our understanding of retinal structure and function: they form symmetrical pairs, they display striking anisotropies in abundance and size across the receptive field, and two of the types are remarkably abundant, direction-selective, and small. Here, we briefly discuss these features.

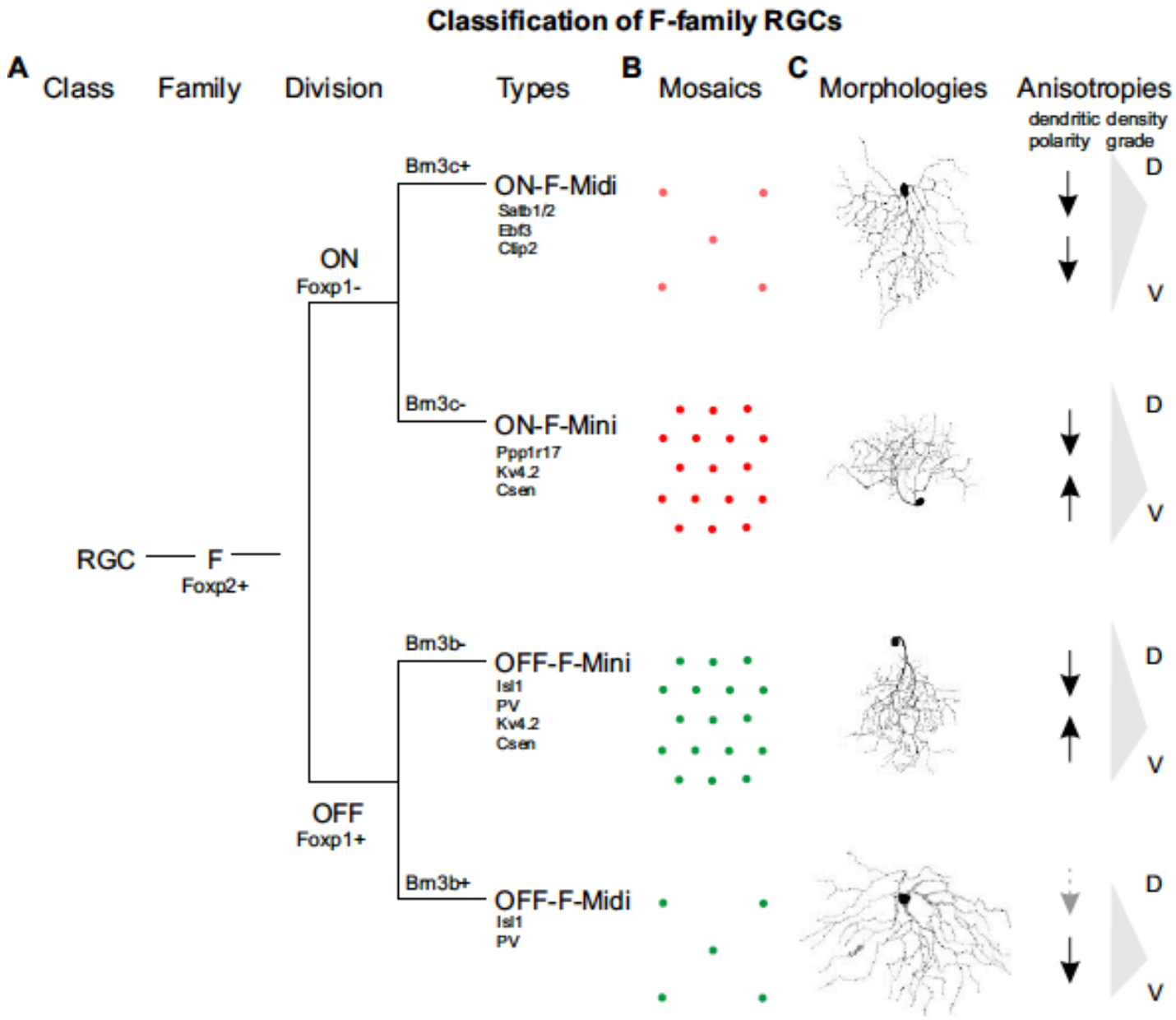

Figure 4.14 Summary of molecular, morphological, and functional properties of F-RGCs.

(A) Proposed scheme for classifying F-RGCs.

(B) Four F-RGC types can be identified by their combinatorial expression of Foxp and Brn3 TFs.

(C) Each member has distinct morphologies and anisotropic organization. The location of cells on the DV axis correlates with changes in density, dendritic orientation, and directional tuning.

4.4.1 F-RGCs are abundant

Less than half of all mouse RGCs have been categorized to date, and we have genetic access to only a fraction of those (Sanes and Masland, 2015). The F-RGCs account for ~25% of all RGCs in central/ventral retina, thereby decreasing by half the number of RGCs that remain to be characterized and more than doubling the number to which we have genetic access.

The abundance of the F-mini RGCs is ~4-fold greater than that of the F-midi types, with F-mini^{ON} and F-mini^{OFF} RGCs each comprising about 8% of all RGCs (16% combined). Thus, they are among the most numerous RGC types in the mouse retina. For comparison, individual alpha- and four ON-OFF DSGC types account for 3-4% of RGCs (Krieger et al., in preparation; Kay et al., 2011). The W3B RGCs, which we described previously (Zhang et al., 2012), and the F-mini RGCs reach a similar density of ~350 cells/mm^2 in central ventral retina, together accounting for over a third of all RGCs in this region.

Given this abundance, it is natural to wonder why these cells have apparently escaped detection in a tissue as intensively studied as mouse retina. Several surveys of have been published in which large numbers of individual mouse RGCs were labeled in seemingly unbiased ways and characterized morphologically (Badea and Nathans, 2004; Coombs et al., 2007; Kong et al., 2005; Sümbül et al., 2014; Sun et al., 2002; Völgyi et al., 2009). It is possible the "Cluster 4" cells described by Kong and "cell o" described by Badea 2011 correspond to the F-midi^{ON} and F-midi^{OFF} cells, respectively, but without molecular correspondence such assignments are speculative. With respect to the F-mini cells, their small size might have led to their being underrepresented in some surveys. In addition, in some cases, the F-mini^{ON} and F-mini^{OFF} RGCs appear to have been misidentified as J-RGCs and W3B-RGCs, respectively (Farrow et al., 2013), owing to their similar lamination pattern and, for the F-mini^{OFF} RGCs, ventral asymmetry.

4.4.2 F-mini RGCs are small

We previously characterized an RGC type called W3B, which serve as object motion sensors, specialized to respond when the timing of a small object's movement differs from that of the background

(Kim et al., 2010; Krishnaswamy et al., 2015; Zhang et al., 2012). We concluded that W3B cells play a prominent role in high-acuity vision and second that these small cells are feature detectors rather than pixel detectors – that is, passive reporters of position and luminance. Our new results replace F-mini^{OFF} and F-mini^{ON} RGCs as the smallest RGCs, with a dendritic field area nearly half that of W3B-RGCs. On the other hand, our results provide further support for the idea that small RGCs need not be pixel detectors – the F-mini RGCs respond selectively to motion in a particular direction.

4.4.3 F-mini RGCs are direction-selective

Computation of directional motion is a topic of great current interest. To date, most studies of direction-selectivity in mouse retina has centered on four types of ooDSGCs, which are similar in structure and physiological properties, but differ in preferred direction (ventral, dorsal, nasal and temporal; Borst and Helmstaedter, 2015; Vaney et al., 2012). Likewise, recent studies have asked whether direction-selective units in higher image-forming centers, such as superior colliculus, dorsal lateral geniculate nucleus and visual cortex inherit their selectivity from the ooDSGCs or compute it de novo (Cruz-Martín et al., 2014; Marshel et al., 2012). Sparse populations of ON-DSGCs have also been studied in detail, however they project to accessory areas but not to image-forming areas. The F-mini^{ON} RGCs are thus the first ON-DSGCs known to project to image-forming areas. To date, only a single population of OFF-DSGC, the J-RGC, has been described (Kim et al., 2008, 2010); the F-mini^{OFF} RGCs are at least twice as abundant and thus will need to be taken into account as well. Importantly, ooDSGCs and J-RGCs appear to compute direction-selectivity by different mechanisms, with dendritic asymmetry being essential for the latter but not (even when it is present) for the former. It remains to be determined how F-mini RGCs, which do have markedly asymmetrical arbors, compute direction.

The two F-mini types add two new members to the class of direction-selective types; the total number is now 10 (4 ooDSGCs, 3 ON-DSGCs, J-RGCs, and 2 F-mini-RGCs). Perhaps more important, the abundance of the F-mini these cells nearly doubles the fraction of DS cells among all RGCs, and may account for the bias for vertical motion selectivity observed within the superior colliculus in some studies

(Dräger and Hubel, 1975; Inayat et al., 2015). Their direction-selectivity might therefore help explain a discrepancy between the large fraction of direction-selective neurons in visual centers of the mouse brain and the modest number of previously identified DS-RGCs.

4.4.4 F-RGCs comprise paramorphic pairs

The four F-RGC types can be viewed as forming pairs in either of two senses: both ON and OFF groups comprise mini-midi pairs, and both mini and midi groups comprise ON-OFF pairs. Of these we view the ON-OFF pairs as more compelling for two reasons. First, the two F-mini RGC types are similar to each other in many respects including size, dendritic asymmetry, abundance and physiological properties, differing primarily in level of dendritic stratification. The same is true for the two F-midi RGC types.

Second, this division corresponds to an organizational principle that has been noted in retinas of higher mammals: that a set of channels has been duplicated to generate ON and OFF representations of each feature detector. This phenomenon, termed paramorphism, is prominent in the primate rabbit and cat retina (Berson, 2008; Famiglietti, 2004, 2005; Famiglietti and Kolb, 1976). In the mouse, it is evident in the paired starburst amacrine cells but has not previously been documented in detail for RGCs. The phenomenon of paramorphism leads to the idea that a small alteration in developmental program could lead to a duplication and diversification of types. We speculate that Foxp1, which is present in both OFF F-RGC types but neither ON F-RGC types could serve as part of such a program. In mouse, methods are available to test this idea.

4.4.5 F-RGCs are anisotropic in size and distribution

In many vertebrates, visual information is not sampled uniformly across the visual field. Rather, RGC densities increase and their dendritic field sizes decrease within anatomically distinct regions, such as the area centralis in cats or the fovea in primates. Because dendritic field area correlates strongly with receptive field area and thus spatial resolution, such areas are associated with high-acuity vision. The

distribution of RGCs in mice has been thought to be relatively uniform across the retina, suggesting uniform spatial sampling (Huberman and Niell, 2011). However recent findings suggest that some RGC types differ in their distribution (Zhang et al., 2012; Bleckert), raising the possibility that mice may also have anatomical regions dedicated to high spatial sampling. We show that all F-RGCs exhibit non-uniform spatial topographies. Although they exhibit striking variance in abundance and size, particularly along the dorsal-ventral axis, these properties co-vary proportionately (they are smaller as their density increases). Of note, the high density and smaller size of F-mini RGCs within the ventral retina implies enhanced spatial sampling from the upper visual field, which may explain their preference for motion on the vertical (dorso-ventral) axis, as opposed to horizontal (nasal-temporal) motion.

4.4.6 Are F-mini-RGCs related to midget RGCs?

A challenge for visual neuroscience –indeed neuroscience generally– is to extend the cell type classification enterprise from model organisms such as mice to primates. We asked here whether the patterns of Foxp and Brn3 isoform expression that defined F-RGCs in mice also labeled discrete subsets of cells in macaque retina. Indeed, we identified Foxp1^{-}/Foxp2^{+}, Foxp1^{+}/Foxp2^{-} and Foxp1^{+}/Foxp2^{+} groups of RGCs, each of which co-expresses one or more Brn3 proteins. Although these groups remain to be characterized, their existence encourages the view that classification schemes derived from and validated in mice will be useful for understanding primate retina.

Most interesting is a potential parallel between mouse F-RGCs and arguably the best studied RGC group in primates, the midget RGCs, which are thought to function in acuity vision. F-mini-RGCs in mice and midget RGCs in primates are the smallest and most abundant types in their respective species, both have highly-branched and tufted dendrites, both are asymmetric (vertically-oriented for minis, fovea-oriented for midgets), and both form "paramorphic" ON-OFF pairs.

Could primate Foxp2^{+} RGCs be midgets? A precise correspondence is unlikely for at least two reasons. First, primate midget RGCs have so far not been reported to be direction-selective, even in peripheral retina, where there receptive fields are sufficiently large to support such a computation (Dacey

and Packer, 2003). Second, Foxp2$^+$ RGCs comprise only ~2% of RGCs in primate parafoveal retina, whereas midget RGCs comprise ~90% of all RGCs in this region. On the other hand, the distribution of Foxp2$^+$ RGCs is remarkably similar to that of midget RGCs: highest near the fovea and declining in abundance (fractional representation) with distance. Another abundant class, parasol RGCs, as well as rare classes of which we are aware, all appear to increase in fractional representation with distance from the fovea (Watanabe and Rodieck, 1989). Thus, an intriguing hypothesis that we are currently testing is that midget RGCs are heterogeneous and that Foxp2$^+$ RGCs represent one midget subtype.

4.5 Experimental Procedures

4.5.1 Preparation of genetically labeled animals

Cdh4^{CreER} and *Cdh13*^{CreER} mice were generated by targeted insertion of CreER followed by a poly-adenylation signal at the translational start site of the *Cdh4* and *13* coding sequences, respectively, using standard methods. *Cdh4*^{CreER} and *Cdh13*^{CreER} mice were crossed with reporter mice containing a *lox-STOP-lox-YFP* cassette. Tamoxifen (2 mg to 8 mg, Sigma) was injected intraperitoneally into double transgenic mice at adult or early post-natal ages to induce desired density of labeled cells. *Foxp2*^{Cre} mice were generated by targeted insertion of a Cre:GFP fusion sequence downstream of an interneral ribosomal entry sequence following the translational stop codon in exon 19 of the *Foxp2* gene. AAV-delivery of a flex-GFP cassette was used to label cells at desired densities.

4.5.2 Histology

Animals were euthanized by intraperitoneal injection of Euthasol (25 μL/10g; Virbac; Fort Worth, TX) and perfused with room-temperature phosphate buffered saline (PBS) followed by chilled 4% paraformaldehyde (PFA) in PBS. Eyes were removed and post-fixed in 4% PFA at 4°C for 1 hour and retinal tissue was isolated. Retinas were prepared for whole mount or cryosection analysis as described previously (Kim et al., 2010). Sections were incubated in blocking buffer (1% horse serum, 0.05% azide, and 0.1% Triton X-100) at room temperature, then incubated in blocking buffer with primary antibodies at 4°C overnight, then with secondary antibodies for >1 hour at room temperature. For whole mounted retinas, primary antibodies were incubated in blocking buffer at 4°C for five days and secondary antibodies at 4°C overnight. Tissue was then flat-mounted on membrane filters, and cover-slipped with Prolong Gold anti-fade reagent (Invitrogen). Brains were post-fixed in 4% PFA at 4°C overnight, immersed successively in 15% sucrose/PBS and 30% sucrose/PBS 4°C overnight, mounted in TFM, frozen, and sectioned (100-200 μm). Thick brain sections were stained and optically cleared using iDISCO reagent #1 (Renier et al., 2014).

4.5.3 AAV-labeling and anterograde tract tracing

Mice were anesthetized by intraperitoneal injection of ketamine/xylazine. A small hole was made in the eye and 1-2 μl of vitreous was removed to relieve intraocular pressure. AAV containing a flex-GFP cassette (University of Pennsylvania) was then injected at varying dilutions to achieve desired density of labeled cells. Cholera toxin B subunit conjugated to Alexa Fluor 555 or 647 (1–2 μl of 1 mg/ml, Invitrogen) was coinjected into the same eye or opposite eye, respectively. After surgery, anesthesia was reversed by intraperitoneal delivery of antisedan, and the mice were observed for healthy recovery. Mice were sacrificed for analysis between 2-4 weeks after injection. Procedures were approved by the animal care and use program at Harvard University.

4.5.4 Image analysis and quantification of RGCs

Images of immunofluorescent retina and brain were acquired on Olympus FV1000 MPE or Zeiss LSM 710 confocal microscopes. Images were processed using Zeiss ZEN or Olympus Fluoview software suites and analyzed using Fiji (NIH) or custom software written in Matlab (Simulink). Spatial distribution of RGCs was analyzed using WinDRP software (Euler, 2003). An estimate of the fraction (f) of a mosaic labeled was computed as the density of the observed population (d_{obv}) divided by the density of nodes comprising a computer-generated equilateral triangular lattice (d_{hex}) of the same side length, s defined by Zhang et al., 2012. For morphological analysis, isolated GFP^+ RGCs were segmented from whole mount retinas using Fiji's Simple Neurite Tracer. To quantify the depth of RGC dendritic stratification, traced cells were rotated on the x-axis and the depth of dendritic stratification was normalized between 0 and 100% (0%, INL; 100%, GCL). Pixel intensities at each depth were normalized between 0 and 100% (0, absence of signal; 100% brightest signal) to control for variability in brightness across labeled cells. Dendritic field area was calculated as the convex hull formed by distal points of the dendritic arbors. Coverage factor was computed as dendritic field area × density (spatial frequency). Dendritic AI was determined by first summing vectors representing each dendrite (to compute preferred direction), then summing the lengths of all the dendrites on the preferred side, subtracting the sum of the lengths on the

null side, and dividing by the lengths of all the dendrites on both sides (Trenholm et al., 2011). Regularity of mosaic spacing was computed as the mean nearest neighbor distance divided by the SD.

4.5.5 Electrophysiology

Electrophysiological analysis was performed as described previously (Kay et al., 2011; Kim et al., 2008). Briefly, mice were dark-adapted for >2 hours and retinas were dissected in oxygenated (95% O2; 5% CO2) Ringer's solution. Relaxing cuts were made and the retina was placed in a recording chamber with ganglion cells facing upward and the ventral-quadrant of the retina marked for orientation. AAV-labeled cells were then targeted under brief fluorescent illumination for cell-attached recording using microelectrodes. Light stimuli were presented by a video projector through a custom-made lens located just below the stage. Receptive field centers were determined with small flashing spots, then direction selectivity was analyzed by presenting moving bars through the receptive field center in eight different directions at varying speeds.

4.6 Acknowledgement

We thank B. Novitch, D. Masland, M. Do, S. Seung, M. Samuel, and A. Krishnaswamy, and for reagents, experimental instruction, helpful discussions, and comments on the manuscript.

4.7 References

Badea, T.C., and Nathans, J. (2004). Quantitative analysis of neuronal morphologies in the mouse retina visualized by using a genetically directed reporter. J. Comp. Neurol. *480*, 331–351.

Badea, T.C., and Nathans, J. (2011). Morphologies of mouse retinal ganglion cells expressing transcription factors Brn3a, Brn3b, and Brn3c: analysis of wild type and mutant cells using genetically-directed sparse labeling. Vision Res. *51*, 269–279.

Berson, D.M. (2008). Retinal Ganglion Cell Types and Their Central Projections. In The Senses: A Comprehensive Reference, (Elsevier), pp. 491–519.

Bisgrove, D.A., and Godbout, R. (1999). Differential expression of AP-2alpha and AP-2beta in the developing chick retina: repression of R-FABP promoter activity by AP-2. Dev. Dyn. *214*, 195–206.

Bleckert, A., Schwartz, G.W., Turner, M.H., Rieke, F., and Wong, R.O.L. (2014). Visual space is represented by nonmatching topographies of distinct mouse retinal ganglion cell types. Curr. Biol. *24*, 310–315.

Borst, A., and Helmstaedter, M. (2015). Common circuit design in fly and mammalian motion vision. Nat. Neurosci. *18*, 1067–1076.

Buffelli, M., Burgess, R.W., Feng, G., Lobe, C.G., Lichtman, J.W., and Sanes, J.R. (2003). Genetic evidence that relative synaptic efficacy biases the outcome of synaptic competition. Nature *424*, 430–434.

Carcieri, S.M., Jacobs, A.L., and Nirenberg, S. (2003). Classification of retinal ganglion cells: a statistical approach. J. Neurophysiol. *90*, 1704–1713.

Catela, C., Shin, M.M., and Dasen, J.S. (2015). Assembly and Function of Spinal Circuits for Motor Control. Annu. Rev. Cell Dev. Biol.

Coombs, J.L., Van Der List, D., and Chalupa, L.M. (2007). Morphological properties of mouse retinal ganglion cells during postnatal development. J. Comp. Neurol. *503*, 803–814.

Cruz-Martín, A., El-Danaf, R.N., Osakada, F., Sriram, B., Dhande, O.S., Nguyen, P.L., Callaway, E.M., Ghosh, A., and Huberman, A.D. (2014). A dedicated circuit links direction-selective retinal ganglion cells to the primary visual cortex. Nature *507*, 358–361.

Dacey, D.M., and Packer, O.S. (2003). Colour coding in the primate retina: diverse cell types and cone-specific circuitry. Curr. Opin. Neurobiol. *13*, 421–427.

Dhande, O.S., and Huberman, A.D. (2014). Retinal ganglion cell maps in the brain: implications for visual processing. Curr. Opin. Neurobiol. *24*, 133–142.

Dräger, U.C., and Hubel, D.H. (1975). Responses to visual stimulation and relationship between visual, auditory, and somatosensory inputs in mouse superior colliculus. J. Neurophysiol. *38*, 690–713.

Duan, X., Qiao, M., Bei, F., Kim, I.-J., He, Z., and Sanes, J.R. (2015). Subtype-specific regeneration of retinal ganglion cells following axotomy: effects of osteopontin and mTOR signaling. Neuron *85*, 1244–1256.

Euler, T. (2003). WinDRP website. http://wvad.mpimf-heidelberg.mpg.de/abteilungen/biomedizinischeOptik/software/WinDRP/index.html.

Famiglietti, E.V. (2004). Class I and class II ganglion cells of rabbit retina: a structural basis for X and Y (brisk) cells. J. Comp. Neurol. *478*, 323–346.

Famiglietti, E.V. (2005). "Small-tufted" ganglion cells and two visual systems for the detection of object motion in rabbit retina. Vis. Neurosci. *22*, 509–534.

Famiglietti, E.V., and Kolb, H. (1976). Structural basis for ON-and OFF-center responses in retinal ganglion cells. Science *194*, 193–195.

Farrow, K., Teixeira, M., Szikra, T., Viney, T.J., Balint, K., Yonehara, K., and Roska, B. (2013). Ambient illumination toggles a neuronal circuit switch in the retina and visual perception at cone threshold. Neuron *78*, 325–338.

Hattar, S., Liao, H.W., Takao, M., Berson, D.M., and Yau, K.W. (2002). Melanopsin-containing retinal ganglion cells: architecture, projections, and intrinsic photosensitivity. Science *295*, 1065–1070.

Huberman, A.D., and Niell, C.M. (2011). What can mice tell us about how vision works? Trends Neurosci. *34*, 464–473.

Huberman, A.D., Manu, M., Koch, S.M., Susman, M.W., Lutz, A.B., Ullian, E.M., Baccus, S.A., and Barres, B.A. (2008). Architecture and activity-mediated refinement of axonal projections from a mosaic of genetically identified retinal ganglion cells. Neuron *59*, 425–438.

Huberman, A.D., Wei, W., Elstrott, J., Stafford, B.K., Feller, M.B., and Barres, B.A. (2009). Genetic identification of an On-Off direction-selective retinal ganglion cell subtype reveals a layer-specific subcortical map of posterior motion. Neuron *62*, 327–334.

Inayat, S., Barchini, J., Chen, H., Feng, L., Liu, X., and Cang, J. (2015). Neurons in the most superficial lamina of the mouse superior colliculus are highly selective for stimulus direction. J. Neurosci. *35*, 7992–8003.

Jeon, C.J., Strettoi, E., and Masland, R.H. (1998). The major cell populations of the mouse retina. J. Neurosci. *18*, 8936–8946.

Kay, J.N., De la Huerta, I., Kim, I.-J., Zhang, Y., Yamagata, M., Chu, M.W., Meister, M., and Sanes, J.R. (2011). Retinal ganglion cells with distinct directional preferences differ in molecular identity, structure, and central projections. J. Neurosci. *31*, 7753–7762.

Kay, J.N., Chu, M.W., and Sanes, J.R. (2012). MEGF10 and MEGF11 mediate homotypic interactions required for mosaic spacing of retinal neurons. Nature *483*, 465–469.

Kim, I.-J., Zhang, Y., Yamagata, M., Meister, M., and Sanes, J.R. (2008). Molecular identification of a retinal cell type that responds to upward motion. Nature *452*, 478–482.

Kim, I.-J., Zhang, Y., Meister, M., and Sanes, J.R. (2010). Laminar restriction of retinal ganglion cell dendrites and axons: subtype-specific developmental patterns revealed with transgenic markers. J. Neurosci. *30*, 1452–1462.

Kong, J.-H., Fish, D.R., Rockhill, R.L., and Masland, R.H. (2005). Diversity of ganglion cells in the mouse retina: unsupervised morphological classification and its limits. J. Comp. Neurol. *489*, 293–310.

Krishnaswamy, A., Yamagata, M., Duan, X., Hong, Y.K., and Sanes, J.R. (2015). Sidekick 2 directs formation of a retinal circuit that detects differential motion. Nature *524*, 466–470.

Lodato, S., and Arlotta, P. (2015). Generating Neuronal Diversity in the Mammalian Cerebral Cortex. Annu. Rev. Cell Dev. Biol.

Marshel, J.H., Kaye, A.P., Nauhaus, I., and Callaway, E.M. (2012). Anterior-posterior direction opponency in the superficial mouse lateral geniculate nucleus. Neuron *76*, 713–720.

Masland, R.H. (2012). The neuronal organization of the retina. Neuron *76*, 266–280.

de Melo, J., Qiu, X., Du, G., Cristante, L., and Eisenstat, D.D. (2003). Dlx1, Dlx2, Pax6, Brn3b, and Chx10 homeobox gene expression defines the retinal ganglion and inner nuclear layers of the developing and adult mouse retina. J. Comp. Neurol. *461*, 187–204.

Osterhout, J.A., Josten, N., Yamada, J., Pan, F., Wu, S., Nguyen, P.L., Panagiotakos, G., Inoue, Y.U., Egusa, S.F., Volgyi, B., et al. (2011). Cadherin-6 mediates axon-target matching in a non-image-forming visual circuit. Neuron *71*, 632–639.

Reese, B.E. (2012). Retinal Mosaics: Pattern Formation Driven by Local Interactions between Homotypic Neighbors. Frontiers in Neural Circuits *6*.

Renier, N., Wu, Z., Simon, D.J., Yang, J., Ariel, P., and Tessier-Lavigne, M. (2014). iDISCO: a simple, rapid method to immunolabel large tissue samples for volume imaging. Cell *159*, 896–910.

Rockhill, R.L., Euler, T., and Masland, R.H. (2000). Spatial order within but not between types of retinal neurons. Proc. Natl. Acad. Sci. U.S.A. *97*, 2303–2307.

Rodieck, R.W. (1991). The density recovery profile: a method for the analysis of points in the plane applicable to retinal studies. Vis. Neurosci. *6*, 95–111.

Rodriguez, A.R., de Sevilla Müller, L.P., and Brecha, N.C. (2014). The RNA binding protein RBPMS is a selective marker of ganglion cells in the mammalian retina. J. Comp. Neurol. *522*, 1411–1443.

Rousso, D.L., Gaber, Z.B., Wellik, D., Morrisey, E.E., and Novitch, B.G. (2008). Coordinated actions of the forkhead protein Foxp1 and Hox proteins in the columnar organization of spinal motor neurons. Neuron *59*, 226–240.

Rousso, D.L., Pearson, C.A., Gaber, Z.B., Miquelajauregui, A., Li, S., Portera-Cailliau, C., Morrisey, E.E., and Novitch, B.G. (2012). Foxp-mediated suppression of N-cadherin regulates neuroepithelial character and progenitor maintenance in the CNS. Neuron *74*, 314–330.

Sanes, J.R., and Masland, R.H. (2015). The types of retinal ganglion cells: current status and implications for neuronal classification. Annu. Rev. Neurosci. *38*, 221–246.

Sanes, J.R., and Zipursky, S.L. (2010). Design Principles of Insect and Vertebrate Visual Systems. Neuron *66*, 15–36.

Sümbül, U., Song, S., McCulloch, K., Becker, M., Lin, B., Sanes, J.R., Masland, R.H., and Seung, H.S. (2014). A genetic and computational approach to structurally classify neuronal types. Nat Commun *5*, 3512.

Sun, W., Li, N., and He, S. (2002). Large-scale morphological survey of mouse retinal ganglion cells. J. Comp. Neurol. *451*, 115–126.

Szmajda, B.A., Grünert, U., and Martin, P.R. (2005). Mosaic properties of midget and parasol ganglion cells in the marmoset retina. Vis. Neurosci. *22*, 395–404.

Tien, N.-W., Pearson, J.T., Heller, C.R., Demas, J., and Kerschensteiner, D. (2015). Genetically Identified Suppressed-by-Contrast Retinal Ganglion Cells Reliably Signal Self-Generated Visual Stimuli. J. Neurosci. *35*, 10815–10820.

Trenholm, S., Johnson, K., Li, X., Smith, R.G., and Awatramani, G.B. (2011). Parallel mechanisms encode direction in the retina. Neuron *71*, 683–694.

Vaney, D.I., Sivyer, B., and Taylor, W.R. (2012). Direction selectivity in the retina: symmetry and asymmetry in structure and function. Nat. Rev. Neurosci. *13*, 194–208.

Völgyi, B., Chheda, S., and Bloomfield, S.A. (2009). Tracer coupling patterns of the ganglion cell subtypes in the mouse retina. J. Comp. Neurol. *512*, 664–687.

Watanabe, M., and Rodieck, R.W. (1989). Parasol and midget ganglion cells of the primate retina. J. Comp. Neurol. *289*, 434–454.

Yonehara, K., Ishikane, H., Sakuta, H., Shintani, T., Nakamura-Yonehara, K., Kamiji, N.L., Usui, S., and Noda, M. (2009). Identification of retinal ganglion cells and their projections involved in central transmission of information about upward and downward image motion. PLoS ONE *4*, e4320.

Zeck, G.M., and Masland, R.H. (2007). Spike train signatures of retinal ganglion cell types. Eur. J. Neurosci. *26*, 367–380.

Zhang, Y., Kim, I.-J., Sanes, J.R., and Meister, M. (2012). The most numerous ganglion cell type of the mouse retina is a selective feature detector. Proc. Natl. Acad. Sci. U.S.A. *109*, E2391–E2398.

Chapter 5: Classification of W3D retinal ganglion cells

Preface:

This work presented in this chapter is my ongoing work to classify a group of retinal ganglion cells labeled dimly in W3 mouse line. I recorded from individual cells followed by dye filling. The preliminary result here indicates that there are at least five different subtypes of RGCs labeled. I will further analyze their characteristics in detail and seek molecular markers for each subtype as the future direction.

3.1 Abstract

The retina conveys visual information to the brain through retinal ganglion cells (RGCs). There are >20 different subtypes of RGCs, each of which carries different information. Thus, it is important to characterize these RGC subtypes in order to understand how our brain processes visual information. Until recently, transgenic or Cre knock-in animals with specific subtypes of RGCs labeled by fluorescent proteins allowed us to specifically study subtypes of RGCs. Here, we study RGCs labeled in a transgenic mouse line called 'W3'. W3 RGCs can be divided into two populations based on their fluorescent intensities. Previous study revealed that W3 bright (W3B) cells are local motion detectors (Krishnaswamy et al., 2015; Zhang et al., 2012). Here, we specifically focus on the other population of W3 cells, whose fluorescent intensity is dim (W3D). Targeted recording followed by dye injection allowed us to understand their physiological and morphological properties, and classify them based on these characteristics. We found that W3D cells are comprised of at least five subtypes: On and Off orientation selective RGCs, W3B like RGCs and two subtype of direction selective RGCs with small receptive fields. Initial screens showed that nearly all W3D cells express molecular marker Kv4.2, and subsets of W3D cells express parvalbumin (PV) and Foxp2. We are now in the process of further analyzing their properties and seeking molecular markers to label each subtype of W3D RGCs.

3.2 Introduction

A part list is essential for understanding neural circuits, because different types of neurons receive different inputs, target to different regions, and have distinct functions (Greig et al., 2013; Molyneaux et al., 2007). Thus, it is important to identify neuronal cell types and describe their properties. This is still a daunting task to the whole brain because of its complexity and neuronal diversity. However, efforts have been made to classify different subtypes of neurons in the retina given its simple structure and regular organization.

The retina is made of 5 major types of neurons: Photoreceptors transduce light signals into electrical signals. These electrical signals are further processed by horizontal cells, bipolar cells and amacrine cells, and then passed to retinal ganglion cells (RGCs). RGCs are the sole output neurons of the retina, which integrate visual information from bipolar cells and amacrine cells and then send information to the other parts of the brain (Masland, 2012; Zipursky and Sanes, 2010). Each of these 5 types of retinal neurons can be subdivided into multiple subtypes, and they form specific synaptic connections with each other. As a consequence, different subtypes of RGCs form parallel channels that are sensitive to different features of the visual fields (Gollisch and Meister, 2010). Thus, it is important to classify different subtypes of RGCs in order to understand how visual information is processed and sent to the rest of the brain.

Previously studies characterizing RGCs by their morphologies or physiologies suggest ~20 subtypes of RGCs (Badea and Nathans, 2004; Coombs et al., 2006; Kong et al., 2005; Sun et al., 2002; Volgyi et al., 2009). Until recently, transgenic or Cre knock-in animals in which subsets of RGCs were labeled enabled us to selectively study or manipulate subtypes of RGCs, which supplements previous approaches and indicates >20 subtypes of RGCs (Badea and Nathans, 2011; Kim et al., 2008). Here, we exploited a mouse line called ‘W3’, in which subsets of RGCs are labeled by GFP. W3 RGCs can be separated into two groups based on different levels of GFP expression. One population has higher level of GFP expression, thus are brighter under the fluorescent microscope (W3B). These cells were studied

previously and they are sensitive to local motion (Krishnaswamy et al., 2015; Zhang et al., 2012). The other population has lower level of GFP expression, whose fluorescence is dimmer (W3D).

In this study, we specifically targeted W3D cells for recording followed by dye injection and morphological reconstruction. Our preliminary results showed that W3D RGCs are comprised of at least five subtypes of RGCs. Two of them form On and Off orientation detectors, namely On and Off cells that preferentially respond to stimuli in certain orientations. One of them appears similar to W3B cells in morphology but is not sensitive to local motion. The last two are small field On and Off RGCs that are direction selective. On of them appears to be F-mini^{on} RGCs. We are currently further analyze their characteristics and seek molecular markers to label them. Initial screens showed that nearly all W3D cells express molecular marker Kv4.2, and subsets of W3D cells express parvalbumin (PV) and Foxp2.

3.3 Methods and Results

3.3.1 W3 RGCs include both W3B and W3D cells

W3 mice were generated in which GFP expression is driven by the regulatory elements of Thy1 gene (Kim et al., 2010). In the retina, only a small proportion of the RGCs were labeled by GFP, possibly due to the effect of the regulatory element near the transgene insertion site (Feng et al., 2000). Density recovery profile analysis showed that the whole population of W3 RGCs doesn't form a single mosaic, indicating mixed populations of RGCs (**Figure 5.1 A, C)**. In fact, two populations of W3 RGCs can be distinguished from each other based on their different levels of GFP expression: One population is brightly labeled and called W3 bright (W3B) RGCs. W3B RGCs form a regular mosaic in the retina with the exclusive radius of ~30 um and density of ~250 cells/um^2 (**Figure 5.1 A, D)**. These cells were reported previously as local motion detectors (Zhang et al., 2012). The other population has lower level of GFP expression, thus dimly labeled. However, these W3 dim (W3D) RGCs cover the retina with density of 350 cells/um^2 and don't form a regular mosaic (**Figure 5.1 A, E)**. This indicates that W3D cells are comprised of multiple subtypes of RGCs.

Vertical sections of W3 retinas showed that W3 RGCs including W3B and W3D cells stratified heavily between the two choline acetyl transferase (ChAT) bands in inner plexiform layer (IPL) (**Figure 5.1 B**, sublamina 3), and sprout sparsely beyond the outer ChAT-positive band (**Figure 5.1 B**, sublamina 1), where they form specific synapses with amacrine cells and bipolar cells, suggesting that W3 RGCs are likely to include both On or On-Off and Off cells.

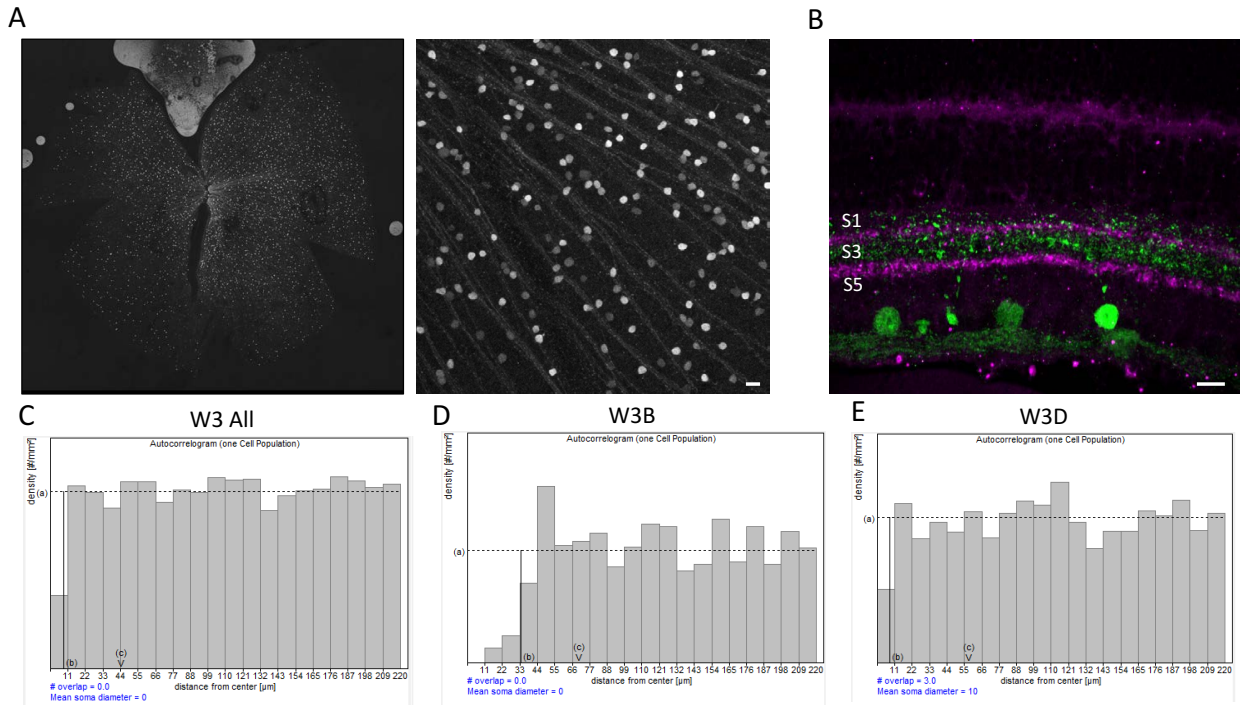

Figure 5.1 W3 RGCs include W3B and W3D RGCs

A. Whole mount of the W3 retina, in which W3B and W3D cells can be easily separated by their fluorescent intensity. Scale bar: 10um.

B. Vertical sections of W3 retina. Purple: ChAT-positive bands. Green: GFP. Scale bar: 20um.

C. Density recovery analysis of All the W3 cells.

D. Density recovery analysis of W3B cells

E. Density recovery analysis of W3D cells

3.3.2 Physiological analysis of W3D RGCs

In order to characterize W3D RGCs, we guided patch electrodes to target W3D RGCs recognized by their fluorescence under a brief flash of blue LED, and recorded from them while showing a variety of stimuli. We first presented a bright spot flashing On and Off on a black background. The spot was centered to the cell body of the recorded cell, and we could tell whether the cell was On cell, Off cell or On-Off cells based on their responses to the light onset and offset. We next presented the same small spot to the center of the cell body, but with the spot radius increasing gradually. We measured and plotted the firing rates of the recorded cell to the onset and offset of the spot. When the spot radius increased, the responses increased first and then decreased. The size (optimal radius) of the spot that could induce the maximal firing rate was used to define the receptive field center of the recorded cell. Finally, we presented light bars moving in eight directions through the receptive field center of the recorded cells. This stimulus was used to tell whether the recorded cells respond strongly to certain directions or not.

Using the set of the stimuli described as above, we found five different subtypes of W3D RGCs. The first two responded transiently when the light was on and off, respectively, thus were On-transient and Off-transient cells (**Figure 5.2 A,A',D,D')**. Both of them had medium sized receptive field centers, with optimal radius around 100um (**Figure 5.2 B, E)**. Interestingly, both these two subtypes of W3D RGCs responded strongly to motions in two opposite directions but not to motions orthogonal to those two directions, thus had preference to a certain orientation (**Figure 5.2 C, F)**. We called these two subtypes of W3D RGCs On- and Off- orientation selective RGCs. The next subtype we found had transient responses when light was Off (**Figure 5.2 G, G')**. The receptive field center of this subtype was smaller than On- and Off- orientation selective RGCs, with optimal radius less than 100um (**Figure 5.2 H)**, and this subtype of RGCs appeared not to be direction selective (**Figure 5.2 I).** The last two subtypes of W3D RGCs were transient On- and Off- RGCs (**Figure 5.2 J,J',M,M')**. These two subtypes of RGCs had strikingly small receptive field centers, with optimal radius around 60um (**Figure 5.2 K, N**). These two subtypes of W3D RGCs responded strongly to moving bars in certain directions, thus were direction selective RGCs (**Figure 5.2 L, O)**.

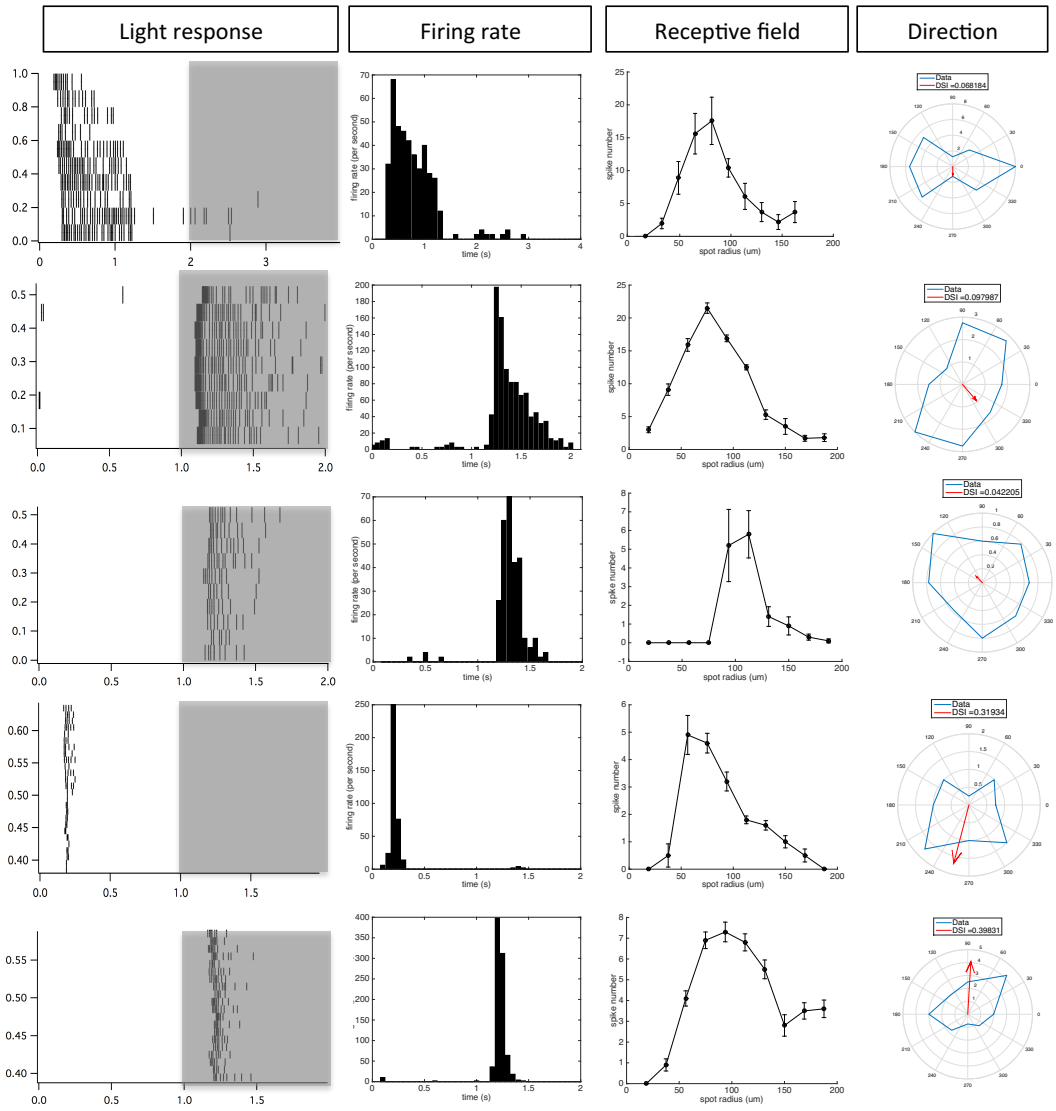

Figure 5.2 Physiological properties of W3D RGCs

A, D, G, J, M. Visual responses of 5 subtypes of W3D RGCs to On- and Off- flashing spots.

A', D', G', J', M'. Histograms of firing rates to flashing spot stimuli.

B, E, H, K, N. Visual responses of 5 subtypes of W3D RGCs to flashing spots of increasing radii.

C, F, I, L, O. Visual responses of 5 subtypes of W3D RGCs to moving bars across the receptive field center in different directions.

3.3.3 Morphological analysis of W3D RGCs

We dye-filled cells after recording to reconstruct their morphologies. These five subtypes of W3D RGCs appeared to have different morphologies. The On- and Off- orientation selective RGCs extended their dendrites to lower and higher sublamina 3 respectively, consistent with their physiological responses. Both On- and Off- orientation selective RGCs had medium-sized dendritic fields, whose radii were about 100um (**Figure 5.3 A, B)**. The third Off-transient W3D RGCs appeared similar to W3B RGCs, as described previously (Zhang et al., 2012). They had dendrites extended to sublamina 3, and dendritic radii of these cells were less than 100um (**Figure 5.3 C)**. Dendrites of the last two subtypes of W3D RGCs, the On- and Off- direction selective RGCs, were extremely small. The dendritic radii were about 50um. The On cells laminated at sublamina 3, while the Off cells also extended their dendrites to sublamina 1, consistent with their physiological responses (**Figure 5.3 D, E)**. The On- direction selective cells appeared to be F-mini^{on} RGCs as we described previously in Chapter 4.

Morphological similarity of the third subtype of W3D RGCs to W3B RGCs made us wonder whether they are local-motion sensitive. We thus performed local motion stimuli to these RGCs and recorded their responses (**Figure 5.4 A)**. These cells showed consistent Off responses to flashing spots, but rarely responded during local motion stimuli (**Figure 5.4 B**, **C**), indicating that they were not local motion detector as W3B RGCs. Thus, we called these cells W3B like (W3BL) cells, just because of their morphological similarity to W3B cells.

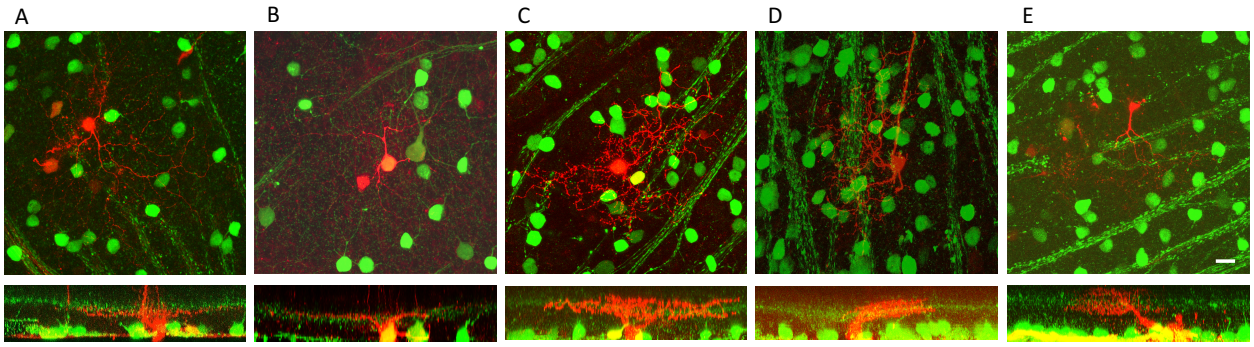

Figure 5.3 Morphological properties of W3D RGCs

Whole mount views and vertical reconstructions of the five subtypes of W3D RGCs: On- (A) and Off- (B) orientation selective RGCs; One subtype that looks similar to W3B RGCs (C); On- (D) and Off- (E) direction selective RGCs with small asymmetric dendrites, which appeared to be On- and Off- F-mini RGCs. Scale bar: 20um.

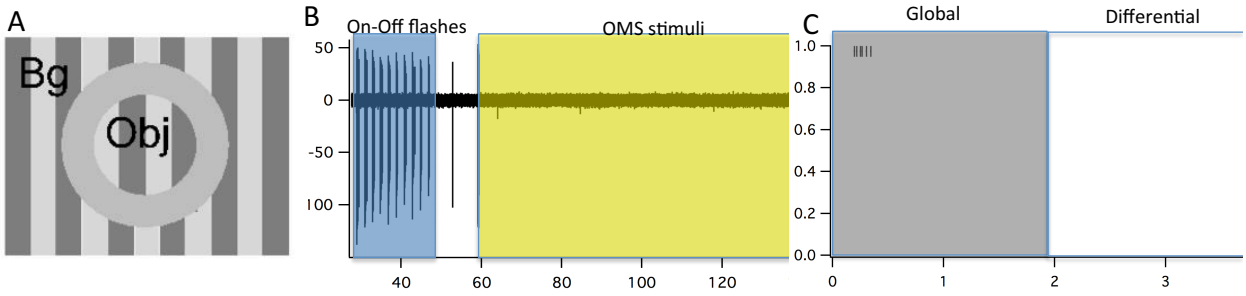

Figure 5.4 W3BL RGCs are not local motion sensitive

A. Local motion stimulus used in this study. For global motion, object images (Obj) moves in the same way as the background images (Bg). For differential motion, Obj moves while Bg doesn't move.

B. W3BL cells respond well to On- and Off- flashes but not to local motion stimulus.

C. Spikes plotted from B. Global and Differential motion were indicated in gray and white period.

3.3.4 Summary of W3 RGCs

Characterization based on morphological and physiological properties of W3D RGCs revealed at least five different subtypes of RGCs. Taking account of W3B RGCs, W3 RGC population includes at least six subtypes of RGCs. W3B RGCs take up 40% of the W3 RGCs. They have distinct properties from others: they are small-sized RGCs responding to light onset and offset, and they are sensitive to local motion. W3D RGCs take up the other 60%, and they include five subtypes of RGCs as described above, although the frequency of each subtype is different: W3BL appeared to be the most among W3D RGCs, and 22.5% of W3 RGCs are W3BL. Each of On- and Off- orientation selective RGCs, and F-mini^{on} RGCs takes up 11.25% of W3 RGCs. The Off direction selective RGCs with small dendritic fields appear to be the least frequent, and they occupy 2.5% of W3 RGCs. Given the small frequency of this subtype, we will not further explore their characteristics. All the W3 RGCs are summarized in **Table 5.1**.

	Percentage	Light responses	DS	OS	Susteined/ Transient	OMS	Receptive field size
W3B	40%	On-Off	-	-	T	+	Small
W3BL	22.5%	Off	-	-	T	-	Small
On-OS	11.25%	On	-	+	T	-	Medium
Off-OS	11.25%	Off	-	+	T	-	Medium
F-mini^{On}	11.25%	On	+	-	T	-	Small
Off-mini	3.75%	Off	+	-	T	-	Small

Table 5.1 Summary of W3 RGCs and their properties

3.3.5 Initial screen for molecular markers

We next seek molecular markers that could label W3D RGCs or subtypes of W3D RGCs. We first examined Kv4.2, a potassium channel modulator, because Kv4.2 was previously reported to be expressed in RGCs laminating in sublamina 3 and sublamina 1(Qu et al., 2009). We stained the W3D retina with antibody against Kv4.2 and found nearly all the W3D RGCs were Kv4.2 positive, while nearly none of W3B cells expressed Kv4.2, indicating that Kv4.2 is a molecular marker for all the W3D RGCs (**Figure 5.5)**. Second, we examined PV, a calcium buffer protein which was reported to be expressed by subsets of RGCs, because On-, Off- orientation selective W3D RGCs and W3BL RGCs appeared similar to PV-positive subtype 2, 4 and 3 RGCs (Farrow et al., 2013). We found ~65% of W3D RGCs were PV-positive, while none of W3B RGCs were PV-positive (**Figure 5.6)**. At last, given F-mini^{on} cells were among W3D RGCs, we stained the W3 retina with antibody against Foxp2, a transcription factor expressed in F-mini^{on} cells, and found ~35% of W3D RGCs were Foxp2 positive (**Figure 5.7 A, B)**. These cells formed a regular mosaic, indicating that they were likely from the single subtype of F-mini^{on} cells (**Figure 5.7 C).**

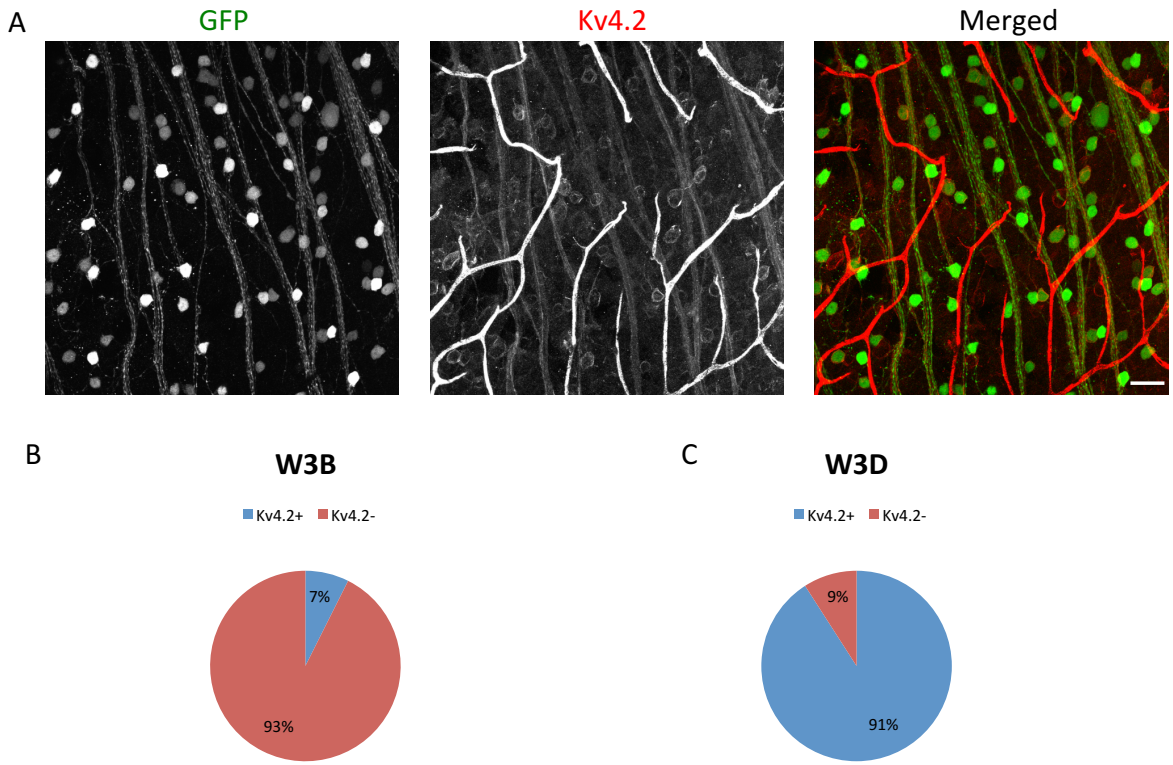

Figure 5.5 W3D RGCs are Kv4.2 positive

A. W3 retina stained with antibodies against GFP and Kv4.2

B. Percentage of W3B RGCs that are Kv4.2 positive

C. Percentage of W3D RGCs that are Kv4.2 positive

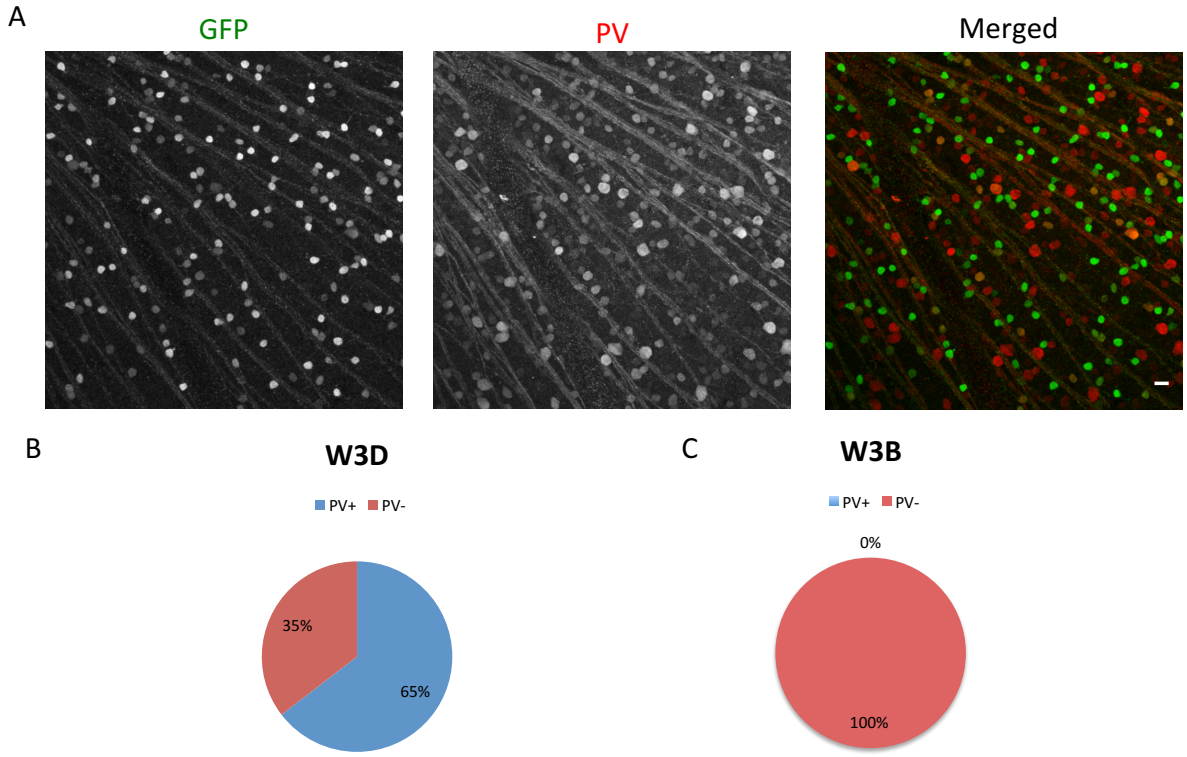

Figure 5.6 Subsets of W3D RGCs are PV positive

A. W3 retina stained with antibodies against GFP and PV

B. Percentage of W3B RGCs that are PV positive

C. Percentage of W3D RGCs that are PV positive

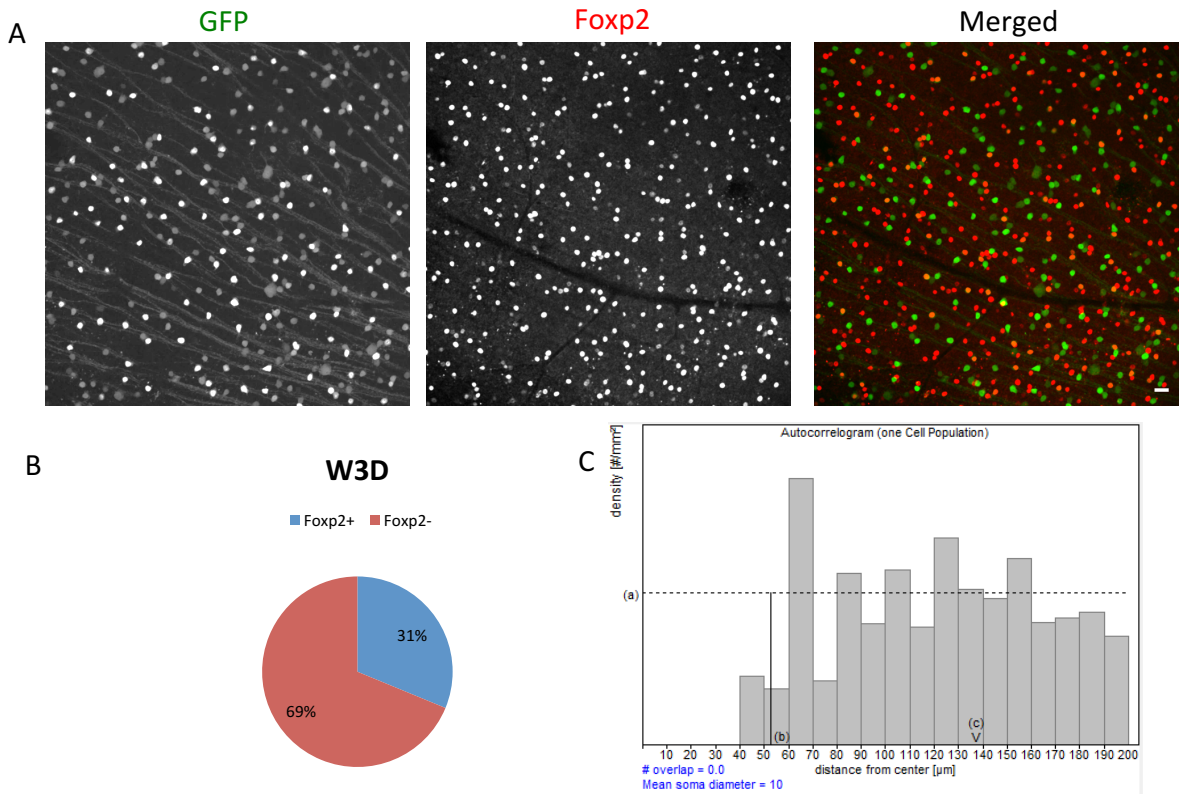

Figure 5.7 Subsets of W3D RGCs are Foxp2 positive

A. W3 retina stained with antibodies against GFP and Foxp2

B. Percentage of W3B RGCs that are Foxp2 positive

C. Percentage of W3D RGCs that are Foxp2 positive

3.4 Discussion

In this chapter, I presented my initial efforts to classify W3D RGCs. Using cell-attached recordings followed by dye injection, I provided evidence for five subtypes of RGCs in W3D cells. Further characterization of these cells is ongoing, and we are also looking for specific molecular markers to these W3D subtypes.

3.4.1 Multiple RGC subtypes labeled in W3D RGCs

The recent effort of using transgenic or Cre knock-in animals to label RGCs enabled us to classify subtypes from a group of RGCs. For example, Opn4-CreER allowed Berson, Hattar and others to find 5 subtypes of intrinsic photosensitive RGCs (ipRGCs), which express photo-pigment melanopsin (Ecker et al., 2010). In previous chapters, I also reported work using Kcng4-Cre line to find 4 subtypes of alpha RGCs, and using Foxp2-Cre line to find 4 subtypes of F-RGCs.

Here I described work in classifying W3D RGCs, which are dimly labeled by GFP in W3 lines. We found five different subtypes of RGCs. These five different subtypes of RGCs have distinct physiological properties and different dendritic field shapes. Thus, it would be very helpful to find molecular markers for each subtype so that we could study them specifically. Jeremy Kay, a former postdoc fellow from our lab profiled gene expression in W3 RGCs using microarray assay after fluorescence-activated cell sorting (FACS) (Kay et al., 2012). However, this method required starting materials from many cells, thus many W3 RGCs were pooled together and the result reflected gene express level at the population level, from which we could not resolve molecules expressed in subtypes of RGCs within the population.

The emerging technique of single cell RNA-sequencing to profile gene expressions at single cell level provides us a way to potentially solve this problem. By detecting gene expression of each W3 cell, and then grouping cells in clusters by their expression profiles, we could specifically test whether cells within one cluster correspond to one subtype of W3 RGCs.

3.4.2 W3 RGCs all laminate at sublamina 3

One striking feature of W3 RGCs including both W3B RGCs and W3D RGCs was that all these cells have dendritic laminations at sublamina 3. This is particularly interesting given that there are at least five different subtypes of W3D RGCs plus one subtype of W3B RGCs. Although all of these cells are marked by GFP expression from the transgene in W3, they are largely different in their physiological properties and dendritic shapes. Thus, one may wonder why they share the same lamination.

One possible answer to this question is that there could be some cell surface molecules expressed by all the W3 RGCs, which guide and anchor the dendrites to sublamina 3 by interacting with other molecules there. But how to find these guidance molecules?

One way depends on gene profiling. These molecules must be expressed by W3 RGCs but not expressed by subtypes of RGCs that don't laminate at sublamina 3. Thus, if we can get gene profile of W3 RGCs by microarray or RNA-sequencing, and compared it with gene profiles of other RGC subtypes, we may able to find candidates of the guidance molecules.

The other intriguing thought comes from the shared expression of GFP by W3 RGCs. The transgene containing GFP at the downstream of the regulatory elements of Thy1 gene was inserted randomly in the mouse genome (Kim et al., 2010). A series of transgenic animals were generated, with different GFP expression patterns, possibly due to the effect of the regulatory element near the transgene insertion site. W3 animals were selected because of its constrained GFP expression in a small subset of RGCs. Thus, the shared expression of GFP in W3 RGCs possibly indicates that W3 RGCs are all affected by the shared regulatory element near the transgene. We guess that the expression of the guidance molecules may also be affected by this shared regulatory element. If we know where the insertion site is, we can know what regulatory elements are near the transgene and further pursue what genes are also regulated by this regulatory element, among which we can possibly find the guidance molecules we are interested in.

3.4.3 Orientation selective RGCs in W3D retina

Computation of orientation is an interesting topic. So far, most studies of orientation selectivity were reported in higher visual regions, such as lateral geniculate nucleus, superior colliculus and visual cortex (Feinberg and Meister, 2015; Hubel and Wiesel, 1959; Scholl et al., 2013), or in the retina of other mammals (Amthor et al., 1989; Bloomfield, 1994; Levick, 1967). In these species, On- and Off- centered orientation selective RGCs were reported to respond to light or dark bars with certain orientations. However, it was still not clear whether in mouse retina, there are orientation selective RGCs.

Here, the initial results from W3D RGCs revealed orientation selective RGCs in mouse retina. Two subtypes were found in W3D RGCs, On-centered and Off-centered, consistent with what was found in other species. Morphological properties of orientation selective W3D RGCs appeared similar to those reported in other species, including dendritic laminations. Thus, it is possible that these cells found in W3D RGCs are the corresponding orientation selective RGCs in mouse retina. However, it is noteworthy that the stimulus used in my study to detect orientation selectivity was different from those used previously. I used light bars moving in different directions and identified cells responding to motion in one axis but not the axis vertical to it. I called these cells orientation selective RGCs. In previous studies, people identified orientation selective cells by showing light or dark bars to the center of the cells with different orientations, and compared their responses (Amthor et al., 1989; Bloomfield, 1994; Levick, 1967). Thus, in order to compare orientation selective W3D RGCs with those reported in other species, it is worth applying stimuli of bars with different orientations to W3D RGCs and examining the responses of these cells.

5.5 References:

Amthor, F.R., Takahashi, E.S., and Oyster, C.W. (1989). Morphologies of rabbit retinal ganglion cells with concentric receptive fields. J Comp Neurol *280*, 72-96.

Badea, T.C., and Nathans, J. (2004). Quantitative analysis of neuronal morphologies in the mouse retina visualized by using a genetically directed reporter. J Comp Neurol *480*, 331-351.

Badea, T.C., and Nathans, J. (2011). Morphologies of mouse retinal ganglion cells expressing transcription factors Brn3a, Brn3b, and Brn3c: analysis of wild type and mutant cells using genetically-directed sparse labeling. Vision Res *51*, 269-279.

Bloomfield, S.A. (1994). Orientation-sensitive amacrine and ganglion cells in the rabbit retina. J Neurophysiol *71*, 1672-1691.

Coombs, J., van der List, D., Wang, G.Y., and Chalupa, L.M. (2006). Morphological properties of mouse retinal ganglion cells. Neuroscience *140*, 123-136.

Ecker, J.L., Dumitrescu, O.N., Wong, K.Y., Alam, N.M., Chen, S.K., LeGates, T., Renna, J.M., Prusky, G.T., Berson, D.M., and Hattar, S. (2010). Melanopsin-expressing retinal ganglion-cell photoreceptors: cellular diversity and role in pattern vision. Neuron *67*, 49-60.

Farrow, K., Teixeira, M., Szikra, T., Viney, T.J., Balint, K., Yonehara, K., and Roska, B. (2013). Ambient illumination toggles a neuronal circuit switch in the retina and visual perception at cone threshold. Neuron *78*, 325-338.

Feinberg, E.H., and Meister, M. (2015). Orientation columns in the mouse superior colliculus. Nature *519*, 229-232.

Feng, G., Mellor, R.H., Bernstein, M., Keller-Peck, C., Nguyen, Q.T., Wallace, M., Nerbonne, J.M., Lichtman, J.W., and Sanes, J.R. (2000). Imaging neuronal subsets in transgenic mice expressing multiple spectral variants of GFP. Neuron *28*, 41-51.

Gollisch, T., and Meister, M. (2010). Eye smarter than scientists believed: neural computations in circuits of the retina. Neuron *65*, 150-164.

Greig, L.C., Woodworth, M.B., Galazo, M.J., Padmanabhan, H., and Macklis, J.D. (2013). Molecular logic of neocortical projection neuron specification, development and diversity. Nat Rev Neurosci *14*, 755-769.

Hubel, D.H., and Wiesel, T.N. (1959). Receptive fields of single neurones in the cat's striate cortex. J Physiol *148*, 574-591.

Kay, J.N., Chu, M.W., and Sanes, J.R. (2012). MEGF10 and MEGF11 mediate homotypic interactions required for mosaic spacing of retinal neurons. Nature *483*, 465-469.

Kim, I.J., Zhang, Y., Meister, M., and Sanes, J.R. (2010). Laminar restriction of retinal ganglion cell dendrites and axons: subtype-specific developmental patterns revealed with transgenic markers. J Neurosci *30*, 1452-1462.

Kim, I.J., Zhang, Y., Yamagata, M., Meister, M., and Sanes, J.R. (2008). Molecular identification of a retinal cell type that responds to upward motion. Nature *452*, 478-482.

Kong, J.H., Fish, D.R., Rockhill, R.L., and Masland, R.H. (2005). Diversity of ganglion cells in the mouse retina: unsupervised morphological classification and its limits. J Comp Neurol *489*, 293-310.

Krishnaswamy, A., Yamagata, M., Duan, X., Hong, Y.K., and Sanes, J.R. (2015). Sidekick 2 directs formation of a retinal circuit that detects differential motion. Nature.

Levick, W.R. (1967). Receptive fields and trigger features of ganglion cells in the visual streak of the rabbits retina. J Physiol *188*, 285-307.

Masland, R.H. (2012). The tasks of amacrine cells. Visual Neuroscience *29*, 3-9.

Molyneaux, B.J., Arlotta, P., Menezes, J.R., and Macklis, J.D. (2007). Neuronal subtype specification in the cerebral cortex. Nat Rev Neurosci *8*, 427-437.

Qu, J., Mulo, I., and Myhr, K.L. (2009). The development of Kv4.2 expression in the retina. Neurosci Lett *464*, 209-213.

Scholl, B., Tan, A.Y., Corey, J., and Priebe, N.J. (2013). Emergence of orientation selectivity in the Mammalian visual pathway. J Neurosci *33*, 10616-10624.

Sun, W., Li, N., and He, S. (2002). Large-scale morphological survey of mouse retinal ganglion cells. J Comp Neurol *451*, 115-126.

Volgyi, B., Chheda, S., and Bloomfield, S.A. (2009). Tracer coupling patterns of the ganglion cell subtypes in the mouse retina. J Comp Neurol *512*, 664-687.

Zhang, Y., Kim, I.J., Sanes, J.R., and Meister, M. (2012). The most numerous ganglion cell type of the mouse retina is a selective feature detector. Proceedings of the National Academy of Sciences of the United States of America *109*, E2391-2398.

Zipursky, S.L., and Sanes, J.R. (2010). Chemoaffinity revisited: dscams, protocadherins, and neural circuit assembly. Cell *143*, 343-353.

Chapter 6: Genetic method for labeling electrically coupled cells: application to retina

Preface:

The work presented in this chapter was done in collaboration with no one. I have performed all experiments and data analysis. This work leads to a manuscript currently under review and was supervised by Josh Sanes.

6.1 Abstract

Understanding how the nervous system functions requires mapping synaptic connections between neurons. Several methods are available for imaging neurons connected by chemical synapses, but few enable marking neurons connected by electrical synapses. Here, we demonstrate that a peptide transporter, Pept2, can be used for this purpose. Pept2 transports a gap junction-permeable fluorophore-coupled dipeptide, beta-alanine-lysine-N-7-amino-4-methyl coumarin-3-acid (βALA). Cre-dependent expression of *pept2* in specific neurons followed by incubation in βALA labeled electrically-coupled synaptic partners. Using this method, we analyze light-dependent modulation of electrical connectivity among retinal horizontal cells.

6.2 Introduction

Because neurons communicate with each other primarily through synapses, mapping patterns of synaptic connectivity is an essential step in understanding how neural circuits function. Synapses are of two types: chemical, in which neurotransmitter released by the presynaptic cell signals to its postsynaptic partner, and electrical, in which currents pass directly from cell to cell through gap junctions (Siegelbaum and Kandel, 2013). To date, chemical synapses have received the vast majority of attention(Sanes and Yamagata, 2009;Yogev and Shen, 2014). In contrast, patterns of electrical connectivity have been studied in relatively few cases (White et al., 1986;Volgyi et al., 2009;Varshney et al., 2011). In part, this inattention stemmed from the belief that electrical synapses were relatively rare in vertebrates. Over the past decade, however, it has become apparent that they are in fact numerous and play diverse roles in developing and adult animals (Connors and Long, 2004;Hormuzdi et al., 2004;Bloomfield and Volgyi, 2009;Cook and Becker, 2009;Li et al., 2012;Yu et al., 2012;Apostolides and Trussell, 2013;Zhu et al., 2013). It is therefore essential to redress the balance.

One obstacle to the study of electrical synaptic connections –perhaps both a cause and an effect of the scant attention they have been paid- is that few methods are available for mapping them in the intact nervous system. Electrical connectivity is most often assessed by impaling a neuron with a microelectrode for injection of a dye that diffuses through gap junctions (Vaney, 1991;Mills and Massey, 1994;Hoshi et al., 2006). This approaches is laborious, and difficult to apply to cells that are small, fragile or deeply buried in tissue. An alternative, intracellular recording of potentials evoked by stimulating a neighboring cell, is even more difficult because it faces the added obstacle of requiring paired recordings. Light microscopic immunohistochemical localization of individual electrical synapses is infeasible, both because gap junctions are often near the limit of optical resolution and because no single component is known that marks all and only electrical synapses. Electron microscopy provides sufficient resolution, but is hampered by the need to connect synapses to cells of origin through reconstruction from serial sections, which is laborious and currently applicably only to small volumes.

Recently, mapping of chemical synaptic connectivity has been aided by a variety of genetic methods for labeling synaptically connected neuronal pairs (Wickersham et al., 2007;Feinberg et al., 2008;Beier et al., 2011;Lo and Anderson, 2011). Parallel methods for mapping electrical synaptic connectivity could provide similar benefits. Recently, one such method was introduced, in which an esterase is targeted to specific cells; it acts on a membrane-permeable substrate to generate a fluorophore that can pass through gap junctions (Tian et al., 2012). Here, we report an alternative method, in which we use cre recombinase-dependent vectors to target a peptide transporter to the membrane of cre-expressing cells in vivo. We then incubated the tissue with a membrane-impermeable fluorophore-conjugated dipeptide that can, once inside the cell, pass through gap junctions from the transporter-expressing cell to electrically connected neighbors (**Figure 6.1**).

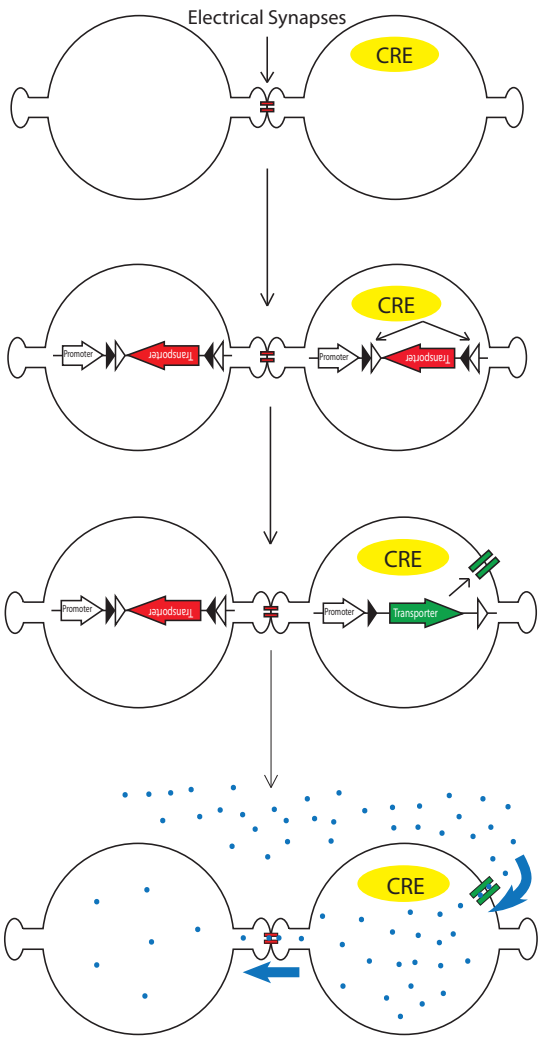

Figure 6.1 Schematic illustration of genetic method for labeling electrically coupled cells from Cre-positive cells.

A channel or transporter is expressed in Cre-positive cells, allowing them to take up gap junction permeable fluorescent substrates. The substrates diffuse through gap junctions to label coupled cells.

6.3 Results

6.3.1 Pept2 mediates labeling of electrically-coupled cells

We used a human embryonic kidney cell line, HEK293, to test transporters and channels that would facilitate entry of membrane-impermeable but gap junction-permeable fluorescent molecules into cells. HEK cells have been reported to express connexin 43 and to form numerous gap junctions when grown as a confluent monolayer (Gemel et al., 2004;Johnson et al., 2013;Patel et al., 2014); we confirmed expression of connexin 43 immunohistochemically (**Figure 6.2 A**) and we confirmed strong coupling by microinjection of neurobiotin, which is widely used to monitor coupling in tissue (**Figure 6.2 B**).

We tested five protein/substrate pairs. Three were channels, TRPV1, TRPA1 and P2X7. All three are non-selective cation channels that are permeable to fluorescent molecules such as, Yo-pro-1 (TRPV1 and TRPA1) and ethidium (P2X7) (Meyers et al., 2003;Chen et al., 2009;Browne et al., 2013). We also tested the fluorescent dye Po-pro-1, which is closely related to Yo-pro-1. The other two proteins were related drug and peptide transporters, Pept1 and Pept2, both of which translocate the AMCA-labeled dipeptides beta-Ala-Lys (βALA) and D-Ala-Lys (Dieck et al., 1999;Groneberg et al., 2001). Ethidium and Po-pro-1 are known to cross gap junctions (Hoshi et al., 2006;Kanaporis et al., 2011) and we used microinjection to show that the same is true for βALA (**Figure 6.2 C**).

In each case, we introduced the channel or transporter plus a fluorescent protein (XFP) by transfection into HEK293 cells, grew them for 1-2 days, then replated them with a 100 fold excess of unlabeled cells. The XFP was chosen to be distinguishable from the fluorophore to be tested. Once the cells reached confluency, we incubated them with the fluorophore. We activated TRPV1, TRPA1 and P2X7 by co-incubation with their ligands, capsaicin, allyl isothiocyanate (AITC) and ATP, respectively. We assessed uptake and transfer by observing substrate in XFP-labeled cells and neighboring XFP-negative cells, respectively (**Figure 6.2 D**).

Signals in cells expressing TRPV1, TRPA1 and P2X7 channels were very dim and fluorophore was rarely detected in neighboring untransfected cells. In contrast, both Pept1 and Pept2 supported robust uptake of βALA, which was then transferred to neighboring cells. Of the two, Pept2 was superior, perhaps reflecting its high affinity (Daniel and Rubio-Aliaga, 2003;Zhang et al., 2004;Biegel et al., 2006) (**Figure 6.2 E**). Uptake was specific in that it was negligible in untransfected cells and was completely blocked by incubation with a 200-fold excess of the competitive inhibitor, Glycine-Glutamine (Gly-Gln) (**Figure 6.2 F**). We therefore used Pept2 for all subsequent studies reported here.

We generated two vectors to express both Pept2 and GFP from a single transcript. In one, *Pept2-GFP*, we fused GFP directly to the C-terminal of Pept2. In the other, *Pept2-p2a-GFP*, the two proteins were separated by the self-cleaving p2a sequence. When tested in HEK 293 cells as above, both constructs worked as efficiently as Pept2 alone. In both cases, uptake was inhibited by Gly-Gln and transfer from GFP-expressing to GFP-negative cells was inhibited by carbenoxolone (CBX) and meclofenamic acid (MFA), two widely used gap junction blockers. (**Figure 6.3 A, B**).

Figure 6.2 Pept2 method enables labeling gap junction-coupled cells.

A. **Cultured HEK cells stained with antibody against connexin 43 (Cx 43). Dapi shows cell nucleus and Neurotrace stains cytoplasm. Connexin 43 is enriched at the cell membrane between neighboring cells.**
B. **HEK cells injected with neurobiotin and stained with Texas red-streptavidin. Red arrow indicates the injected cell.**
C. **HEK cells injected with βALA. Red arrow indicates the injected cell.**
D. **Schematic illustration of the method for testing channels or transporters capable of importing small fluorescent substrate that can permeate gap junctions.**
E. **HEK cells were transfected with GFP and Pept2, then mixed with untransfected cells and incubated with βALA. βALA diffused from GFP positive cells to adjacent coupled cells.**
F. **HEK cells were transfected with GFP, GFP+Pept2 or Pept2-GFP. Uptake of βALA was eliminated by Pept2 inhibitor Gly-Gln.**

Scale bars in A-C, E, F: 20μm.

Figure 6.2 Pept2 method enables labeling gap junction-coupled cells. (continued)

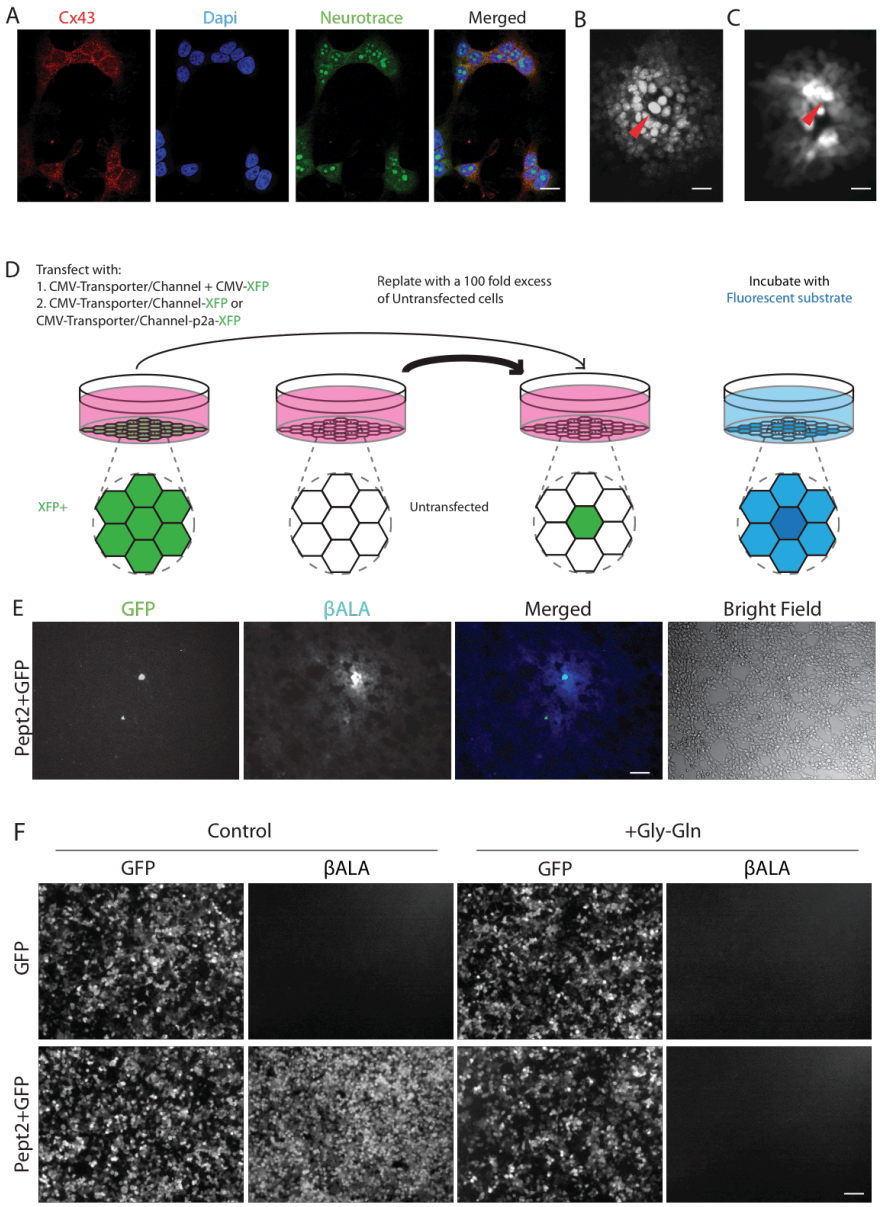

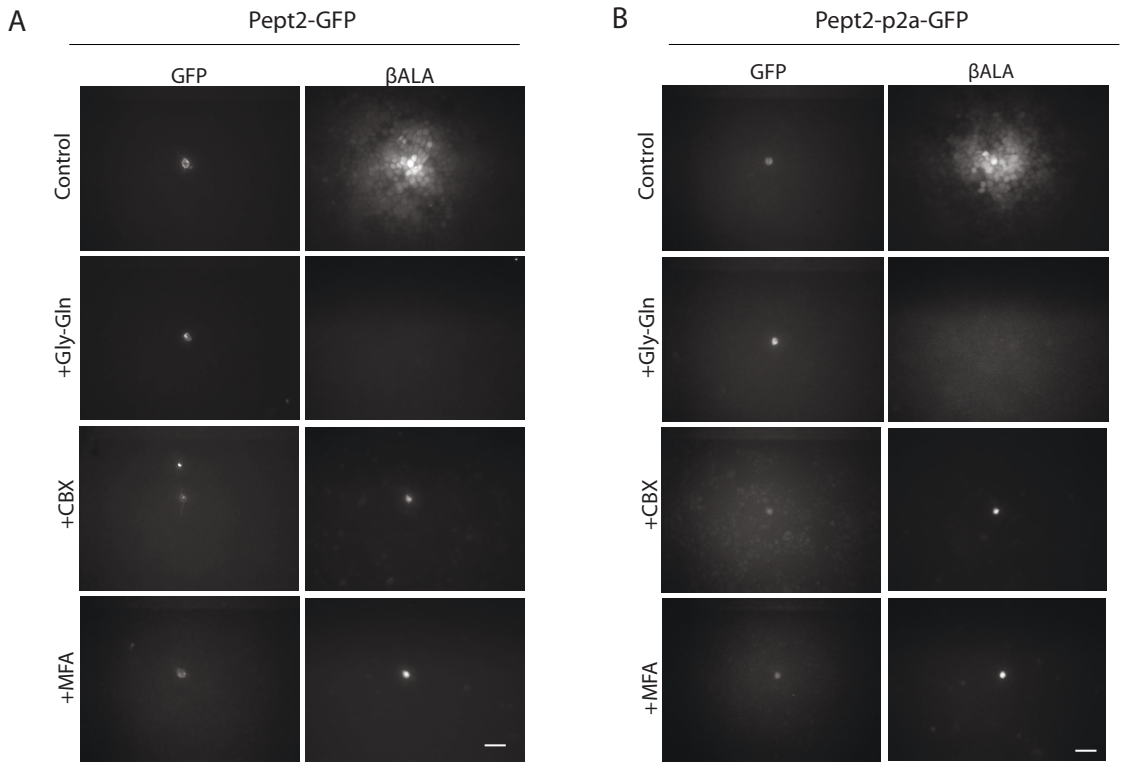

Figure 6.3 Both Pept2-GFP and Pept2-p2a-GFP mediate βALA uptake.

HEK cells were transfected with Pept2-GFP (A) or Pept2-p2a-GFP (B). Uptake of βALA was blocked by Pept2 inhibitor Gly-Gln. Diffusion of βALA to coupled cells was blocked by gap junction blockers MFA and CBX. Scale bar: 20μm.

6.3.2 Quantitative measurement of gap junction strength

To quantify the strength of gap junctional coupling, we developed an analysis based on the equation that describes the diffusion of βALA from the probe cell to the coupled cells (see Methods and Materials). We assume that the fluorescent intensity of βALA is proportional to the concentration of βALA. Therefore, at steady state, when the concentration of βALA in each cell no longer changes with time, the fluorescent signal of βALA from the probe cell to coupled cells follows an exponential decay (**Figure 6.4 A**). We measured the intensity of label in probe and coupled cells following a 4 hour incubation. The labeling pattern was well described by the diffusion equation (**Figure 6.4 B**). Thus, even though βALA levels may not have reached the steady state following this period of incubation, our method provides a reasonable approximation of coupling.

To test the ability of this method to detect changes in coupling, we varied the concentration of the gap junction blockers, MFA and CBX. In both cases, the fluorescent intensity of βALA from the probe cell to coupled cells was well fitted by an exponential, with increasing concentrations of inhibitor leading to decreased diffusion and thus faster decay (**Figure 6.4 C, D, E, F**). From each curve we estimated the decay constant and used it to derive coupling strength S, which reflects how strongly two adjacent cells are coupled by gap junctions (**Figure 6.4 G, H**). Coupling was nearly abolished by 10μM CBX and 40μM MFA.

Figure 6.4 Pept2 method enables quantification of gap junction strength between cultured cells.

A. Schematic illustration and measurement of the βALA signals for quantification of gap junction strength.

B. βALA signals from the probe cell to coupled cells follow an exponential decay.

C. Inhibition of βALA diffusion between gap junction-coupled cells by MFA at indicated concentrations. Scale bar: 50μm.

D. Decay curves fitted from results in D.

E. Coupling strength S calculated based on curves in D. *, $p < 0.05$; **, $p < 0.01$, n = 5 probe cells for each condition.

F. Inhibition of βALA diffusion between gap junction-coupled cells by CBX at indicated concentrations. Scale bar: 50μm

G. Decay curves fitted from results in F.

H. Coupling strength S calculated based on G. *, $p < 0.05$; **, $p < 0.01$, n = 5 probe cells for each condition.

Figure 6.4 Pept2 method enables quantification of gap junction strength between cultured cells.

(continued)

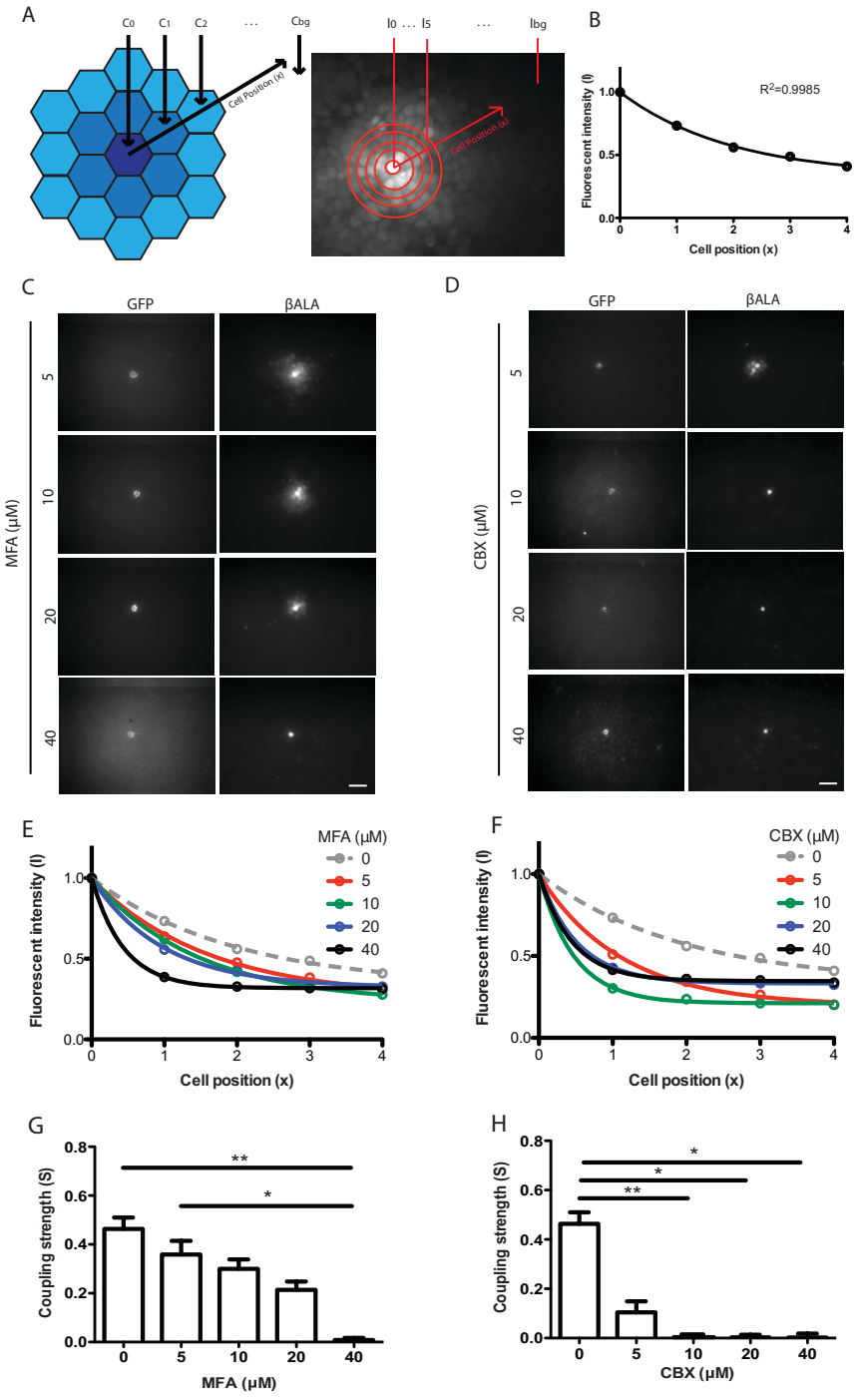

6.3.3 Pept2-mediated labeling of electrically-coupled retinal neurons

We chose mouse retina for tests in vivo, because it can be incubated with substrate as a thin, flat explant and because specific patterns of electrical coupling among its neurons have been mapped in detail (Bloomfield and Volgyi, 2009;Volgyi et al., 2009). Initial tests revealed, however, that βALA labeled a population of cells in wild-type retina, leading to signals that obscured some of the coupling we hoped to detect. Immunolabeling revealed that the labeled cells were predominantly Muller glia (glutamine synthetase and Sox9-positive; **Figure 6.5 A**), and uptake was abolished by co-incubation with Gly-Gln (**Figure 6.5 B**). These results suggested that Muller glia express *pept2*, which has been reported to be expressed by some glial populations in brain (Berger and Hediger, 1999;Dieck et al., 1999;Zimmermann and Stan, 2010). We therefore obtained targeted Pept2 null mutants (*pept2*$^{-/-}$), which are viable and fertile (Shen et al., 2003). Uptake of βALA into Muller glia was abolished in retinas from *pept2*$^{-/-}$ mice (Supplementary figure 1C). No reported neural phenotypes have been reported for *pept2*$^{-/-}$ (Shen et al., 2003) and we detected no changes in numbers, positions or arbors of any retinal cell types examined (**Figure 6.6**). We therefore used *pept2*$^{-/-}$ mice for studies in vivo.

To express Pept2 in cre-expressing neurons, we generated the adeno-associated virus (AAV) serotype 2, AAV-DiO-Pept2-GFP in which a double-floxed inverted open-reading-frame (DiO) sequence renders expression of a Pept2-GFP fusion cre-dependent (**Figure 6.7 A**). To ensure that labeling was sparse, we used mouse line in which one retinal ganglion cell (RGC) type, J-RGCs, express Cre fused with estrogen receptor (CreER; (Kim et al., 2008)). In this line, recombinase activity is induced by tamoxifen in a dosage-dependent fashion. We infected mouse retina with high-titer AAV-DiO-Pept2-GFP and administered a low dose of tamoxifen 10 days later so that Pept2 would be expressed in small numbers of J-RGCs.

GFP-expressing J-RGCs were readily recognizable by their strikingly asymmetric dendritic arbors (**Figure 6.7 B**). Coupling partners of J-RGCs were amacrine cells in the inner nuclear layer (INL) but not other RGCs, consistent with coupling patterns of presumptive J-RGCs determined by microinjection (Hoshi and Mills, 2009;Volgyi et al., 2009). MFA (100μM) blocked transfer of βALA to the coupled amacrine cells (**Figure 6.7 C**), indicting that βALA had been transferred from J-RGCs via electrical synapses. Thus, the Pept2 method enables labeling of electrically coupled neurons in mouse retina.

We also introduced Pept2 into horizontal cells, which are electrically coupled to each other in many species, including mice (Kaneko, 1971;Dacheux and Raviola, 1982;Mills and Massey, 1994;Bloomfield et al., 1995;Dacey, 1999;Dowling, 2012). For this purpose we injected AAV-DiO-Pept2-GFP subretinally into Sdk2-CreER; *pept2*$^{-/-}$ mice; Sdk2 is a synaptic recognition molecules that is expressed by horizontal cells as well as by specific populations of RGCs and amacrine cells (Krishnaswamy et al., 2015)

Probe (GFP-positive) cells were strongly labeled by βALA, and a set of neighboring cells were labeled less strongly. Both probe and coupled cells were identifiable as horizontal cells based on their size, shape, mosaic arrangement (**Figure 6.7 D**) and labeling with anti-calbindin (see below). As with J-RGCs, uptake by probe cells persisted but transfer was abolished in the presence of MFA (100μM), confirming that transfer reflected gap junctional coupling (**Figure 6.7 E**). Together, these results demonstrate that the Pept2 method can be used to detect electrically coupled neurons in vivo.

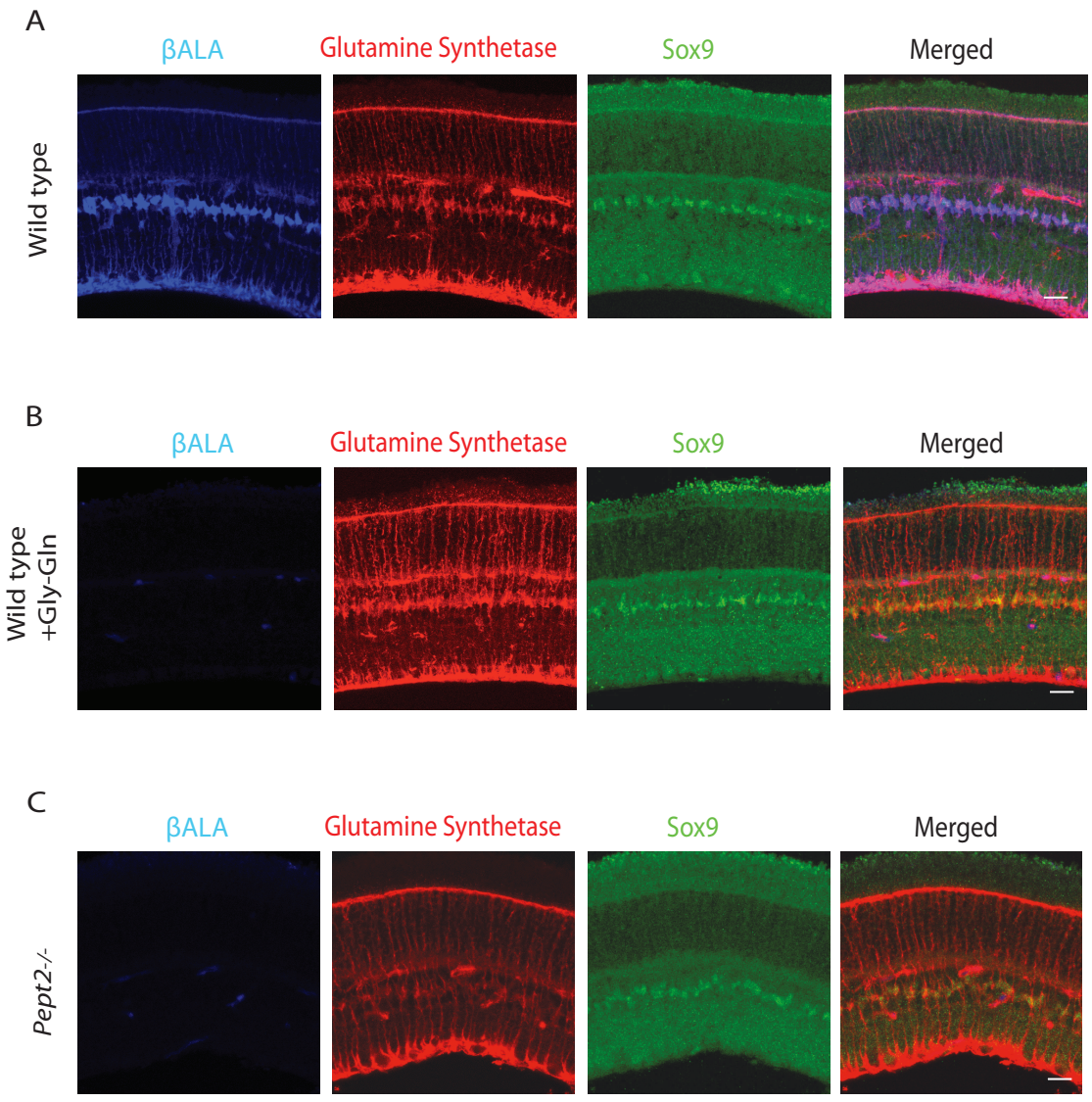

Figure 6.5 Muller glial cells express endogenous pept2 and take βALA.

A-C. βALA uptake in wild type retina (A), wild type retina treated with Gly-Gln (B) and *pept2*$^{-/-}$ retina (C). Sections were stained with antibody to glutamine synthetase and sox 9, which are molecular markers for Muller glia cells. Scale bar: 20µm.

Figure 6.6 Normal retinal architecture in *pept2*$^{-/-}$ animals.

Sections of *pept2*$^{-/-}$ retinas stained with antibodies to cell-type specific markers. No differences between wild type and pept2$^{-/-}$ retinas were detected:

Brn3a labels most RGCs; AP2 labels all amacrine cells; Chx10 labels all bipolar cells; Anti-ChAT labels somas and dendrites of starburst amacrine cells; Anti-protein kinase C (PKC) labels rod bipolar cells and a small subset of amacrine cells; Anti-disabled (DAB) labels AII amacrines; Anti-Secretagogin labels subsets of bipolar cells; Anti-calbindin labels horizontal cells, subsets of RGCs and amacrine cells, including starburst amacrine cells; Anti-HCN4 labels type 3a bipolar cells; Anti-Arrestin labels cone photoreceptors.

Scale bar: 20µm.

Figure 6.6 Normal retinal architecture in *pept2*$^{-/-}$ animals. (continued)

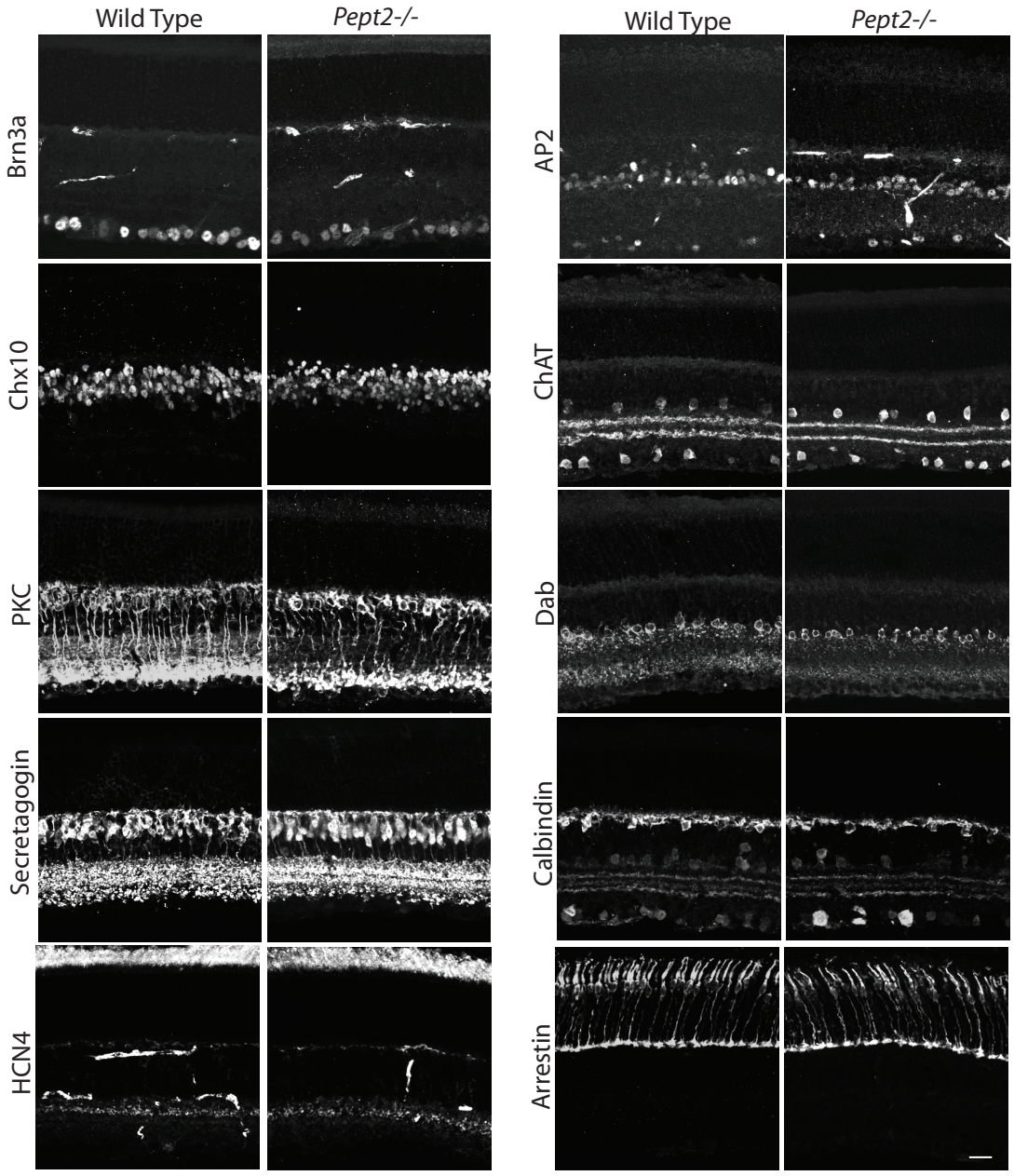

Figure 6.7 Pept2 method enables quantification of gap junction strength between cultured cells.

A. **Schematic illustration and measurement of the βALA signals for quantification of gap junction strength.**
B. **βALA signals from the probe cell to coupled cells follow an exponential decay.**
C. **Inhibition of βALA diffusion between gap junction-coupled cells by MFA at indicated concentrations. Scale bar: 50μm.**
D. **Decay curves fitted from results in D.**
E. **Coupling strength S calculated based on curves in D. *, $p < 0.05$; **, $p < 0.01$, n = 5 probe cells for each condition.**
F. **Inhibition of βALA diffusion between gap junction-coupled cells by CBX at indicated concentrations. Scale bar: 50μm**
G. **Decay curves fitted from results in F.**
H. **Coupling strength S calculated based on G. *, $p < 0.05$; **, $p < 0.01$, n = 5 probe cells for each condition.**

Figure 6.7 Pept2 method enables quantification of gap junction strength between cultured cells. (continued)

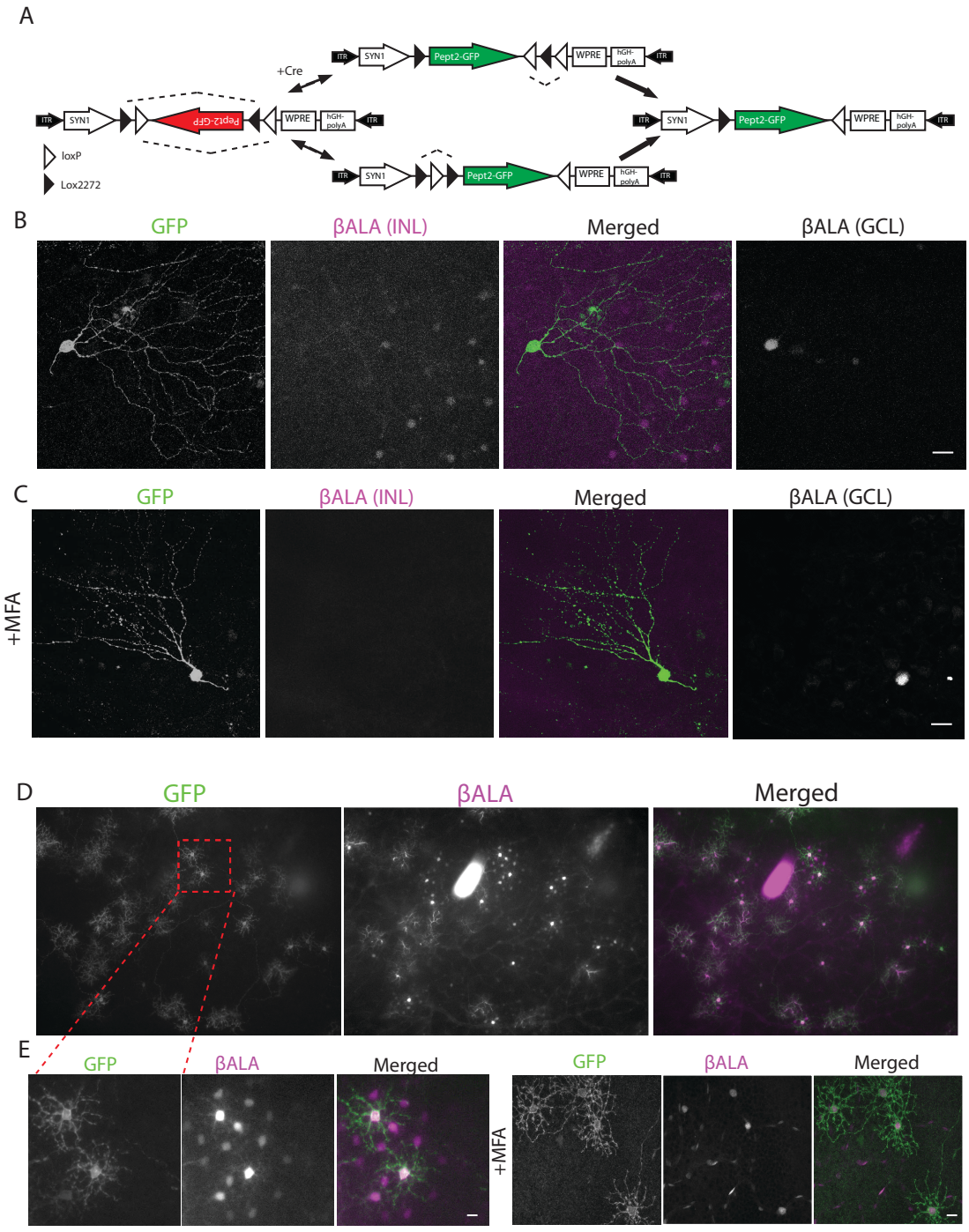

6.3.4 Light-dependent electrical coupling of horizontal cells

The strength of horizontal cell coupling is modulated by light in several species, with coupling stronger in dark-adapted than in light-adapted retinas (Teranishi et al., 1983;Piccolino et al., 1984;Godley and Wurtman, 1988;Dong and McReynolds, 1991;Xin and Bloomfield, 1999;He et al., 2000;Zhang et al., 2011;Dowling, 2012) Using the Pept2 method, we found that coupling strength is also light-dependent in mice: uptake of βALA into GFP-positive cells did not differ detectably between light- and dark-adapted retinas, but coupling strength was greater in the latter case (**Figure 6.8 A, B**). Thus, electrical coupling of horizontal cells is modulated by illumination in mice as it is in other species.

The ability of the Pept2 method to assay coupling of large numbers of cells over a large area allowed us to ask whether the effect of light-adaptation was local or whether it spread to dark-adapted regions of the same retina. For this purpose, we mounted dark-adapted Sdk2-CreER; *pept2*$^{-/}$ retina infected with AAV-DiO-Pept2-GFP on a membrane filter with a small window in it, and placed it in a dish perfused with Ringer's solution. We illuminated the entire retina with a dim background light (1nW/cm^2) and shone a bright spot (1μW/cm^2) through the window region (**Figure 6.8 C**). The membrane filter was opaque and the periphery of the dish was lightproof, so only the portion of the retina within the window was illuminated. Nonetheless, coupling was equivalent for cells inside the window (light-adapted) and outside the window (dark adapted; **Figure 6.8 D**). Similar results were obtained in six separate experiments, with the coupling midway between that observed for fully light-adapted and fully dark-adapted retinas (**Figure 6.8 E**). This result suggests that electrical synaptic strength is modulated based on the 'averaged' light level across a broad expanse of retina instead of its local level.

We considered two alternative explanations for how the result in **Figure 6.8 D, E** might have arisen. A trivial explanation is that light scattered from the window or penetrated the opaque filter to illuminate the nominally dark-adapted retina. The more interesting possibility is that long-distance lateral connections mediate the effect. To distinguish these alternatives, we made cuts between the portions of

the retina that lay inside and outside the window before illuminating the central region. In this case, coupling of cells inside the window was low whereas coupling of cells outside the window was equivalent to that in fully dark-adapted retina (**Figure 6.8 F, G, H**). This result indicates that lateral connections lead to an equalization of coupling across the retina.

Figure 6.8 Analysis of light dependent electrical coupling between horizontal cells.

A. **Coupling between horizontal cells is stronger under dim light than under bright light. Horizontal cells are identified by the marker calbindin (Calb).**
B. **Quantification of electrical coupling strength S in A. **, $p < 0.01$, n = 73 starter cells in bright light, n = 45 starter cells in dim light.**
C. **Schematic of assays to measure gap junction strength between horizontal cells under local stimulus in intact retina.**
D. **Coupling strength of illuminated horizontal cells in a ~4mm^2 window (IN) and those in an adjacent unilluminated region (OUT).**
E. **Quantification of gap junction strength from 6 separate retinas treated as in D. n = 5-19 starter cells for each condition per retina.**
F. **Schematic of assays to measure gap junction strength between horizontal cells under local stimulus in cut retina.**
G. **Coupling strength of illuminated horizontal cells in a ~4mm^2 window (Cut_IN) and those in an adjacent unilluminated region (Cut_OUT) from cut retina.**
H. **Quantification of gap junction strength from 3 separate retinas treated as in G. n = 5-19 starter cells for each condition per retina.**

Scale bars in A, D, E: 20µm.

Figure 6.8 Analysis of light dependent electrical coupling between horizontal cells. (continued)

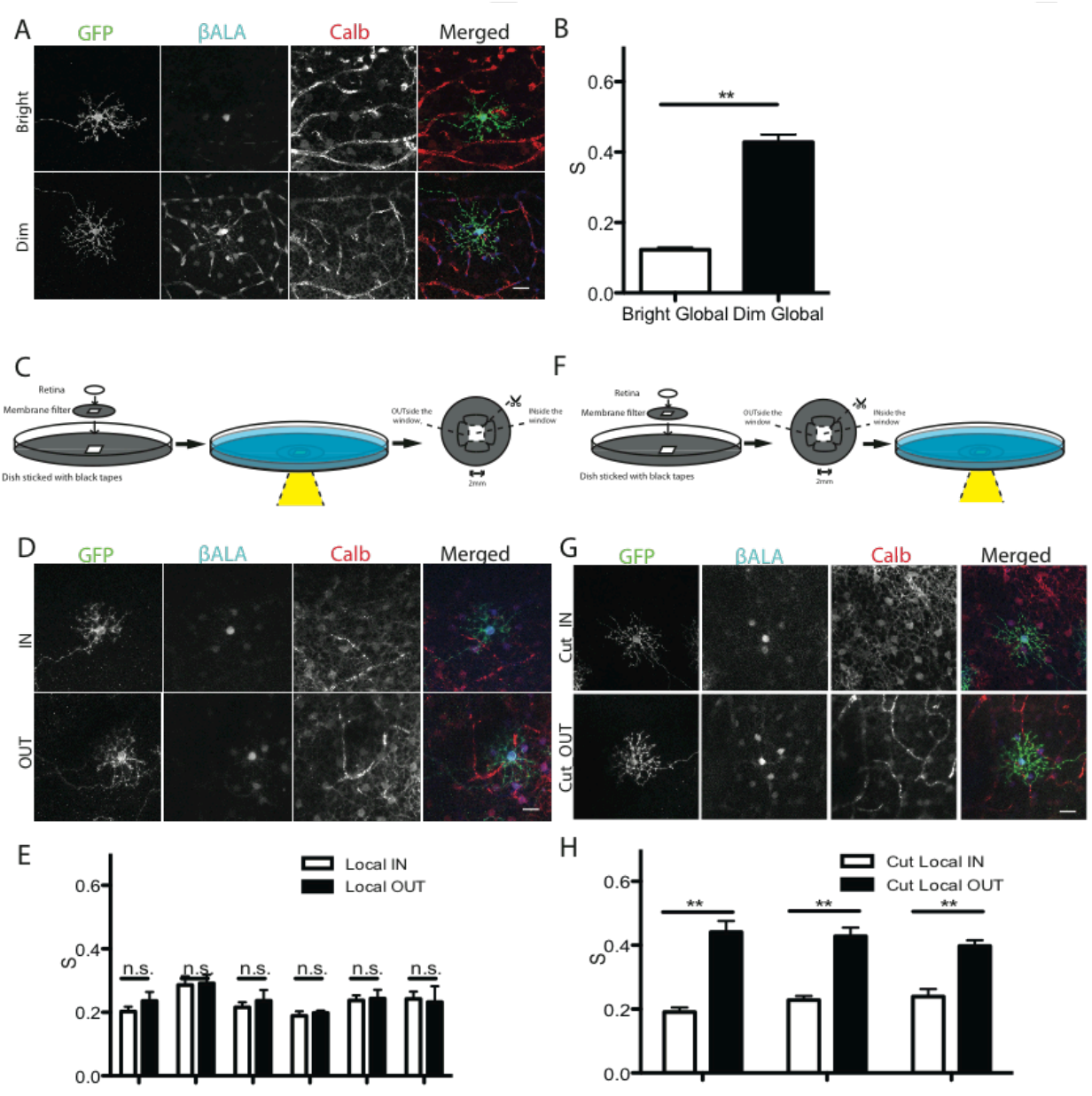

6.4 Discussion

The purpose of this work was to develop a method for efficiently mapping electrical synaptic connections from genetically defined neurons. We introduced a method based on a dipeptide transporter Pept2 and its fluorescent substrate βALA. Using transfection and virus infection, we tested the Pept2 method in cultured cells and the retina. In both case, we observed expected coupling patterns, consistent what was reported previously. Fluorescence measured in the experiments allowed us to quantify gap junction strength, and to study modulation of gap junction connections by illumination.

6.4.1 Choice of Pept2

We started this study by screening 3 channels, TRPV1, TRPA1 and P2X7, and 2 transporters, Pept1 and Pept2. In the cases of TRPV1, TRPA1 and P2X7, levels of fluorescent substrates in the transfected cells were low and electrically coupled cells were rarely detected. This observation could be explained in at least two ways: First, prolonged activation of these channels can injure transfected cells (Jancso, Kiraly et al. 1977, Browne 2013). Formation of a non-selective pore in these channels, a process called pore-dilation (Meyers et al., 2003;Chen et al., 2009;Browne et al., 2013), allows permeation of potentially damaging cations, such as Ca^{2+}. To circumvent this problem, we attempted to shorten the activation period or use a Ca^{2+} free incubation solution, but this had little effect. Alternatively, the permeability of these channels to large cations may depend less on pore-dilation than on activation of a secondary downstream pore (Bautista and Julius 2008). In this case, introducing fluorophores into the transfected cells would require co-expression of the secondary channel or transporter, which may not have been present in the cells we tested.

In contrast, Pept1 and Pept2, which transport di- and tri-peptides and related drugs (Biegel et al., 2006;Newstead et al., 2011;Smith et al., 2013), were suitable for introduction of fluorophores into cells. Of the two, Pept2 proved to be superior, likely because of its higher affinity: Pept2 can bind and transport

βALA into the cell efficiently even when the extracellular concentration is low. This low concentration of βALA causes low-level background, thus increases ratio of signal to noise (Daniel and Rubio-Aliaga, 2003;Zhang et al., 2004;Biegel et al., 2006).

6.4.2 Advantages of the Pept2 method

The Pept2 method relies on two properties. First, Pept2 efficiently transports βALA into cells. Previous studies have demonstrated that Pept2 is an oligopeptide-proton symporter. It functions as a secondary active transporter by direct coupling to H^+-ATPase, or by indirect coupling to an ATPase through other transporters, for instance, coupling to a Na^+/H^+ exchanger which in turn couples to a Na^+/K^+ ATPase) (Beyenbach and Wieczorek, 2006;Sala-Rabanal et al., 2008;Newstead et al., 2011;Smith et al., 2013). Active transport allows Pept2 to transport βALA across the membrane against concentration gradient, allowing the intracellular concentration to reach higher level than the extracellular concentration. Indeed, we observed brighter βALA signals in the transfected cells than in the bath solution. Second, βALA can diffuse readily through gap junctions. Results from microinjection indicate that ideal fluorescent tracer for gap junction coupling should be small and positively charged(Mills and Massey, 1998;Kanaporis et al., 2011). βALA has a net charge of +1, and a molecular weight of 432, comparable to 323 of Neurobiotin, a widely used tracer; and 579 of Po-pro-1, a recently reported tracer(Hoshi et al., 2006). We thus expected it to cross gap junctions and decomstrated that this was the base by direct injection into HEK cells, cultured neurons and retinal neurons (**Figure 6.1**).

Compared with microinjection, the most widely used method for labeling electrically coupled neurons, the Pept2 method has at least two advantages. First, expressing Pept2 by transfection or virus infection enables us to label multiple cells at once, whereas cells must be targeted one by one for microinjection. Second, microinjection requires impaling a target cell with an electrode, whereas the Pept2 method is non-invasive, and maintains the integrity of the cell. Thus, the Pept2 method allows study of electrical coupling from small or fragile cells deeply buried in tissue, which poses challenges for microinjection.

6.4.3 Limitations of the Pept2 method

Although the Pept2 method has advantages, it is currently limited in some ways. First. endogenous Pept2 is expressed by glial cells in the brain (Saito et al., 1996;Berger and Hediger, 1999;Dieck et al., 1999), and by Muller glial cells in the retina (Supplementary Figure 1). This endogenous Pept2 expression led to background signals that obscured signals in labeled neurons. We therefore performed studies in *pept2*$^{-/-}$ mice so that probe cells and their electrically coupled cells could be visualized. This is obviously burdensome. Going forward, one could seek transporters that are not expressed in neuronal or glial cells, for instance, one derived from plants or fungi. Second, AMCA, the fluorophore used in this study, has low quantum yield compared with other fluorophores, such as fluorescein (Lavis and Raines, 2008). We used AMCA because βALA was commercially available. It should be possible, however, to synthesize the di-peptide conjugated to brighter fluorophores.

6.4.4 Modulation of electrical coupling between horizontal cells

The Pept2 method allowed us to study modulation of electrical coupling between neurons, a phenomenon that occurs in many neuronal circuits (Bargmann and Marder, 2013). Specifically, we analyzed light dependent modulation of electrical coupling between horizontal cells. This modulation has been documented in other species (Teranishi et al., 1983;Piccolino et al., 1984;Godley and Wurtman, 1988;Dong and McReynolds, 1991;Xin and Bloomfield, 1999;He et al., 2000;Zhang et al., 2011;Dowling, 2012), and is believed to function in the following way: in dim light, coupling is high, averaging signals from multiple photoreceptors and increasing the receptive field of the horizontal cells. This increase has the effect of enhancing the sensitivity of the retinal circuit at the expense of resolution. In bright light, coupling is decreased, sacrificing sensitivity for resolution (Masland 2001, Bloomfield and Volgyi 2009, Dowling 2012). We used the Pept2 method to confirm that light also modulates coupling of horizontal cells in mouse retina, and then asked whether the modulation was confined to the illuminated area. We found that electrical coupling between horizontal cells was modulated based on the ‘averaged’ light level

across a large area of retina. This contrast-averaged adaptation is different from conventional contrast adaptation at the photoreceptor level, which is local: exposed to a bright spot, only photoreceptors within the stimulus became light adapted and less sensitive to light level. This spatial restriction generates the afterimage (dark sensation) when eyes are moved away from a bright spot (Virsu, 1978). Thus, both local and global contrast adaptation exist in the mouse retina.

The long-distance modulation of electrical coupling between horizontal cells could be explained by long-range lateral connections within the retina.Based on current knowledge, light dependent modulation depends on dopamine: light leads to activation of dopaminergic amacrine cells in the retina, and causes dopamine release. Dopamine binds to dopaminergic receptors in horizontal cells and weakens the electrical coupling (Lasater, 1987;DeVries and Schwartz, 1989). Dopaminergic amacrine cells extend long processes that can span up to half of the whole retina (Zhang, Stone et al. 2004). Thus, we suggest that processes of dopaminergic amacrine cells underlie the ability of the retina to average light over a large area.

In summary, the Pept2 method enables us to label neurons coupled by electrical synapses, thus opening up the possibility of completely mapping synaptic connectivity within a neural circuit. Combined with other techniques, such as functional imaging and gene profiling, it may also allow study of functional properties and molecular mechanism of electrical coupling. Finally, the ability of the Pept2 method to assess modulation of electrical coupling can be used in other systems and under different conditions.

6.5 Methods and materials

6.5.1 Animals:

JamB-CreER and Sdk2-CreER mice were generated in our lab and have been described previously (Kim et al., 2008;Krishnaswamy et al., 2015). JamB-CreER mice label J-RGCs, which are OFF-type direction selective RGCs responding to upward motion. Sdk2-CreER mice label horizontal cells, as well as specific subtypes of amacrine cells and RGCs. *pept2*$^{-/-}$ mice, in which endogenous *pept2* expression was eliminated, were a kind gift from D. Smith (University of Michigan)(Shen et al., 2003). Mice were maintained on a C57B6 background. All experiments were conducted in accordance with protocols approved by the Institutional Animal Care and Use Committees at Harvard University.

6.5.2 Molecular biology:

Using standard molecular cloning techniques, coding sequences of Pept1 (mouse), Pept2 (human) and P2X7 (mouse) were inserted downstream of the CMV promoter in the plasmid of pCMV-N1-EGFP to generate pCMV-Pept1, pCMV-Pept2 and pCMV-P2X7. Constructs of pCMV-TRPV1 and pCMV-TRPA1 were gifts from R. Gaudet (Harvard University).

pCMV-Pept2-GFP was generated by fusing the coding sequence of Pept2 (without STOP codon) to the N terminal of EGFP in the plasmid of pCMV-N1-EGFP. pCMV-Pept2-p2a-GFP was generated by linking the coding sequence of Pept2 (without STOP codon) to EGFP using p2a sequence: 5′-CGGAAGCGGAGCTACTAACTTCAGCCTGCTGAAGCAGGCTGGAGACGTGGAGGAGAACCCTGGACCTA-3′(Kim et al., 2011).

AAV plasmid pAAV-hSyn1-DiO-WPRE was a kind gift from B. Lowell (Harvard Medical School). The Pept2-GFP sequence was cloned into this plasmid. The final vector was verified by sequencing and packaged in serotype 2 capsids following procedures described previously(Guo et al., 2012).

6.5.3 Cell culture:

HEK293 cells were seeded in 24-well plates and maintained in Dulbecco-modified Eagle's minimal essential medium supplemented with 10% fetal calf serum. Plasmids were transfected into ~80% confluent HEK cells using lipofectamine 2000 reagent (Life Technology). 500ng of the channel or transporter DNA together with 500ng pCMV-XFP DNA were transfected. For pCMV-Pept2-GFP and pCMV-Pept2-p2a-GFP, a total of 500ng DNA was transfected.

After transfection, HEK cells were grown for another 1 to 2 days, and then dissociated by pipetting. Dissociated cells were mixed with untransfected HEK cells at a ratio of 1:100, replated in a 24-well plate, and grown for another day.

The assay for uptake and transfer was based on procedures described previously(Dieck et al., 1999). After aspiration of the culture medium, HEK cells were washed twice and preincubated for 10 min with HEPES-buffered saline (HBS): 145 mM NaCl, 5.4 mM KCl, 1.8 mM $CaCl_2$, 1 mM $MgCl_2$, 20 mM HEPES, and 20 mM glucose, pH = 7.2. The HBS was aspirated and the cells were incubated for 5min-1 hour for TRPV1, TRPA1 and P2X7 and 1-6 hours for Pept1 and Pept2 with HBS containing fluorescent substrates. Substrate concentrations were: 100μM for Yo-pro-1 and Po-pro-1 (Life Technology), 100μM for Ethidium (Sigma) and 40μM for βALA (Biotrend). Capsaisin(1μM; Sigma), allyl isothiocyanate (300μM; Sigma) or ATP (5mM, Sigma) were included to activate TRPV1, TRPA1 and P2X7 channels, respectively. After incubation, the cells were rapidly washed twice with ice-cold HBS, and then fixed with 4% paraformaldehyde (PFA) at 4 °C for 10min. Fixed cells were imaged using a Nikon inverted fluorescence microscope.

To test the specificity of Pept2-dependent uptake of βALA, 8mM Gly-Gln was applied together with 40μM βALA for the incubation. To determine whether intercellular movement of βALA depended

on gap junctions, HEK cells were preincubated with HBS containing 100μM CBX or MFA for 10min before βALA was applied.

6.5.4 Quantification of gap junction strength from in vitro assays:

The diffusion of βALA from probe cells to coupled cells can be described by the following diffusion equations:

$$J(x,t) = -D\frac{\partial}{\partial x}C(x,t) \quad (1)$$

$$\frac{\partial}{\partial t}C(x,t) = -\frac{\partial}{\partial x}J(x,t) - k_{out}C(x,t) + k_{in}C_{solution} \quad (2)$$

Cell position *x* is the number of cells from the probe cell (*x* = 0) to a coupled cell away from probe cell (Fig. 4A). *C(x, t)* indicates the concentration of βALA at a cell with position *x* at time *t*, and $C_{solution}$ is the concentration of βALA. *J(x, t)* indicates the flow of βALA at cell with position *x* at time *t*. k_{in} and k_{out} are rate constants for passage of βALA from the solution into the cell and from the cell to the solution. In the absence of Pept2, application of βALA in the solution leads to background uptake at concentration of C_{bg}:

$$k_{out}C_{bg} = k_{in}C_{solution} \quad (3)$$

At steady state when concentration of βALA in the cells doesn't change with time, we have

$$\frac{\partial}{\partial t}C(x,t) = 0 \quad (4)$$

At steady state, the concentration of βALA in the probe cell is C_0, and the diffusion equations have the solution:

$$C(x) = (C_0 - C_{bg})e^{-\lambda x} + C_{bg} \quad (5)$$

which has the form of an exponential decay, with decay constant

$$\lambda = \sqrt{\frac{k_{out}}{D}} \qquad (6)$$

We assume the measured fluorescent intensity (*I*) is proportional to the concentration (*C*) of βALA, thus

$$I(x) = \left(I_0 - I_{bg}\right)e^{-\lambda x} + I_{bg} \qquad (7)$$

Normalizing fluorescent intensity to that of probe cell I_0, we get

$$I_{normalized}(x) = \left(1 - \frac{I_{bg}}{I_0}\right)e^{-\lambda x} + \frac{I_{bg}}{I_0} \qquad (8)$$

We fit data with this curve to get the decay constant λ.

Gap junction strength *S* can then be defined as the proportion of substrate in the probe cell diffuses into the directly coupled cells:

$$S = \frac{(C_0 - C_{bg})e^{-\lambda(x+1)}}{(C_0 - C_{bg})e^{-\lambda x}} = e^{-\lambda x} \qquad (9)$$

6.5.5 Retinal assays:

Using methods described previously, AAV-hSyn1-DiO-Pept2-GFP was delivered subretinally(Samuel et al., 2014) to Sdk2-CreER; *pept2*$^{-/-}$ animals to label horizontal cells, and delivered intravitreally(Hong et al., 2011) to JamB-CreER; *pept2*$^{-/-}$ animals to label J-RGCs. For virus injection, adult animals were anaesthetized by intraperitoneal injection of ketamine/xylazine. A $30^{1/2}$G needle was used to make a small hole in the temporal eye, below the cornea, and 2μL AAV-DiO-Pept2-GFP was injected with a Hamilton syringe and a 33G blunt-ended needle. Injected animals were euthanized and their retinas were dissected 4 weeks following injection.

Mice were dark adapted for at least 1 hour prior to euthanasia. Retinas were dissected under infrared illumination in Mouse Ringers' solution (140 mM NaCl, 2.5 mM KCl, 2 mM $CaCl_2$, 1 mM $MgCl_2$, 22 mM $NaHCO_3$, and 10 mM glucose) oxygenated with 95% O2, 5% CO2 at room temperature. The retina was then moved to a 6cm petri dish perfused with oxygenated Mouse Ringers' at 32-34 °C. βALA was added to the Mouse Ringers' to a final concentration of 40μM, and the incubation was continued for ~4 hours. After incubation, the retina was rinsed twice with ice-cold oxygenated Mouse Ringers', and then fixed with 4% paraformaldehyde (PFA) at 4 °C for 30min. The retina was then processed for immunostaining and imaging.

To study light-dependent modulation of gap junction strength, a ~2mm aperture was cut into an opaque nitrocelluose filter(HABG01300, Millipore) and the dissected retina was mounted on the filter. The filter was then mounted into a lightproof 6cm petri dish. Stimulation from a digital-light-processing projector (Dell) was focused onto the aperture. Stimulation intensity was $1\mu W/cm^2$. Background light intensity was $1nW/cm^2$. 30 min after the onset of light stimulation, βALA was added to the Mouse Ringers'. After incubation, the retina with filter paper was rapidly washed twice with ice-cold oxygenated Mouse Ringers' and fixed with 4% paraformaldehyde (PFA) at 4 °C for 30min. Following additional washes in PBS, the part of the retina within the aperture was separated from the rest by a sharp blade, and the two parts were processed for immunostaining and imaging.

To test whether the transfer of βALA was through gap junction, 100μM MFA was applied 10 min before adding βALA.

6.5.6 Immunohistochemistry:

Fixed retinas were either frozen and sectioned at 20μm in a cryostat or stained as whole mounts. Retina sections or whole mounts were incubated in PBS with 3% donkey serum and 0.3% Triton X-100

for blocking, followed by primary antibodies for ≥24 hours at 4°C and secondary antibodies for ~4 hours. Retinas were then washed with PBS and mounted in Fluoromount G (Southern Biotech).

Primary antibodies used in this study were: rabbit anti-GFP (1:1000, Millipore); rabbit and mouse anti-calbindin (1:2000, Swant and 1:100, Swant); goat anti-choline acetyltransferase (ChAT) (1:400, Millipore); mouse anti-Brn3a (1:1000, Millipore); goat anti-Chx10 (1:200, Santa Cruz); mouse anti-AP2 (1:1000, DSHB); mouse anti-HCN4 (1: 1000, clone N114.10); rabbit anti-PKC alpha (1:1000, P4334 in Sigma); rabbit anti-secretagogin (1:4000, Biovendor); rabbit anti-arrestin (1:200, Milipore); rabbit anti-glutamine synthetase (1:1000, BD Biosciences); rabbit anti-sox9 (1:1000, Chemicon); mouse anti-connexin 43 (1:50, Life Sciences); rabbit antibody to Dab1 (a kind gift from B. Howell, SUNY Upstate Medical University). Secondary antibodies were conjugated to DyLight 649 (Jackson ImmunoResearch) , Alexa Fluor 568 or Alexa Fluor 488(Invitrogen) and used at 1:500.

6.5.7 Imaging and quantification of signals:

Retinal images were taken with Zeiss LSM-710 confocal microscope using 405, 488, 568 and 647 lasers with a step size of 0.5 μm and a 40X NA 1.3 lens. Images were then analyzed using ImageJ (NIH) software.

To quantify electrical synaptic strength between horizontal cells, the βALA signal in the starter GFP-positive horizontal cell was measured as I_0. Horizontal cells surround this cell were identified by immunostaining for the marker calbindin. Because horizontal cells form a mosaic in mouse retina, we took the six horizontal cells that are closest to the probe cell as directly coupled cells, and measured βALA signals in them as I_1. The electrical synaptic strength S was defined as the proportion of substrate in the starter cell diffuses into the directly coupled cells. Adjusting for the background signals, we calculated the electrical synaptic strength as following:

$$S = \frac{Averaged\ I_1 - I_{bg}}{I_0 - I_{bg}} \qquad (10)$$

6.6 Acknowledgements

We thank Sanes lab members for useful discussion and comments on this work, Monica Sala-Rabanal (Washington University of Saint Louis) for Pept2 cDNA, Rachelle Gaudet (Harvard University) for pCMV-TRPV1 and pCMV-TRPA1 plasmids, Brad Lowell (Harvard Medical School) for the AAV plasmid, and Brian Howell (SUNY upstate medical university) for Dab1 antibody. This work is supported by grant NS029169 to J.R.S.

6.7 References

Apostolides, P.F., and Trussell, L.O. (2013). Regulation of interneuron excitability by gap junction coupling with principal cells. *Nat Neurosci* 16**,** 1764-1772.

Bargmann, C.I., and Marder, E. (2013). From the connectome to brain function. *Nat Methods* 10**,** 483-490.

Beier, K.T., Saunders, A., Oldenburg, I.A., Miyamichi, K., Akhtar, N., Luo, L., Whelan, S.P., Sabatini, B., and Cepko, C.L. (2011). Anterograde or retrograde transsynaptic labeling of CNS neurons with vesicular stomatitis virus vectors. *Proc Natl Acad Sci U S A* 108**,** 15414-15419.

Berger, U.V., and Hediger, M.A. (1999). Distribution of peptide transporter PEPT2 mRNA in the rat nervous system. *Anat Embryol (Berl)* 199**,** 439-449.

Beyenbach, K.W., and Wieczorek, H. (2006). The V-type H+ ATPase: molecular structure and function, physiological roles and regulation. *J Exp Biol* 209**,** 577-589.

Biegel, A., Knutter, I., Hartrodt, B., Gebauer, S., Theis, S., Luckner, P., Kottra, G., Rastetter, M., Zebisch, K., Thondorf, I., Daniel, H., Neubert, K., and Brandsch, M. (2006). The renal type H+/peptide symporter PEPT2: structure-affinity relationships. *Amino Acids* 31**,** 137-156.

Bloomfield, S.A., and Volgyi, B. (2009). The diverse functional roles and regulation of neuronal gap junctions in the retina. *Nat Rev Neurosci* 10**,** 495-506.

Bloomfield, S.A., Xin, D., and Persky, S.E. (1995). A comparison of receptive field and tracer coupling size of horizontal cells in the rabbit retina. *Vis Neurosci* 12**,** 985-999.

Browne, L.E., Compan, V., Bragg, L., and North, R.A. (2013). P2X7 receptor channels allow direct permeation of nanometer-sized dyes. *J Neurosci* 33**,** 3557-3566.

Chen, J., Kim, D., Bianchi, B.R., Cavanaugh, E.J., Faltynek, C.R., Kym, P.R., and Reilly, R.M. (2009). Pore dilation occurs in TRPA1 but not in TRPM8 channels. *Mol Pain* 5**,** 3.

Connors, B.W., and Long, M.A. (2004). Electrical synapses in the mammalian brain. *Annu Rev Neurosci* 27**,** 393-418.

Cook, J.E., and Becker, D.L. (2009). Gap-junction proteins in retinal development: new roles for the "nexus". *Physiology (Bethesda)* 24**,** 219-230.

Dacey, D.M. (1999). Primate retina: cell types, circuits and color opponency. *Prog Retin Eye Res* 18**,** 737-763.

Dacheux, R.F., and Raviola, E. (1982). Horizontal cells in the retina of the rabbit. *J Neurosci* 2**,** 1486-1493.

Daniel, H., and Rubio-Aliaga, I. (2003). An update on renal peptide transporters. *Am J Physiol Renal Physiol* 284**,** F885-892.

Devries, S.H., and Schwartz, E.A. (1989). Modulation of an electrical synapse between solitary pairs of catfish horizontal cells by dopamine and second messengers. *J Physiol* 414**,** 351-375.

Dieck, S.T., Heuer, H., Ehrchen, J., Otto, C., and Bauer, K. (1999). The peptide transporter PepT2 is expressed in rat brain and mediates the accumulation of the fluorescent dipeptide derivative beta-Ala-Lys-Nepsilon-AMCA in astrocytes. *Glia* 25**,** 10-20.

Dong, C.J., and Mcreynolds, J.S. (1991). The relationship between light, dopamine release and horizontal cell coupling in the mudpuppy retina. *J Physiol* 440**,** 291-309.

Dowling, J.E. (2012). *The retina : an approachable part of the brain.* Cambridge, Mass.: Belknap Press of Harvard University Press.

Feinberg, E.H., Vanhoven, M.K., Bendesky, A., Wang, G., Fetter, R.D., Shen, K., and Bargmann, C.I. (2008). GFP Reconstitution Across Synaptic Partners (GRASP) defines cell contacts and synapses in living nervous systems. *Neuron* 57**,** 353-363.

Gemel, J., Valiunas, V., Brink, P.R., and Beyer, E.C. (2004). Connexin43 and connexin26 form gap junctions, but not heteromeric channels in co-expressing cells. *J Cell Sci* 117**,** 2469-2480.

Godley, B.F., and Wurtman, R.J. (1988). Release of endogenous dopamine from the superfused rabbit retina in vitro: effect of light stimulation. *Brain Res* 452**,** 393-395.

Groneberg, D.A., Doring, F., Eynott, P.R., Fischer, A., and Daniel, H. (2001). Intestinal peptide transport: ex vivo uptake studies and localization of peptide carrier PEPT1. *Am J Physiol Gastrointest Liver Physiol* 281**,** G697-704.

Guo, P., El-Gohary, Y., Prasadan, K., Shiota, C., Xiao, X., Wiersch, J., Paredes, J., Tulachan, S., and Gittes, G.K. (2012). Rapid and simplified purification of recombinant adeno-associated virus. *J Virol Methods* 183**,** 139-146.

He, S., Weiler, R., and Vaney, D.I. (2000). Endogenous dopaminergic regulation of horizontal cell coupling in the mammalian retina. *J Comp Neurol* 418**,** 33-40.

Hong, Y.K., Kim, I.J., and Sanes, J.R. (2011). Stereotyped axonal arbors of retinal ganglion cell subsets in the mouse superior colliculus. *J Comp Neurol* 519**,** 1691-1711.

Hormuzdi, S.G., Filippov, M.A., Mitropoulou, G., Monyer, H., and Bruzzone, R. (2004). Electrical synapses: a dynamic signaling system that shapes the activity of neuronal networks. *Biochim Biophys Acta* 1662**,** 113-137.

Hoshi, H., and Mills, S.L. (2009). Components and properties of the G3 ganglion cell circuit in the rabbit retina. *J Comp Neurol* 513**,** 69-82.

Hoshi, H., O'brien, J., and Mills, S.L. (2006). A novel fluorescent tracer for visualizing coupled cells in neural circuits of living tissue. *J Histochem Cytochem* 54**,** 1169-1176.

Johnson, K.E., Mitra, S., Katoch, P., Kelsey, L.S., Johnson, K.R., and Mehta, P.P. (2013). Phosphorylation on Ser-279 and Ser-282 of connexin43 regulates endocytosis and gap junction assembly in pancreatic cancer cells. *Mol Biol Cell* 24**,** 715-733.

Kanaporis, G., Brink, P.R., and Valiunas, V. (2011). Gap junction permeability: selectivity for anionic and cationic probes. *Am J Physiol Cell Physiol* 300**,** C600-609.

Kaneko, A. (1971). Electrical connexions between horizontal cells in the dogfish retina. *J Physiol* 213**,** 95-105.

Kim, I.J., Zhang, Y., Yamagata, M., Meister, M., and Sanes, J.R. (2008). Molecular identification of a retinal cell type that responds to upward motion. *Nature* 452**,** 478-482.

Kim, J.H., Lee, S.R., Li, L.H., Park, H.J., Park, J.H., Lee, K.Y., Kim, M.K., Shin, B.A., and Choi, S.Y. (2011). High cleavage efficiency of a 2A peptide derived from porcine teschovirus-1 in human cell lines, zebrafish and mice. *PLoS One* 6**,** e18556.

Krishnaswamy, A., Yamagata, M., Duan, X., Hong, Y.K., and Sanes, J.R. (2015). Sidekick 2 directs formation of a retinal circuit that detects differential motion. *Nature*.

Lasater, E.M. (1987). Retinal horizontal cell gap junctional conductance is modulated by dopamine through a cyclic AMP-dependent protein kinase. *Proc Natl Acad Sci U S A* 84**,** 7319-7323.

Lavis, L.D., and Raines, R.T. (2008). Bright ideas for chemical biology. *ACS Chem Biol* 3**,** 142-155.

Li, Y., Lu, H., Cheng, P.L., Ge, S., Xu, H., Shi, S.H., and Dan, Y. (2012). Clonally related visual cortical neurons show similar stimulus feature selectivity. *Nature* 486**,** 118-121.

Lo, L., and Anderson, D.J. (2011). A Cre-dependent, anterograde transsynaptic viral tracer for mapping output pathways of genetically marked neurons. *Neuron* 72**,** 938-950.

Meyers, J.R., Macdonald, R.B., Duggan, A., Lenzi, D., Standaert, D.G., Corwin, J.T., and Corey, D.P. (2003). Lighting up the senses: FM1-43 loading of sensory cells through nonselective ion channels. *J Neurosci* 23**,** 4054-4065.

Mills, S.L., and Massey, S.C. (1994). Distribution and coverage of A- and B-type horizontal cells stained with Neurobiotin in the rabbit retina. *Vis Neurosci* 11**,** 549-560.

Mills, S.L., and Massey, S.C. (1998). The kinetics of tracer movement through homologous gap junctions in the rabbit retina. *Vis Neurosci* 15**,** 765-777.

Newstead, S., Drew, D., Cameron, A.D., Postis, V.L., Xia, X., Fowler, P.W., Ingram, J.C., Carpenter, E.P., Sansom, M.S., Mcpherson, M.J., Baldwin, S.A., and Iwata, S. (2011). Crystal structure of a prokaryotic homologue of the mammalian oligopeptide-proton symporters, PepT1 and PepT2. *EMBO J* 30**,** 417-426.

Patel, D., Zhang, X., and Veenstra, R.D. (2014). Connexin hemichannel and pannexin channel electrophysiology: how do they differ? *FEBS Lett* 588**,** 1372-1378.

Piccolino, M., Neyton, J., and Gerschenfeld, H.M. (1984). Decrease of gap junction permeability induced by dopamine and cyclic adenosine 3':5'-monophosphate in horizontal cells of turtle retina. *J Neurosci* 4**,** 2477-2488.

Saito, H., Terada, T., Okuda, M., Sasaki, S., and Inui, K. (1996). Molecular cloning and tissue distribution of rat peptide transporter PEPT2. *Biochim Biophys Acta* 1280**,** 173-177.

Sala-Rabanal, M., Loo, D.D., Hirayama, B.A., and Wright, E.M. (2008). Molecular mechanism of dipeptide and drug transport by the human renal H+/oligopeptide cotransporter hPEPT2. *Am J Physiol Renal Physiol* 294**,** F1422-1432.

Samuel, M.A., Voinescu, P.E., Lilley, B.N., De Cabo, R., Foretz, M., Viollet, B., Pawlyk, B., Sandberg, M.A., Vavvas, D.G., and Sanes, J.R. (2014). LKB1 and AMPK regulate synaptic remodeling in old age. *Nat Neurosci* 17**,** 1190-1197.

Sanes, J.R., and Yamagata, M. (2009). Many paths to synaptic specificity. *Annu Rev Cell Dev Biol* 25**,** 161-195.

Shen, H., Smith, D.E., Keep, R.F., Xiang, J., and Brosius, F.C., 3rd (2003). Targeted disruption of the PEPT2 gene markedly reduces dipeptide uptake in choroid plexus. *J Biol Chem* 278**,** 4786-4791.

Siegelbaum, S.A., and Kandel, E.R. (2013). "Overview of synaptic transmission," in *Principles of neural science,* eds. E.R. Kandel, J.H. Schwartz, T.M. Jessell, S.A. Siegelbaum & A.J. Hudspeth. 5th ed (New York: McGraw-Hill), pp. 177-188.

Smith, D.E., Clemencon, B., and Hediger, M.A. (2013). Proton-coupled oligopeptide transporter family SLC15: physiological, pharmacological and pathological implications. *Mol Aspects Med* 34**,** 323-336.

Teranishi, T., Negishi, K., and Kato, S. (1983). Dopamine modulates S-potential amplitude and dye-coupling between external horizontal cells in carp retina. *Nature* 301**,** 243-246.

Tian, L., Yang, Y., Wysocki, L.M., Arnold, A.C., Hu, A., Ravichandran, B., Sternson, S.M., Looger, L.L., and Lavis, L.D. (2012). Selective esterase-ester pair for targeting small molecules with cellular specificity. *Proc Natl Acad Sci U S A* 109**,** 4756-4761.

Vaney, D.I. (1991). Many diverse types of retinal neurons show tracer coupling when injected with biocytin or Neurobiotin. *Neurosci Lett* 125**,** 187-190.

Varshney, L.R., Chen, B.L., Paniagua, E., Hall, D.H., and Chklovskii, D.B. (2011). Structural properties of the Caenorhabditis elegans neuronal network. *PLoS Comput Biol* 7**,** e1001066.

Virsu, V. (1978). Retinal mechanisms of visual adaptation and afterimages. *Med Biol* 56**,** 84-96.

Volgyi, B., Chheda, S., and Bloomfield, S.A. (2009). Tracer coupling patterns of the ganglion cell subtypes in the mouse retina. *J Comp Neurol* 512**,** 664-687.

White, J.G., Southgate, E., Thomson, J.N., and Brenner, S. (1986). The structure of the nervous system of the nematode Caenorhabditis elegans. *Philos Trans R Soc Lond B Biol Sci* 314**,** 1-340.

Wickersham, I.R., Lyon, D.C., Barnard, R.J., Mori, T., Finke, S., Conzelmann, K.K., Young, J.A., and Callaway, E.M. (2007). Monosynaptic restriction of transsynaptic tracing from single, genetically targeted neurons. *Neuron* 53**,** 639-647.

Xin, D., and Bloomfield, S.A. (1999). Dark- and light-induced changes in coupling between horizontal cells in mammalian retina. *J Comp Neurol* 405**,** 75-87.

Yogev, S., and Shen, K. (2014). Cellular and molecular mechanisms of synaptic specificity. *Annu Rev Cell Dev Biol* 30**,** 417-437.

Yu, Y.C., He, S., Chen, S., Fu, Y., Brown, K.N., Yao, X.H., Ma, J., Gao, K.P., Sosinsky, G.E., Huang, K., and Shi, S.H. (2012). Preferential electrical coupling regulates neocortical lineage-dependent microcircuit assembly. *Nature* 486**,** 113-117.

Zhang, A.J., Jacoby, R., and Wu, S.M. (2011). Light- and dopamine-regulated receptive field plasticity in primate horizontal cells. *J Comp Neurol* 519**,** 2125-2134.

Zhang, E.Y., Emerick, R.M., Pak, Y.A., Wrighton, S.A., and Hillgren, K.M. (2004). Comparison of human and monkey peptide transporters: PEPT1 and PEPT2. *Mol Pharm* 1**,** 201-210.

Zhu, P., Frank, T., and Friedrich, R.W. (2013). Equalization of odor representations by a network of electrically coupled inhibitory interneurons. *Nat Neurosci* 16**,** 1678-1686.

Zimmermann, M., and Stan, A.C. (2010). PepT2 transporter protein expression in human neoplastic glial cells and mediation of fluorescently tagged dipeptide derivative beta-Ala-Lys-Nepsilon-7-amino-4-methyl-coumarin-3-acetic acid accumulation. *J Neurosurg* 112**,** 1005-1014.

Chapter 7: Conclusion and future directions

My thesis focused on a fundamental question in neuroscience -- how to classify subtypes of neurons in neural circuits. Different subtypes of neurons receive different inputs, project to different areas and form their own stereotyped connections. The diversity of neuronal subtypes and their physiological properties underlies the ability of neural circuits in generating complex behaviors and performing cognitive tasks. Thus, it is very important to classify and register each subtype of neurons in the nervous system.

In my thesis work, I used the retina as a model system and classified a variety of RGCs. I have shown success in classifying three groups of RGCs – alpha RGCs, F-RGCs and W3D RGCs – using morphological, physiological and molecular criteria. Similar methods can now be used to classify other RGCs. In addition, my results illustrate how to tackle this problem in the brain.

Along the way, I found a molecular marker of alpha RGCs, osteopontin, that could be used to promote axon regeneration. This can be potentially used to treat axon damage caused by spinal cord injury. Also, I developed a molecular genetic method to trace neurons coupled by electrical synapses, and I used it to probe electrical coupling from a subtype of RGCs, J-RGCs. This method can potentially be applied to other neuronal subtypes to study their electrical synaptic connections.

In this chapter, I will summarize the results from previous chapters and list possible future directions that have been uncovered in my thesis.

7.1 Summary of studies

7.1.1 RGCs can be classified into subtypes

Genetic labeling of groups of RGCs in a transgenic or cre knock-in mouse line allowed us to target and study these RGCs specifically. My thesis work started from analyzing mouse lines with specific groups of RGCs labeled. To describe and classify different subtypes of RGCs labeled in these lines, I applied morphological, physiological and molecular criteria. Combination of these criteria allowed us to describe different RGC subtypes in detail and distinguish them in a precise manner. To include all these properties, I targeted individual cells with patch pipette for recording and then dye-filled these cells to reconstruct their morphologies. Molecular properties were acquired by immunohistochemistry screening.

In Chapter 2, I described classification of alpha RGCs labeled in Kcng4-Cre lines. Analysis of alpha RGCs using above three criteria allowed us to classify them into four subtypes, each of which has distinct morphological and physiological property: Off-sustained, Off-transient, On-sustained and On-transient alpha RGCs. Among them, On-transient subtype appeared to be a new subtype. This demonstrated the ability of using combined criteria to find new subtypes.

In Chapter 4, I talked about a new group of RGCs, F-RGCs, labeled by transcription factor Foxp2, and their classifications. We found four subtypes of F-RGCs with distinct morphological, physiological and molecular properties. Two subtypes of F-RGCs with small dendritic fields, F-mini RGCs, have asymmetric dendrites and direction selectivity to where their dendrites point. The other two subtypes of F-RGCs have relatively large dendritic fields and are not direction selective.

Chapter 5 showed my ongoing work to classify RGCs labeled in a transgenic mouse line called W3. Two groups of RGCs are labeled in W3 retina based on their different expression levels of fluorescent proteins. Previous studies showed that the brightly labeled cells, W3B-RGCs, comprise a single population of object motion sensors (Krishnaswamy et al., 2015; Zhang et al., 2012). I focused on the other larger population labeled dimly, W3D RGCs. The preliminary results showed that there are at least five subtypes of W3D RGCs with different morphological and physiological properties.

These results from my thesis indicate that RGCs can be classified into subtypes. Besides these RGCs I described, one well-known example of RGC subtypes classified previously was On-Off direction selective RGCs. All of On-Off direction selective RGCs have dendrites co-laminated with processes of starburst amacrine cells, but based on their direction selectivity, these cells can be classified into four subtypes with preferred directions pointing dorsally, ventrally, nasally and temporally (Barlow and Hill, 1963; Barlow and Levick, 1965; Kim et al., 2008; Levick, 1967; Oyster and Barlow, 1967). Recently, work from our lab revealed molecular markers to three subtypes of On-Off direction selective RGCs: Mmp17 is expressed in subtype with nasal preferred direction, and Col25a1 labels subtypes responding strongly to objects moving dorsally and ventrally (Kay et al., 2011). Together, all these subtypes of RGCs classified are summarized in **Figure 7.1.**

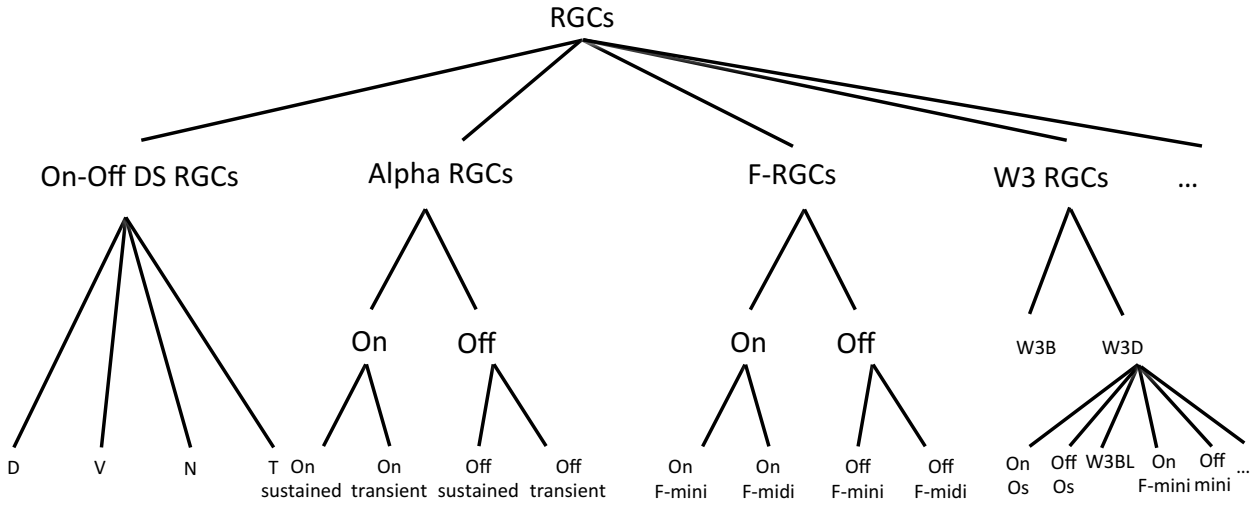

Figure 7.1 Summary of subtypes of RGCs classified

7.1.2 Role of osteopontin in promoting axon regeneration

The studies described in Chapter 3 described the role of osteopontin, a molecular marker for all the alpha RGCs, in promoting axon regeneration. We noticed that RGCs differ dramatically in their abilities to survive and regenerate after axotomy. Alpha RGCs preferentially survive and regenerate compared with other RGCs. Osteopontin (OPN), a molecule I found to be specifically expressed in alpha RGCs, is sufficient to increase mTOR activity. By applying OPN in combination with growth factors, we were able to promote axon regeneration of RGCs. Thus, our work revealed the difference of regeneration abilities among subtypes of RGCs and found out a new agent to promote axon regeneration.

7.1.3 A molecular genetic method to map electrical synaptic connections

In Chapter 6, I reported my work in developing a method that can be used to map electrical synaptic connections from genetically defined neurons. Lack of methods that can map electrical synaptic connections from a genetically targeted neuron hinders us from getting a complete understanding of the neural circuit. To solve the problem, I developed a method to label cells connected to a probe cell by electrical synapses, making use of a dipeptide transporter Pept2. Expressing Pept2 in the probe cell in a Cre-dependent way makes the probe cell take a gap junction permeable fluorescent dipeptide, beta-alanine-lysine-AMCA, which then diffuses and labels the coupled cells. I tested this method in cell culture and validated it in mouse retina using AAV carrying Pept2. Finally, I applied this method to J-RGCs and horizontal cells, and studied modulation of gap junction connections between horizontal cells under different light conditions.

7.2 Future directions

7.2.1 What is the role of Kcng4 in alpha RGCs and Foxp2 in F-RGCs?

In Chapter 2 and 4, I described four subtypes of alpha RGCs labeled in Kcng4-Cre lines and four subtypes of F-RGCs labeled in Foxp2-Cre lines. Alpha RGCs share molecular characters that distinguish them from other RGCs: Kcng4-Cre, neurofilament and osteopontin. In Chapter 3, I have reported the role

of osteopontin in promoting axon regeneration. Thus, one interesting question is what is the role of Kcng4, a potassium channel modulator in alpha RGCs. Given that Kcng4-Cre mouse can also serve as a knockout animal, one can specifically look at the phenotypes of alpha RGCs in Kcng4 knockout animals. Likewise, Foxp2 is the molecular signature of F-RGCs, and it is a transcriptional factor important in brain development (Shu et al., 2007), and normal functions in auditory and motor systems (Kurt et al., 2012; Shu et al., 2005). The function of Foxp2 in F-RGCs is unknown, and it is worth examining phenotypes of F-RGCs in Foxp2 knockout animals given the animals are available (French et al., 2007).

7.2.2 How does F-mini RGCs compute direction selectivity?

Four subtypes of F-RGCs were reported in Chapter 4. Among them, two subtypes with asymmetric dendrites and small dendritic fields were direction selective. Thus, one interesting question is how they compute direction selectivity. In mouse retina, most of the studies have focused on four subtypes of On-Off direction selective RGCs, which differ in their preferred directions. On-Off direction selective RGCs co-fasciculate and form synapses with starburst amacrine cells, which is important in their direction selectivity (Borst and Helmstaedter, 2015; Vaney et al., 2012). However, the two subtypes of F-mini RGCs don't appear to co-fasciculate with starburst amacrine cells, indicating that they have different mechanisms of computing direction selectivity than On-Off direction selective RGCs. There are also three subtypes of On-direction selective RGCs, which differ in their preferred directions (Barlow et al., 1964; Sun et al., 2006). But direction selectivity of these On-direction selective RGCs also depends on synapses formed between them and starburst amacrine cells. So far, only one Off-direction selective RGCs, J-RGCs, was reported (Kim et al., 2008), whose direction selectivity depends on their asymmetric dendrites. F-mini RGCs also have asymmetric dendrites. Thus, it remains to be determined whether their direction selectivity depends on this characteristic, and beyond this, what is the circuit mechanism of direction selectivity of F-mini RGCs.

7.2.3 Mapping retinal circuits of alpha RGCs and F-RGCs

As I mentioned above, in order to understand how alpha RGCs and F-RGCs have their characteristic physiological properties, it is important to map circuits of these cells in the retina. For example, we can use connectomic techniques to reconstruct synaptic connections from F-RGCs or alpha RGCs from electron microscopy images or super resolution images (Helmstaedter et al., 2013; Kim et al., 2014; Sigal et al., 2015). Alternatively, we can test whether specific synaptic connections exit between F-RGCs or alpha RGCs and certain bipolar cells or amacrine cells. This can be done by expressing channelrhodopsin in presynaptic neurons, activating these neurons with two-photon stimulation and recording synaptic inputs from the postsynaptic neurons (Duan et al., 2014; Krishnaswamy et al., 2015).

7.2.4 Mapping electrical coupling from other neurons using Pept2

Pept2 method described in Chapter 6 provides an efficient way to map electrical synaptic connections from genetically defined neurons. I used it to map electrical synaptic connections from a subtype of RGCs called J-RGCs. In the future, it is worth applying it to other subtypes of RGCs to understand their electrical coupling and how this contributes to the function of these cells. Moreover, given that there are more and more evidence showing electrical coupling plays diverse roles in developing and adult animals (Apostolides and Trussell, 2013; Bloomfield and Volgyi, 2009; Connors and Long, 2004; Cook and Becker, 2009; Hormuzdi et al., 2004; Li et al., 2012; Yu et al., 2012; Zhu et al., 2013), it will be valuable to apply it to different subtypes of neurons in other part of the brain, for example, interneurons in the cortex which form extensive electrical synaptic connections. We can use Pept2 method to map electrical coupling from these neurons, study its formation during development and understand how it is modulated under different conditions.

7.4 References

Apostolides, P.F., and Trussell, L.O. (2013). Regulation of interneuron excitability by gap junction coupling with principal cells. Nat Neurosci *16*, 1764-1772.

Barlow, H.B., and Hill, R.M. (1963). Selective sensitivity to direction of movement in ganglion cells of the rabbit retina. Science *139*, 412-414.

Barlow, H.B., Hill, R.M., and Levick, W.R. (1964). Retinal Ganglion Cells Responding Selectively to Direction and Speed of Image Motion in the Rabbit. J Physiol *173*, 377-407.

Barlow, H.B., and Levick, W.R. (1965). The mechanism of directionally selective units in rabbit's retina. J Physiol *178*, 477-504.

Bloomfield, S.A., and Volgyi, B. (2009). The diverse functional roles and regulation of neuronal gap junctions in the retina. Nat Rev Neurosci *10*, 495-506.

Borst, A., and Helmstaedter, M. (2015). Common circuit design in fly and mammalian motion vision. Nat Neurosci *18*, 1067-1076.

Connors, B.W., and Long, M.A. (2004). Electrical synapses in the mammalian brain. Annu Rev Neurosci *27*, 393-418.

Cook, J.E., and Becker, D.L. (2009). Gap-junction proteins in retinal development: new roles for the "nexus". Physiology *24*, 219-230.

Duan, X., Krishnaswamy, A., De la Huerta, I., and Sanes, J.R. (2014). Type II cadherins guide assembly of a direction-selective retinal circuit. Cell *158*, 793-807.

French, C.A., Groszer, M., Preece, C., Coupe, A.M., Rajewsky, K., and Fisher, S.E. (2007). Generation of mice with a conditional Foxp2 null allele. Genesis *45*, 440-446.

Helmstaedter, M., Briggman, K.L., Turaga, S.C., Jain, V., Seung, H.S., and Denk, W. (2013). Connectomic reconstruction of the inner plexiform layer in the mouse retina. Nature *500*, 168-174.

Hormuzdi, S.G., Filippov, M.A., Mitropoulou, G., Monyer, H., and Bruzzone, R. (2004). Electrical synapses: a dynamic signaling system that shapes the activity of neuronal networks. Biochim Biophys Acta *1662*, 113-137.

Kay, J.N., De la Huerta, I., Kim, I.J., Zhang, Y., Yamagata, M., Chu, M.W., Meister, M., and Sanes, J.R. (2011). Retinal ganglion cells with distinct directional preferences differ in molecular identity, structure, and central projections. J Neurosci *31*, 7753-7762.

Kim, I.J., Zhang, Y., Yamagata, M., Meister, M., and Sanes, J.R. (2008). Molecular identification of a retinal cell type that responds to upward motion. Nature *452*, 478-482.

Kim, J.S., Greene, M.J., Zlateski, A., Lee, K., Richardson, M., Turaga, S.C., Purcaro, M., Balkam, M., Robinson, A., Behabadi, B.F*., et al.* (2014). Space-time wiring specificity supports direction selectivity in the retina. Nature *509*, 331-336.

Krishnaswamy, A., Yamagata, M., Duan, X., Hong, Y.K., and Sanes, J.R. (2015). Sidekick 2 directs formation of a retinal circuit that detects differential motion. Nature.

Kurt, S., Fisher, S.E., and Ehret, G. (2012). Foxp2 mutations impair auditory-motor association learning. PLoS One *7*, e33130.

Levick, W.R. (1967). Receptive fields and trigger features of ganglion cells in the visual streak of the rabbits retina. J Physiol *188*, 285-307.

Li, Y., Lu, H., Cheng, P.L., Ge, S., Xu, H., Shi, S.H., and Dan, Y. (2012). Clonally related visual cortical neurons show similar stimulus feature selectivity. Nature *486*, 118-121.

Oyster, C.W., and Barlow, H.B. (1967). Direction-selective units in rabbit retina: distribution of preferred directions. Science *155*, 841-842.

Shu, W., Cho, J.Y., Jiang, Y., Zhang, M., Weisz, D., Elder, G.A., Schmeidler, J., De Gasperi, R., Sosa, M.A., Rabidou, D*., et al.* (2005). Altered ultrasonic vocalization in mice with a disruption in the Foxp2 gene. Proceedings of the National Academy of Sciences of the United States of America *102*, 9643-9648.

Shu, W., Lu, M.M., Zhang, Y., Tucker, P.W., Zhou, D., and Morrisey, E.E. (2007). Foxp2 and Foxp1 cooperatively regulate lung and esophagus development. Development *134*, 1991-2000.

Sigal, Y.M., Speer, C.M., Babcock, H.P., and Zhuang, X. (2015). Mapping Synaptic Input Fields of Neurons with Super-Resolution Imaging. Cell *163*, 493-505.

Sun, W., Deng, Q., Levick, W.R., and He, S. (2006). ON direction-selective ganglion cells in the mouse retina. J Physiol *576*, 197-202.

Vaney, D.I., Sivyer, B., and Taylor, W.R. (2012). Direction selectivity in the retina: symmetry and asymmetry in structure and function. Nat Rev Neurosci *13*, 194-208.

Yu, Y.C., He, S., Chen, S., Fu, Y., Brown, K.N., Yao, X.H., Ma, J., Gao, K.P., Sosinsky, G.E., Huang, K*., et al.* (2012). Preferential electrical coupling regulates neocortical lineage-dependent microcircuit assembly. Nature *486*, 113-117.

Zhang, Y., Kim, I.J., Sanes, J.R., and Meister, M. (2012). The most numerous ganglion cell type of the mouse retina is a selective feature detector. Proceedings of the National Academy of Sciences of the United States of America *109*, E2391-2398.

Zhu, P., Frank, T., and Friedrich, R.W. (2013). Equalization of odor representations by a network of electrically coupled inhibitory interneurons. Nat Neurosci *16*, 1678-1686.